Faculty of Science and Engineering

Department of Imaging and Applied Physics

Nanoparticle Synthesis and the Addition of Group IV Elements for the Destabilisation of Magnesium Hydride

Anna-Lisa Chaudhary

This thesis is presented for the Degree of

Doctor of Philosophy

of

Curtin University

June 2013

Declaration

To the best of my knowledge and belief this thesis contains no material previously published by any other person except where due acknowledgement has been made. This thesis contains no material which has been accepted for the award of any other degree or diploma in any university.

Signature: ……

Date:……..

Dedicated to my loving husband Deeptangshu and

our two beautiful children Ettan and Keirra

Abstract

Hydrogen based energy systems have the capacity to produce clean, sustainable energy now and for future generations. This thesis explores the science behind hydrogen storage in metal hydrides for the ultimate goal of producing clean energy from hydrogen. Tailored hydrogen storage systems coupled with hydrogen powered fuel cells provide the flexibility of energy on demand for both mobile and stationary applications. This important field of research in metal hydride materials is the focus of this thesis for the Doctor of Philosophy degree.

The destabilisation of magnesium based alloys in combination with group IV elements, namely, silicon, germanium and tin is the area of research on which this work is based. The synthesis of silicon nanoparticles for the purpose of increasing desorption reaction kinetics with magnesium hydride is achieved experimentally. Silicon nanoparticles are synthesised using mechanochemical ball milling in a lithium chloride salt matrix. This matrix is then removed and the silicon nanoparticles characterised in terms of morphology, crystallinity and particle size. The nanoparticles were largely amorphous in nature and as a result phase identification was undertaken using methods such as electron energy loss spectroscopy and energy filtered transmission electron microscopy. The silicon nanoparticles were then mixed with magnesium hydride to observe the kinetic behaviour of the desorption reaction.

This thesis also analysed mixtures of MgH_2 and Si processed under different conditions to obtain varying crystallite/particle sizes. These mixes are then compared with the synthesised silicon mixture with respect to desorption reaction kinetics. Kinetic parameters such as nucleation activation energy, growth activation energy, rate limiting step, reaction constant and pre-exponential factor were determined. The aim was to gain an understanding of the relationship between crystallite size or particle size with chemical kinetics of MgH_2 with Si. Reaction kinetic information was then obtained and these results correlated with varying crystallite/particle sizes.

The next chapter looks at the reversibility of the Mg-Si-H system, namely magnesium silicide absorption. Here magnesium silicide nanoparticles are synthesised using mechanochemical methods similar to the method used to synthesise silicon. Nanoparticles are synthesised to give the absorption reactants the shortest diffusion distances possible to overcome the reaction barriers associated with this reaction. Hydrogenation is attempted at pressures above 1 kbar, 200°C. Several high pressure experiments are done to further analyse the absorption process for magnesium silicide.

The final chapter introduces Ge and Sn to the Mg-H system for thermodynamic destabilisation. A comparison was made with the Mg-Si system using isothermal and temperature programmed desorption experiments. $NaMgH_3$ is also destabilised with Si and the kinetic behaviour observed. The addition of group IV elements, Si, Ge and Sn to Mg-based hydrides led to the successful destabilisation of MgH_2 and $NaMgH_3$ resulting in hydrogen release at lower temperatures. The extent that these group IV elements affected desorption properties of MgH_2 and the effect of Si on $NaMgH_3$ is explored. Mg based alloys are formed and a discussion of thermodynamic equilibrium conditions and the difficulty in obtaining these conditions due to kinetic limitations is also discussed.

This Ph.D. thesis has endeavoured to further define the behaviour of magnesium based hydrogen storage systems. Thermodynamic and kinetic limitations are addressed through the synthesis of nanoparticles and both desorption and absorption reactions performed. The hypotheses of improved reaction kinetics using nanoparticles are explored. Finally, the conclusions are presented and a section on future work is included. These suggestions will further enhance the scientific knowledge gained from this research.

Acknowledgements

I would like to acknowledge all the people that have supported me through the course of my Ph.D. as you have been invaluable to my success. Thank you to Prof. Craig Buckley and Dr. Drew Sheppard for their supervision and guidance. You have both taught me how to be a true scientist; questioning all results from all angles. I would also like to thank the members of the Hydrogen Storage Research Group at Curtin University, Mark Paskevicius, Tian Huyong, Julie Murshidi and Somwan Chumphongphan for all the discussions both scientific and otherwise. A very big thank you to all those in the Department of Physics who have been extremely encouraging over the years, especially, Robert Loss, Melat Habtemariam, Glen Lawson, Mary Cukrov, Mark Winstanley, Grace Lamont and Carly Fleming.

To my family; you have all been extremely supportive throughout this experience. A special mention goes to my husband, Deeptangshu and of course our two children, Ettan and Keirra who were both born during the first two years of my studies. Also, to my parents, Christopher and Aurora who have been supportive of me regardless of my decision and have always had confidence in me and my abilities. To all my friends including the HDR students, mothers from Mother's group, mothers from Playgroup, parents from school, work colleagues past and present, thank you for being who you are and encouraging me when I needed it most.

Finally, I would like to acknowledge Curtin University for granting the Postgraduate Scholarship and Research Scholarship (CUPS and CURS) as well as the Australian Commonwealth Scientific and Research Organisation (CSIRO) for providing funding for the project including Dr. Jonian Nikolov, my supervisor from CSIRO. Thank you to the staff at the National Hydrogen Materials Reference Facility at Griffith University for undertaking one of the high pressure experiments. The TEM was carried out using facilities at the Centre for Microscopy, Characterisation and Analysis (CMCA), The University of Western Australia, which are supported by University, State and Federal Government funding. I also acknowledge Prof. Martin Saunders and Dr Alexandra Suvorova from the CMCA for their invaluable advice. I

would like to acknowledge the facilities, scientific and technical assistance of the Centre for Materials Research, Curtin University Electron Microscopy Laboratory.

Table of Contents

List of Figures

List of Tables

Chapter 1: Background

Aglaonike (2nd Century BCE, Ancient Greece) the first female astronomer (shown seated).

1.1 Introduction

Hydrogen based energy systems have the capacity to produce clean, sustainable energy now and for future generations. As global energy demands rise, so do concerns over climate change and depleting fossil fuel resources[1]. In turn, the shift towards energy production from renewable resources has gained considerable momentum[2, 3]. Tailored hydrogen storage systems coupled with hydrogen powered fuel cells provide the flexibility of energy on demand systems for both mobile and stationary applications. Finding an efficient and safe way to store hydrogen is one of the challenges to hydrogen fuel usage[4, 5]. It is this important field of research, hydrogen storage systems, that provides the platform for this Doctor of Philosophy thesis.

Hydrogen fuel has two main benefits: (1) it reduces atmospheric pollution, thereby addressing the climate change issue and (2) as an alternative fuel for mobile applications, it addresses the issue of depleting crude oil resources. Hydrogen is a non-polluting fuel, only emitting water vapour during energy conversion and can be produced sustainably from water using a range of renewable energy sources including solar photovoltaic, geothermal, solar-thermal, wind, hydro photo-electrochemical or biomass based electricity.

Hydrogen gas (H_2) has a low density (0.085 kg m^{-3} at 15°C, 1 bar) leading to one of the best energy density compared to gasoline, diesel, propane, coal or lithium batteries, however it has a very poor energy to volume ratio[6]. Current methods of H_2 storage such as compressed gas or liquid have many safety implications for mobile applications due to the low boiling point of hydrogen (20.4 K). A safer method is to store hydrogen in solid form as a metal hydride. An ideal metal hydride for transport applications must be able to react with H_2 gas near ambient temperature and pressure, have favourable sorption enthalpies and be able to undergo a number of absorption-desorption cycles without compromising its properties.

Magnesium (Mg) has generated a lot of interest as a hydrogen storage material. In the form of MgH_2, it is inexpensive, abundant and has a high hydrogen storage

capacity (7.6 wt.%). However, the strong bonds between magnesium and hydrogen lead to high thermodynamic stability (ΔH = 74 kJ mol^{-1} H_2, ΔS = 133 J mol^{-1} H_2 K^{-1})[7]. Also, sluggish reaction kinetics during the dehydrogenation process in bulk samples [8] have limited its practical use. This Ph.D. thesis explores changes in thermodynamic stability and reaction kinetics of MgH_2 hydrogen storage systems to move towards renewable, cheap and efficient source of energy.

1.2 Background

1.2.1 The Global Demand for Energy

The supply and demand for energy in modern society is a major driving force for global economies, government policies, environmental impact analyses, and is also an indicator for everyday living standards. To put the term 'energy' into context, it is first necessary to look at its definition. The scientific definition of 'energy' is the capacity of a physical system to perform work such as potential, kinetic, chemical, thermal, or electrical, measured in the International System of Units, Joules (J). To translate this definition on a global scale in the 21st century the term 'energy' is used to describe the production of primary fuel sources and is commonly measured in tonnes of oil equivalent (toe, where 1 toe = 42 GJ). To use a local example for types of energy sources, primary fuel supplies from Australia are outlined in Figure 1.1. Demand for this energy covers a broad range of areas including those outlined in Figure 1.2, with only 33% of this energy supply being used for the domestic market; the remainder providing the Australian economy with a significant export commodity.

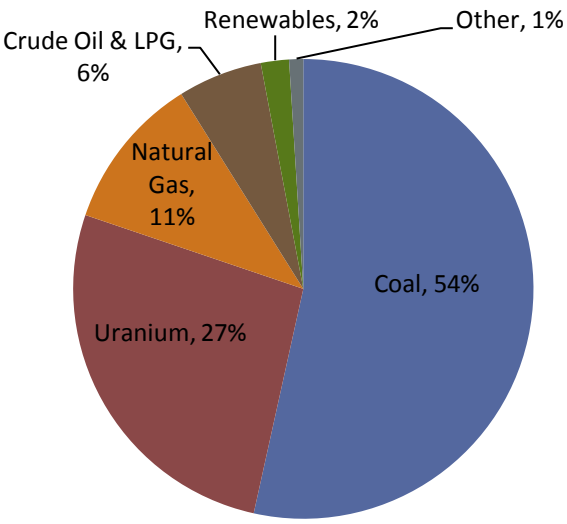

Figure 1.1: Australian Primary Fuel Supply Sources (Data adapted from [9]).

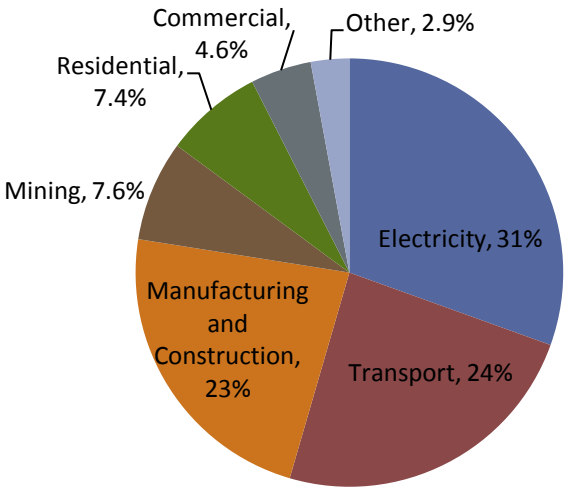

Figure 1.2: Australian Energy Demand (Data adapted from [9]).

The demand for energy is on the increase not only in Australia but worldwide. According to the International Energy Agency (IEA) global energy consumption is predicted to increase approximately 1.5% per year between 2007 and 2030 from 12000 Mtoe to 17000 Mtoe[10]. Currently, the dominant sources supplying these energy needs are non-renewable fossil fuels such as coal, gas and crude oil and account for up to 80% of global demand. Renewable energy, on the other hand, accounts for less than 1% of today's world energy supply and is only predicted to

increase a further 1% to the year 2030[10]. These future demands on energy have created a market for more environmentally responsible energy use and production that is beneficial not only for the current generation but also for those in the future. It is therefore a challenge to provide a sustainable supply of energy from renewable resources in order to meet the ever increasing demand.

1.2.2 The Need for Alternative Energy Systems

Despite the unimpressive figures for current renewable energy supply, there are many compelling arguments to introduce renewable energy technologies on a much larger scale. Firstly, global warming studies indicate severe consequences to our environment if we continue to emit greenhouse gases (GHG) at the current rate[11]. Climate change scientists from around the world have monitored rapid increases in carbon emissions in the last decade. As explained in Section 1.2.1, energy is largely consumed in sectors such as electricity generation, transport and manufacturing and are therefore the main emitters of carbon pollution within Australia. The rise in carbon based atmospheric gases have been attributed to extreme changes in weather patterns causing natural disasters such as drought, floods and cyclones to occur more frequently. Atmospheric temperature is also predicted to rise to levels that will melt both the north and south ice caps therefore endangering coastal and island communities due to sea level increases.

Another consequence of the rise in GHG is the changes in habitat that render extinction for some flora and fauna. Such strong scientific evidence on human influenced climate change has led to the introduction of government policies to reduce GHG emissions and to develop clean energy technology, including the Australian Federal Government (Clean Energy Bill 2011). This legislation puts a monetary value on carbon emitted into the atmosphere, therefore providing incentive for alternative non-carbon energy sources to be established on a national scale. It is therefore critical that environmental, social and economic impacts due to climate

change be reduced by the development of alternative non-carbon polluting energy generation.

Further to the environmental consequences, another problem is the use of non-renewable resources for energy production. For example, concerns over the limits to crude oil extraction have already been the subject of several studies including Abrams and Wiener [1] highlighting the future need for alternatives.

Renewable energy sources account for 2% of Australia's energy production (Figure 1.1). These include wind, solar photovoltaic, thermal solar, wave, geothermal, biomass for electricity, biodiesel and ethanol production for transport applications. A comprehensive definition of the most common renewable energies can be found in Section 1.5.1. There is also a number of accredited renewable energy sites located across Australia as shown in Figure 1.3. Although the introduction of the Clean Energy Bill will allow these technologies to be more economically competitive, to date, none have become widespread due to the high costs of manufacture and infrastructure compared to existing technologies.

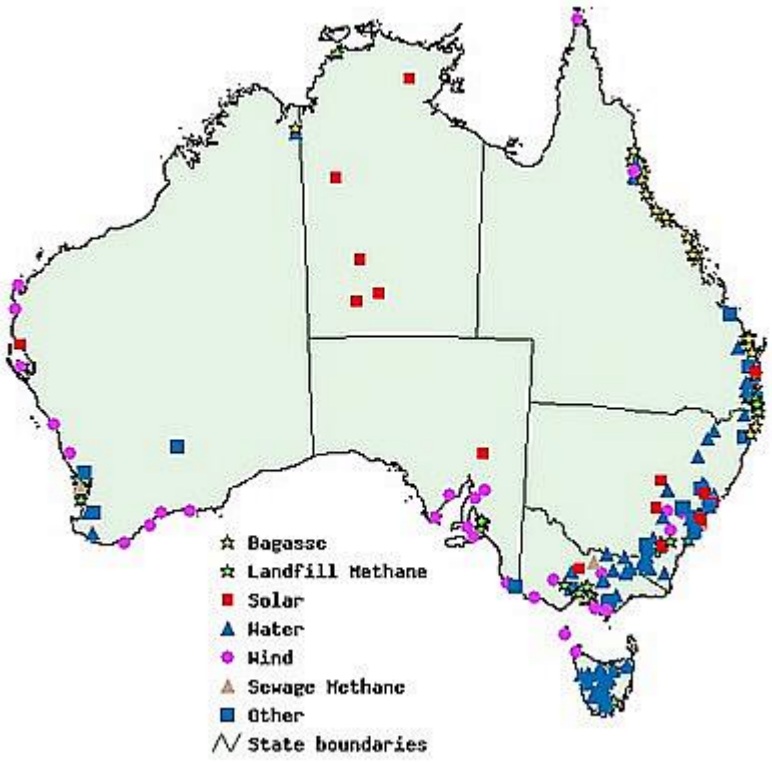

Figure 1.3: Map of Accredited Renewable Energy Sites in Australia Adapted from[12].

Of the many renewable energy sites in Australia, there is a noticeable absence of the use of hydrogen. This could be due to several reasons, including the lack of knowledge of the efficiency of a hydrogen system, lack of investment into hydrogen technologies, the high cost of hydrogen storage and transport as well as the high energy requirements to produce hydrogen gas (further detailed in Section 1.5.1). This thesis aims to address these issues by exploring the science behind magnesium hydride destabilisation using group IV elements.

1.3 Significance

A hydrogen based energy system has environmental, social and economic implications. The previous section has provided general background information

referring to the global demand for clean energy and how hydrogen storage fits into this global picture. This section further highlights the importance of hydrogen technology development with regard to the environment, financial stability and social improvement to outline the significance of the forth-coming dissertation.

Firstly, the environmental advantage of the use of hydrogen to fuel energy demand for transportation vehicles would be the reduction of the most significant GHG, carbon dioxide, in the atmosphere. There is worldwide support for reduced carbon dioxide emissions as there are currently 192 parties committed to the United Nations Convention on Climate Change (UNFCCC) Kyoto Protocol, including Australia (ratified in 2007). This Protocol is a legally binding agreement to reduce GHG emissions to a specified target. The use of hydrogen, when produced from renewable sources, is an excellent solution to this environmental problem as well as achieving the Kyoto Protocol GHG emission reduction targets.

The link between environmental consequences of global warming also has an important implication for economic management. For example, the recent droughts and floods that have occurred across Australia in the past decade have led to all tiers of government subsidising losses from businesses and aiding in natural disaster clean ups, hence lowering economic growth. Another economic consideration is the cost of energy itself. In Australia, the cost of household electricity has increased up to 40% in the past five years[13] and this is likely to become a worldwide trend. Several factors have contributed to this rise, including upgrading infrastructure, the increase in peak demand and in increase in the cost of fuel[14]. The rising cost of energy has a trickle on effect by increasing transportation and manufacturing costs, which is then passed onto the consumer. Cost has been a major obstacle to the widespread introduction of a hydrogen economy. These rising energy costs for both mobile and stationary fossil fuel based energy system will lead to hydrogen becoming a more viable alternative thus providing advantages economically as well as environmentally.

Following on from environmental and economic impacts is social responsibility. Current energy production is controlled by countries which supply fossil fuels such as crude oil and coal which has an impact on cost as well as worldwide distribution. A hydrogen based system on the other hand, when developed in conjunction with

renewable energy, can cater for autonomous and localised energy production minimising reliance on the current suppliers. Using hydrogen in place of fossil fuel also aims to combat climate change thus reducing the risk of rising sea levels which may also impact island and coastal communities. Renewable production of hydrogen also ensures a long term solution to fossil fuel depletion therefore securing the production of energy for future generations.

In order to highlight the practical advantages of hydrogen as an energy carrier, the entire system from production to use will be analysed with the main focus of this thesis being the aspect of hydrogen storage. Despite decades of research[15, 16, 17, 18, 19, 20] the production of hydrogen storage units coupled with commercially available electrolyser and fuel cell technologies is in its infancy. Many studies have focused on each of these components individually, that is, hydrogen production from renewable energy[21, 22], hydrogen storage systems[23, 24, 25] and hydrogen operated fuel cells [26]. This Ph.D. thesis will add to the knowledge gained by these previous publications and use a well-known hydrogen storage material, magnesium hydride in combination with group IV elements silicon, germanium and tin. The purpose is to develop an alternative system for stationary and mobile applications by recognising the operating conditions necessary for hydrogen storage and selecting economical viable materials. Thus a competitive alternative to fossil fuels can be offered.

Material costs, operating costs and safety of current hydrogen storage technologies are the primary reasons limiting its widespread use. The use of inexpensive metal hydrides such as magnesium hydride has the potential to address all of these issues and has therefore been selected for further study in this doctoral thesis. Like all materials in the area of hydrogen storage, magnesium hydride currently has limitations and it is these weaknesses that will be further addressed.

Despite years of research on magnesium and its alloys as a material for hydrogen storage, several issues are yet to be overcome including its thermodynamic stability and strong affinity to oxygen. This doctoral thesis aims to address these issues in detail. This includes the investigation into nanoscale hydrogen materials to improve reaction kinetics with a more thermodynamically viable system, Mg-Si-H. Other systems of using $NaMgH_3$ with Si and MgH_2 with Ge and Sn will also be discussed.

The investigation of hydrogen storage in magnesium based alloys in this thesis will not only further scientific knowledge on the topic but bring alternative energy solutions closer to reality.

1.4 Thesis Outline

Outlined here is a brief introduction to each of the chapters that will be presented in this Ph.D. thesis. The topics cover a range of materials using a variety of methods for material identification and characterisation.

Chapter 1: Background

This chapter opens the thesis and contains several sections to introduce the topic of hydrogen storage in magnesium hydrides. The background and significance sections explain the broader topic of the increasing international demand for energy and need to find clean, non-polluting solutions for future requirements. Included here is the literature review, a critical analysis of published material based on the thesis theme of magnesium hydride destabilisation and it explores shortfalls of the materials on which this research is based.

Chapter 2: Methodology

In order to synthesise and characterise hydrogen storage materials, a wide range of techniques are used. This chapter highlights the methods including a brief theoretical introduction to each of the techniques and reasons behind their use. There is also discussion on various differences, limitation and adaptations on traditional methods and how it applies to the analysis of hydrogen storage materials.

Chapter 3: Synthesising Si Nanoparticles

Reaction kinetics is the limiting factor of MgH_2 desorption with Si. To overcome this issue, nanoparticles of Si are synthesised using mechanochemical ball milling. The focus of this work is to synthesise small particles of Si (< 10 nm) to shorten the diffusion distances of MgH_2 with Si as H_2 is liberated during dehydrogenation thus

improving kinetic rates. This chapter describes in detail the method of synthesis and characterisation of the Si nanoparticles.

Chapter 4: Studying Desorption Kinetics of MgH_2 with Si

Magnesium hydride and silicon powders are prepared using various methods to produce a range of particles ranging in size from microns through to nanometres. The methods of mixing included ultrasonication, ball milling and cryomilling for different times. These methods result in varying particle and crystallite size that in turn influence the desorption behaviour of the decomposition reaction. Presented here is a morphological and crystallite size analysis for each of the preparation methods and how it relates to the reaction kinetics of the system.

Chapter 5: Synthesising Mg_2Si Nanoparticles for High Pressure Hydrogenation

The objective of this study is to reduce kinetic limitations of the reaction between Mg_2Si and H_2 by synthesising Mg_2Si nanoparticles. Nano-sized particles limit the migration distance for Mg atoms from the Mg_2Si matrix to produce MgH_2 and Si, thus potentially improving the reversibility of the Mg-Si-H system. Mg_2Si nanoparticles are synthesized using a reduction reaction undertaken by solid-liquid mechanochemical ball milling. High pressure hydrogen measurements are undertaken to attempt hydrogen absorption of the Mg_2Si nanoparticles. Under these absorption conditions bulk Mg_2Si cannot absorb hydrogen, demonstrating the kinetic benefit of nanoscopic Mg_2Si.

Chapter 6: Destabilising MgH_2 and $NaMgH_3$ using Group IV Elements Si, Ge and Sn

The addition of group IV elements of Si, Ge and Sn to Mg-based hydrides has led to the successful destabilisation of MgH_2 and $NaMgH_3$ resulting in hydrogen release at lower temperatures. The extent that these group IV elements affect desorption properties of MgH_2 and the effect of Si on $NaMgH_3$ is investigated. The aim of this study is to use similar chemistry of Si by replacing it with Ge or Sn, to observe the differences in the diameter of the group IV elements and whether it has an effect on the diffusion rate of the elements in the Mg_2M phase (M = Si, Ge, Sn). With respect

to $NaMgH_3$ with Si, it is 10 kJ mol^{-1} H_2 more stable than MgH_2, therefore at higher temperatures; the diffusion rate will improve without the equilibrium pressure becoming impractically high.

Chapter 7: Conclusions and Future Work

The final chapter of this thesis summarises the work on magnesium alloys as hydrogen storage materials. Conclusions have been given regarding the advantages and disadvantages of the research and recommendations for future research in this topic have been outlined.

1.5 Literature Review

It has been established in Section 1.2.2 that there is a need for clean, renewable and sustainable energy and that hydrogen systems are a solution to addressing these needs. To elaborate on this area of research, a comprehensive literature review was undertaken. This section is a critical review and analysis of published literature on hydrogen storage systems including that of magnesium hydride based systems. This literature review also identifies shortfalls in the current field of research that will provide a platform to base the research for this doctoral thesis.

1.5.1 Renewable and sustainable hydrogen energy systems

Renewable and sustainable energy systems are the future of global energy supply. Renewable energy is a rapidly growing industry as it provides key sustainable solutions as the viable alternative to fossil fuels. Hydrogen is an energy carrier and is the most abundant element in the universe; however, hydrogen naturally exists in compounds such as water (H_2O) or organic materials such as methane (CH_4). To be used as a source of energy, high purity hydrogen needs to be obtained and this is usually achieved *via* various separation methods depending on the raw material.

Table 1.1 shows both conventional and renewable energy methods of producing hydrogen from these compounds and the relative CO_2 emissions. The key issue for producing sustainable future energy is the reduction of global greenhouse gases; therefore, conventional methods will be excluded from this study. Instead, electrolysis powered by renewable energy will be further explained and how a hydrogen storage system is required for this technology to be feasible for various applications.

Table 1.1: Production of hydrogen using different methods and CO_2 emission[27].

Method		Current Global production of H_2 (%)	H_2 from H_2O (%)	CO_2 emission (kg) per kg of H_2 production at 75% efficiency
Conventional	Steam reforming of natural gas (methane)	48	50	7.33
	Partial oxidation of hydrocarbons	30	5.3	12.35
	Coal gasification	18	70	29.33
Renewable (Electrolysis)	Solar PV	4	100	0
	Wind power			
	Hydropower			

The process of electrolysis (Eqn. 1.1) uses electrical input to decompose water molecules (H_2O) into oxygen (O_2) and hydrogen gas (H_2)[28]. The main advantage of this process is that renewable energy can be used to produce hydrogen gas without any CO_2 emissions therefore minimising the effect of GHG on the environment. Despite its environmental advantage, electrolysis is an energy intensive process and calculations show that approximately 53 kWh is needed to produce 1 kg of hydrogen operating at 75% efficiency[29]. A recent study on a commercially available electrolyser only has an efficiency up to 60% with 0.48 A cm^{-2} of current density[30]. This high energy process increases the cost of hydrogen production significantly when compared to the more conventional methods therefore reducing its economic viability and rendering the current global production of hydrogen using electrolysis to only 4%.

Eqn. 1.1 $2H_2O(l) \rightarrow H_2(g) + 2O_2(g)$ **(ΔG^0 = 236.83 kJmol^{-1}, at 1 bar, 25°C)**

For environmentally responsible hydrogen to be produced using electrolysis, that is, without any GHG emissions, renewable energy is required. Renewable energy is defined as the energy production from the naturally occurring energy currents and includes non-carbon technologies such as solar energy, hydropower, wind, tide and waves and geothermal as well as carbon neutral such as biomass[31]. A brief summary of some of the most common renewable energy in use today is given in Table 1.2. Renewable energy, once established also provides a platform for sustainable energy production. By definition renewable sources such as solar and wind will not undergo depletion rates similar to that of coal or crude oil thus providing a viable alternative to currently employed energy systems. The disadvantage of these forms of renewable energy is cost as well as the lack of ability to store the energy for on-demand power supply. Hence the need for a compatible technology for hydrogen storage that can store hydrogen and produce energy as required.

Table 1.2: Current Renewable Energy Technologies.

Technology	Definition
Solar thermal	Concentrated solar power using mirrors to capture the thermal energy from the sun to heat water, oil or molten salt to produce steam for powering an electrical generator.
Solar photovoltaic (PV)	PV cells that directly convert solar energy to electricity.
Wind	Rotating turbine blades that drive an electrical generator hence the development of wind farms.
Wave	Use of sub-surface buoys anchored to the seabed to pump seawater at high pressure to shore. This water turns a generator to create electricity.
Geothermal	Hot geological formations where the rock is fractured hydraulically and water is pumped down and circulated repeatedly, transferring heat to the surface to generate electricity
Biomass	Plant matter converted into electricity by decomposing under controlled conditions to produce a hydrogen rich gas that can run a turbine or a fuel cell.

1.5.2 Electrolyser and Fuel Cell Technology

In order to design an efficient and cost effective hydrogen storage unit, it is important to understand the components of a complete energy system. Firstly, the production of hydrogen *via* renewable energy and secondly, the use of hydrogen with a fuel cell in order to produce electricity for a range of applications including both mobile and stationary. Figure 1.4 shows a complete system for stationary energy supply. Similarly, a mobile system would produce hydrogen using an electrolyser; store this hydrogen in a bulk system before being stored on-board. The fuel cell would then use this on-board hydrogen to run the motor of a moving vehicle. This section briefly describes both the production of hydrogen using electrolysis and also the production of energy from hydrogen using fuel cells and the criteria required to match a hydrogen storage system to each.

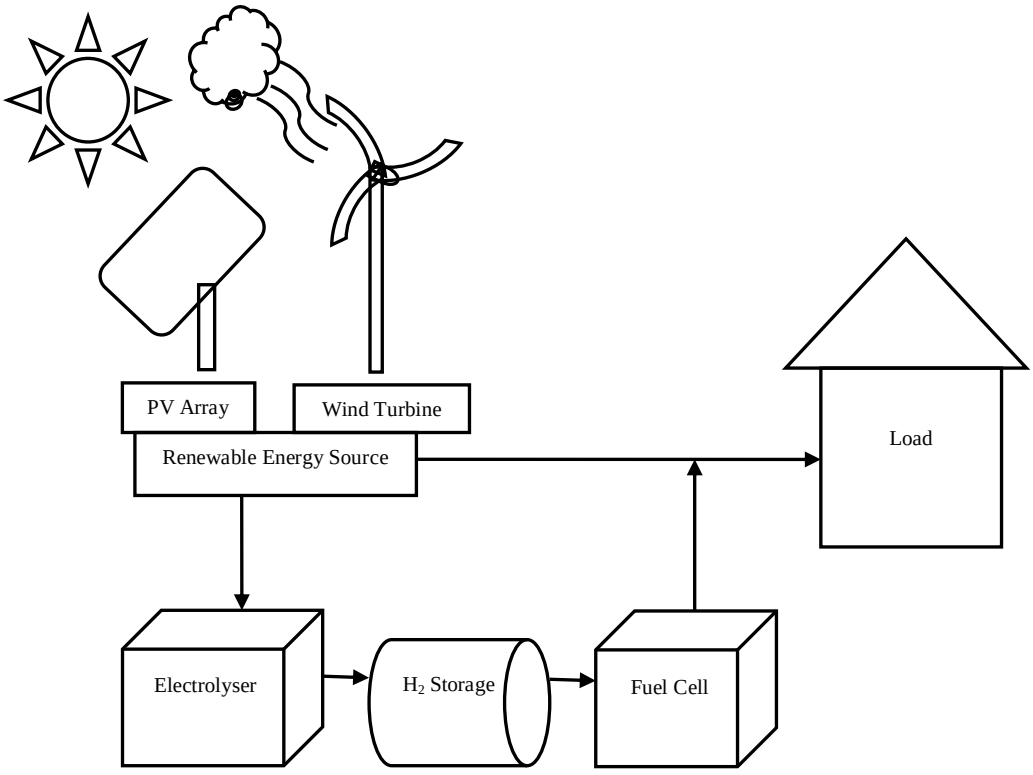

Figure 1.4: Renewable Energy Stand Alone Power System (SPS).

There are a number of commercially available technologies that use electrolysis to produce pure hydrogen *via* electricity generated from renewable sources. The three main types of electrolysers are alkaline, solid oxide and proton exchange membranes (PEM) each defined by the electrolyte used. Although each manufacturer has varying specifications, typical operating conditions of available electrolysers are given in Table 1.3. The use of solid oxide cells for the production of hydrogen is not readily available commercially and will not be further analysed in this study. On the other hand, alkaline and PEM technologies have been developed over the past few decades and warrants further analysis in order to produce and use hydrogen within a complete energy system.

Table 1.3: Characteristics of commercially available electrolysers (data adapted from [28]).

Cell type	Alkaline	Proton Exchange Membrane	Solid Oxide
Operating Pressure (bar)	3 – 30	1 – 70	1
Operating temperature (°C)	50 – 100	80 – 100	800 – 1000
Electrolyte / Membrane	KOH / NiO	Solid / proton exchange polymer membrane	Zirconia ceramics
Energy efficiency (%)	75 – 90	80 – 90	80 – 90

When used in combination with the aforementioned renewable energy supplies, an electrolyser can produce hydrogen without the by-product of greenhouse gases. Coupling renewable energy with an electrolyser requires several criteria to be met. Firstly, the electrolyser must match the energy source, that is, the PV panels or wind turbine energy in terms of current and voltage must match that of the electrolyser itself.[16] Another consideration is that the electrolyser must operate near maximum power output in order to provide maximum efficiency[16]. Likewise, operating conditions of a hydrogen storage system should be matched to the electrolyser. As alkaline and PEM types of electrolyser are most suitable for the production of hydrogen, pressures ranging from atmospheric to a maximum of 70 bar and

temperatures from room temperature to 100°C would be optimum for hydrogen storage materials. These materials will be further investigated in later sections.

In order to match currently available fuel cells to specific applications for hydrogen storage systems, it is first necessary to define the fuel cell and its operating conditions. A fuel cell works on the reverse electrochemical reaction to an electrolyser creating energy rather than consuming it. Fuel cells generate power by combining hydrogen (pure, from a hydrogen storage system) and oxygen (from air) *via* the electrochemical reaction shown in Eqn. 1.2 where the by-products include water and heat. There is a broader range of fuel cells compared to electrolysers and a summary of these and their operating conditions is given in Table 1.4.

Eqn. 1.2 $$H_2(g) + \frac{1}{2}O_2(g) \rightarrow H_2O(l)$$ **($-\Delta G^0$ 237 kJmol^{-1}, at 1 bar, 25°C)**

Table 1.4: Types of Fuel Cells (data adapted from[28]).

Cell type	Alkaline (AFC)	Proton Exchange Membrane (PEMFC)	Solid Oxide (SOFC)	Molten Carbonate (MCFC)	Phosphoric Acid (PAFC)
Operating Pressure (bar)					
Operating temperature (°C)	100 – 200	50 – 100	600 – 1000	650	150 – 200
Electrolyte / Membrane	KOH	Thin permeable polymer membrane	Ceramic metal oxides	Salt carbonates (NaCO3 or MgCO3)	Phosphoric acid
Electrode Catalyst	Platinum	Platinum		Nickel	Platinum
Energy Output	10 kW – 100 kW	1 – 250 kW	1 kW – 3 MW	2 – 100 MW	50 kW – 11 MW
Energy efficiency (%)	60 – 70	45 – 60	35 – 60	60 – 80	40 – 80

There are a number of benefits when a fuel cell is used to create electricity over other types of energy producing technology. For example, current exchange densities for the anodic reaction are at least three to five orders of magnitude higher than any other fuel at low to intermediate temperatures[28]. Fuel cells also provide a system of

energy that has zero greenhouse gases or air pollutants therefore addressing the growing demand for clean energy systems as outlined in Section 1.2.2.

Similar to electrolysers, fuel cell costs have been a major drawback to the use of this clean technology. In order to reduce these costs and provide high purity hydrogen, a suitable storage system is yet to be developed. Some of the criteria that needs to be addressed when coupling a storage system with either stationary or mobile fuel cells include, the ability to quickly respond to energy demand (reaction kinetics), high efficiency, moderate operating temperatures and pressure (thermodynamics), suitable power output range for the particular application, being a reasonable physical size for its practical use, and above all, to conform to safety requirements[16].

1.5.3 Important factors to consider for any hydrogen storage system

The United States Department of Energy (DOE)[32] is a federal government department in charge of addressing energy, environmental and nuclear issues through science and innovation within the United States of America. As a result of its considerable investment into energy solutions, it has become a world leader in energy research including hydrogen storage technology and has developed a detailed list of future targets for on-board hydrogen storage systems. A summary of these targets is given in Table 1.5 and a full table of these targets with the associated definitions and footnotes can be found in Appendix A.

Table 1.5: Abstract of DOE technical targets for on-board hydrogen storage systems (updated 2009).

Storage Parameter	Units	2010	2015	Ultimate
System Gravimetric Capacity:	wt. % H_2		5.5	7.5
Usable, specific energy from H_2	$kWhkg^{-1}$ ($kg\ H_2 kg^{-1}$ system)	1.5 (0.045)	1.8 (0.055)	2.5 (0.075)
System Volumetric Capacity:	$kWhL^{-1}$	0.9	1.3	2.3
Usable energy density from H_2	($kg\ H_2 L^{-1}$ system)	(0.028)	(0.040)	(0.070)
Storage System cost:	gge^{-1} at pump	3–7	2–4	2–4
Fuel Cost	(gge: gasoline gallon equivalent)			
Durability/Operation:	°C	-30/50	-40/60	-40/60
Operating ambient temperature				
Min/Max delivery temperature	°C	-40/85	-40/85	-40/85
Operational cycle life (1/4 tank to full)	Cycles	1000	1500	1500
Min delivery storage pressure from system; FC = fuel cell, ICE = internal combustion energy	bar	5 (FC) 35 (ICE)	5 (FC) 35 (ICE)	3 (FC) 35 (ICE)
Max delivery storage pressure from system	bar	12 (FC) 100 (ICE)	12 (FC) 100 (ICE)	12 (FC) 100 (ICE)
Onboard efficiency	%	90	90	90
Charging/Discharging Rates	Min ($kg\ H_2\ min^{-1}$)	4.2 (1.2)	3.3 (1.5)	2.5 (2.0)
System fill time (5 kg)				
Fuel Purity (H_2 from storage)	% H_2	99.97% dry basis		
Environmental Health and Safety		Meets or exceeds applicable standards		
Permeation and Leakage				
Toxicity				
Safety				
Loss of useable H_2	(gh^{-1})kg H_2 stored	0.1	0.05	0.05

These targets provide guidelines for research and development teams around the globe however, not all applications need to adhere to such strict criteria. Forklifts are an example that can withstand a heavier 'fuel storage' system and which means that materials with lower capacity than outlined in the table above can be considered. Several companies have already undergone trials using a hydrogen storage/fuel cell system to eliminate harmful gases in a closed environment such as a warehouse[33, 34,

[35, 36, 37]. Further, stationary uses for energy such as a remote area power supply broaden the criteria. Research in this field is relatively new and shows a lot of promise for current hydrogen storage materials[38, 39, 40, 41].

1.5.4 Hydrogen storage categories

Hydrogen can be stored in a range of media across a number of technologies that all have the objective of developing practical hydrogen storage applications. Regardless of the application, storing hydrogen using metal hydrides requires certain material characteristics to be known before a storage system can be designed. These characteristics include material synthesis, activation, hysteresis, reversible capacity, operating temperatures and pressures, hydrogenation kinetics, cycle life and decrepitation. Figure 1.5 shows several methods and materials in relation to the DOE targets outlined in Table 1.5. In terms of volumetric capacity and gravimetric capacity, many materials exceed the ultimate DOE targets set for on-board hydrogen storage. However, other criteria such as operating temperatures, operating pressures and cyclability fall short of the requirements. This section further details each of the hydrogen storage technologies indicating advantages and disadvantages of each.

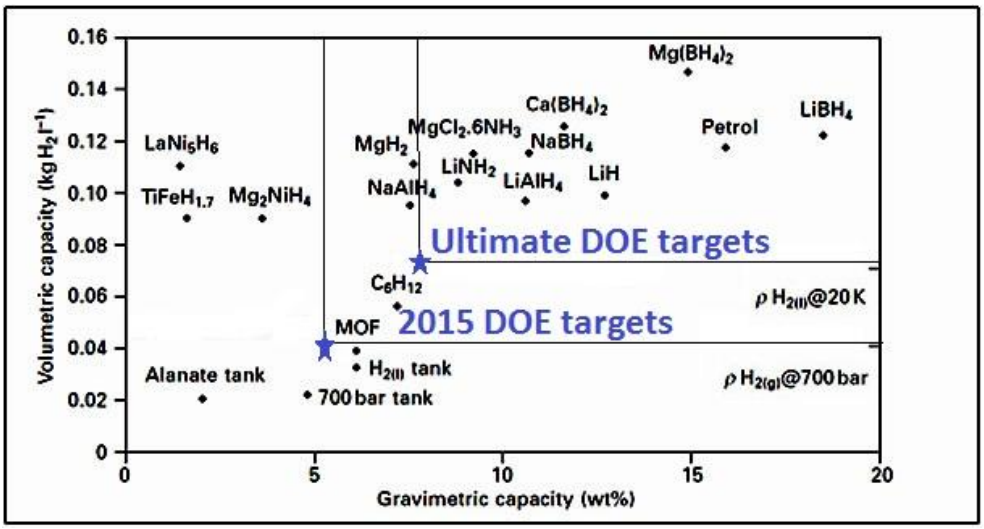

Figure 1.5: Hydrogen Storage Capacities for a range of storage media, including system capacities for stores based on liquid hydrogen, compressed hydrogen and hydrides. For reference the density of liquid hydrogen and hydrogen gas at 700 bar are given on the right hand side of the graph. (N.B. gravimetric capacity for both is 100%). Adapted from [42].

1.5.4.1 Compressed gas

The storage of hydrogen in pressure vessels is already widely used for current applications such as on-board vehicles. Similar to the existing storage of compressed natural gas, these vessels have a working pressure ranging from 35 MPa (350 bar) through to 70 MPa (700 bar)[5]. Despite compressed gas cylinders dominating current hydrogen storage methods there are several disadvantages. These include, the high weight of the high strength storage containers; high pressure safety concerns; high energy required to compress the gas to 35 – 70 MPa (15 – 20% of energy content of the hydrogen required for compression); and tank embrittlement due to the charging and discharging of the cylinder[42, 43]. Another concern is the limitation of materials used for the pressure vessels. A cylindrical storage tank is ideal for compressed gas however this geometry limits space for a transport vehicle therefore limiting its practical use[42]. It is for these reasons that is would be difficult for compressed gas hydrogen storage to be able to meet the DOE targets listed in Table 1.5.

1.5.4.2 Liquid storage

Liquefied gas storage is a well-established technology. It has a much higher energy density than compressed gas and is easier to transport. The disadvantage of liquefied hydrogen is that the liquefaction, storage and handling of cryogenic boiling liquids not only require large amounts of energy but also complex tank systems and infrastructure to meet safety requirement which would increase costs. The process of liquefying hydrogen involves the hydrogen being compressed to 30 bar. The gas is cooled with liquid nitrogen to 80 K. To further reduce the temperature to 30 K, expansion turbines are used. Joule-Thomson valves are then employed to obtain a temperature of 20 K (–253°C). This process requires 20 to 30% of the energy content of the hydrogen. Storage in cryogenic liquefied form, takes place in an open system leading to issues with boil off as well as loss of hydrogen due to diffusion, or impurities.

1.5.4.3 Physically bound hydrogen

This method employs physically bound hydrogen gas to a high surface area substrate such as carbon based materials, aerogels, carbon nanotubes, zeolites, metal organic frameworks and polymers of intrinsic microporosity. Hydrogen molecules are held onto the surface through weak van der Waals interactions which has a low enthalpy of adsorption of 4 – 10 $kJmol^{-1}$ [42]. These materials have gravimetric and volumetric capacities close to DOE targets (Table 1.5) with excellent cyclability. However, the system operates at 77 K requiring liquid nitrogen to be used during adsorption especially since the reaction is exothermic. The use of cryogenic liquids is a major setback to physisorbed hydrogen storage due to the boil off of liquid nitrogen and the tank design; however it is a cheaper alternative to liquid hydrogen as it operates at a higher temperature.

1.5.4.4 Chemically bound hydrogen

Chemically bound hydrogen is the focus of this thesis as magnesium and its alloys readily form metal hydrides when reacted with hydrogen. This mechanism involves the hydrogen gas reacting with a chemical to form a solid chemical compound which can also be released through thermal decomposition. In contrast to physisorption, where hydrogen molecules are bound to a surface *via* van der Waals forces, hydrogen atoms are chemically bound with other atoms. Hydrogen stored in this solid state method has several advantages over gas and liquid methods. Firstly, as shown in Figure 1.5, volumetric densities far exceed those of gas and liquid. Secondly, this solid state method of hydrogen storage is capable of storing and releasing hydrogen at near atmospheric temperatures and pressures that potentially allows them to be matched to the electrolyser/fuel cell systems described in Section 1.5.2 (pressures of 1 – 70 bar at temperatures close to 100°C). Thirdly, the safety risks are lower compared to compressed gas and liquid hydrogen storage.

There are a few distinct categories of this type of hydrogen storage including ionic hydrides, covalent hydrides and metal hydrides and each will be discussed briefly.

1.5.4.4.1 Ionic hydrides

Ionic hydrides are where the metal hydrogen (M-H) bond displays ionic characteristics rather than covalent characteristics and consist of a hydrogen atom bound to an electropositive metal[44]. These are formed from alkali metal or alkaline earth metals and examples include LiH and NaH.

1.5.4.4.2 Covalent hydrides

Covalent hydrides are defined by the strong, localised bonding in the two or three centres of a discrete unit. This class covers a range of compounds such as alane, boranes, borohydrides, hydrocarbons, amines, amides and ammonia complexes.[44]

1.5.4.4.3 Interstitial hydrides

In contrast to covalent hydrides, interstitial hydrides form a M-H bond that is highly delocalised and can exist as a multi-centred compound, similar to that of metallic bonding. Metal alloy hydrides and metal hydride intermetallic compounds fall into this category. Metal alloy hydrides are characterised by varying composition and substitution in a primary element such as Pd, Ti or Zr. These materials have attractive hydrogen storage properties such as $Ti_{0.97}$-$Zr_{0.019}$-$V_{0.439}$-$Fe_{0.097}$-$Cr_{0.045}$-Al-$_{0.026}$-$Mn_{1.5}$ alloy which can reversibly store hydrogen at ambient temperature[45]. Intermetallic compounds consist of homogeneous composition and crystal structure and include AB_5 (e.g. $LaNi_5$), AB_2 Laves Phases (e.g. $MgCu_2$), AB (TiFe) and A_2B (Mg_2Ni) materials. A and B are defined as elements that have a high affinity for hydrogen (A) and a low affinity for hydrogen (B)[43].

1.5.5 Hydrogen Storage Drawbacks

Research spanning several decades[46, 47, 48, 49, 50, 51, 52] has made improvements in metal hydride characteristics but there are still obstacles that need to be addressed including those detailed by Srinivasan[28]:

- Thermal management is required i.e. a cooling system is required for exothermic hydrogen absorption and heating is required for endothermic hydrogen desorption.
- The kinetics of the system can be sensitive to impurities.
- The presence of O_2 in the system can be a potential fire hazard. The small particle size of metal hydrides can make them pyrophoric in the presence of O_2 thus consequent safety concerns arise.
- The expense of the overall system is too high.

This thesis addresses some of these issues including thermal management, kinetics and high expense. With respect to thermal management and expense, materials such magnesium and silicon will be investigated as they are abundant and inexpensive. The combination of these two materials lowers thermodynamic stability thus reducing operating temperatures and the need for energy consuming thermal management systems. Kinetic limitations of the reactions involving magnesium with group for elements, silicon, germanium and tin will also be explored to improve the transport of hydrogen into and out of the system. For these reasons, this thesis will focus on the improvement of metal hydrides systems specifically relating to magnesium and associated alloys.

1.5.6 Why are Magnesium Based Metal Hydrides ideal?

Magnesium hydride (MgH_2) in its pure form has been synthesised and characterised since the 1950s[53, 54] and continues to provide scientific interest in the area of hydrogen storage today. The reason this material has sparked such interest over the past sixty years within the scientific and engineering communities is that it has many advantages (Section 1.5.6.1) that match the hydrogen storage criteria mentioned in Section 1.5.3 and MgH_2 based systems can potentially provide long term clean global energy storage solutions. The Mg-H_2 system is exothermic on absorption and endothermic on desorption[8]. MgH_2 in its pure form has high thermodynamic stability and slow reaction kinetics (1.5.6.2), limiting its widespread use as a hydrogen storage material. Reaction kinetic issues have largely been over come through particle size reduction and the addition of catalysts[55, 56, 57, 58, 59]; however there are still challenges to improving the system (mentioned in Section 1.5.4.4) that provide the basis of the research for this thesis. There are a number of review papers that already provide detailed information on magnesium hydride materials[5, 42, 51]. The literature review included here is a brief summary of these papers and how the research in this thesis was formulated to further investigate MgH_2 based materials. This section also critically analyses the shortfalls of past studies, therefore providing

future direction for magnesium based hydrides and a platform for the research presented in this doctoral thesis.

1.5.6.1 Advantages of MgH_2

The abundance of magnesium within the Earth's crust makes it accessible for practical applications including the storage of hydrogen. Magnesium is an alkaline earth metal and is the eighth most abundant element in the Earth's crust (approximately 2% by mass)[60]. Similar to hydrogen, rather than existing in its pure elemental form, it occurs naturally in compounds, for example as a salt ($MgCl_2$) or in minerals such as dolomite, $(CaMg)(CO_3)_2$ or magnesite, $MgCO_3$. China is currently the world's largest producer of magnesium, producing 650,000 tonnes in the year 2010[61]. Magnesium is also recyclable and recycling plants are in operation around the world including, Japan, Germany, UK and USA[61]. This high availability of magnesium ensures that it is competitive globally in terms of cost as detailed in the next section.

Overall hydrogen storage system cost is one of the DOE criteria yet to be achieved (Appendix A). However, the cheaper the raw materials are to manufacture, the more cost effective the system will be. The current market price for pure magnesium is US\$3.0 kg^{-1} (Table 1.6); a relatively inexpensive material when compared to other metal prices that are viable hydrogen storage candidates (Table 1.6). Silicon, germanium and tin prices have been added for comparison as these materials will be used throughout the research presented in this thesis.

Table 1.6: Current market prices of high purity raw materials (mt: metric tonne)(Source: http://www.metalprices.com/).

Metal	Price (US$/kg)	Purity (%)	Date Sourced
Magnesium	$3.20	99.9	27/04/13
Lanthanum	$1800	99	27/04/12
Nickel	$24.20	Premium grade	24/05/13
Calcium	$2.25	99.9	13/05/13
Lithium	$64.50	99	27/04/12
Silicon	$2.50	99	27/04/12
Yttrium	$110	Metal	27/04/12
Copper	$9.40	Bar	28/04/12
Chromium	$12.90	99.2	27/04/12
Zinc	$2.30	Ingot	28/04/12
Vanadium	$398	99.5	27/04/12
Iron Ore	$0.14	62 Fe	27/04/12
Aluminium	$2.40	Ingot	28/04/12
Germanium	$1250	99.99	31/03/12
Tin	$26.30	Ingot	28/04/12

Hydrogen storage capacity is another attractive feature of pure magnesium metal. The absorption of hydrogen into magnesium has a high reversible weight fraction capacity (7.6%)[8]. Further, Sakintuna *et. al.*[51] refers to magnesium as having the highest energy density of all reversible hydrogen storage materials (9 MJ kg^{-1} Mg). Other functional properties of magnesium include its light weight, heat resistance, vibration absorbing, reversibility with no hysteresis, and recyclability[51]. Despite these advantages there are also limiting factors to the widespread use of magnesium as a hydrogen storage material and these are explained in the next section.

1.5.6.2 Disadvantages of MgH_2

There are several disadvantages to storing hydrogen in magnesium resulting in its limited commercial use. Firstly, MgH_2 has high thermodynamic stability. The Mg-H bonds are quite stable which leads to a high enthalpy of dissociation (76.1 $kJmol^{-1}$ [62]) resulting in a high desorption temperature of over 300°C. A number of studies, both theoretical and experimental, have attempted to reduce the dissociation enthalpy of MgH_2 and will be further discussed in Section 1.5.7. Another major issue of the Mg-H_2 system is its slow reaction kinetics. Dornheim *et. al.*[63] describes the reaction of magnesium in several distinct steps for both absorption and desorption. The absorption mechanism consists of a physisorption surface reaction, dissociation and chemisorption, diffusion of hydrogen into the subsurface and bulk lattice sites and finally hydride formation by nucleation and growth. For desorption the mechanism can be described as the initial nucleation of magnesium followed by hydrogen atom diffusion into the surface and the formation of hydrogen molecules that physically desorb. A final disadvantage of the use of magnesium metal is its strong affinity to oxygen and air. When exposed to air, magnesium forms a highly stable oxide layer (MgO). This layer inhibits the diffusion of hydrogen into the magnesium matrix thus increasing activation energies[51]. The formation of MgO also increases the difficulty of using conventional alloying techniques to produce intermetallic magnesium compounds for hydrogen storage. Despite these setbacks for the use of MgH_2, the advantages are readily apparent. Hence, many studies have been undertaken to overcome these difficulties and are discussed in the next section.

1.5.7 Optimising the MgH_2 system for practical applications

1.5.7.1 Thermodynamics

The thermodynamic properties of a hydrogen storage system are important to define and analyse as it is these properties that determine its suitability for practical

operating systems. This study largely explores materials that have operational temperatures and pressures close to that of the electrolyser/fuel system in order to minimise the need for compressors and other auxiliary equipment, which in turn reduces the cost of the overall system. As mentioned in the previous section, MgH_2 has high thermodynamic stability resulting in impractical operating temperatures above 300°C at atmospheric pressure. In order to understand how the thermodynamics of a system can be alternated it is first necessary to define what is meant by thermodynamics of a metal hydride system.

Gross *et. al.*[44] defines thermodynamics as the study of equilibrium states and the transitions between them. In order to derive an equation that relates temperature and pressure to a system's thermodynamic properties (enthalpy, entropy, Gibbs free energy), each component needs to be understood. Firstly, the change in enthalpy (ΔH) of a system is defined as the relationship between the work of the system (ΔU), the pressure at the boundary of the system (p) and the volume (ΔV) (Eqn. 1.3). Entropy (ΔS) is a state variable measuring the amount of disorder within a given system with the unit of energy divided by temperature ($J\ K^{-1}$). Entropy is a function of the amount of thermal energy that is not available to do work in a closed system and can be expressed using the first law of thermodynamics for a reversible system (Eqn. 1.4). Further, Gibbs free energy (ΔG) is the portion of the total system that is available for work and can be expressed using Eqn. 1.5. By substituting Eqn. 1.3 into Eqn. 1.5, the Gibbs free energy equation is reached where temperature and pressure are constant i.e. in equilibrium. The equilibrium of a metal hydride with H_2 gas involves these enthalpic and entropic elements, (Eqn. 1.6), where ΔG is the change in Gibbs free energy (kJ), ΔH, the change in enthalpy ($kJ\ mol^{-1}$ of H_2), T, temperature (K) and ΔS is the change in entropy ($J\ K^{-1}\ mol^{-1}$ of H_2).

Eqn. 1.3 $$\boldsymbol{dH = dU + pdV}$$

Eqn. 1.4 $$\boldsymbol{dU = TdS - pdV}$$

Eqn. 1.5 $$dG = dU + pdV - TdS$$

Eqn. 1.6 $$\Delta G = \Delta H - T\Delta S$$

To further understand the thermodynamic properties of a metal hydride system, magnesium hydride will be used as an example. Eqn. 1.7 shows the reaction of magnesium with hydrogen gas to form magnesium hydride. The enthalpy of reaction is the change in enthalpy during the reaction and in this case is equal to 74 kJ per mole H_2[7] which is exothermic and results in an equilibrium temperature of 282°C at 1 bar of pressure. This reaction has three distinct phases as shown in the phase diagram or pressure composition temperature (PCT) isotherm given in Figure 1.6 (a). During the first stage of the reaction (I), low concentrations of H_2 dissolve into the metal lattice and a solid solution or α-phase forms with the same crystal structure as the host metal[44], in this case, magnesium (Mg). As the pressure and hydrogen concentration increases, nucleation or β-phase develops (II) in coexistence with the α-phase. The plateau pressure at which this occurs is referred to as the equilibrium pressure. A pure β-phase (tetragonal, TiO_2 rutile structure) is reached when further increases in hydrogen pressure/concentration (III) take place[8].

Eqn. 1.7 $$Mg(s) + H_{2(g)} \leftrightarrow MgH_2(s)$$

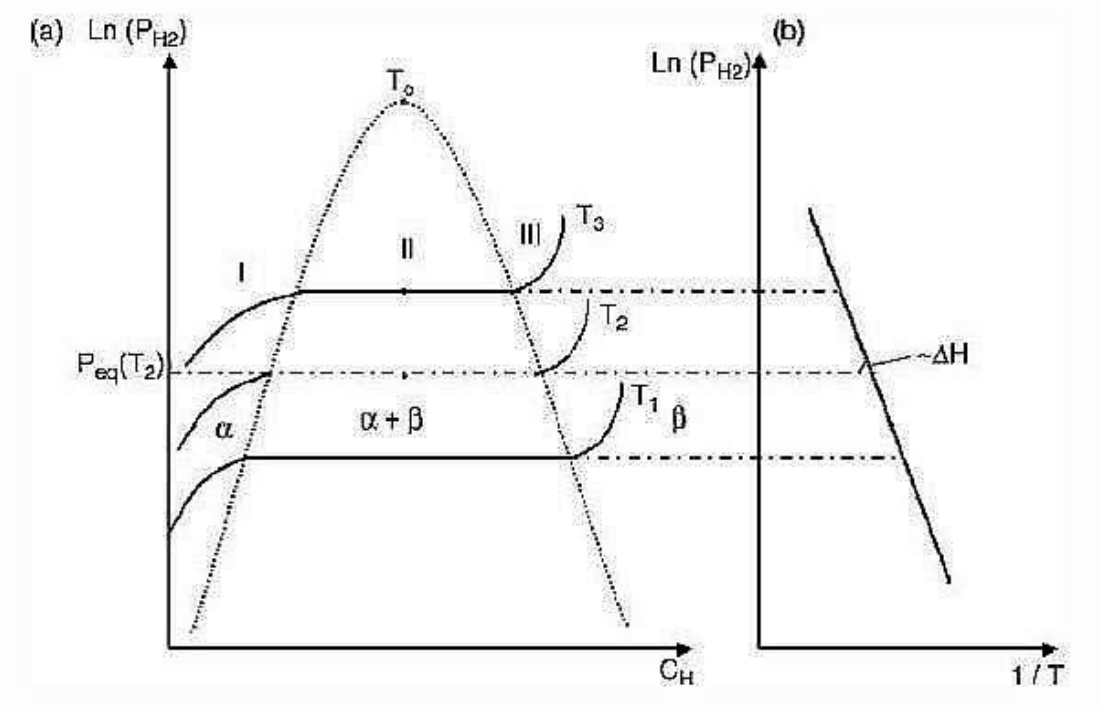

Figure 1.6: (a) Schematic of a pressure-composition-temperature (PCT) isotherm. α is the solid solution of hydrogen and β is the hydride phase. (b) van't Hoff plot giving the enthalpy of hydride formation, ΔH[64].

For a given material, equilibrium pressures at different temperatures are given by the van't Hoff plot (Figure 1.6 (b)). The van't Hoff is derived from the van't Hoff equation (Eqn. 1.9) that defines the relationship between the equilibrium constant (K), temperature and change in enthalpy, ΔH. Gaseous equilibrium further extends the definition of K to mean fugacity (f). Fugacity has units of pressure and is related to the concentration of the gas leaving the phase in which it is bound[65, 66]. (see Section 2.11.1 for more information). The relationship between the equilibrium constant and Gibbs energy is given in Eqn. 1.8, where R is the universal gas constant. Therefore, the slope of the van't hoff plot relates to the enthalpy (ΔH) and the intercept relates to the entropy (ΔS) of sorption (Eqn. 1.9).

Eqn. 1.8 $$\frac{dlnK}{dT} = \frac{\Delta H}{RT^2}$$

Eqn. 1.9 $$\Delta G = -RTlnK = \Delta H - T\Delta S$$

1.5.7.1 Thermodynamic Stability

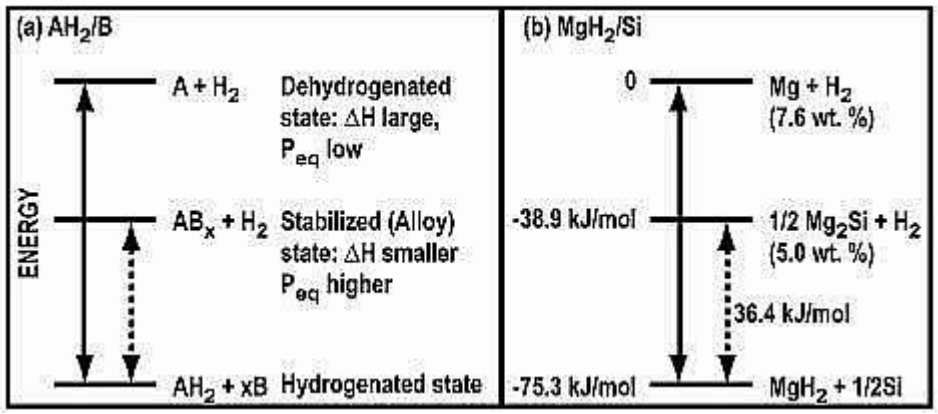

Figure 1.7: Energy diagrams illustrating hydride destabilization through alloy formation upon dehydrogenation[67].

Using similar criteria to Alapati[68], the thermodynamic parameters will be used to identify temperatures and pressures of a system that would be compatible with electrolysers and fuel cells. Alapati[68] estimates, using the Gibbs free energy equation, that for $95 \leq \Delta S \leq 140$ JK^{-1} mol^{-1} (entropic contributions for most metal hydride reactions is 130 $JK^{-1}mol^{-1}$ [69]) and for the temperature of the system to be suitable for electrolyser/fuel cell technologies, i.e. 50 – 150°C, this requires that enthalpic values be in the range of $30 \leq \Delta H \leq 60$ kJ mol^{-1} H_2. Using these criteria, ΔH values much more than 60 kJ mol^{-1} of H_2 will result in impractical hydrogen pressures and below 30 kJ mol^{-1} per H_2 reversibility will be reduced. One such system has that fits this criteria is shown in Vajo[67] which adds Silicon (Si) to MgH_2 desorption thus lowering the enthalpy required to release hydrogen (Figure 1.7, Eqn.1.10). The ideal behaviour of the Mg-Si-H system has created further interest in the field of hydrogen storage[64, 70] as it can theoretically store and release hydrogen at 20°C at atmospheric pressure. However, kinetic limitations are apparent[71] and reversibility has been difficult to achieve[72]. This Mg-Si-H_2 system will be further explored in consequent chapters

(Chapters 3 – 5) of this thesis as it theoretically has potential to meet much of the hydrogen storage criteria previously discussed.

Eqn.1.10 $$2MgH_2 + Si \rightarrow Mg_2Si + H_2$$

1.5.7.2 Reaction Kinetics

During hydrogen absorption, the formation of a MgH_2 layer around a metallic Mg core slows the diffusion rate of hydrogen atoms into the Mg matrix[8]. The formation of a nucleation site for the growth of the β-phase MgH_2 in the Mg matrix of a particles occurs at one or more points on the surface of the particle. These points are very well separated therefore the growth of the β-phase occurs outward from these points and in some cases eventually coalesces. The diffusion of H_2 in MgH_2 is very slow $D = 1.5 \times 10^{-16}$ m^2 s^{-1} [73] or 1.1×10^{-20} m^2 s^{-1} [74] depending on how the diffusion is measured. This is the principal factor that appears to lead to the presence of segments of untransformed Mg in particles even when exposed to a high pressure hydrogen environment.

When studying the reaction kinetics of materials it is important to consider factors such as the rate limiting step, heat of reaction, thermal conductivity, embrittlement, sample size, crystallite size, particle size, surface properties and purity. Some studies have found correlations between some of these factors. One example is that the rate of diffusion of hydrogen into the metallic matrix is dominated by particle size[75]. Other factors that have an impact on reaction kinetics include the presence of defects in the metallic matrix[76], grain boundaries[77] and catalysts[78, 79, 80] such as transition metals[81].

The Mg-Si-H system is economically advantageous as a hydrogen storage medium for renewable energy systems whilst moving towards sustainable energy production. In theory, Mg_2Si is an ideal material for hydrogen storage applications as it is predicted to have a hydrogen equilibrium pressure of 1 bar at 20°C or 100 bar at

150°C (*HSC Chemistry* 6.12 software, 2007, Outotech Research). Despite this, kinetic limitations prevent rehydrogenation from occurring and the most vigorous attempt to directly rehydrogenate Mg_2Si, up to 350°C and 1850 bar, was unsuccessful[72]. Hydrogen desorption from MgH_2 in the presence of Si is achievable, forming Mg_2Si. However, absorbing hydrogen into magnesium silicide (Mg_2Si) remains problematic due to severe kinetic limitations. The objective of this study is to reduce these kinetic limitations by synthesising Si nanoparticles for enhanced kinetics during MgH_2 desorption and Mg_2Si nanoparticles for H_2 absorption. The aim of synthesising nanoparticles is to limit the migration distance between each material for both desorption and absorption reactions, thus improving the reversibility of the Mg-Si-H system. Secondary to this, in Chapter 6, a systematic study comparing the effect of Si, Ge and Sn on MgH_2 as well as Si on $NaMgH_3$ will be explored. This will aid in the understanding of how the Group IV elements destabilises the Mg based hydrides to fulfil the aims of the thesis.

1.1 Summary

The introductory chapter of this doctoral thesis outlines the background and significance of the research project. The global need for clean energy is the main driving factor behind this research and the requirement to provide a cost effective energy supply using renewable energy coupled with a suitable storage system and finally linking this storage system with fuel cell technology. Also, discussed is an analysis of the literature, published in the area of hydrogen storage, specifically focussing on the research questions related to hydrogen storage in magnesium based materials. Group IV elements including, Si, Ge and Sn therefore have been added at various particle sizes to MgH_2 to further develop the possibility of reversible hydrogen storage in magnesium hydride with improved thermodynamic and reaction kinetic parameters.

Chapter 2: Experimental

Elena Cornaro Piscopia (1646 – 1684, Italy) First woman to receive a Doctor of Philosophy Degree.

2.1 Introduction

Throughout the duration of this doctoral thesis research, a number of synthesis methods and analytical techniques were studied and modified to obtain the best experimental results possible with minimal uncertainty. This chapter explains each of the methods in detail to give the results of the work a sound basis and also to give the reader a clear scientific methodology from which the discussion and conclusions in future chapters are based. Included in this chapter are the reasons behind the use of the technique, details of the equipment and software, basic theories and principles as well as the differences, limitations and adaptations of the methods due to the nature of the hydrogen storage materials studied.

2.2 Materials

Table 2.1 gives a list of material information (in alphabetical order) from the suppliers used throughout the course of experiments.

Table 2.1: Summary of materials used as provided by the manufacturer.

Chemical	Chemical Formula	Purity (%)	Supplier
Argon Gas	Ar	99.997	BOC Australia
Ethanol	CH_3OH	99.8	VWR BDH Prolabo
Helium Gas	He	99.999	BOC Australia
Hydrogen Gas (Ultra-High Purity)	H_2	99.9995	BOC Australia
Germanium	Ge	≥ 99.999	Sigma-Aldrich
Lithium (granules)	Li	99.9	Sigma-Aldrich
Lithium aluminium hydride	$LiAlH_4$	95	Aldrich
Lithium chloride	LiCl	≥ 99	Sigma-Aldrich
Lithium hydride (powder, -30 mesh)	LiH	95	Aldrich
Magnesium (turnings reagent grade)	Mg	98	Sigma-Aldrich
Magnesium chloride	Mg_2Cl	≥ 98, < 0.5% insoluble	Sigma-Aldrich
Magnesium hydride	MgH_2	H_2 storage grade, 95	Sigma-Aldrich
Magnesium oxide	MgO	≥ 99	Sigma-Aldrich
Nitrogen Gas	N_2	99.99	BOC Australia
Silicon (powder, -325 mesh)	Si	99	Sigma-Aldrich
Silicon tretrachloride	$SiCl_4$	99.998	Aldrich
Sodium borohydride	$NaBH_4$	99.99	Aldrich
Tetrahydrofuran (THF)	$(CH_2)_4O$	Anhydrous 99.9 with 250 ppm BHT inhibitor	Sigma-Aldrich
Tin	Sn	≥ 99	Sigma-Aldrich
Toluene	$C_6H_5CH_3$	Anhydrous 99.8	Sigma-Aldrich

2.3 Sample Preparation

All sample preparation described in this thesis was undertaken in a controlled inert atmosphere of argon (Unilab Glovebox, mBraun, Germany). The automatic gas purifier unit maintained low oxygen (O_2 < 1 ppm) and moisture (H_2O < 1 ppm) levels to avoid sample contamination and limit any reactions with either O_2 or H_2O. To load and unload samples in and out of the glovebox, two antechambers were used. Each antechamber was evacuated for a minimum of 10 min and flushed several times with argon prior to accessing the main section of the glovebox.

2.4 Material Synthesis

2.4.1 Milling

Traditionally milling is a technique used for reducing particle size of materials to a fine powder. Recently, this technique has now been adapted to tailor materials with enhanced physical and mechanical properties[55, 82], to produce new phases[83] and even to synthesise new materials[84, 85]. Two well-known techniques, rod milling and ball milling are described in this section in detail as these methods were used to mix powders, reduce particle size and to synthesize fine powdered materials with sizes in the nanometre range.

2.4.2 Cryomilling

Rod milling at cryogenic temperatures is referred to as cryomilling. A Spex SamplePrep 6850 Freezer Mill (USA) was used to reduce particle size and mix powders, especially when soft materials were used (Table 2.2). Milling these soft materials at room temperature would result in agglomeration and cold welding, hence the need to increase brittleness by lowering operational temperatures. Each sample was weighed and along with a stainless steel rod shaped impactor (145.5 g) was placed in either a 190 mL polycarbonate vial capped with stainless steel ends or a 14.3 cm^3 custom made stainless steel canister with stainless steel caps. These canisters were loaded into the freezer mill then immersed in liquid nitrogen (77 K) and allowed to reach thermal equilibrium before commencing the grinding cycle. The mill pulverizes the materials by magnetically shuttling the steel rod impactor back and forth against two stationary end plugs.

The following parameters were programmed into the mill:

- Cycle, number of cycles: One cycle consists of a period of grinding time (*T1*) followed by a period of cooling time (*T2*).
- *T1*, Grinding time: Length of time for the grinding period.
- *T2*, Re-cooling Time: Length of time for the cooling period between grinding periods.
- *T3*, Pre-cooling Time: Time of the pre-cooling period prior to actual grinding.
- Rate, Impact Frequency: Number of back and forth movements of the impactor per second.

Table 2.2: Comparison of material hardness.

Material	Mohs Scale of Hardness Scale 1 softest – 10 hardest
Li	0.6
Sn	1.5
Mg	2.5
LiCl	3.0
MgH_2	4.0 [86]
Ge	6.0
Stainless Steel	5.5 - 6.3
Si	6.5

2.4.3 Ball milling

Ball milling was used for material preparation, powder blending, particle and crystallite size reduction. This technique was also used to induce mechanochemical reactions to form nano-sized particles. All ball milling was undertaken in an argon atmosphere at room temperature in a 316 stainless steel custom made ball milling canister with an internal chamber volume of 650 cm^3 (Figure 2.1) set onto a Glen Mills Turbula T2C Shaker-Mixer. The canister was designed such that no corners or dead space could trap powder and cause uneven mixing. To avoid contamination

from either moisture or oxygen, the canister was sealed at both ends with rubber o-rings and tightly fastened stainless steel plates. 316 stainless steel balls were used at various ball-to-powder ratios.

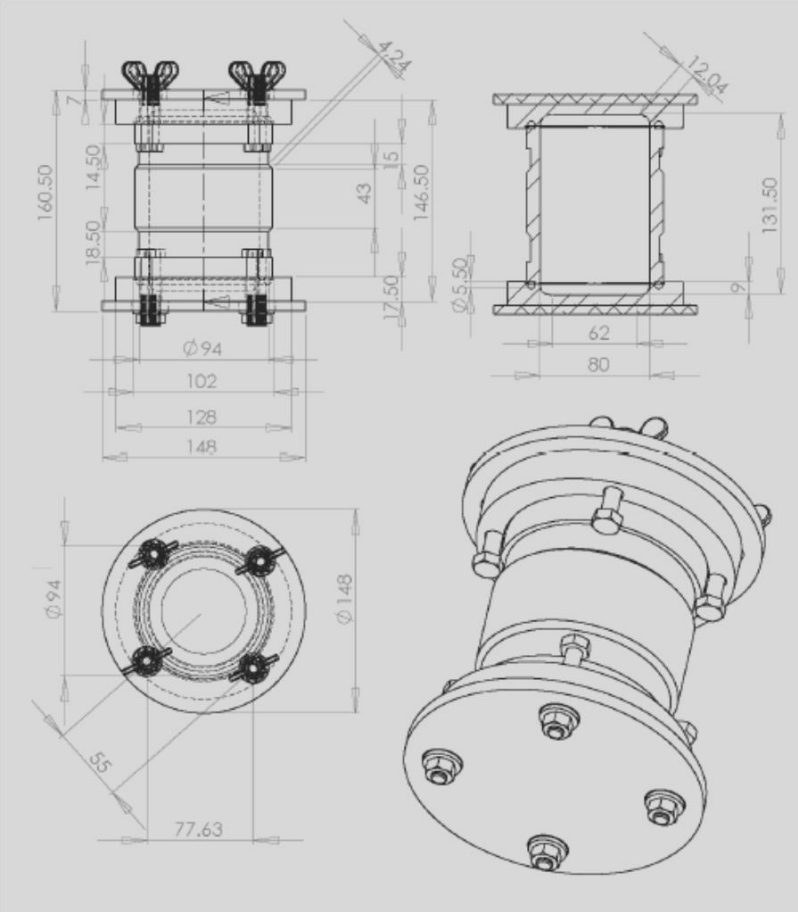

Figure 2.1: Custom-made ball milling canister. All measurements are given in mm [87].

2.4.4 Mechanochemical Synthesis

Mechanochemcial ball milling is a recently developed method to synthesise nanoparticles within a salt matrix[84, 88, 89]. This method is unique in that it combines low temperature chemical reactions with high energy mechanical processing[84]. In addition, the use of a soluble salt matrix can control the size of the nanoparticle formed during the reaction.

In the work presented here, both silicon and magnesium silicide nanoparticles were separately synthesised using mechanochemical ball milling in a lithium chloride salt matrix. Once the reactions were complete, the samples were placed in fluorinated ethylene propylene (FEP) centrifuge tubes (Nalgene, Oak Ridge) with THF. The tubes were sealed with Teflon tape used on the sealing cap assembly provided from the manufacturer to prevent any leakage. THF was used as the solvent to dissolve the LiCl as it is inert when mixed with Si or Mg_2Si. To aid in the dissolution of LiCl a stir bar was placed in the tube with the sample and then placed on a magnetic stirrer for a minimum of 30 min. A centrifuge was used (Kokusan H-103N Japan (3000 rpm), or Universal 320, Hettich, Germany (9000 rpm)) to separate the nanoparticles from the salt solution. The THF-salt solution was decanted with a glass pipette so that the solid particles remained and a new THF volume was added. The centrifugal separation process was repeated several times to remove as much LiCl as possible. After the final 'wash', the THF solution was decanted to a low level without disturbing the nanoparticles and the remaining THF was evaporated under Ar atmosphere, leaving pure nanoparticles.

2.4.5 Ultrasonication

Ultrasonication is the irradiation of a liquid sample with high frequency sound waves. These waves cause microscopic gas bubbles to form and collapse which in turn causes a pressure wave that agitates the solution. This method was used for both material synthesis and sample preparation prior to characterisation. For each application, an ultrasonic bath from Unisonics (Australia) was used. This bench-top chamber used sonic energy provided by piezoelectric transducers bonded to the tank bottom with a frequency of 40 kHz. Water was used as the medium inside the ultrasonic chamber and the experimental samples were sealed in small sample vials/flasks mixed with an inert medium, such as toluene or THF, within the argon glovebox to prevent exposure to water and air. For material synthesis, the method used in this thesis is described in Wu *et. al.*[90]. Here ultrasonic solution reduction was

used to form germanium nanocrystals under ambient conditions. Similarly, this method was employed to produce silicon nanoparticles (Chapter 3). Ultrasonication is also commonly used as a sample preparation method for the separation of nanoparticles prior to microscopy analysis[91]. For both transmission electron microscopy (Section 2.7) and scanning electron microscopy (Section 2.9) samples were suspended in either THF or toluene, sealed in a sample vial and placed in the ultrasonication chamber for 30 min. Ethanol and other oxygen containing solvents were not suitable as these were highly reactive with the sample.

2.5 X-Ray Diffraction (XRD)

X-Ray diffraction measurements were conducted using a Bruker D8 Advance X-ray diffractometer (Curtin University) with Bragg-Brentano geometry (Figure 2.2) and a copper anode tube (λ = 1.5418Å). Generally a 2θ range of 10° – 100° with a step size of 0.02° and 0.7 s of count time per step were used however, these conditions were modified to produce better diffraction patterns when necessary. A LynxEye detector that can measure 192 angular ranges simultaneously was used with the diffractometer. The instrumental parameters for this set up are given in Table 2.3. Each sample holder was placed on a rotating stage in order to reduce preferred orientation of crystals.

Table 2.3: XRD parameters for the LynxEye detector.

Parameter	Value
Primary soller slits (°)	2.5
Secondary soller slits (°)	2.5
Fixed antiscatter slit (mm)	8
Motorised divergence slit (°)	0.3°
Pixels	192 pixels covering 3.0°
Voltage (kV)	40
Current (mA)	40

For samples with a high Ni content, the XRD settings were altered to reduce the measurement of fluorescence, that is, the higher background created when elements such as iron, manganese and nickel are measured. These settings do not reduce the fluorescence from the samples; rather, it reduces the measurement of fluorescence thus lowering the background values detected. Comparisons of the default and background reduction settings are given in Table 2.4.

Table 2.4: Setting changes from default to Ni rich.

Parameter	Default settings	Settings to reduce fluorescence measurement
Lower level discriminator (V)	0.11	0.18
Window width (V)	0.14	0.05
Measured range (V)	0.11 to 0.25	0.18 to 0.23

Bruker *Diffracplus EVA* version 16 and *Diffracplus TOPAS* version 4.2 were used to analyse the XRD data. *Diffracplus EVA* was used to identify phases present in the XRD pattern and powder diffraction files were then obtained from the International Centre for Diffraction Data (ICDD) database (PDF4+ 2012 edition). Values from the equipment geometry were entered into the instrumental parameters setup *Diffracplus TOPAS* before any data analysis was done (Table 2.5). The fundamental parameter (FP) approach[92] was employed within the Rietveld refinement process with all XRD data analysis to determine quantitative data and crystallite size of the materials present in the sample.

Table 2.5: TOPAS Fundamental Parameter settings for LynxEye Detector experimental setup.

Goniometer radii	Value
Primary radius (mm)	250
Secondary radius (mm)	250
Equatorial Convolutions	
2ϑ angular range of LPSD (°)	3
FDS angle (°)	0.3
Beam spill, sample length (mm)	20
Axial Convolutions Full Axial Model	
Source length (mm)	12
Sample length (mm)	25
RS length (mm)	17
Primary Soller (°)	2.5
Secondary Soller (°)	2.5
N Beta	30

2.5.1 Theory of XRD

X-ray diffraction is the measurement of the intensity of X-rays scattered from electrons bound to atoms. Waves scattered at atoms at different positions arrive at the detector with a relative phase shift therefore measuring intensity yield information about the relative atomic positions[93]. The principle of XRD is based on Bragg's law (Eqn. 2.1) where λ is the wavelength of the incident X-ray beam, 2θ is the angle of incidence between the incident ray and the scattering planes, half the value of the peak position, d is the distance between atomic layers in a crystal and is calculated from n, an integer. The diffraction of the X-ray beam can be expressed in terms of a set of crystallographic planes, *hkl* or Miller indices which determines the peak position within a diffraction pattern. All crystalline materials have a unique diffraction pattern (or 'finger print') and therefore this technique can be used to identify crystalline substances.

Eqn. 2.1 $$n\lambda = 2d_{hkl}sin\theta$$

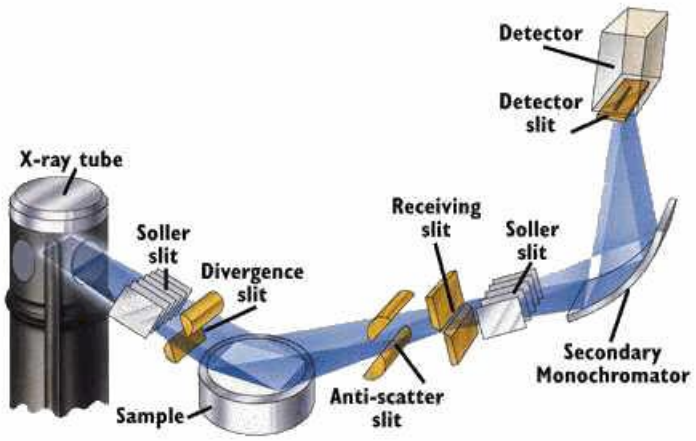

Figure 2.2: Bragg-Brentano Geometry used for XRD[94].

The powder diffraction method[95] was used for phase identification and to obtain structure information of the materials, provided the samples were crystalline in nature. This method can analyse a sample of powered material that consists of many small crystals in random orientation. From the Bragg reflections measured by the instrument, intensity and 2θ values data are collected. These values can then be matched to published data stored in the ICDD database and therefore crystalline phases and structure can be identified. For unknown phases, further analysis is required through methods such as the Rietveld refinement.

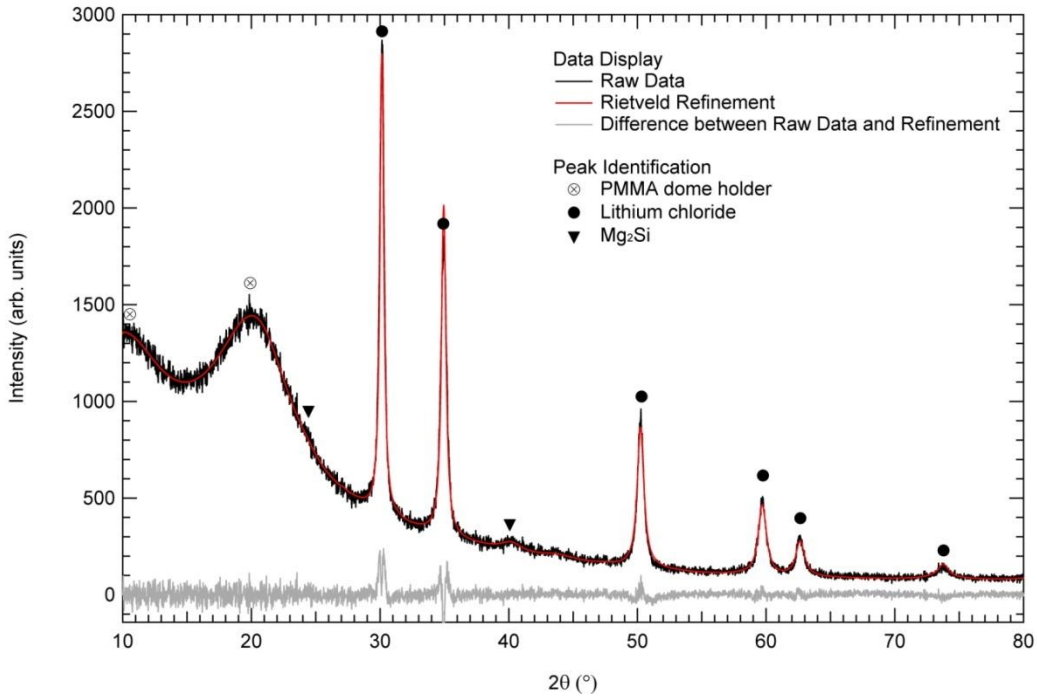

Figure 2.3: XRD data example showing raw data (black), Rietveld refinement (red) and difference curve (grey).

Rietveld analysis refines the parameters defined by the instrumentation in combination with the material to fit a model to the whole XRD pattern. The method uses the least squares refinement until the calculated values best fit the observed pattern. The calculated values are based on the refined models for the crystal structure(s), diffraction optics effects, instrumentation factors and lattice parameters[96]. One important aspect of Rietveld analysis is the calculation of crystallite size from the diffraction pattern. The relationship between peak broadening due to small crystallite size and the Bragg reflections can be expressed using the Scherrer equation (Eqn. 2.2)[92]. The Scherrer Equation calculates crystallite size using the parameters, L, the crystal dimension, 0.94, a numerical constant related to the Gaussian approximation of the peak maxima and the half maximum peak widths, β, the full maximum half width and λ, the wavelength of the X-ray beam. This equation assumes that the crystals are free from strain and faulting therefore the only effect of peak broadening is due to small crystallite size.

Eqn. 2.2 $$L = \frac{0.94\lambda}{\beta cos\theta}$$

An extension of the Scherrer equation is used by TOPAS to calculate crystallite size. TOPAS uses the LVol-IB (volume weighted mean column height) that incorporates Lorentzian and Gaussian convolutions varying in 2θ as a function of $1/\cos(\theta)$ and $\tan(\theta)$ respectively[97].

Goodness of fit and uncertainties were taken from *TOPAS* in terms of the Rietveld weighted profile value, R_{wp}, (the lower the value the better the fit), the difference curve (shown as the grey plot Figure 2.3, the difference between the raw data and the calculated refinement values) and the *TOPAS* generated uncertainties using the bootstrap method of error determination. A point to note is that these uncertainties are for the mathematical fit of the calculated pattern to the measured pattern.

2.5.2 Adaption of XRD techniques for Hydrogen Storage Materials

2.5.2.1 Air-tight specimen holder

Powder diffraction samples are usually prepared on an XRD holder that exposes the sample to air. Due to the nature of hydrogen storage materials, that is, high reactivity to air and/or water, samples had to be kept in an inert atmosphere during collection of the diffraction pattern. All materials were analysed in a Bruker supplied airtight specimen holder ring with dome type, X-ray transparent cap. The base and dome of holders were made from poly(methyl methacrylate) (PMMA) and were sealed together in the Ar atmosphere glovebox using a rubber o-ring thus preventing exposure to air and moisture (Figure 2.4). The presence of the PMMA dome resulted in the appearance of two amorphous humps at low 2θ angles around 10° and 20° (Figure 2.3).

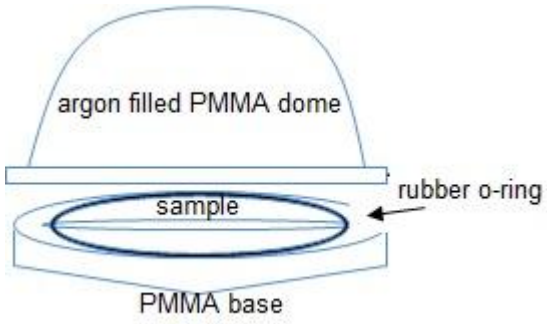

Figure 2.4: PMMA specimen holder for environmentally sensitive samples.

2.5.2.2 Limited sample quantities

Some of the materials synthesised were made in quantities too small to completely fill an air-tight specimen holder shown in Figure 2.4. XRD measurements were made possible using a silicon crystal low background specimen holder with a PMMA dome to seal the sample in Ar. The drawback to using this type of holder was that the intensity of the small amount of sample was diminished by the existence of the amorphous humps at 10° and 20° 2θ. To improve the intensity of the material some XRD was performed replacing the PMMA dome with a 300 nm thick aluminium leaf. This leaf was sealed onto the low background holder using petroleum jelly to prevent exposure to air without the PMMA bubble.

2.5.2.3 Amorphous specimens

The technique used to synthesise nanosized silicon (Chapter 4) led to the production of amorphous samples. In order to increase the possibility of detecting any crystalline particles in these samples the primary soller was removed thus increasing the intensity of the XRD pattern. The primary soller controls the axial divergence of the X-ray beam before it reaches the sample. Removal of this soller allows the air scattering to be more apparent in the primary beam, thus increasing the background in the resultant diffraction pattern. This was therefore accounted for when the Rietveld modelling was undertaken in Bruker *Diffracplus TOPAS* version 4.2.

2.6 Small Angle X-ray Scattering

Small Angle X-ray Scattering (SAXS) was conducted on a laboratory Bruker NanoSTAR SAXS instrument (Germany) at Curtin University. Borosilicate capillaries (Charles Supper, Germany) were used in order to reduce attenuation of the holding media. The capillaries were loaded in argon atmosphere, temporarily sealed before being taken out of the glovebox and sealed with a flame to prevent oxygen and water contamination. A long distance detector (LDD) position of 65 cm away from the sample was used with a copper anode tube (λ = 1.5418 Å). Values of the *q*-range were taken from 0.014 to 0.3 $Å^{-1}$ (q values below 0.014 $Å^{-1}$ were not used as these values are affected by the beam stop, Figure 2.5). *q* (Eqn. 2.3) is the reciprocal lattice vector and relates to particles having structure in real space [98].

Eqn. 2.3 $$q = \frac{4\pi}{\lambda} . \sin\theta \ (\mathrm{nm}^{-1})$$

Photon counts were collected on a multi-wire 2D detector. An example of the 2D pattern collected by the detector is given in Figure 2.5. The data sets were then integrated to obtain a 1D data range of intensity and *q*. The data displayed in this thesis has had the background subtracted and was adjusted onto absolute scale using the calibration standard S2907 provided by the Oak Ridge National Laboratory.

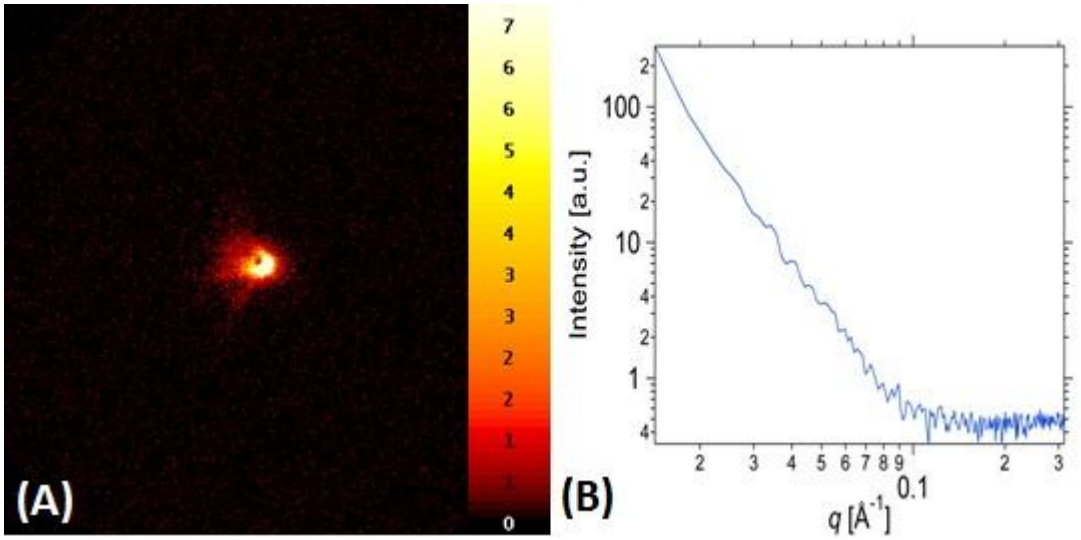

Figure 2.5: [A] 2D image collected from SAXS showing the intensity of the argon filled borosilicate capillary and the beam stop. The scale from 0 – 7 to the right of the pattern indicates the intensity, 0 = no intensity, 7 = maximum intensity. [B] Plot of Intensity vs *q* on a log-log scale after the data from [A] has been integrated to 1D.

2.6.1 Theory of SAXS

SAXS is an analytical method used to determine the average structural information of particles within the size range of approximately 1 to 100 nm. Different to the reflection geometry of XRD (Figure 2.2), SAXS uses transmission geometry (Figure 2.6). The properties of a bulk sample volume can be determined when X-rays are transmitted through the sample and the average values of the structure parameters such as particle size are obtained[99]. A requirement for SAXS analysis is that the particles being analysed must have an electron density different to that of the surrounding material that is it must have contrast[99]. In this context, contrast is the difference between the scattering densities in a volume element of the particle (solute) with respect to the matrix material or solvent[100]. For the particles to be visible, high contrast and minimal absorption losses are achieved by the solvent being less dense than the solute[99].

Figure 2.6 is a schematic of the SAXS system where X-rays with an applied radiation wavelength λ, are collimated into a fine beam to pass through a sample [100]. This beam is scattered at an angle 2θ due to the X-rays being scattered by the electrons

within the atoms that make up the sample. The beam then creates a 2D interference pattern where the intensity varies from position to position relative to the scattering angle 2θ[99]. The resultant pattern integrated from the 2D detector in terms of the reciprocal lattice vector, q, in units of inverse length nm^{-1}.

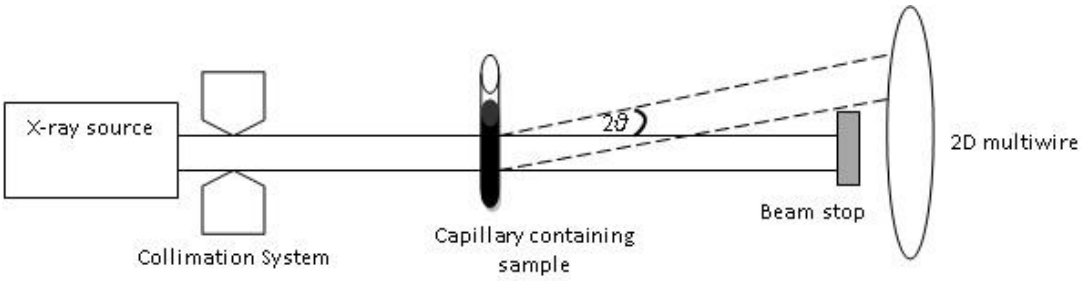

Figure 2.6: Simplified schematic of SAXS instrumentation where 2θ is the scattering angle (adapted from [100]).

2.6.2 SAXS Data Processing

2.6.2.1 Absolute Intensity

Absolute scale is defined as intensities that are normalised by the flux density of the primary beam and the illuminated sample[100]. Particle size, surface area, volume fraction and molecular weight determination can be performed when intensities are calibrated to a standard. The method used to determine absolute intensity for SAXS data was similar to the method described in detail in Buckley[101] so only a brief summary is provided here.

The samples were calibrated with a S2907 standard (Oak Ridge National Laboratory (ORNL), Tennessee, USA). S2907 is a highly cross-linked polyethylene sample that has a strong scattering pattern and has been pre-calibrated with respect to the ORNL suite of SAXS standards at the Daresbury Synchrotron SAXS beamline[102]. This standard has a distinct reference peak at q = 0.0227 $Å^{-1}$ due to the alternation of

crystalline lamellae with amorphous regions[102]. Table 2.6 lists all the required data to analyse the sample with respect to background subtraction as well as absolute values. Glassy carbon has a known transmission τ_{GC} = 0.13 and is therefore used to calculate the transmission of the sample (Eqn. 2.4).

Eqn. 2.4 $$\tau_x = \frac{I_{xGC} - \tau_{GC} I_x}{I_{bGC} - \tau_{GC} I_b}$$

For example, the transmission of the standard S2907 was calculated, τ_{st} = 0.4746 from Eqn. 2.4 and the data collected from the Bruker NanoSTAR SAXS instrument. Transmission values should not lie outside 0 and 1 and if the value is outside this range, the contrast between the sample and the background is not enough for a distinct difference in scattering densities and a pattern will not be obtained.

Table 2.6: List of SAXS samples required to calculate absolute intensities.

Intensity Nomenclature	Sample Description	Run Time (s)
Sample to be analysed		
I_x	Sample in sealed capillary in Ar atmosphere	10800
I_{xGC}	Sample in sealed capillary in Ar with glassy carbon	100
Background Subtraction		
I_b	Sealed capillary in Ar atmosphere without the sample	10800
I_{bGC}	Sealed capillary in Ar atmosphere without the sample with glassy carbon	100
I_{noise}	Background noise, no sample, X-rays off	10800
Absolute Scale		
I_{st}	S2907 standard from ORNL	10800
I_{stGC}	S2907 standard from ORNL with glassy carbon	100
I_{stb}	Background for the standard, i.e. vacuum, no standard	10800
I_{stbGC}	Background for the standard, i.e. vacuum, no standard, with glassy carbon	100

Eqn. 2.5 is the calculation used to correct the raw data obtained from SAXS. This equation takes transmission of the sample and background subtraction into account to ensure that the only scattering remaining is related to the sample itself. The

individual scattering intensities obtained for the corrected data can be found in Figure 2.7.

Eqn. 2.5 $$I_c = I_x - \tau_x I_b - (1 - \tau_x) I_{noise}$$

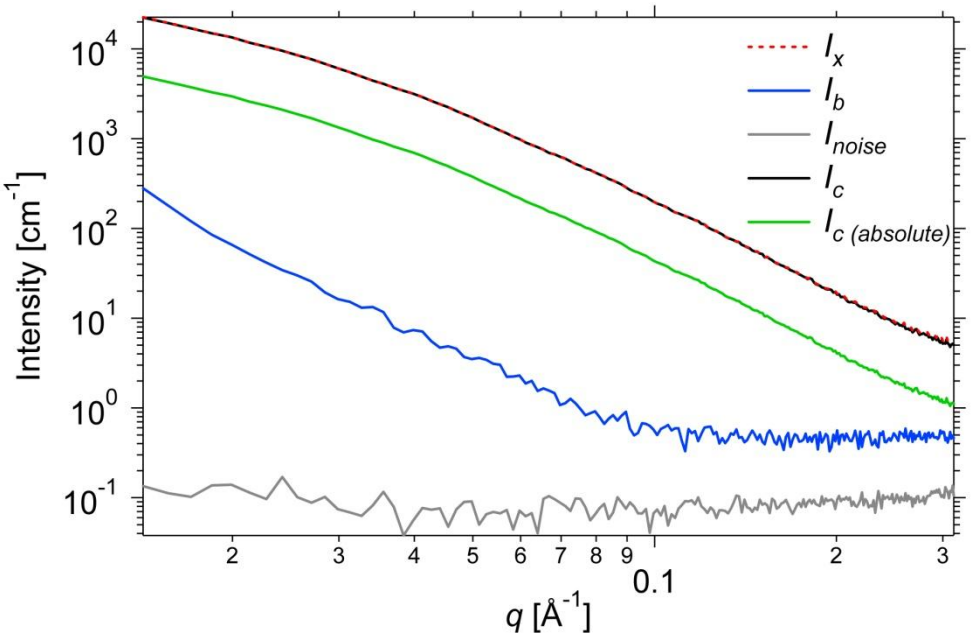

Figure 2.7: SAXS intensity patterns of the sample, background subtractions (noise and blank capillary), corrected sample pattern and the absolute scale sample pattern.

When analysing a range of q values, data resolution must be taken into account. At the lower limit of q, the presence of primary beam is governed by the quality of the collimation system and position of the beam stop (Figure 2.6). The upper limit is determined by the fading of the signal to noise level, hence the increase in noise present at higher q values.

As stated earlier in this section, the data must be represented on an absolute scale in order for parameters such as surface area to be calculated. Absolute intensity is calculated as a function of thickness, linear attenuation coefficient of the solid phase,

number of photons detected at time t and the transmission values of the sample relative to the S2907 standard (Eqn. 2.6). The resultant data on an absolute scale in the given example is shown by the green curve in Figure 2.7.

Eqn. 2.6

$$I_{abs}(q) = I_{abs,st}\frac{I_c(q)}{I_{st}}\frac{t_{st}}{t_x}\frac{d_{st}}{d_x}\frac{\tau_{st}}{\tau_x}(cm^{-1})$$

2.6.2.2 Unified Model

A unified model approach was used to approximate the morphological information obtained from SAXS data analysis. This approach can be applied to a wide range of *q* values giving a range of information related to different structure levels. Figure 2.8 shows four distinct structural levels, A (aggregate structure) and C (surface scattering from the surface of primary particles) based on the power law regime and B (primary particles) based on the Guinier regime. The D region is not considered in the unified model as it accounts for diffraction from the crystalline lattice. A detailed look at the mathematical concepts underlying the unified model approach can be found in Beaucage and Schaefer[103]. The data analysis to determine average bulk particle size and surface area have been based on these calculations so will not be further derived in this section.

The Irena SAS Macros (release 2.16, 2007) package was used with Igor Pro (Version 6.02A, Wavemetrics, Oregon, 2007) to apply the unified fit model to the raw SAXS data. Using this approach, each of the aforementioned regions were modelled to obtain the power-law prefactor constant, B the Guinier exponential prefactor, G and the radius of gyration R_g[103]. The scattering profile shown in Figure 2.8 (B) is used to calculate the radius of gyration of the particle. This has a direct relationship with the shape determination of the particle. Depending on the shape of the particles further information can be calculated. For example, the Guinier approximation for the radius, *r*, for a spherical particle is given in Eqn. 2.7.

Eqn. 2.7 $$R_g = \sqrt{\frac{3}{5}}\mathrm{r}$$

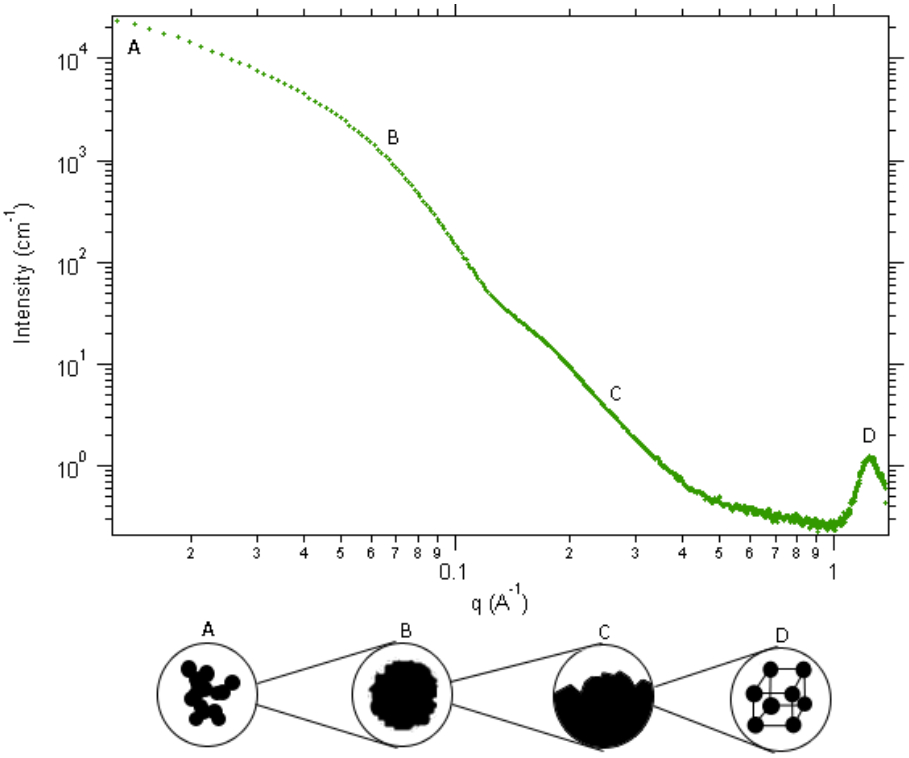

Figure 2.8: A visual representation of scattering vector range related to the physical system of the sample. A: aggregate structure, mass fractal regime, B: primary particles, Guinier regime, C: surface scattering of primary particles, D: diffraction of the atomic lattice[103].

2.7 Synchrotron Powder Diffraction

Experiments were performed at the Australian Synchrotron Facility, Melbourne at the 10-BM-1 Powder Diffraction beamline (experiments done by Mark Paskevicius and Drew Sheppard, members of the Hydrogen Storage Research Group, Curtin University). This beamline delivers monochromatic synchrotron X-rays in the energy range of 5 to 30 keV from a bending magnet source. All samples were carefully placed in 0.3 mm diameter borosilicate capillaries (Charles Supper, Germany) which were sealed using a small flame to ensure no contamination from oxygen or moisture

during the experiments. A National Institute Standards of Technology (NIST) supplied LaB_6 standard was used to calibrate the diffraction line positions and line shapes used for powder diffractometry. The beam wavelength was calculated to be 1 Å and diffraction angles from 20 – 100° 2θ were measured with an exposure time of 1 – 5 min. A pattern was produced from an empty glass capillary tube to determine the background. The imaging plates (IP) used to capture the data (BAS-MS, Fuji Film, Japan) in the translating cassette had a radius of 573 mm, equipped with radioactive fiducial markers for absolute angular calibration.

2.7.1 Synchrotron Radiation Background

Synchrotron radiation is electromagnetic radiation emitted by charged particles moving at a highly relativistic velocity in a circular orbit[104]. At a facility like the one used at Melbourne, Australia for these experiments, electrons are injected into and stored in the ring orbit to provide an intense and stable radiation source. Synchrotron facilities typically consist of three components, a linear accelerator, the synchrotron and the storage ring. In the linear accelerator, electrons are injected at a low energy then accelerated on a fixed circular orbit. They are then transferred to the synchrotron which consists of an array of magnets for focusing and bending the electron beam as well as straight sections for accelerating the particles. Once the particles have reached the required energy they are transferred to a storage ring where the magnetic field remains constant.

Synchrotron radiation from a photon source can be used for a number of analytical techniques[104] and its advantages include:

- Large d-spacing range from a continuous spectrum from the infrared (λ = 750 – 106 nm) to the X-ray (λ = 0.01 – 10 nm) region.

- Improved signal to noise ratio owing to the high current electrons accumulated in the storage ring.
- High brilliance of the source, because of the small cross section of the electron beam and the high degree of collimation of the radiation.
- Absolute predictability of all the properties of the source.
- Cleanliness of the source, since the light emission takes place in an ultra-high vacuum.

2.8 Transmission Electron Microscopy (TEM)

A JEOL 3000F transmission electron microscope (TEM) with a field emission gun (FEG) at the Centre for Microscopy, Characterisation and Analysis (CMCA) at the University of Western Australia was used for all transmission electron microscopy. The TEM was operated at a voltage of 300 kV with a 1M pixel Gatan 694 MSC digital camera, a Gatan GIF 2000 energy filter (for electron energy loss spectra (EELS) and energy filtered transmission electron microscopy (EFTEM)). All specimens were placed on a single tilt sample holder. Samples for TEM were prepared by suspending nanoparticles in toluene (Anhydrous 99.8%, Sigma-Aldrich) within a sealed vial and ultrasonicated in a water bath for 30 min. Once the vial was placed in an Ar atmosphere glovebox, the solution was added dropwise to a 200 mesh copper grid with holey carbon film. The TEM grids were exposed to air for a short period of time when loading into the vacuum chamber of the instrument.

2.8.1 Theory of TEM

TEM is an ideal tool for analysing nanomaterials and is complementary to the SAXS technique. Similar to SAXS, TEM is also a transmission method but instead of X-rays transmitting through the sample, electrons pass through and interact with the

sample to give structural, composition and chemical information. A focused beam of electrons with a wavelength of less than 1 Å can provide atomic resolution images of the materials and their defects as well as spectroscopic data and electron diffraction patterns from crystalline materials[105]. This electron beam probe travels through a series of aberration corrected magnetic lenses to provide the user with images and an array of data related to the nanoparticles being analysed. DigitalMircrograph™ version 3.4.7, 2003, Gatan Software (USA) was used to analyse the data obtained from the TEM.

Interaction with the beam causes the specimen to undergo elastic as well as inelastic scattering. Elastic scattering is an electron-nucleus interaction where there is a change in direction and hence momentum but no energy loss. Elastic scattering occurs as Bragg diffraction in crystalline specimens. Inelastic scattering is primarily an electron-electron interaction encompassing a change of momentum as well as energy loss. This is further explained in the energy loss spectroscopy section below.

2.8.2 High Resolution TEM

High resolution transmission electron microscopy or HRTEM is a phase contrast imaging technique, used to investigate the crystallinity of the sample by identifying lattice planes and defects. This technique can give details about a specimen below a resolution of 0.2 nm including lattice plane distances. In order to obtain such high resolution the beam must be parallel to the specimen and located in a very thin region of the sample[105]. By measuring the distance between each of the lattice planes, an average distance can be determined. This information directly relates to the d-spacing of a crystal lattice, specific to that particular material. This method can identify phases within a sample based on its crystal lattice by matching the information stored in the International Centre for Diffraction Data (ICDD) database (PDF4+ 2012 edition).

2.8.3 Electron Energy Loss Spectroscopy

Electron energy loss spectroscopy (EELS) uses inelastic electron interaction to measure the amount of energy lost by electrons after passing through the specimen [105]. Characteristic energy loss peaks identify the elements present. Fine structure of these peaks can provide information on valence states and bonding. Energy-loss spectrum can be explained using single scattering, requiring the sample to be very thin (< 100 nm). Inelastic interaction include photon excitations, inter and intra band transitions, plasmon excitations and inner-shell ionizations. The two major characteristics of inelastic scattering are the energy loss E, and scattering semi-angle θ [105] (Figure 2.9).

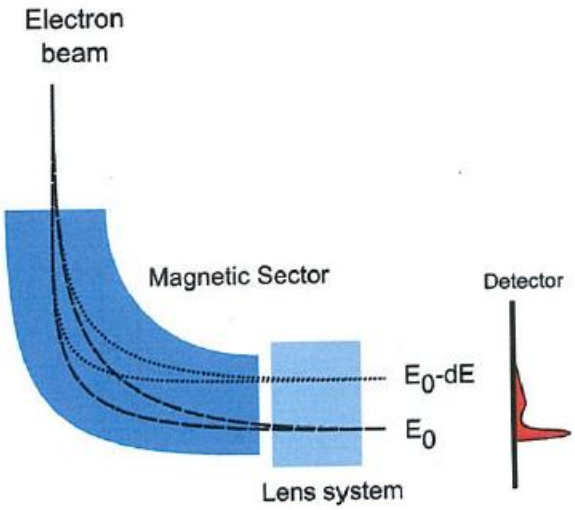

Figure 2.9: Gatan Image Filter showing energy loss spectra[106].

2.8.4 Energy Filtered TEM (EFTEM)

Energy filtered transmission electron microscopy or EFTEM selects an energy loss range at a specific energy identified by the EEL spectrum and turns them back into an image[105]. This provides information such as elemental distribution images or

maps. While EELS can be used to determine what elements are present in the sample, EFTEM can be used to map the location of these elements (Figure 2.10).

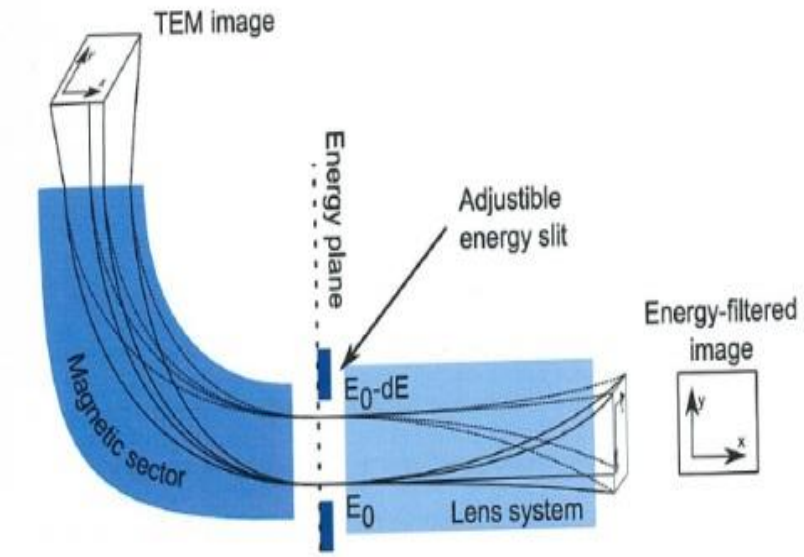

Figure 2.10: Gatan Image Filter GIF for EFTEM[106].

2.8.5 Energy Dispersive X-ray spectroscopy (EDS)

Energy dispersive X-ray spectroscopy is a microanalysis technique used to identify the composition of the sample. X-rays are generated when the electrons beam hits the sample and these X-rays give unique energies depending on the element with which it interacts. An Oxford instruments EDS was attached to the TEM for elemental analysis and INCA-Analyser software was used to collect and analyse the data. Spectra were collected using an accelerating voltage with the range of 10 – 20 kV and a working distance of 7.7 mm and a 60 μm aperture. A count time of 300 s was used to obtain both the EDS as well as the elemental image maps. The high count time of 300 s was used to ensure a high signal to noise ratio.

2.9 Scanning Electron Microscopy (SEM)

A Zeiss Neon 40EsB scanning electron microscope (SEM) was used for high resolution Scanning Electron Microscopy (SEM) (Zeiss, Germany). Samples for the SEM were prepared in a similar method to the TEM samples, by suspending the nanoparticles in toluene within a sealed vial that was placed in a water bath for 30 min. Once the vial was placed in the Ar atmosphere glovebox, the solution was added dropwise to a stainless SEM stub with or without carbon tape depending on the sample. The SEM stubs were then coated with a 2 – 4 nm coating of high atomic elements, either gold or platinum to produce a conductive layer and reduce charging of the sample during its interaction with the electrons in the SEM. All samples were exposed to air for a short period of time when in and out of the coating instrument as well as loading into the SEM chamber.

Secondary electron, backscattered electron and X-ray (for energy dispersive spectroscopy, Oxford Instruments EDS) detectors were used to obtain various high resolution images of the samples analysed. These techniques will be explained in more detail in the following section.

2.9.1 Theory of SEM

Scanning electron microscopy is a useful analytical tool that uses a series of electromagnetic lenses in combination with a range of apertures for observing surface images of a material. Samples can be analysed in bulk form to obtain morphological, structural and composition information with techniques using secondary electrons (SE), backscattered electrons (BSE) and auger electrons (AE) (Figure 2.11).

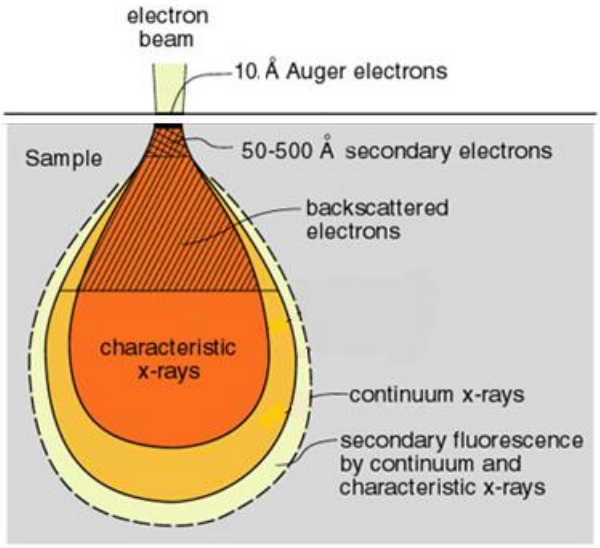

Figure 2.11: Electron beam (EB) and interaction volume diagram for secondary electrons (SE), backscattered electrons (BSE), Auger electrons (AE) and X-ray quanta (X). Adapted from[107].

SE are generated by inelastic interactions between the specimen and the electron beam that leave the specimen from the first few nanometres indicating its very narrow interaction volume at the surface[108]. This kind of interaction can produce images at high resolution (1 – 10 nm) and can allow the user to obtain surface topography images[108]. Backscattered electrons are obtained in a broader region and are caused by multiple energy losses and multiple scattering through large angles of the electron beam (EB)[108]. When using the BSE Detector, the number of backscattered electrons reaching a BSE detector is proportional to the mean atomic number of the sample (Z). A brighter BSE intensity correlates with greater average Z in the sample and dark areas have lower average Z; this distinguishes different phases within the sample. Auger electrons (AE), like SE, leave from a very thin layer from the surface of the sample and can be related to the de-excitation energy released when an electron moves to fill a vacancy in the ionised shell that occurs in the form of an X-ray quantum of energy[108]. This study largely used SE and BSE to obtain high resolution images. EDS was also used (Section 2.8.5) to determine the elemental phases present in the sample and EDS mapping was done to view where each element was present within the field of view.

2.10 Differential Scanning Calorimetry (DSC)

Thermal analysis was undertaken using a DSC 6000 (Perkin Elmer, Waltham, Massachusetts, USA) with a Cryofill liquid nitrogen cooling system. The DSC was calibrated using materials with known thermal transitions (Table 2.7). 10 mg (± 10%) samples were measured and hermetically sealed in aluminium pans in an argon atmosphere glovebox. The sample filled pan was placed in a furnace chamber with a reference pan, an empty hermetically sealed aluminium pan. Nitrogen was used as the purge gas at a rate of 20 mL min^{-1} in the furnace chamber to reduce any influence of water or air on the measurements during the experiment. The chamber was heated at a constant rate according to the programmed heating ramp (2, 5, 7, or 10°C min^{-1}) from 25°C to 445°C. Data were recorded and analysed using Pyris Thermal Analysis software (Perkin Elmer, Version 10.1.0412, 2009).

Uncertainty was calculated from accuracy of the DSC[109], calibration error, precision of the microbalance used to weight samples and any mathematical errors based on the processing of the data (for example, activation energy regression values of the straight line).

Table 2.7: DSC calibration materials and their respective transition temperatures.

Material	Thermal Transition Melting Point (°C)	
	Literature	Measured
Indium	156.6	157.1
Zinc	419.5	420.1

2.10.1 Theory of DSC

Differential scanning Calorimetry or DSC measures the difference in heat flow due to thermal transitions of a sample. In the case of hydrogen storage metal hydride, hydrogen absorption is an exothermic reaction and hydrogen desorption is an

endothermic reaction[43]. The more stable the bonds between the metal and the hydrogen, the higher the enthalpy or energy needed for either absorption or desorption to occur. The DSC measures these transitions by keeping the temperatures of the sample and of the reference material identical. The recorder records the increase in electric power necessary to attain this identity of temperatures as a function of time. The integral of the curve recorded in the course of a transition gives the heat of transition. This technique enables the measurement of the temperature dependence of specific heats. The heat flux systems of the desorption curves presented in Figure 2.12 show the endotherms decreasing with heat flow as endothermic transitions are the result of a negative temperature differential.

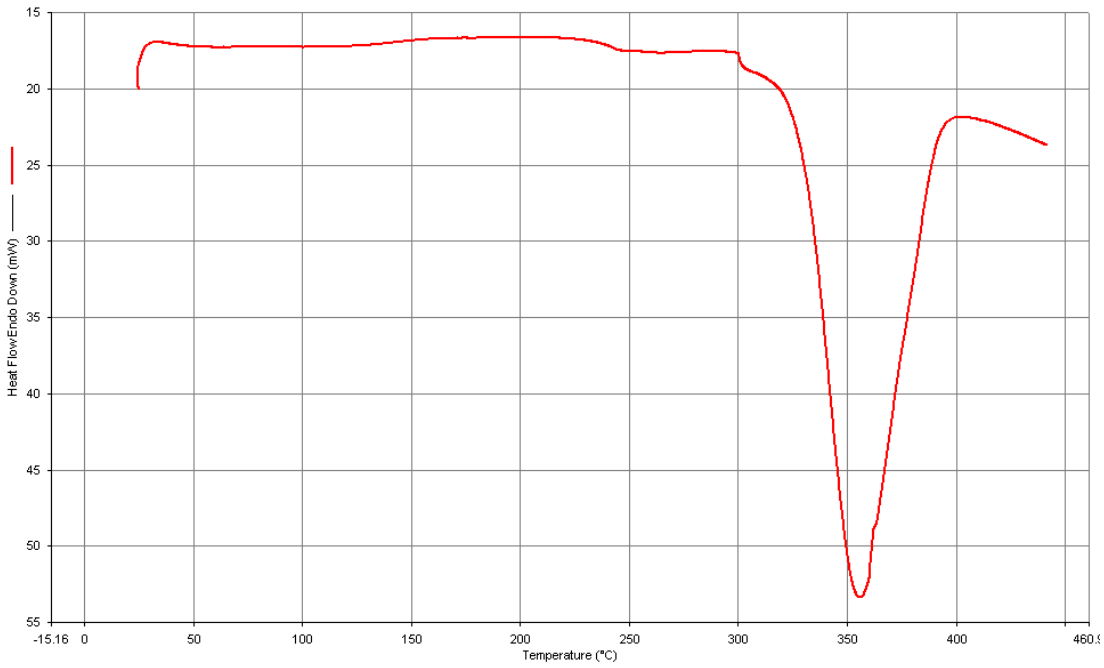

Figure 2.12: DSC curve of heating ball milled Si and MgH_2 at 10°C min^{-1}.

2.11 Manometric Sieverts Apparatus

Sorption (adsorption / absorption / desorption) measurements were performed at two locations, Curtin University, Perth Australia and Griffith University, Brisbane, Australia. Both locations had custom made manometric Sievert's apparatus that could measure hydrogen storage properties over a wide range of temperatures and pressures. Each setup was different and is named according to the maximum rated pressure for the rig. These rigs are built on the principle of Sievert's Law (Eqn. 2.8). Here, the solubility of hydrogen as it moves into a solid phase at thermodynamic equilibrium with a metal is proportional to the square root of the partial pressure of the gas[110]. In recent years, formalized method development for hydrogen storage materials has been published in the 'Recommended Best Practices for the Characterization of Storage Properties of Hydrogen Storage Materials'[44]. Where appropriate, these practices have been incorporated into the methodology and have been referenced accordingly.

Uncertainty was calculated from volume calibration error, precision of the pressure gauge, thermocouple, microbalance used to weight samples and the mathematical errors from processing of the data.

Eqn. 2.8 $$H_{solid} = K_s P^{1/2}$$

Where: H_{solid} **= concentration of hydrogen in the metal**

K_s **= Sievert's constant**

P **= equilibrium hydrogen pressure**

2.11.1 Theory of Sieverts Apparatus

Sieverts apparatus is a key piece of equipment used to measure hydrogen storage properties of a sample. This method can be described as using a known volume of hydrogen (reference volume, Figure 2.14) at a known temperature and pressure in combination with a sample cell that has the sample contained inside. The sample cell can be held at room temperature or placed into a furnace at a set temperature. Once the system has reached thermal equilibrium, changes in pressure with time are measured. A change in pressure can be directly related to the number of moles of hydrogen absorbed or desorbed by the sample. This information can be further used to calculate the hydrogen capacity of the material, reaction kinetics of the system, thermodynamic behaviour and cycling properties.

One aspect to note when studying hydrogen gas is the interaction between the molecules and the environment in which they are surrounded. Hydrogen at atmospheric pressure displays ideal gas behaviour, that is, the relationship between the number of moles of hydrogen, its pressure and temperature can be expressed in terms of the ideal gas law (Eqn. 2 9).

Eqn. 2 9 $$\boldsymbol{pV = nRT}$$

Where:

***p* = pressure**

***V* = volume**

***n* = number of mol**

***T* = temperature**

***R* = universal gas constant**

Under these conditions, hydrogen molecules are only influenced by the environment (temperature, pressure, volume) in which they are present. In other words, there is no

significant interaction between the molecules themselves. This ideal gas behaviour occurs below a hydrogen *p* of 10 bar (there is a 6% deviation from the ideal gas law up to *p* of 10 bar)[44]. When the *p* increases above atmospheric pressure and temperature, these interactions become more frequent and the variable, compressibility, *Z*, must be taken into account. The term, *Z*, is the fugacity capacity constant and is a dimensionless compressibility factor incorporated in the equation of state as a function of pressure and temperature (Eqn. 2.10). The deviation of *Z* from the value of 1 is a measure of the deviation from ideal gas behaviour.

Eqn. 2.10 $$\boldsymbol{Z = \frac{pV}{nRT}}$$

2.11.2 Kinetic Measurements

Reaction kinetic properties are important to measure as it determines how fast or slow the sorption process occurs. These experiments are conducted under isothermal conditions and the change of hydrogen concentration recorded over time. Typical desorption reaction kinetic curves are shown in Figure 2.13. The rate of reaction is dependent on a number of factors including particle size, temperature and how close the pressure is to thermodynamic equilibrium. The closer the conditions are to thermodynamic equilibrium the slower the reaction.

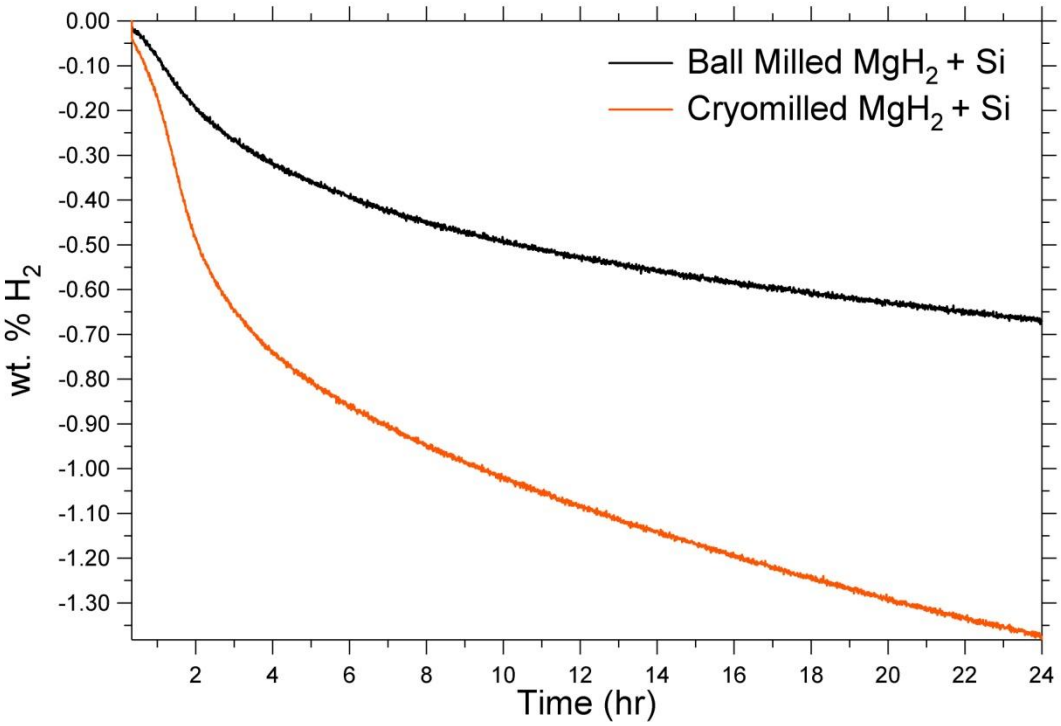

Figure 2.13: Desorption kinetic curves for MgH_2 and Si powders mixed using ball milling (black) and cryomilling (orange) techniques at 300°C.

2.11.3 Calibrations

All volume calibrations were done in accordance to the standard procedure for calibrating a volume using the pressure method, outlined in Gross *et. al.*[44]. Firstly, the volume of the calibration vessel (V_{cal}) was measured by filling with ethanol and recording the weight and temperature. Corresponding density data for ethanol at this temperature was obtained and used to calculate V_{cal}. This calibration vessel volume was used in Eqn. 2.11 to measure the reference volume of the Sieverts apparatus (Figure 2.14 or Figure 2.15). Each reference volume was measured at least four times and the average and two standard deviations (95% confidence interval) calculated. All calculations used the international system of unit (SI). To ensure the system was not affected by adiabatic heating or cooling, a minimum of 20 min was allowed to pass before a measurement was taken.

Eqn. 2.11

$$V_{ref} = \frac{\frac{P_2 V_{cal}}{Z_2 T_2}}{\frac{P_1}{Z_1 T_1} - \frac{P_2}{Z_2 T_2}}$$

Where: V_{ref} **= reference volume**

P_1 **= initial pressure of** V_{ref}

T_1 **= initial temperature of** V_{ref}

Z_1 **= initial compressibility of** H_2 **in** V_{ref}

P_2 **= pressure at equilibrium**

T_2 **= temperature at equilibrium**

Z_2 **= compressibility of** H_2 **at equilibrium**

The empty sample cell volume was determined in order to accurately calculate sample hydrogenation properties. The determination of the sample volume, V_s, was based upon the value of the reference volume, V_{ref} (Eqn. 2.11). Data for the V_s calculation was also measured after 20 mins to cancel adiabatic heating and cooling effects. Again, a minimum of four measurements were recorded and the error was taken at two standard deviations or a 95% confidence interval.

Eqn. 2.12

$$V_s = V_r \left(\frac{\frac{P_r}{Z_r T_r} - \frac{P_e}{Z_e T_e}}{\frac{P_e}{Z_e T_e}} \right)$$

Where: P_r **= initial pressure of** V_{ref}

T_r **= initial temperature of** V_{ref}

Z_r **= initial compressibility of** H_2 **in** V_{ref}

P_e **= pressure at equilibrium**

T_e **= temperature at equilibrium**

Z_e **= compressibility of** H_2 **at equilibrium (**P_e **and** T_e**)**

The procedure used to determine the sample volume of the cell at non-ambient temperatures is the same as used to determine Eqn. 2.13. The difference being that the cell and a portion of the connecting tubing was heated to a specific temperature in a thermocouple controlled furnace. Due to the temperature gradient over the sample side volume, two calculations were used to approximate the sample side volume; the ambient portion (V_s), Eqn. 2.12 , and the thermally stable non-ambient portion heated by the furnace (V_{na}), Eqn. 2.13.

Eqn. 2.13

$$V_{na} = \frac{V_r\left(\frac{P_r}{Z_r T_r} - \frac{P_e}{Z_e T_e}\right) - V_s\left(\frac{P_e}{Z_e T_e}\right)}{\left(\frac{-P_e}{Z_e T_e} + \frac{P_e}{Z_{ena} T_{na}}\right)}$$

Where: T_{na} **= temperature of the non-ambient region**

Z_{ena} **= compressibility of** H_2 **in the non-ambient region at (**P_e **and** T_{na}**)**

2.11.4 Sieverts Apparatus: 75 and 150 bar rigs

The manometric Sieverts apparatus at Curtin University consists of a series of tube fittings separated by valves connected to a high purity hydrogen gas bottle (Figure 2.14). All the fittings were made from either 316 or 316L stainless steel and can be safely used up to a temperature of 500°C. Labec tube furnaces rated to 1200°C (Laboratory Equipment P/L, Australia) were used to obtain sample temperatures above room temperature. Rosemount pressure transducers model 3051S, precision 0.01%, accuracy, 0.02%, were used to monitor pressure. For the gauges that did not read absolute pressure, atmospheric pressure was also recorded and the percentage reading from the Rosemount transducers was converted to an absolute pressure value using Eqn. 2.14.

Eqn. 2.14 $$P_{bar} = \frac{\%.FS-(AtmP-100)}{100}$$

Where: **% = percentage reading from the Rosemount transducer**

***FS* = full scale pressure range of the pressure transducer in units of bar**

***AtmP* = atmospheric pressure reading**

Reference temperature was measured using either a K-type thermocouple or a RTD 4 wire platinum thermistor. Thermocouples used to measure the temperature of the sample were either K-type or N-type.

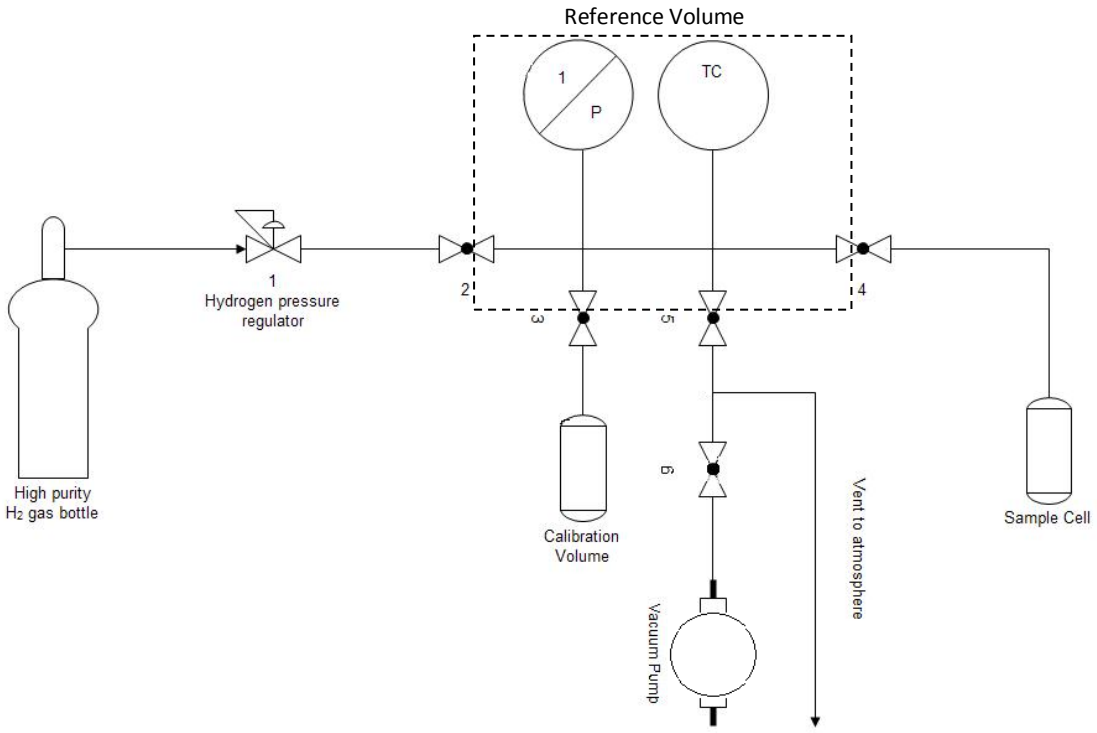

Figure 2.14: Schematic of the 75 and 150 bar rigs at Curtin University.

Sorption measurements were undertaken by placing a material in the sample cell in the Argon atmosphere glovebox and closing the valve to the sample (*V4*, Figure 2.14). Once connected to the manometric Sieverts apparatus, the system was

evacuated to eliminate the Ar. Changes in hydrogen pressure during the experiment were recorded over time. This information was used to calculate the change in weight percent of material relative to the hydrogen gas absorbed or desorbed within the experimental time. All absorption measurements were above thermal equilibrium to avoid desorption taking place. Desorption measurements were initially conducted under vacuum and an increase in pressure recorded to observe hydrogen release from the system. In order to calculate the number of moles absorbed or desorbed the following equations were used (Eqn. 2.15 - Eqn. 2.22):

For samples at ambient temperature:

Eqn. 2.15 $$n_{system,ambient} = n_r + n_s - n_e$$

Eqn. 2.16 $$n_r = \frac{P_r V_r}{Z_r R T_r}$$

Eqn. 2.17 $$n_s = \frac{P_s (V_s - V_{sample})}{Z_s R T_s}$$

Eqn. 2.18 $$n_e = \frac{P_e (V_r + V_s - V_{sample})}{Z_e R T_e}$$

Where: n_r = initial number of moles in V_{ref}

n_s = initial number of moles in V_s

n_e = number of moles of H_2 at equilibrium

P_s = initial sample side volume pressure

T_s = initial sample side volume temperature

Z_s = compressibility of H_2 at associated with P_s and T_s

V_{sample} = the solid volume of sample based on mass and density

R = universal gas constant

For samples at non-ambient temperatures:

Eqn. 2.19 $$n_{system,non-ambient} = n_r + n_s - n_e$$

Eqn. 2.20 $$n_r = \frac{P_r V_r}{Z_r R T_r}$$

Eqn. 2.21 $$n_s = \frac{P_s(V_s - V_{na})}{Z_s R T_s} + \frac{P_s(V_{na} - V_{sample})}{Z_{na} R T_{na}}$$

Eqn. 2.22 $$n_e = \frac{P_e V_r}{Z_e R T_e} + \frac{P_e(V_s - V_{na})}{Z_e R T_e} + \frac{P_e(V_{na} - V_{sample})}{Z_{ena} R T_{na}}$$

Where: V_{na} **= sample side volume of the non-ambient region**

T_{na} **= temperature of the non-ambient region**

Z_{na} **= initial compressibility of** H_2 **associated with** P_s **and** T_{na}

Z_{ena} **= compressibility of** H_2 **associated with** P_e **and** T_{na}

2.11.5 Sieverts Apparatus: High Pressure, 2 kbar rigs

A custom made Sieverts apparatus high pressure rig was used to obtain hydrogen pressures above 1 kbar at the laboratory situated at Curtin University. This method was different to the 75 and 150 bar rigs due to the physical differences in the design (Figure 2.15) as the rating of each of the parts had to withstand pressures greater than 1 kbar. All parts including the valves and sample cell were supplied by Autoclave Engineers (Pennsylvania, USA) and were rated to a minimum of 2 kbar. High pressure data were recorded with a Presens Precise pressure gauge rated up to 2 kbar with an accuracy of 0.02% and a K-type thermocouple attached to the outside of the sample cell near the location of the sample.

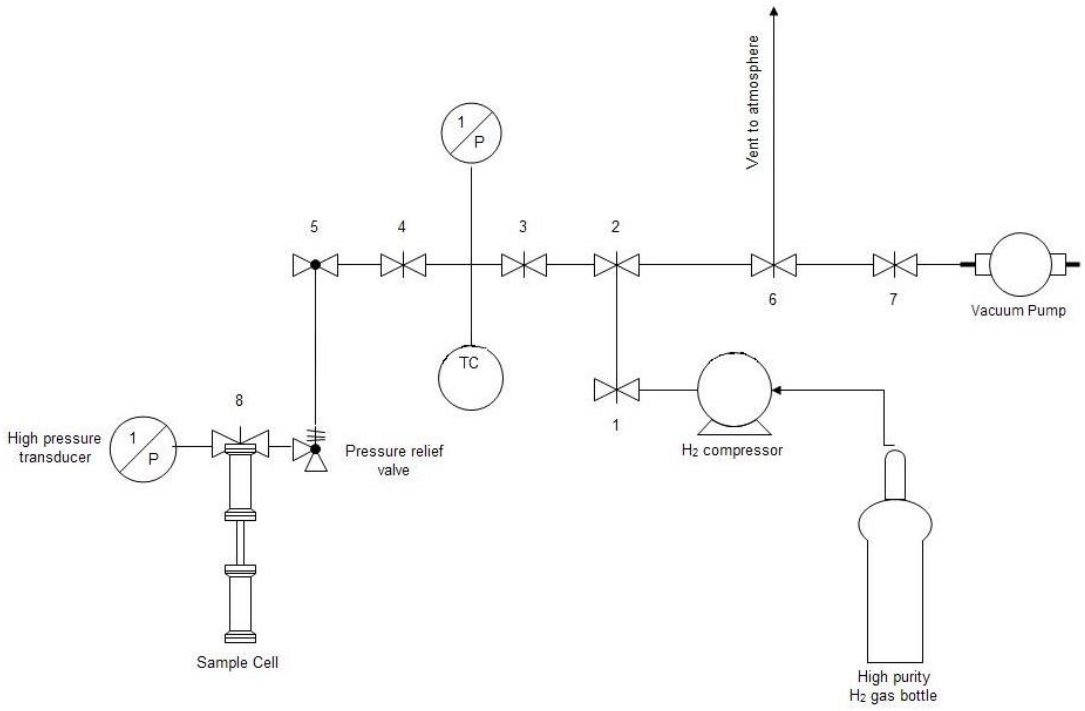

Figure 2.15: Schematic of the high pressure rigs at Curtin University.

In order to obtain pressures higher than the ultra-high purity hydrogen gas bottle, a gas compressor was used. The maximum pressure obtained using the compressor was directly dependent on the bottle pressure, that is, the higher the pressure in the bottle, the higher the pressure obtained by using the compressor. When the hydrogen gas bottle was full, at approximately 120 bar, the compressor was able to achieve a pressures of approximately 300 bar in the entire high pressure rig. Similar to the 75 and 150 bar rigs, the sample to undergo absorption was placed in the sample cell in the glovebox under argon atmosphere. There was no filter manufactured to the required pressures of 1 – 4 kbar, therefore, a quantity of glass wool was placed directly above the sample in the cell. The equations used to calculate changes in the number of moles of hydrogen during absorption subtract this additional volume in the sample cell. This can be seen in the series of equations given in Eqn. 2.23 - Eqn. 2.28.

All fittings were tightened using a torque wrench to ensure appropriate torque was applied according to the ratings of the parts supplied by Autoclave Engineers.

Cryogenic cooling with liquid nitrogen was used to obtain pressures above 1 kbar. This was done by opening the valves between the gas bottle, the compressor and all the valves to the sample cell. Once the compressor was at maximum pressure (i.e. 300 bar), the sample cell was placed in liquid nitrogen with all valves remaining open. Once the cell had reached 77 K, the valve to the cell (*V8*, Figure 2.15) was closed; the cell removed from the liquid nitrogen bath and allowed to reach room temperature. Absorption measurements were taken at room temperature and non-ambient room temperature. The number of moles absorbed was calculated according to changes in pressure and these equations are listed below (Eqn. 2.23 - Eqn. 2.28).

For samples at ambient temperature:

Eqn. 2.23 $$n_{system,ambient} = n_s - n_e$$

Eqn. 2.24 $$n_s = \frac{P_s(V_s - V_{sample} - V_{filter})}{Z_s R T_s}$$

Eqn. 2.25 $$n_e = \frac{P_e(V_s - V_{sample} - V_{filter})}{Z_e R T_e}$$

For samples at non-ambient temperatures:

Eqn. 2.26 $$n_{system,non-ambient} = n_s - n_e$$

Eqn. 2.27 $$n_s = \frac{P_s(V_s - V_{na})}{Z_s R T_s} + \frac{P_s(V_{na} - V_{sample} - V_{filter})}{Z_{na} R T_{na}}$$

Eqn. 2.28 $$n_e = \frac{P_e(V_s - V_{na})}{Z_e R T_e} + \frac{P_e(V_{na} - V_{sample} - V_{filter})}{Z_{ena} R T_{na}}$$

Where: V_{filter} = the solid volume of the glass wool filter based on mass and density

High pressure measurements were also conducted at Griffith University using another custom made high pressure rig (Figure 2.16). This manometric Sieverts apparatus also used a Presens Precise pressure gauge rated up to 2 kbar with an accuracy of 0.02%. Temperatures were monitored using a 4-wire platinum resistance thermometer. The design of this rig did not require the use of liquid nitrogen to obtain high pressures. Rather, the pressure was ramped up using various hydrogen materials located in sections of the rig. A heat gun was used to heat a low pressure hydrogen store in the first section. This was followed by applying heat to a high pressure hydrogen storage material. Finally, a motorised piston was engaged incrementally to further increase the pressure to just below 2 kbar. Equations similar to those in Eqn. 2.23 - Eqn. 2.28 were used to calculate absorption properties of the sample material.

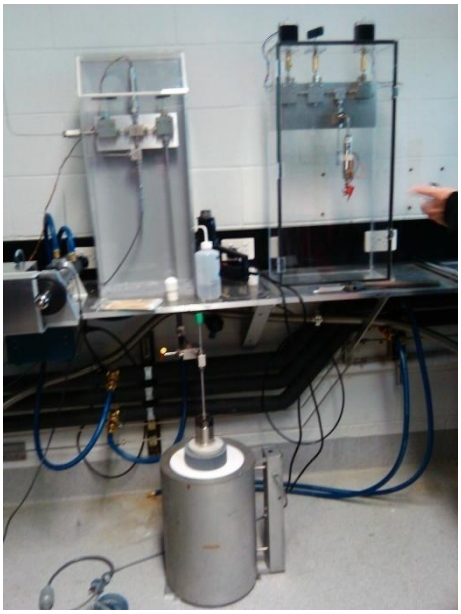

Figure 2.16: Picture of the high pressure rig at Griffith University.

2.12 Residual Gas Analysis

Mass spectroscopy was used to identify gases released from materials whilst ramping at a specified heat rate. Measurements were taken with a Stanford Research Systems

Residual Gas Analyzer (RGA) 300 under vacuum. This method uses a turbo vacuum pump to achieve low pressure atmosphere (10-5 millibar) and identifies gases released from the system according to the atomic mass unit (amu) of the gas (Figure 2.17).

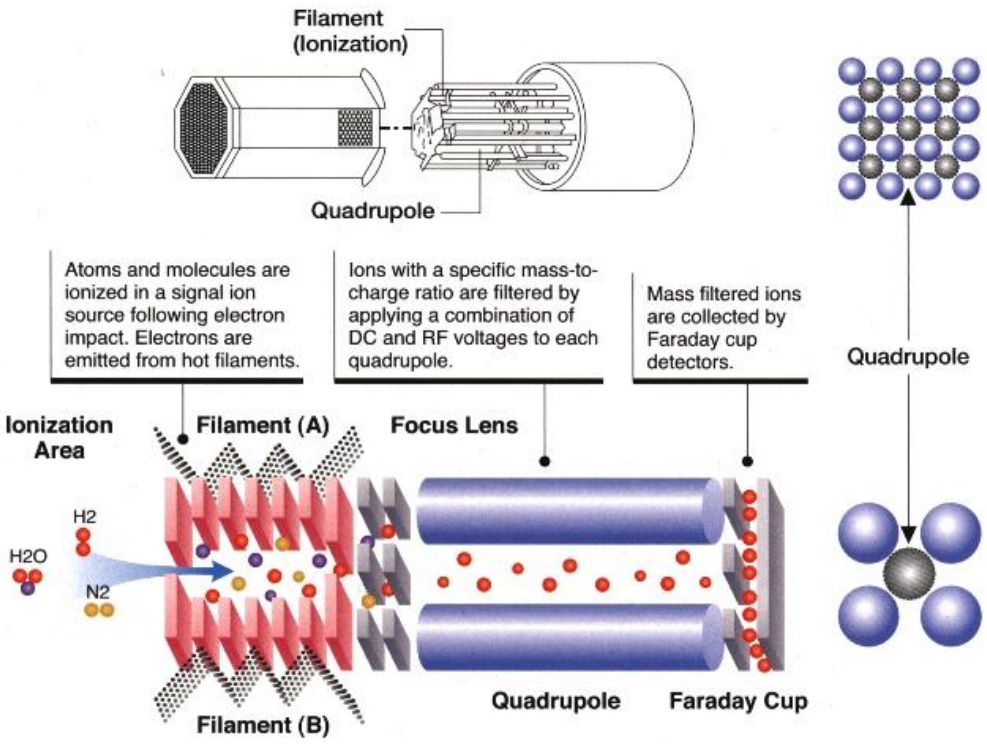

Figure 2.17: An illustration of the RGA operation[111].

RGA measurements used approximately 20 – 30 mg of material loaded into a sample cell in the argon atmosphere glovebox. This cell was sealed and then connected to the RGA equipment, the valve opened and the system was outgassed at room temperature until all traces of argon were gone. An N-type thermocouple was attached to the outside of the cell within proximity of the sample being analysed. The RGA300 monitored mass spectrums of gases released from the sample when heated from room temperature up to 600°C at a rate of 2°C min^{-1}.

Chapter 3: Synthesising Si Nanoparticles

"Science, regarded as the pursuit of truth, …can only be attained by patient and unprejudiced investigation."

Mary Somerville (1780 – 1892, Scotland)

This chapter is the first of four experimental chapters within this Ph.D. thesis. Presented here is the synthesis of silicon nanoparticles for the purpose of increasing desorption reaction kinetics with magnesium hydride. Faster reaction kinetics can lead to a more suitable material for hydrogen storage purposes as outlined in Chapter 1. Where relevant, the methodology for each experiment has been briefly outlined in this chapter and full details can be found in Chapter 2. Here, Si nanoparticles were successfully synthesised to an average size of approximately 10 nm. These nanoparticles will be mixed with MgH_2 to observe the reaction kinetics of desorption (Chapter 4).

3.1 Introduction

Nano dimensional silicon including nanoparticles, nanowires and thin films, have widespread applications including the communication optoelectronic devices[112], integrated circuits[113], solar cells[114, 115], medicine[116] and more recently, hydrogen storage[117]. The main advantage of nano-sized Si semiconductor material is that the quantum confinement effects[118, 119] lead to excellent optical and electronic properties. With respect to hydrogen storage, silicon has been proven to reduce the stability of metal hydrides[67, 117] during the desorption reaction thus modifying the thermodynamics of the system.

As mentioned in Chapter 1, Mg has generated a lot of interest as a hydrogen storage material in the form of MgH_2, as it is inexpensive, abundant and has a high hydrogen storage capacity of 7.6 wt.%. However, the high thermodynamic stability (ΔH = 74 kJ mol H_2^{-1}, ΔS = 133 J mol H_2^{-1} K^{-1})[7] and sluggish reaction kinetics[8] have limited its practical use. The kinetic issues in the Mg-H system have largely been overcome with a range of additives and catalysts introduced *via* ball milling, that provide particle size refinement and enable very fast reaction kinetics[52]. However, the thermodynamics of the pure Mg-H system are not able to be altered enough to provide low temperature operation, even by 7 nm MgH_2 particles exhibiting thermodynamic destabilisation[7]. Vajo *et. al.*[67] pioneered the work using Si to destabilise magnesium hydride (Eqn. 3.1). Vajo *et. al.*[67] found that by adding Si to

MgH_2, the equilibrium pressure at 300°C rose from 1.65 to > 7.5 bar. Further, theoretical calculations have shown that the Mg-Si-H system has ideal operating conditions, namely, equilibrium pressures of 1 bar at 20°C and 100 bar at 150°C with a reduction of hydrogen storage capacity of pure MgH_2 from 7.6 % to 5 %. The Mg-Si-H system also has reduced enthalpy of dehydrogenation from 75.3 kJ mol^{-1}, for pure MgH_2, to 36.4 kJ mol^{-1} [67]. Despite these promising theoretical properties, the conditions have not yet been achieved experimentally due to slow reaction kinetics.

Eqn. 3.1 $$2MgH_2 + Si \rightarrow Mg_2Si + H_2$$

Several factors have been studied in the past to overcome reaction kinetic limitations including reducing diffusion distances by using smaller particle sizes and introducing defects[67]. Bystrzycki *et. al.*[64] showed that the reduction of diffusion distances and an increase in surface area using nanoscale materials significantly influenced reaction rates. Bystrzycki *et. al.*[64] ball milled a stoichiometric mixture of MgH_2-Si to achieve a reduction in crystallite size to less than 40 nm for both reactants with a mean particle size of 0.5 μm. Diffusion of Mg at low temperatures is expected to be very slow and will inevitably control the reaction between MgH_2 and Si. Bystrzycki *et. al.*[64] proved there was no significant desorption below 200°C and only a release of 3.4 wt.% after 3 hours at 250°C. Similarly, another study that ball milled these two components showed only 0.03% hydrogen release at 150°C over a 24 hour period with the majority of the hydrogen desorbing at temperatures between 250 and 300°C.[72] These studies indicate that a reduction in crystallite size to the nano-scale level is not enough to overcome reaction kinetic barriers. Particle size also has an influence on the reaction kinetics[64, 89], therefore, the focus of this work is to synthesise small particles of Si (< 10 nm) to enhance the diffusion of Mg to bond with Si and release H_2 during dehydrogenation thus improving kinetic rates.

Several techniques have been developed to produce Si nanostructures including vapour phase synthesis (10 – 20 nm nanoparticles)[120], high temperature aerosol

reaction (20 – 40 nm nanoparticles)[120], magnetron co-sputtering (0.65 – 15.4 nm nano clusters)[121] and Si implantation (1.5 – 2.4 nm nanocrystals)[122], however these processes are laboratory based and would be difficult to scale up to produce nanoparticles on a larger scale[123].

Ultrasonic solution reduction methods have been able to produce Ge and ZnO nanoparticles less than 10 nm in size with a narrow size distribution[90, 124, 125] therefore making it an ideal method to produce Si nanoparticles in this range. Ultrasonication is the continuous formation, growth and implosive collapse of bubbles in a liquid[125]. The chemical reaction that occurs during the formation and collapse of these bubbles is also known as sono-chemical synthesis. The growth of particles are limited by this continuous acoustic cavitation[125] thereby producing small particles of a narrow size distribution. A simple method was developed by Wu *et. al.*[90] to produce Ge nanoparticles at room temperature within 30 min using metal hydrides to reduce $GeCl_4$ in an inert tetrahydrofuran solution. Presented in this chapter is an extension of this idea, replacing $GeCl_4$ with $SiCl_4$ to produce Si nanoparticles.

Another promising nanoparticle synthesis technique used in this study is mechanochemical ball milling. This technique is a high energy, room temperature batch process that uses a mechanically assisted chemical reaction. An example of large scale synthesis of Si nanoparticles was investigated by Lam *et. al.*[123] using Eqn. 3.2.

Eqn. 3.2 $\mathbf{C\ (graphite) + SiO_2 \rightarrow Si + CO_2}$

Although this technique produced Si nanoparticles, this reaction is not thermodynamically favourable as theoretical calculations using *HSC Chemistry* 6.12 software (Outotech Research), showed that the Gibbs free energy of reaction to be positive for the temperatures under which the reaction took place ($\Delta_r G_{298K}$ = 466.7 kJ mol^{-1}, $\Delta_r G_{423K}$ = 438.9 kJ mol^{-1}). These thermodynamics combined with slow

reaction kinetics is a problem for this reaction to form Si as it took an impractical length of time to complete, 7 to 10 days. An alternative method for nanoparticle production is mechanochemical ball milling within a soluble salt matrix[84]. Recent publications have applied this method to the synthesis of nanomaterials for hydrogen storage[85, 89]. However, problems such as isolation and degradation of the nanoparticles have, in some cases, limited their practical application in this field[89]. This chapter showcases synthesizing nanoparticles of Si *via* mechanochemical ball milling where a LiCl buffer phase is used to limit the growth of Si particles thus controlling the size of the nanoparticles produced. The hypothesis of improved reaction kinetics through small particles size reduction is explored in the next chapter when the Si nanoparticles are mixed with MgH_2 and desorption reaction kinetic behaviour analysed.

3.2 Ultrasonic Solution Reduction

Silicon tetrachloride, $SiCl_4$, solution was diluted with anhydrous tetrahydrofuran (THF) to a concentration of 0.5 M. The reducing agent lithium aluminium hydride, LiAlH4, was dissolved in THF to the same concentration to prepare for the reaction shown in Eqn. 3.3. The reducing agent was added to a three necked round bottom flask. The flask was connected to a high purity N_2 cylinder then put into an ultrasonic bath. The N_2 flowed throughout the system and the $SiCl_4$ was added drop wise to the LiAlH4 solution. Reactions were carried out under an inert atmosphere and ambient temperature and pressure for a total of 30 min similar to the method outlined in Wu *et. al.*[90].

Eqn. 3.3 $\boldsymbol{SiCl_4 + LiAlH_4 \rightarrow Si + LiCl + AlCl_3 + 2H_2 \quad \Delta_r G_{298K} = -340.4\ kJ\ mol^{-1}}$

After the cessation of ultrasonication, the solution was added dropwise and dried onto an X-Ray Diffraction (XRD) Low Background Holder (LBH) with an airtight

polymethyl methacrylate (PMMA) airtight dome. The sample was prepared in an Ar atmosphere glovebox to reduce contamination from either O_2 or H_2O. XRD was used to identify the crystalline phases present. The resultant diffractogram is given in Figure 3.1 (A) with the only crystalline material detected being LiCl. The PMMA dome was removed and the XRD run again to observe any differences (Figure 3.1 (B)). The diffractogram without the PMMA dome showed the $AlCl_3$, not detected previously, formed a complex with H_2O thus indicating the presence of amorphous $AlCl_3$ after the reaction (Eqn. 3.3) was completed. In both XRD patterns no Si was detected so the material was further analysed using transmission electron microscopy (TEM). No excess $SiCl_4$ or $LiAlH_4$ was detected using XRD; implying that the reaction had gone to completion.

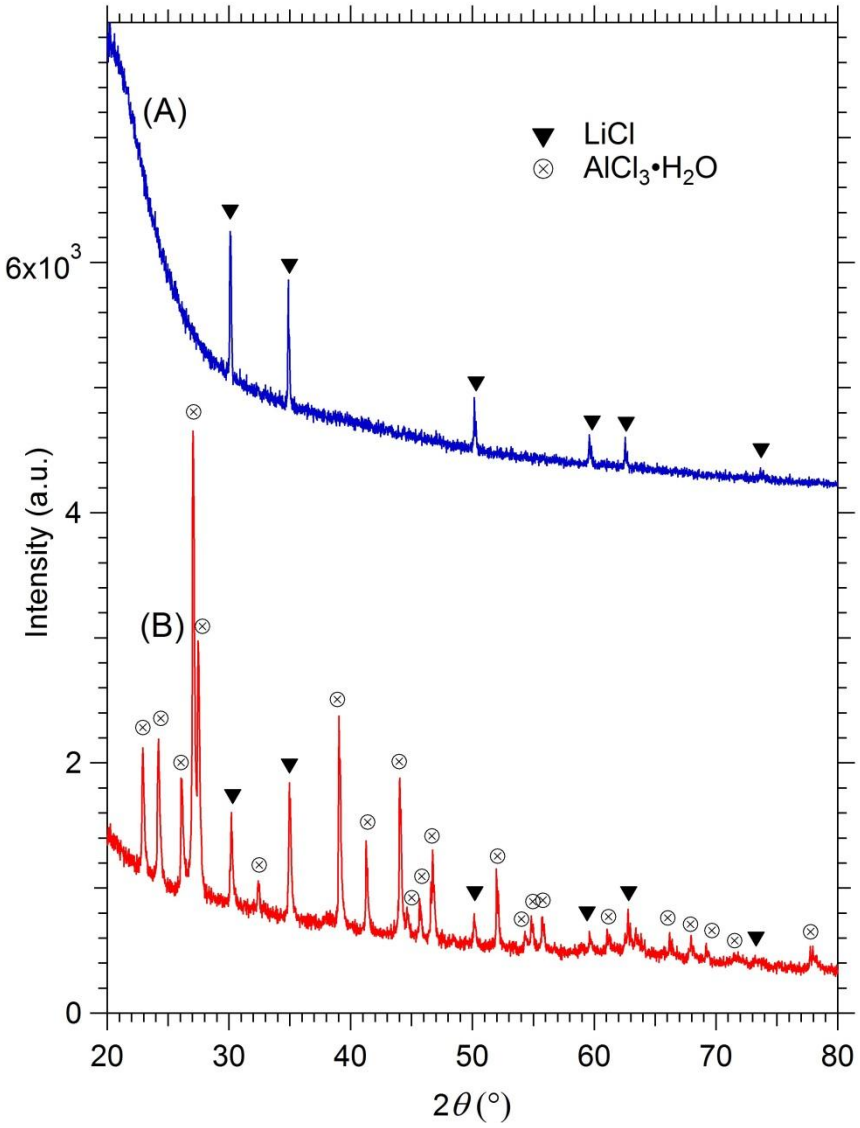

Figure 3.1: XRD Diffractograms of the products from Eqn. 3.3 on the LBH (A) with the PMMA dome (B) without the PMMA dome i.e. exposed to air.

There were two distinct sizes of particles found using TEM, firstly, the presence of large particles (Figure 3.2 (A)) that reacted under the electron beam. It was assumed that these were either $AlCl_3$ or LiCl particles as they appeared to continually change size, indicating degradation was possibly taking place even when exposed to the 300 KeV beam for less than 1 min. Similar LiCl degradation was observed when placed under a TEM instrument operating at a lower keV value of 200 KeV[126]. Another smaller size particle range was also found using the TEM and is shown in Figure 3.2 (B). These particles were ≤ 10 nm in size and spherical in shape similar to the nanoparticles synthesised in the Wu *et. al.* Publication[90]. In order to identify the

crystal structure of the smaller particles, high resolution TEM (HRTEM) was performed.

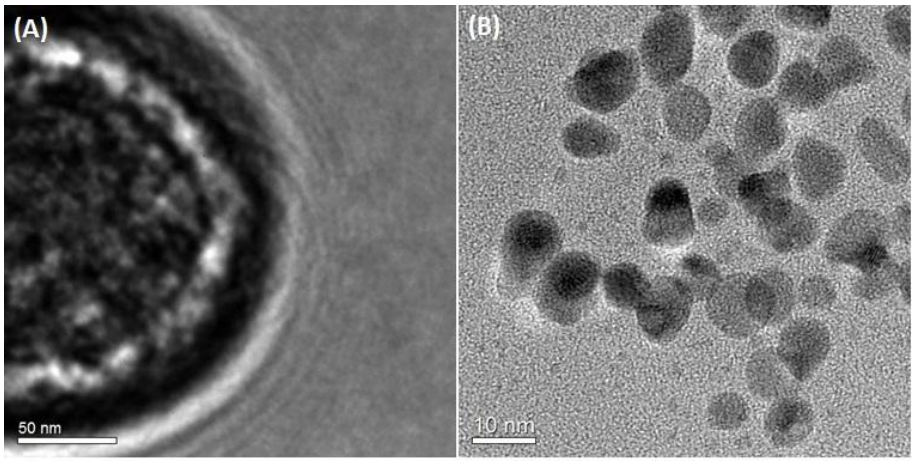

Figure 3.2: TEM micrographs of (A) large particle produced from ultrasonic reduction reaction (B) small particles ≤ 10 nm in size.

Using HRTEM it was possible to detect lattice planes of the smaller particles and measure the d-spacing between them. HRTEM identifies the crystallographic planes present in the sample that corresponds to certain d-spacing of materials. This is not a phase identification tool; rather, the compositions present can be inferred based on the distances between planes. Gatan software, DigitalMicrographTM was used to measure the distances between the planes. The HRTEM showed the distance between one set of planes having a d-spacing of 3.12 Å (Figure 3.3 (A)). This corresponds to the (1 1 1) hkl reflection of Si. There is another set of planes present could be $AlCl_3$ (Figure 3.3 (B)), which had a d-spacing of 2.4 Å (hkl reflection (2 2 0)), however, this plane could also match the (2 2 0) plane of Si with a d-spacing of 2.35 Å (within error). The images shown in Figure 3.3 are not in good focus hence the lattice planes appear outside the particles rather than inside them. This, however, does not have a significant impact on the lattice spacing measurements. Since crystalline silicon was detected using HRTEM but not XRD it was assumed that there was too little sample or that the sample was mainly amorphous. Due to the low volume of Si being produced with ultrasonication solution reduction it was deemed

impractical for the amount of sample required for MgH_2 desorption. Therefore, an alternative method, mechanochemical ball milling, was investigated.

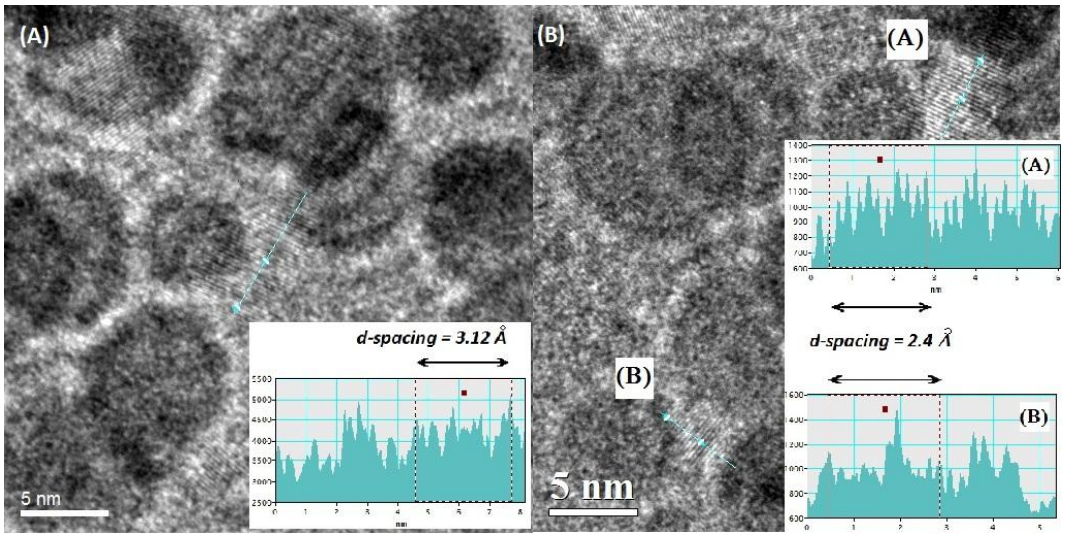

Figure 3.3: HRTEM showing (A) Si lattice planes (B) $AlCl_3$ / Si lattice planes. The peaks and troughs indicate the d-spacing. Several peaks and troughs were measured and divided by the total to achieve the d-spacing values indicated above.

3.3 Mechanochemical Synthesis

The two liquid-solid reactions pathways proposed for the synthesis of silicon nanoparticles *via* mechanochemical ball milling are given in Eqn. 3.4 and Eqn. 3.5. Firstly, thermodynamic feasibility was determined using *HSC Chemistry* 6.12 software, 2007, Outotech Research. It was found that both reactions were thermodynamically favourable based on the large negative value for the Gibbs free energy value. Therefore, both reactions were predicted to proceed at room temperature to form Si and LiCl salt clusters. Particle size was controlled by adding LiCl to the reactants as a buffer to limit particle growth from the beginning of the reaction.

Eqn. 3.4 $SiCl_4 + 4LiH \rightarrow Si + 4LiCl + 2H_2 \quad \Delta_r G_{298K} = -637 \text{ kJ mol}^{-1}$

Eqn. 3.5 $SiCl_4 + 4Li \rightarrow Si + 4LiCl \quad \Delta_r G_{298K} = -910 \text{ kJmol}^{-1}$

3.3.1 Synthesis of Si from $SiCl_4$ and LiH

The synthesis of Si particles was first explored using $SiCl_4$ and LiH as starting reagents without further purification (Eqn. 3.4). Initially, a ball to powder (BTP) ratio of 60:1 was used with a milling time of 6 h. The X-Ray Diffraction (XRD) pattern after 6 h of reaction time is given in Figure 3.4 (A). These processing conditions showed the presence of LiH and $SiCl_4$ without any Si or LiCl. Although $SiCl_4$ is a liquid at room temperature, a match was obtained using Bruker Diffracplus EVA version 16 for a pattern from the Inorganic Crystal Structure Database (ICSD). The ICSD number for $SiCl_4$ was published in 1986[127] at 163 K. Although the XRD was run at a temperature (room temperature ~ 298 K) much higher than the ICSD data, it still gave an indication that the reactants still remained in the material. Therefore, it was clear that 6 h was not enough time for the reaction to go ahead. The ball milling was repeated with a BTP ratio of 74:1 and increased milling times of 12, 18 and 24 h until the reaction went to completion. Figure 3.4 (B) shows the XRD pattern from the 24 h reaction where there was no evidence of either LiH or $SiCl_4$. The only product detectable was LiCl with some stainless steel 316 (SS 316) contamination due to the long milling time. The primary soller was removed (as described in Chapter 2) to increase the intensity of the sample in the X-ray beam however, there was still no evidence of crystalline Si.

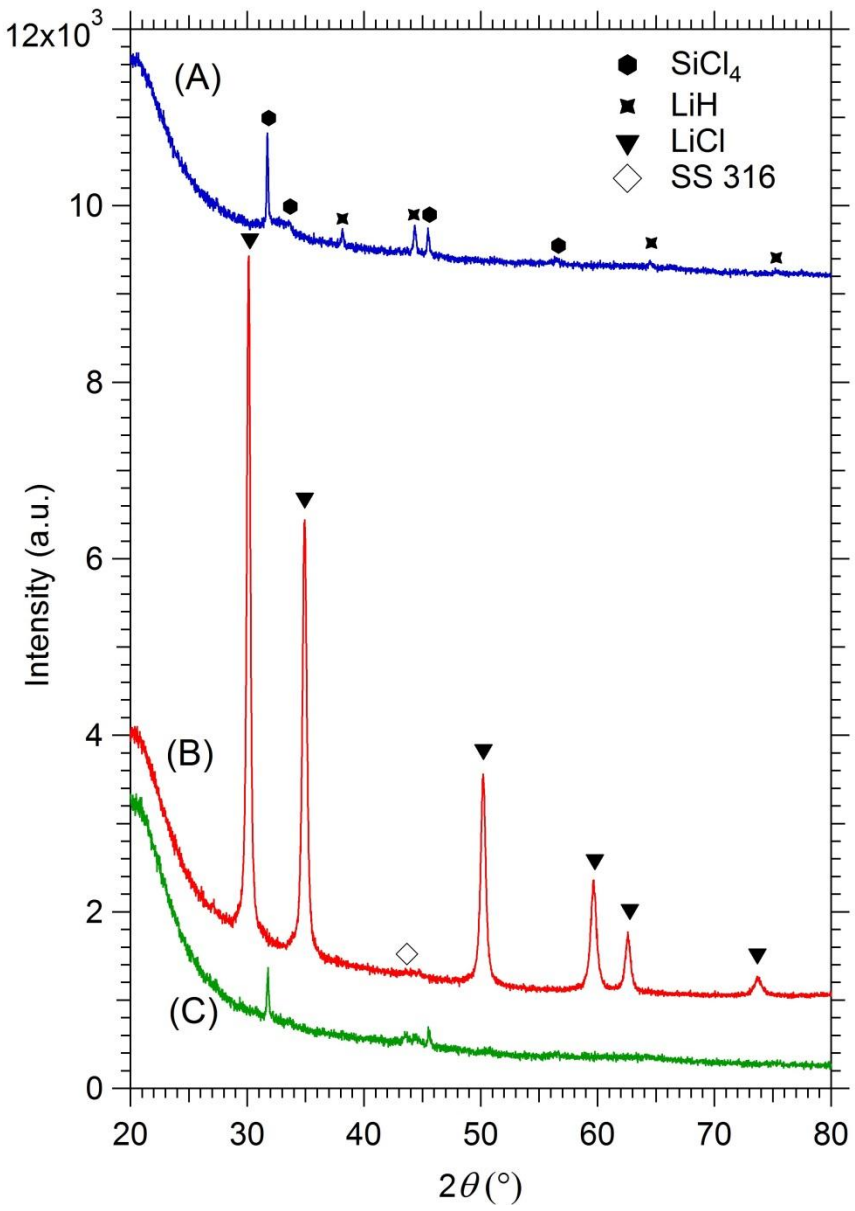

Figure 3.4: XRD diffractograms from Eqn. 3.4 (A) 6 h reaction time, 60:1 BTP ratio (B) 24 h reaction time, 74:1 BTP ratio (C) 24 h reaction time, 74:1 BTP ratio washed with tetrahydrofuran.

TEM was undertaken to determine if there were particles of Si present in the LiCl salt. Images from the small quantity of sample on the carbon coated copper grid showed big particles that proved to be unstable in the electron beam (field emession gun (FEG) at 300 keV) similar to the LiCl produced from Eqn. 3.3. Continual degradation of the LiCl salt made it difficult to obtain images of the sample.

However, it was possible to take some images of the larger particles greater than 100 nm that showed darker smaller particles embedded within (Figure 3.5 (A)).

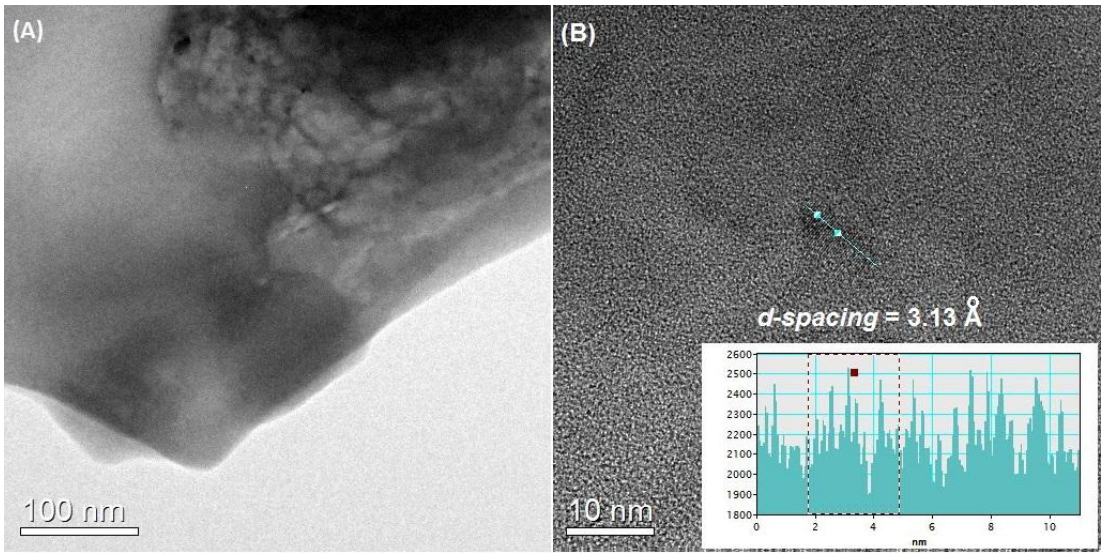

Figure 3.5: TEM micrograph of Si and LiCl from Eqn. 3.4 (A) Large particle with small particles evident in upper right hand corner (B) Lattice planes of Si (insert: region of interest measurements showing a d-spacing of 3.13 Å).

High resolution TEM (HRTEM) showed evidence of stable lattice planes. That is, the particle did not degrade under the beam (Figure 3.5 (B)). A region of interest analysis was done using the Gatan software, DigitalMicrographTM and this showed the distance between each of the planes measured a d-spacing 3.13 Å (Figure 3.5 (B) inset). This corresponds to the (1 1 1) hkl reflection of Si. It was extremely difficult to find further evidence of the Si lattice planes for the remainder of the sample so it was determined that the sample needed to be separated from the LiCl salt before further analysis could be undertaken.

Tetrahydrofuran (THF) was chosen as a solvent to 'wash' the LiCl from the Si nanoparticles as it was able to dissolve the LiCl whilst remaining relatively inert to the silicon nanoparticles. XRD was used to analyse the phases present (Figure 3.4 (C)) after washing. The XRD could no longer detect any LiCl indicating that the majority had been successfully separated from the remainder of the sample. However,

this sample underwent a reaction time of 24 h and there was evidence of the $SiCl_4$[127] after the LiCl was separated from the sample. This indicates that the reaction did not go to completion as assumed prior to washing. Another interesting point to note: when the LiCl-THF solution was decanted from the particles, a grey insoluble material was present. It appeared to be less dense than the solution as it floated to the top during centrifugation. XRD of this grey material showed that it contained remnants of LiH left over from the initial reaction. This material could not be completely separated from the intended Si product. Therefore, this reaction was not considered practical for the production of Si nanoparticles and no further experimentation was done with LiH (Eqn. 3.4).

3.3.2 Synthesis of Si from $SiCl_4$ and Li

The next approach to Si synthesis was the ball milling of $SiCl_4$ with Li (Eqn. 3.5). BTP ratios of 60:1 and 90:1 were trialled over a 24 h reaction period without adding any LiCl as a buffer agent to the reactants. Another sample was prepared using LiCl as a buffer agent to control the size of Si during its formation. LiCl was added to the reaction (Eqn. 3.5) with a LiCl to Si ratio of 10:1 based on the final products. Pre-milling the solid reactants (Li + LiCl) aids in the production of smaller particles during mechanochemical ball milling[128]. Therefore, the sample that contained the LiCl buffer, a stoichiometric amount of $SiCl_4$ was added to the powders after pre-milling for approximately 3 h and then ball milled for a further 24 hrs with BTP of 90:1.

The resulting diffractogram from the 90:1 reactions, 24 h without and with buffer (Eqn. 3.5) are shown in Figure 3.6. Similar to the previous reaction (Eqn. 3.4) processed under similar conditions, the reaction appears to go to completion as there were no reactants present in the diffractogram. To confirm this, the sample was washed with THF and again XRD was done on a single crystal low background holder with the Bruker supplied poly methyl methacrylate (PMMA) dome holder. No LiCl was detected after washing and, unlike Eqn. 3.4, this liquid-solid reaction

(Eqn. 3.5) had no reactants remaining. Again, there was no evidence of crystalline Si from the diffractogram (Figure 3.6 (B)).

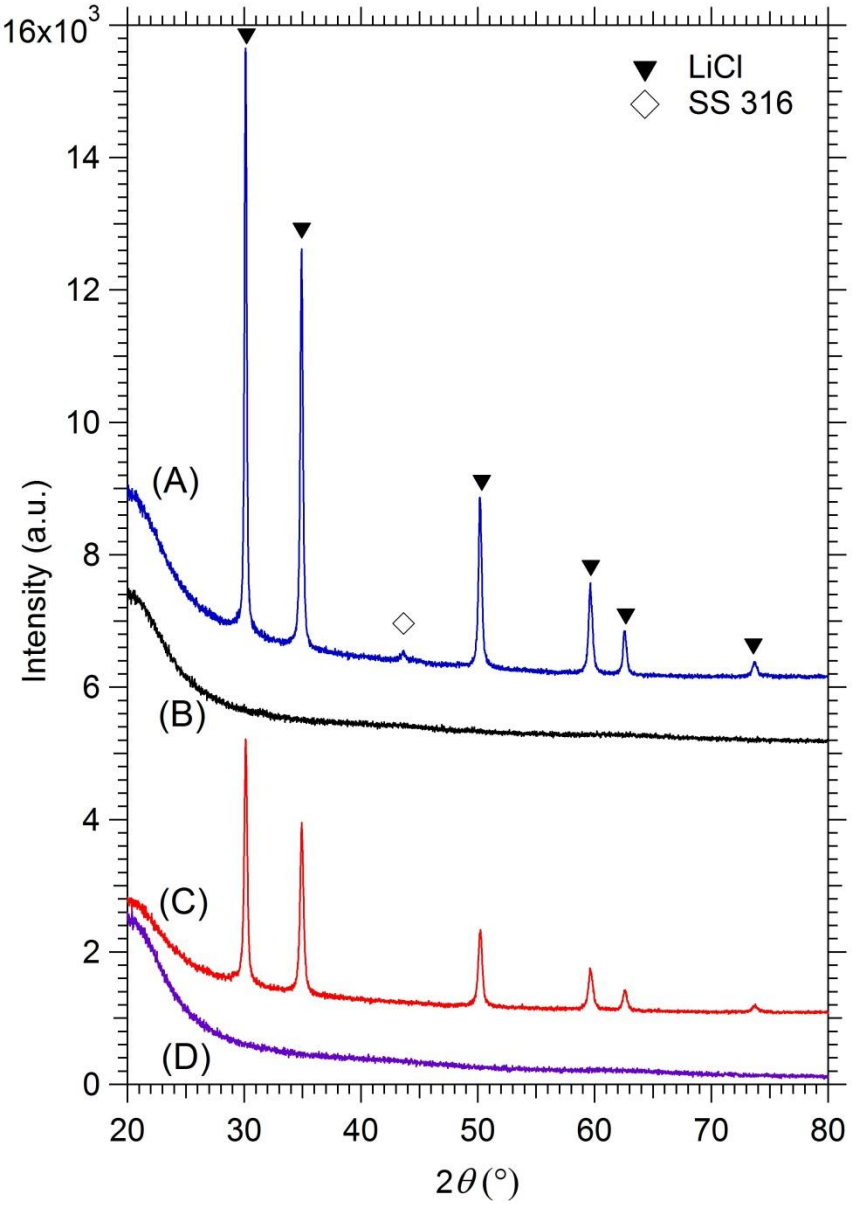

Figure 3.6: XRD diffractograms from Eqn. 3.5 with PMMA amorphous hump at 20° 2θ (A) 24 h reaction time, 90:1 BTP ratio no buffer (B) Sample (A) washed with THF (C) 24 h reaction time, 90:1 BTP ratio with 10:1 buffer to product (Si) ratio (D) Sample (C) washed with THF.

In an attempt to crystallize the particles synthesised from Eqn. 3.5, the two samples were heated to 475°C for 18 h, one sample in the LiCl (that is prior to washing with THF) and the other after washing with THF. According to Poffo *et. al.*[129] amorphous

Si particles undergo crystallization at 451°C when heated at a rate of 10°C min^{-1}. At a faster heating rate (40°C min^{-1}), this crystallization transition was observed at 660°C.[130] However, in both studies, the existence of O_2 contamination could not be completely ruled out and this was discussed in Poffo *et. al.*[129] as the reason for the large discrepancy between the two values. It was assumed that there was little or no O_2 contamination in the synthesised particles and this will be discussed further in this section that explains the results from the Electron Energy Loss Spectroscopy (EELS) data. The XRD patterns from the heated unwashed and washed Si samples are given in Figure 3.7 (A) and Figure 3.7 (B) respectively. The results show that Si did not undergo crystallization at 475°C as there was still no evidence of crystalline Si in the XRD. For comparison, the XRD for crystalline Si as supplied from Sigma Aldrich has been given in Figure 3.7(C). The sample cell was made from SS 316 and has a temperature rating of 537°C (Swagelok, Australia) therefore higher annealing temperatures were not safely achievable.

The amorphous silicon phase typically shows broad halos centered at 28° and 50° 2θ in an XRD pattern.[131] In an attempt to detect the presence of these broad halos for Si, XRD was performed with a 300 nm thick aluminium leaf in place of the PMMA, argon filled dome. This was done to prevent the scattering from the amorphous PMMA dome at lower values of 2θ. Also, Al foil helps reduce the effect of the argon (Ar) when the PMMA dome is used. The dome is filled with Ar from the glovebox which is a strong X-ray absorber compared to air. When the dome and Ar are taken into consideration, the X-ray intensity that reaches the detector is ~ 65% less compared to air alone. The Al leaf was sealed onto a single crystal low background holder using petroleum jelly to prevent exposure to air.

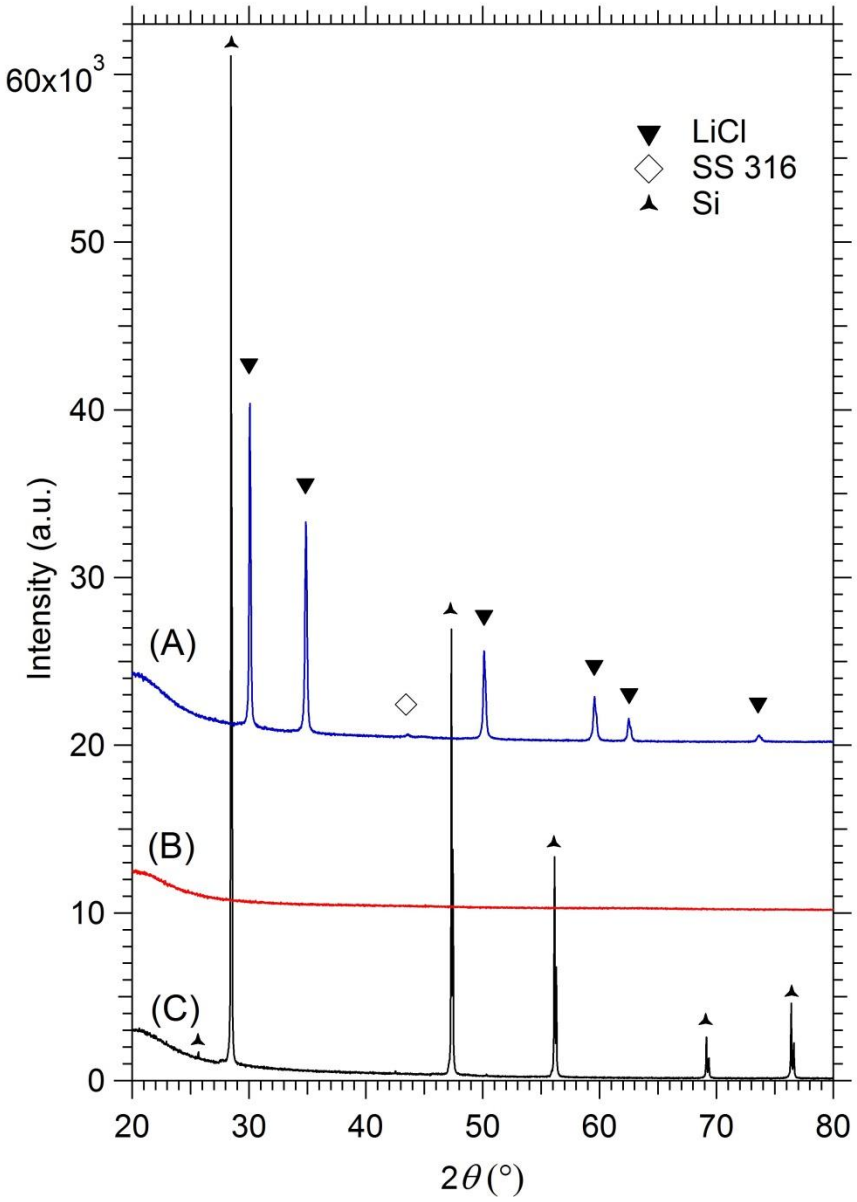

Figure 3.7: (A) LiCl + Si products heated to 475°C for 18 h (B) Washed Si heated to 475°C for 18 h (C) Si powder as supplied from Sigma Aldrich.

Figure 3.8 (A) shows the XRD pattern of Si covered with the Al foil and Figure 3.8 (B) shows the Al foil layer diffractogram on its own. It should also be noted that Figure 3.8 (A) shows a peak at 32° 2θ that can be attributed to the LiCl·H_2O complex. LiCl is extremely hygroscopic so any trace amounts of LiCl remaining from the initial reaction would react with H_2O in the atmosphere as the Al foil does not form a perfect seal.

Figure 3.8 clearly shows that there is evidence of two amorphous regions, one centred around 28° and the other at 50° 2θ. This is in agreement with Wang *et. al.*[131] where amorphous Si humps were shown to have similar XRD results. Therefore, it can be concluded that amorphous Si particles were synthesised using mechanochemical ball milling.

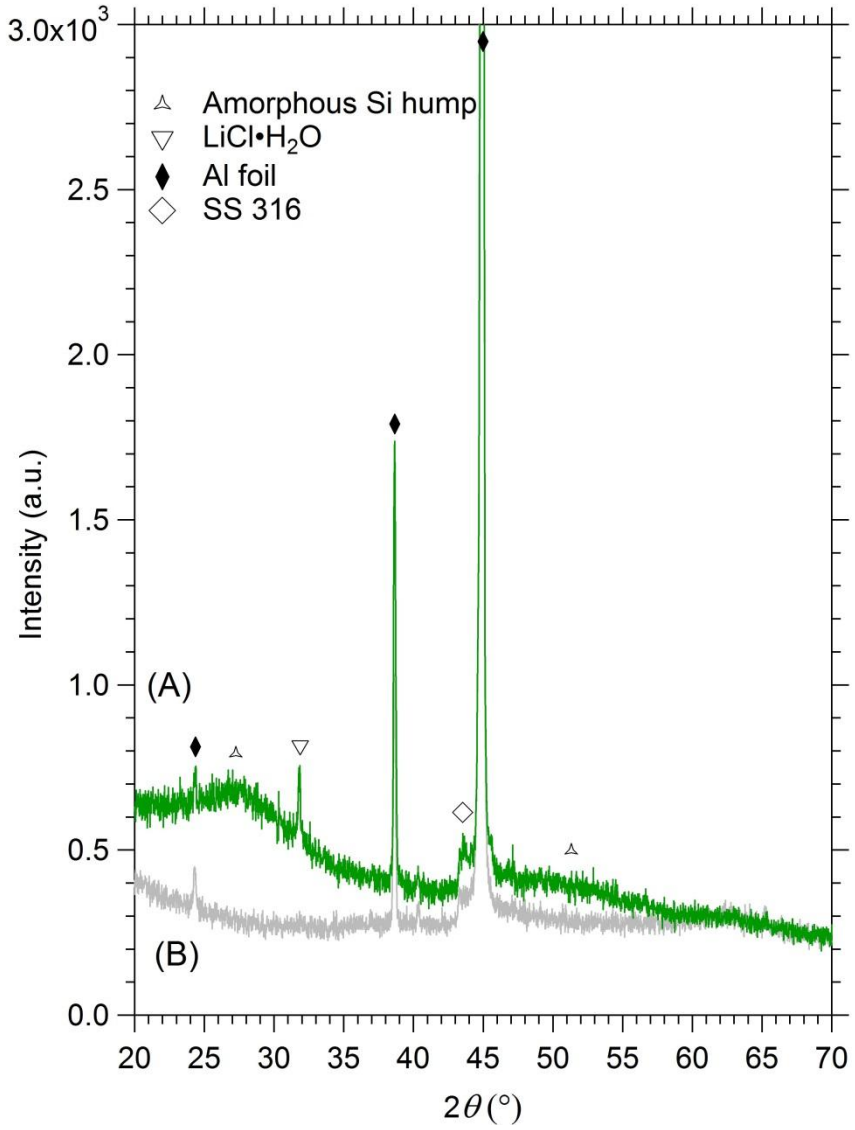

Figure 3.8: XRD of (A) Washed Si nanoparticles with Al foil barrier (B) Al foil barrier, no sample.

The formation of an amorphous material is not uncommon during mechanochemical ball milling as it has been shown in a number of studies[75, 130, 131]. Amorphicity occurs as a result of particles being strained to a critical stress level beyond which the microcracks start to propagate and thereby create new surface area[132]. This means that the actual specific fracture energy used for fragmentation is not only the energy needed to break chemical bonds when forming a new material; but also involves an activation energy at the crack tip. This energy is partially converted to heat and partially used to alter the atomic structure near the crack surface to a depth of many atomic layers, transforming the material to an amorphous state or to a surface of higher energy as the material rapidly cools down[132].

Further analysis was done using high resolution Scanning Electron Microscopy (SEM) and Transmission Electron Microscopy imaging (TEM). Samples for both TEM and SEM were prepared by suspending the Si nanoparticles in toluene in a sealed vial and ultrasonicated in a water bath for 30 minutes. Dispersing nanoparticles in a non-polar organic medium, such as toluene, is a major challenge as the particles tend to aggregate very easily[113]. Toluene, however, does not contain any oxygen that could react with the sample, and was therefore used for ultrasonication.

The technique known as Electron Energy Loss Spectroscopy (EELS) on the TEM was used to confirm the presence of Si. Unlike XRD that relies on the diffraction of crystalline samples to produce a phase identifying pattern; EELS uses inelastic electron scattering to measure the energy loss from the electron beam after transmitting through the sample. The energy loss information can identify elements present in the sample as well as give bonding information.

Firstly, the products of the synthesis reaction, Si and LiCl, were placed onto the grid and analysed under the electron beam. When a spectrum is collected from the detector, K-, L- or M-edges appear depending on which core electrons are present in the atom. Pure Si has a K-edge at 1839 eV and a $L_{2,3}$-edge at 99.2 eV[133], Figure 3.9 shows the complete spectrum (A), the location of the background (B) subtracted to obtain the $L_{2,3}$-edge (C) information for Si. When silicon is oxidised the $L_{2,3}$-edge typically moves to higher energy (~ 106 eV). The energy of the Si $L_{2,3}$-edge obtained

from the sample is therefore more characteristic of silicon than any oxidised form of the element.

The same method was used to identify the K-edge of Li at 60 eV[133] (Figure 3.10) bonded to the $L_{2,3}$-edge of Cl at 200 eV[133] (Figure 3.11). The lighter the element the more difficult it is to detect the energy loss from the electron as it is close to the zero loss peak and any plasmons that may be present. No other elements were detected from the EELS spectra.

Once the sample was washed with THF, the process was repeated on the particles that were separated from the solution. The resultant spectrum is given in Figure 3.12. Again, the pure Si $L_{2,3}$-edge was at ~100 eV indicating that the Si had not oxidized and pure Si remained.

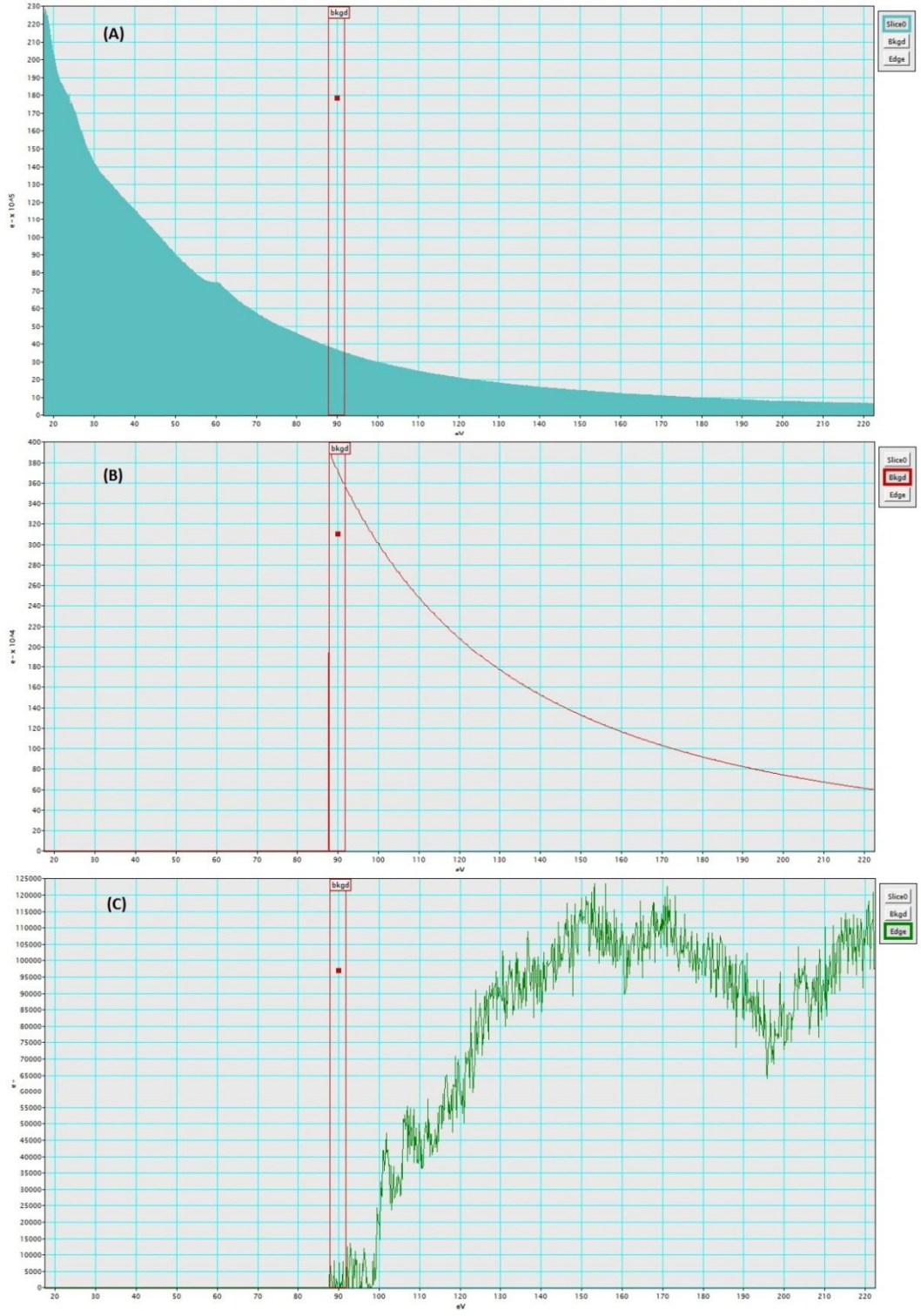

Figure 3.9: Si in LiCl sample: Si EELS spectra analysis 99 eV Si-$L_{2,3}$ edge 150 eV L_1 edge (pure Si)[133].

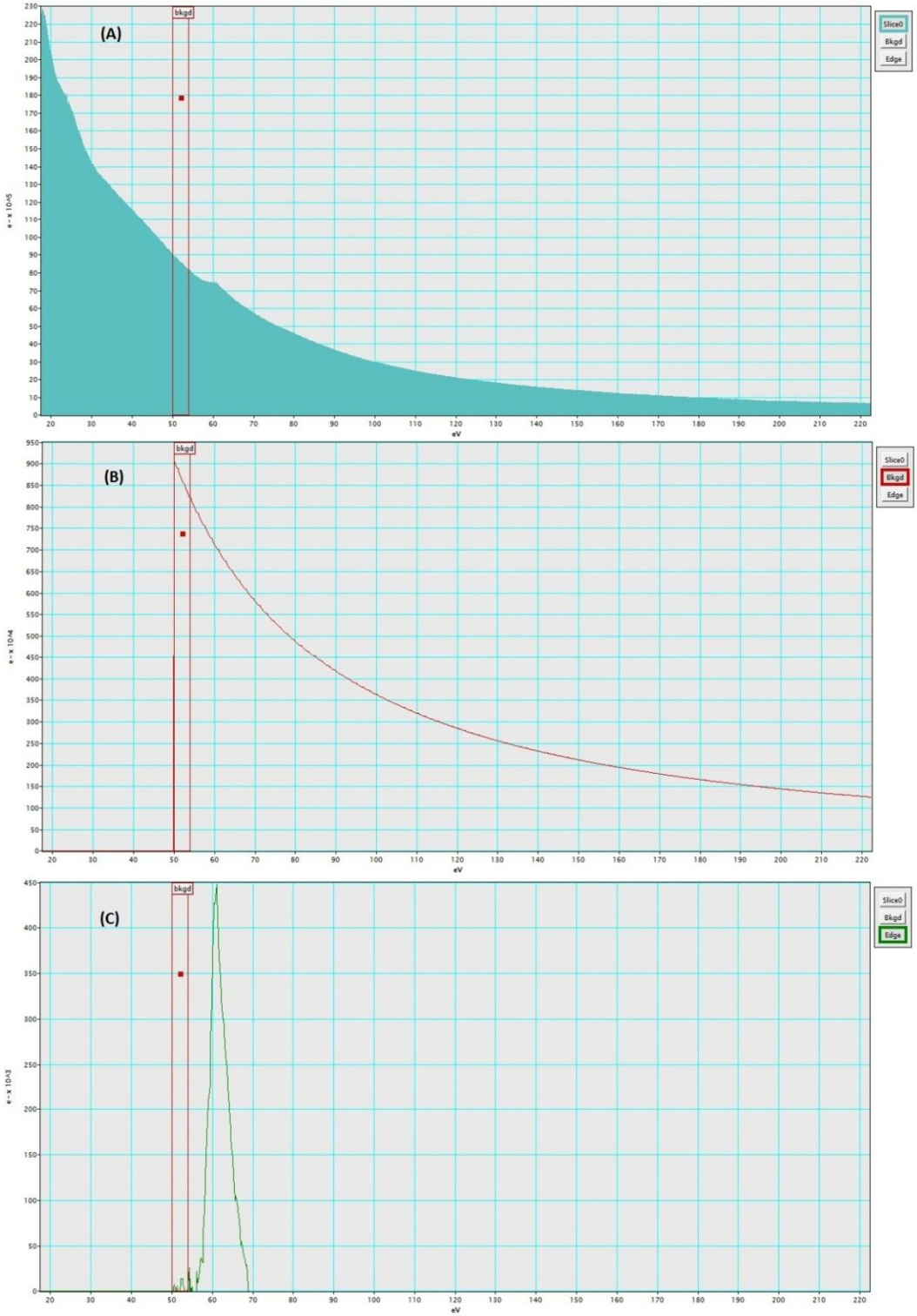

Figure 3.10: Si in LiCl sample: Li EELS spectra analysis 60 eV Li K-edge similar to LiF edge[133].

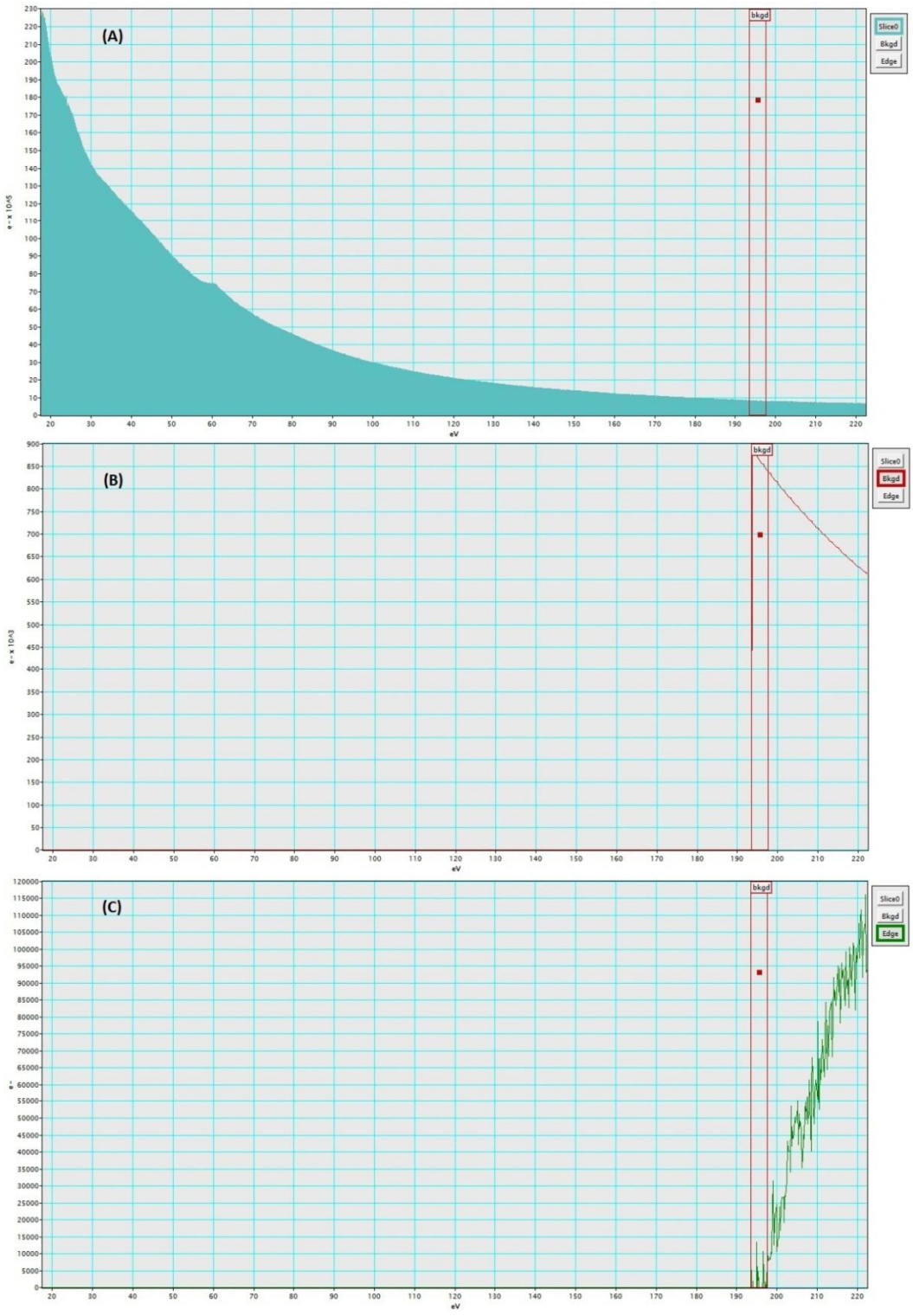

Figure 3.11: Si in LiCl sample: Cl EELS spectra analysis 200 eV Cl-$L_{2,3}$ edge similar to NaCl edge[133].

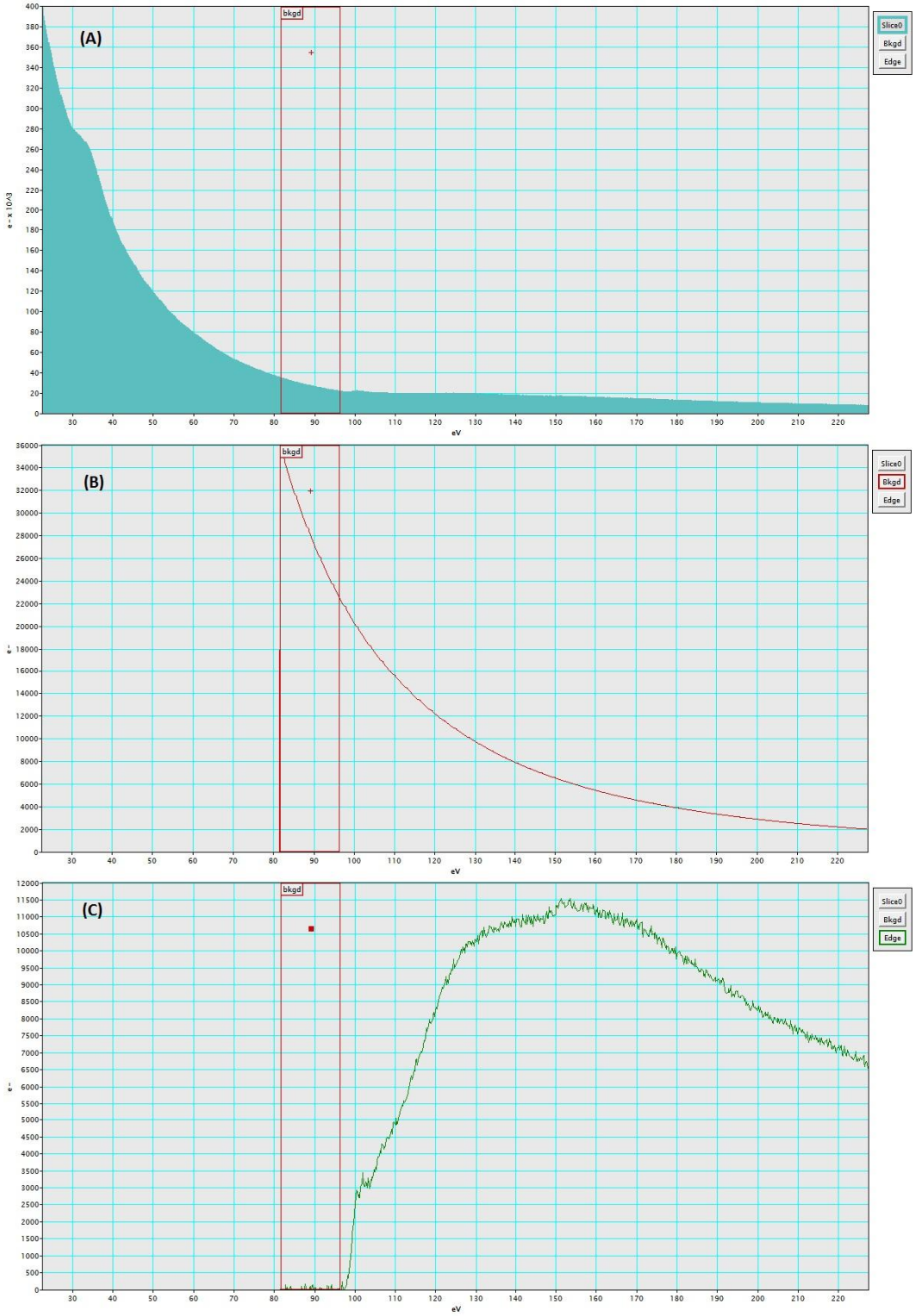

Figure 3.12: Washed Si sample: Si EELS spectra analysis 99 eV Si-$L_{2,3}$ edge 150 eV L_1 edge (pure Si)[133].

In order to obtain a map of the elements detected using EELS, Energy Filtered TEM (EFTEM) was done. This method uses the energy loss information from EELS to produce an elemental image[105]. This is done by specifying energy values immediately before and after the EELS detected edge (pre-edge 1, pre-edge 2 and post-edge, Figure 3.13) and using the pre-edge data to fit and remove a background from the post-edge data to obtain an image of the element distribution. This has been done for the Si in the LiCl salt matrix (Figure 3.14) as well as the washed Si sample (Figure 3.15).

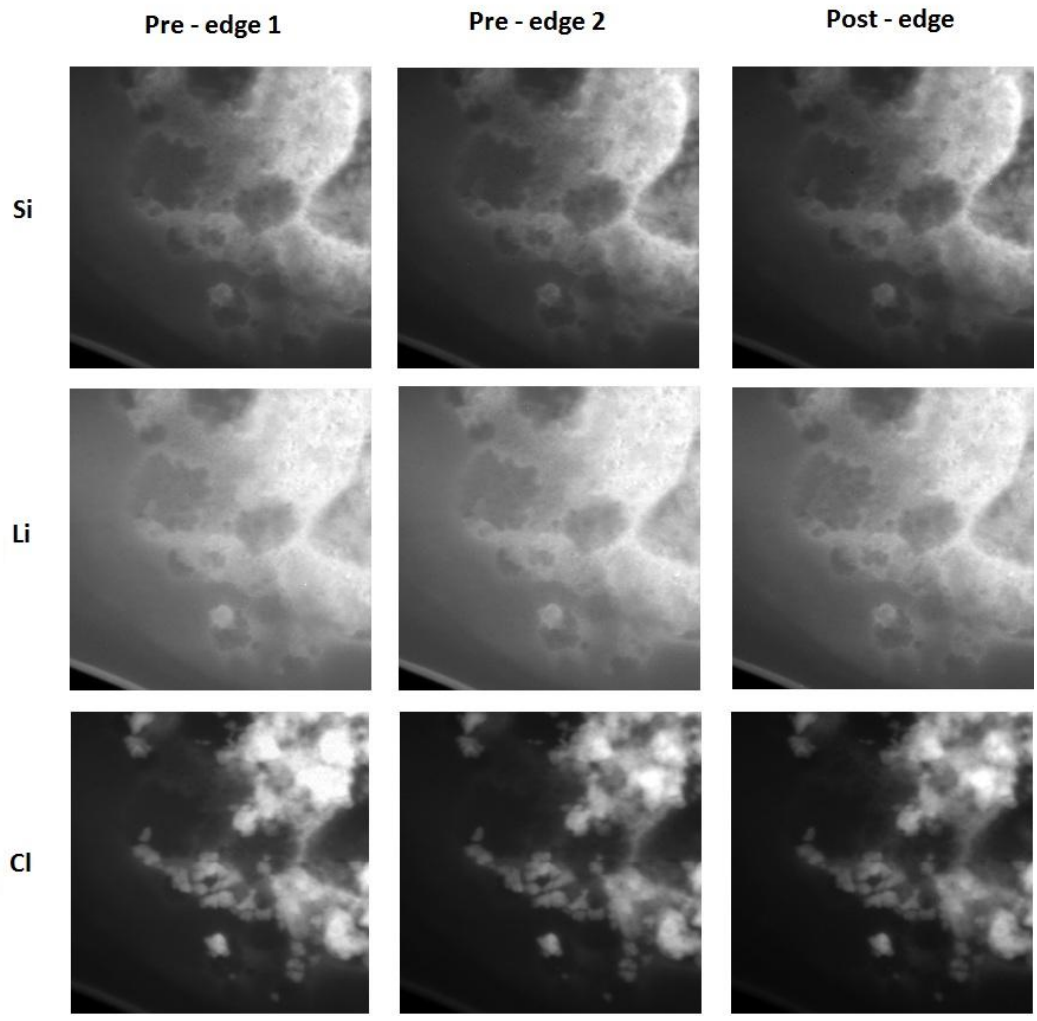

Figure 3.13: Si in LiCl sample: EFTEM element maps showing two pre-edges and one post-edge.

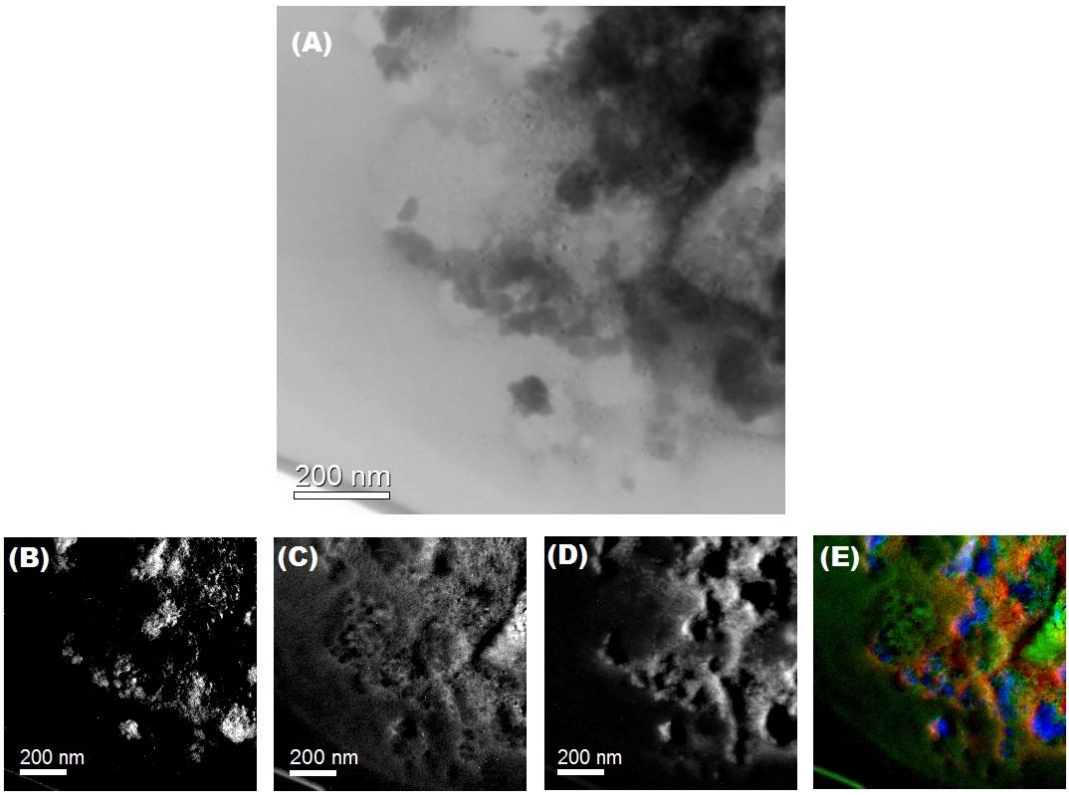

Figure 3.14: Si in LiCl sample: (A) TEM micrograph image. Element maps: (B) Si EFTEM (C) Li EFTEM (D) Cl EFTEM (E) EFTEM Red (Cl) Green (Li) Blue (Si) image stack.

Figure 3.14 shows a series of images used to map the elements present in the sample, Si, Li and Cl. Each element was mapped using EFTEM taken from the pre- and post-edges shown in Figure 3.13. The resultant maps for the unwashed sample are given at the bottom of Figure 3.14. The final image is an overlay of the falsely coloured elements, Si shown in blue, Li in green and Cl in red.

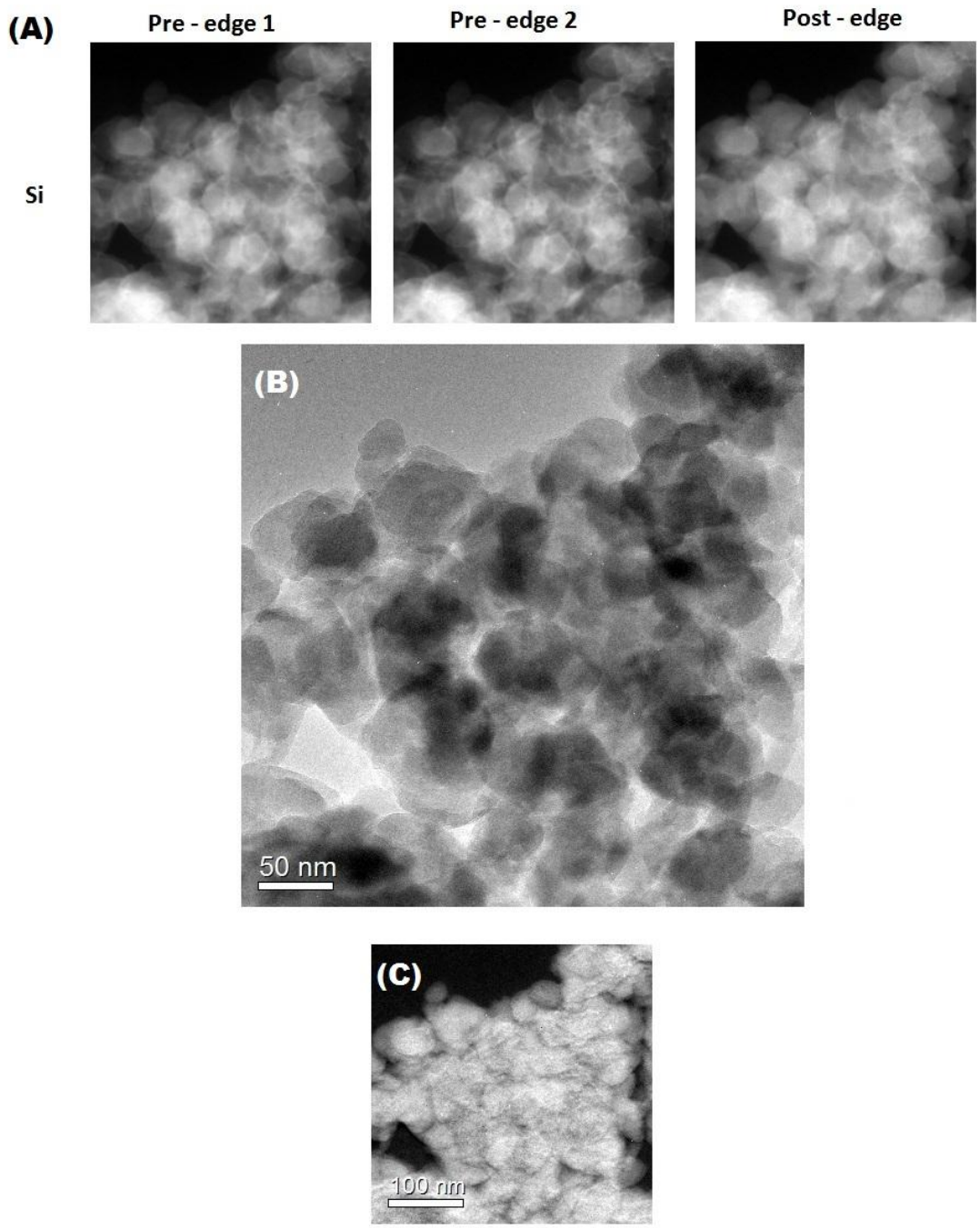

Figure 3.15: Washed Si : (A) EFTEM element maps showing two pre-edges and one post-edge. (B) TEM micrograph (C) Si EFTEM map.

The EFTEM analysis was also performed on the washed Si sample by taking the pre- and post-edge images (Figure 3.15 (A)) to obtain a Si map (Figure 3.15 (C)). The

map (Figure 3.15 (C)) corresponds very well to the TEM image (Figure 3.15 (B)). This indicates that a majority of the particles shown in the image can be accounted for with the Si map therefore, identifying Si containing nanoparticles.

SEM images of samples made from Eqn. 3.4 and Eqn. 3.5 with and without the LiCl salt matrix are given in Figure 3.16. The unwashed samples (Figure 3.16 (A) and (C)) show two morphological phases of material, with bigger size particles surrounded by much smaller particles. The images of the washed samples (Figure 3.16 (B) and (D)) clearly show spherical particles without the background of the bigger particles. From this, it can be concluded that the Si nanoparticles are sphere like and are highly agglomerated once separated from the LiCl salt.

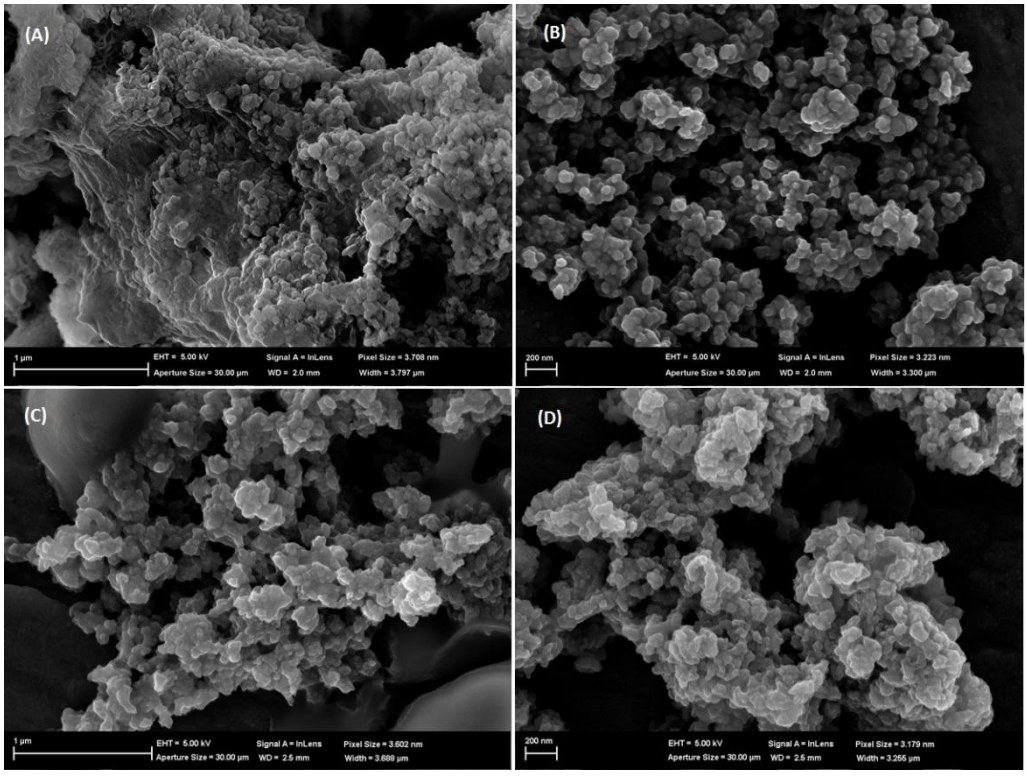

Figure 3.16: SEM micrographs showing synthesised Si nanoparticles (A) without buffer in LiCl salt (B) sample (A) after washing with THF (C) with buffer in LiCl salt (D) sample (C) after washing with THF.

TEM images of the Si particles in LiCl show the two phases a little less clearly (Figure 3.17). The images do however show small dark particles embedded in a larger matrix, presumably Si in LiCl salt. The TEM images of the washed samples both without buffer (Figure 3.18) and with buffer (Figure 3.19) show more distinct outlines of particles. It is difficult to gauge the size of the individual particles due to the high level of agglomeration despite ultrasonication of the sample during preparation.

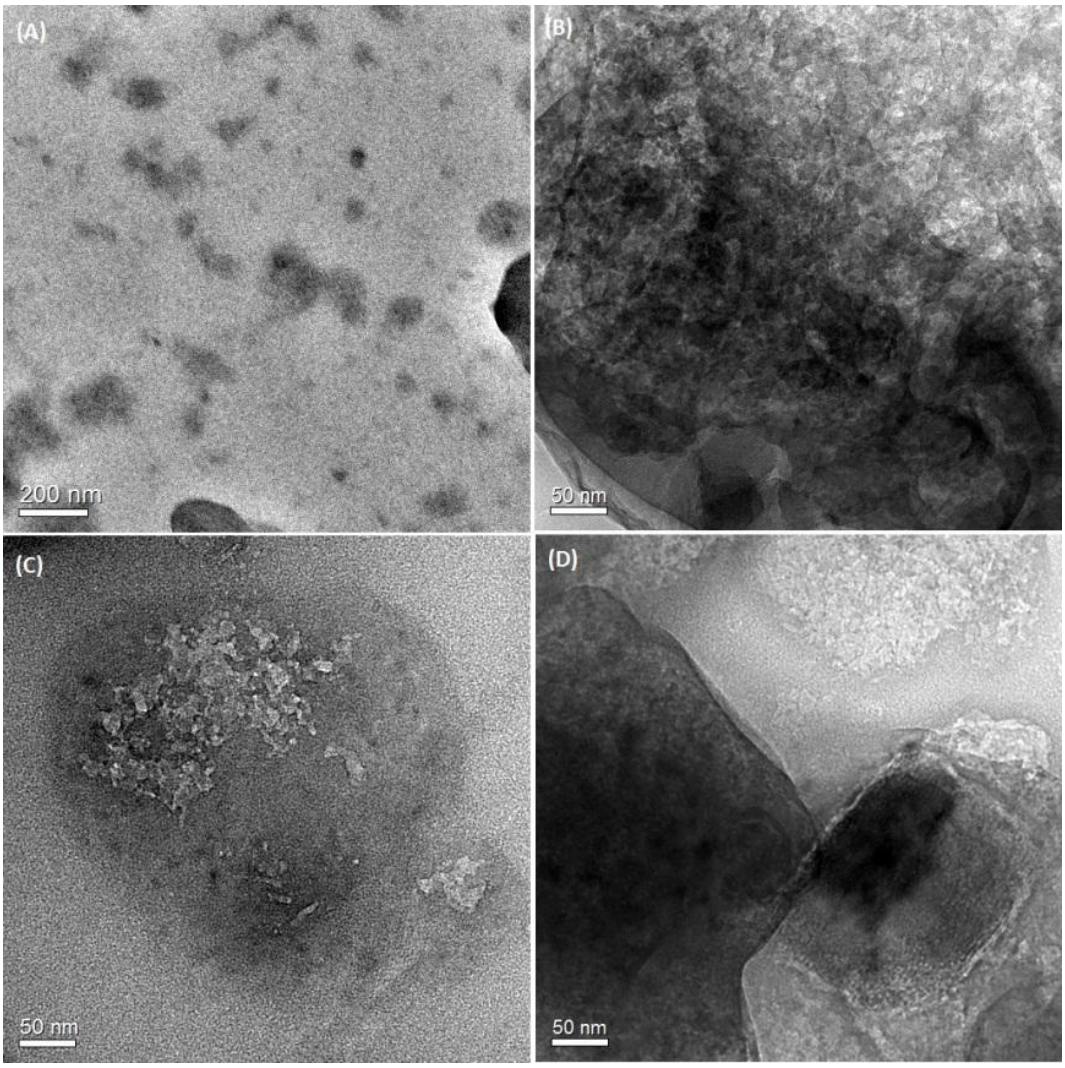

Figure 3.17: TEM images of Si in LiCl salt synthesised with (A) & (B) no buffer at different magnification (C) & (D) with buffer.

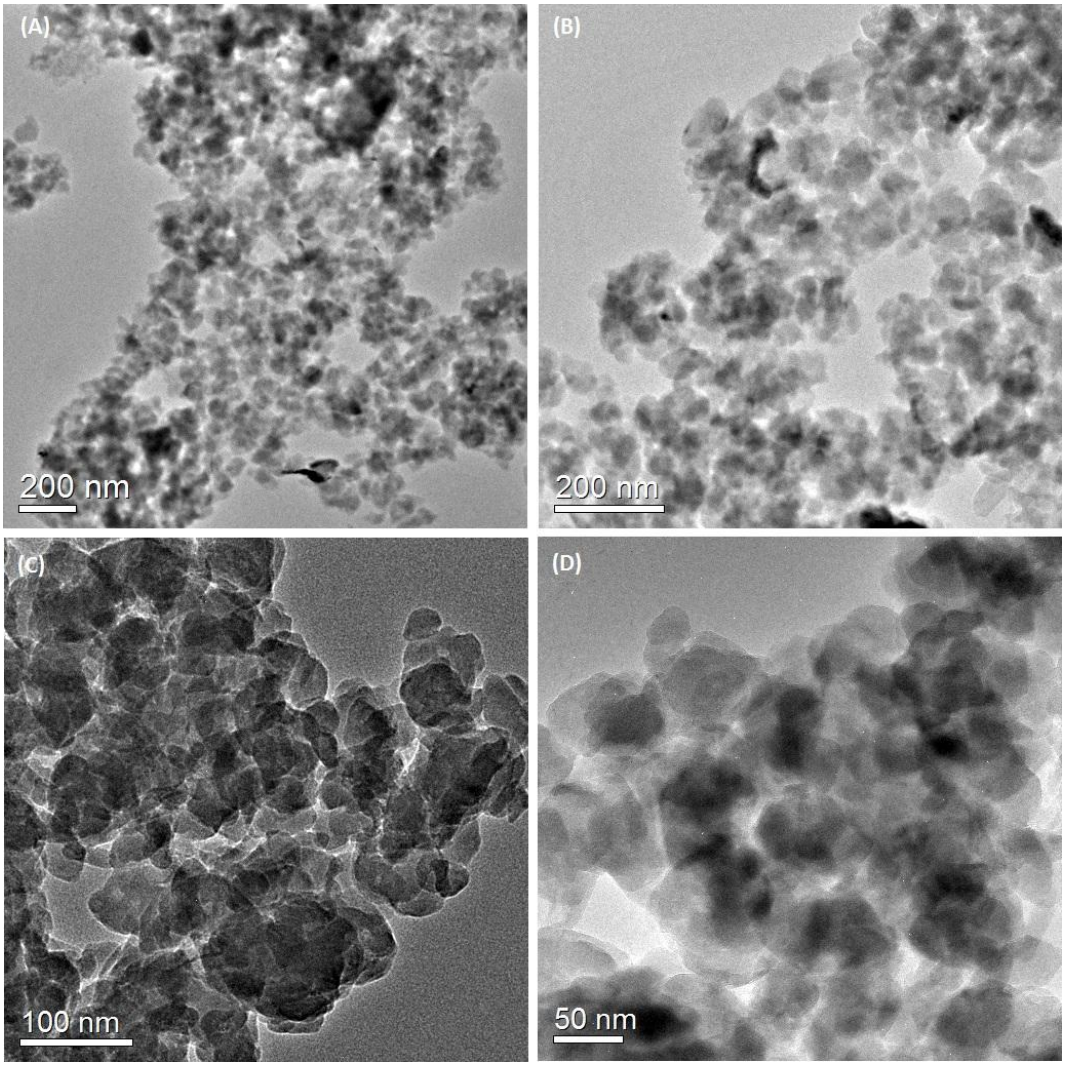

Figure 3.18: TEM images of Si washed produced from Li reaction without buffer.

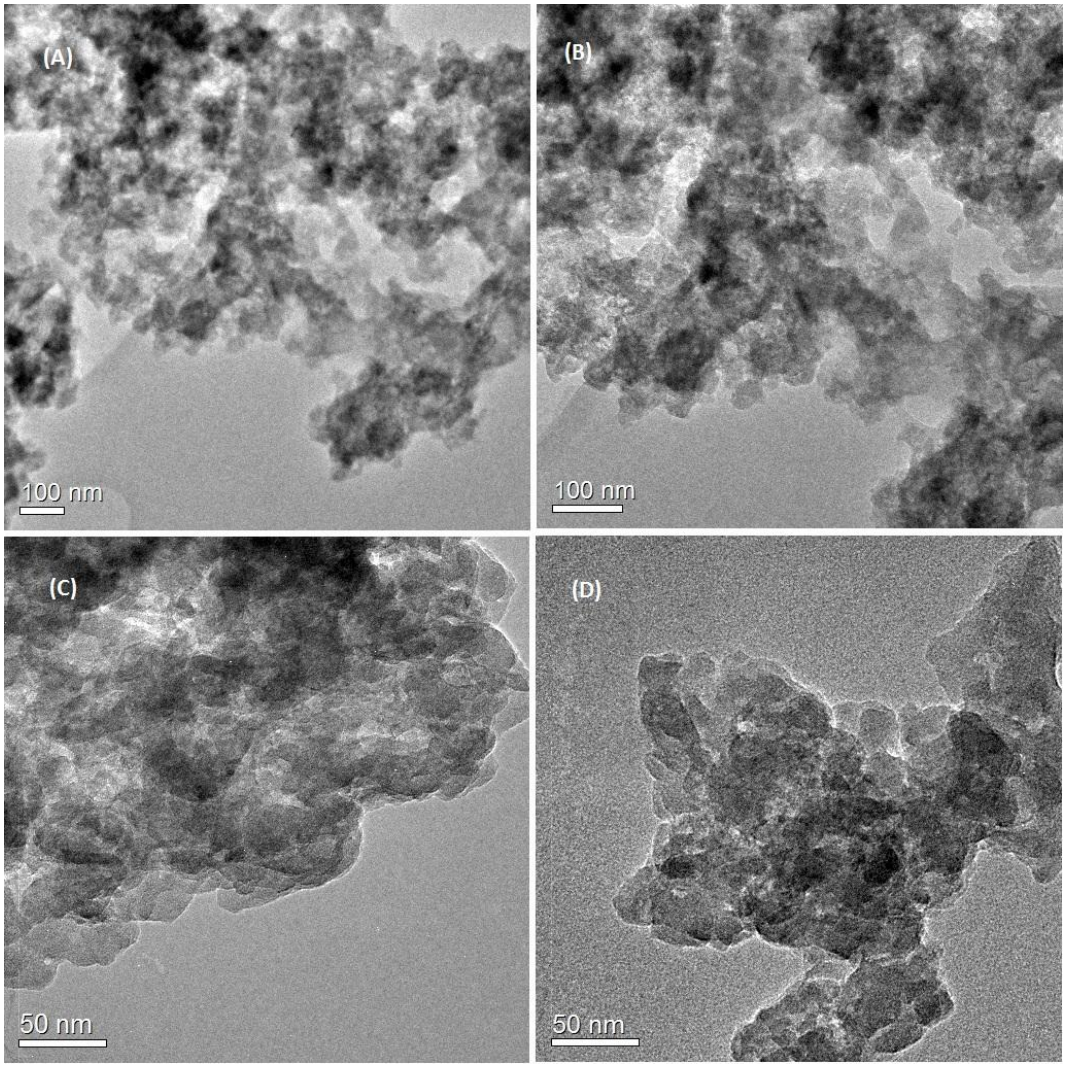

Figure 3.19: TEM images of Si washed produced from Li reaction with buffer.

Small Angle X-ray Scattering (SAXS) was performed on each sample to measure particles size for reaction given in Eqn. 3.5 without buffer (Figure 3.20) and with buffer present in the reactants (Figure 3.21). Each sample was prepared using the method described in Chapter 2. In order to show how the data were processed, the raw data together with the transmission and background corrected data are given in Figure 3.20 (A) and Figure 3.21 (A). The background comprises of both a blank glass capillary as well as the noise of the detector (data taken with the X-rays turned off). The data have also been put onto an absolute scale where the y-axes are plotted as intensity with units of cm^{-1} and the x-axes are plotted as Q with units of $Å^{-1}$.

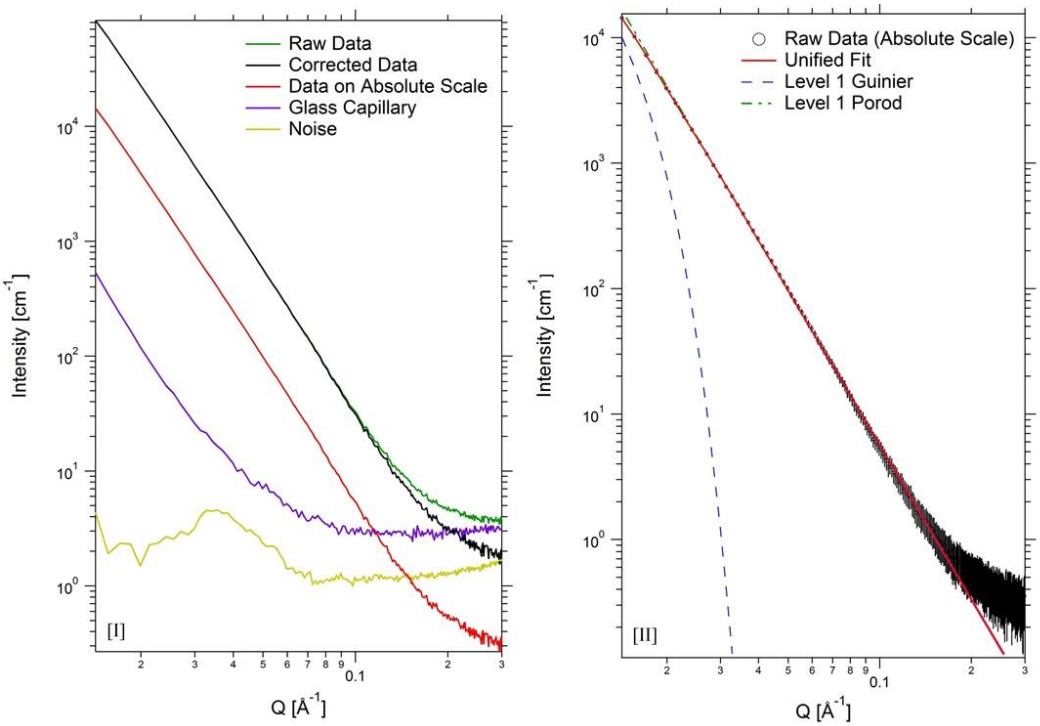

Figure 3.20: SAXS data of Si nanoparticles synthesised without buffer (Eqn. 3.5) (A) Raw and corrected data for absolute scale (B) Unified fit modelling.

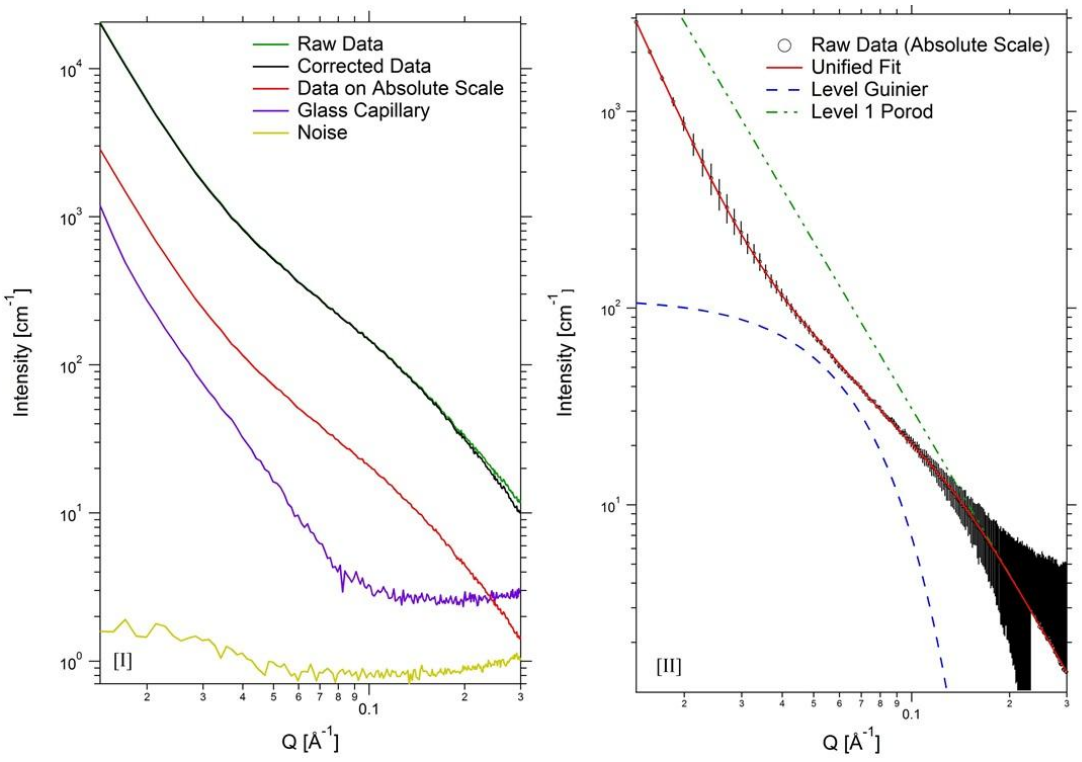

Figure 3.21: SAXS data of Si nanoparticles synthesised with buffer (Eqn. 3.5) (A) Raw and corrected data for absolute scale (B) Unified fit modelling.

The National Institute of Standards and Technology (NIST) developed Small Angle Scattering (SAS) data analysis package (Irena Macros for Igor Pro 6.0, release 2.32, 2008) was used to fit a model for particle size analysis. Taking the evidence from the SEM of spherical morphology, the unified fit model was used to calculate a single figure for average bulk particle size of the sample. This model is described in detail in Beaucage[103] and divides the raw data into the Guinier part and the power law tail in order to calculate the radius of gyration. From this an average particle diameter of 51 nm without buffer and 13 nm with a 10:1 LiCl:Si buffer ratio (Eqn. 3.5) was determined (Figure 3.20 (B) and Figure 3.21 (B)). The Guinier approximation for a sphere (Eqn. 3.6) was used to calculate the average diameter (twice the radius, *r*) of the particles from the radius of gyration (R_g) obtained from the unified fit model (Table 3.1).

Eqn. 3.6 $$R_g = \sqrt{\frac{3}{5}}r$$

Table 3.1: Table of radius of gyration with corresponding diameter.

Reaction	R_g (nm)	*D* (nm)
Without LiCl buffer	19.7	51
With 10:1 LiCl:Si buffer	5.1	13

3.4 Conclusion

Si nanoparticles were synthesised using ultrasonic solution reduction and mechanochemical synthesis. A number of different reaction pathways were used and it was determined that mechanochemical ball milling with $SiCl_4$ and Li was the best method to produce the volume of particles required for mixing with MgH_2 and

consequent desorption studies. Mechanochemical ball malling produced amorphous Si nanoparticles identified using XRD (location of amorphous humps) and the TEM techniques EELS and EFTEM. Morphology images from SEM and TEM suggest that the particles are spherical and the unified fit modelling on the data from SAXS gave an average bulk size of 51 nm for the Si made without additional buffer added to the reactants and 13 nm for the Si made with a 10:1 LiCl:Si buffer ratio.

Chapter 4: Studying Desorption Kinetics of MgH_2 with Si

"Science makes people reach selflessly for truth and objectivity; it teaches people to accept reality, with wonder and admiration, not to mention the deep awe and joy that the natural order of things brings to the true scientist."

Lise Meitner (1878 – 1968, Austria)

Chapter 4 expands on the ideas presented in previous chapters regarding reaction kinetics. One of the objectives of this thesis is to improve reaction kinetic rates of MgH_2 desorption through the use of nanoparticles; so this work also includes the Si nanoparticles synthesised in Chapter 3. The aim of this chapter is to gain an understanding of the relationship between crystallite size or particle size with chemical kinetics of MgH_2 mixed with Si. Here mixtures of MgH_2 have been mixed with Si under different processing conditions to obtain varying crystallite/particle sizes. Reaction kinetic information is then obtained and these results correlated with varying crystallite/particle sizes. Similar to all the experimental chapters (Chapters 3 – 6) the methodology can be found in Chapter 2.

4.1 Introduction

Metal hydride reaction kinetics gives an indication on how fast hydrogen moves into and out of the solid metal matrix (Eqn. 4.1). Many publications have focused on reducing kinetic barriers of hydrogen absorption into magnesium metal (Mg)[49, 134, 135, 136]. Absorption, or hydrogenation, of Mg is a three dimensional diffusion reaction following a nucleation and growth mechanism[137]. The nucleation step has been determined to be pressure dependent and is the rate limiting step for initial hydrogenation[49]. Growth of MgH_2 occurs at the interface between hydrogen and magnesium from the particle surface[49] and proceeds faster along lattice defects such as dislocation and vacancies[138].

Eqn. 4.1 $$\boldsymbol{Mg(s) + H_2(g) \leftrightarrow MgH_2(s)}$$

The literature identifies three main barriers to fast absorption kinetics for the Mg-H system. The first point to consider is the strong affinity of Mg to O_2 and the resulting surface oxide layer[139, 140] that acts as a physical barrier for chemisorption of H. Secondly, hydrogen disassociation on a clean Mg surface has a high activation

energy[141]. Thirdly, for particle sizes beyond 30 – 50 μm, the hydride layer impedes hydrogen diffusion and further hydrogenation does not proceed beyond this point[134]. There are reports in the literature regarding the rate limiting step of the bulk absorption reaction of Mg + H_2. It has been widely accepted that chemisorption is the initial limiting step followed by nucleation and growth. However, difficulties in fitting kinetic models to experimental data have become apparent due to the contradictions between studies that have analysed the rate limiting step. For example, an absorption study on bulk, unmilled Mg + H_2[134] showed that nucleation is pressure dependent and that interface growth of MgH_2 was found to be rate determining (using Sieverts apparatus). On the other hand, Fernandez *et. al.*[142] found that kinetic behaviour consisted of fast nucleation followed by two dimensional (2D) diffusion controlled growth (using Sieverts apparatus) or possibly a constant nucleation rate followed by 2-D diffusion controlled growth. In support of the diffusion controlled mechanism is another study by Huot *et. al.*[57], since their model shows that growth through the MgH_2 phase was slower than nucleation (using Sieverts apparatus). Contradictory to all of these studies, Bohmhammel *et. al.*[143], found that dissociative chemisorption of hydrogen is the rate limiting step by using a different technique, isothermal Differential Scanning Calorimetric (DSC) measurements. Some of these discrepancies have been attributed to non-isothermal conditions from heat transfer effects however controlled heat transfer conditions also showed that these discrepancies were still present[144].

Despite non-conformity of the mechanism of hydrogen absorption behaviour in Mg, improvements have been developed to increase the kinetic rate. These improvements include crystallite/particle size reduction[57, 75, 77, 145, 146] and catalysts addition[63, 78, 147]. The rate mechanisms of hydrogen diffusing through the Mg metallic matrix show that nanocrystalline materials exhibited nucleation and growth similar to bulk materials. Most of the literature agrees that the rate determining step is diffusion controlled of hydrogen through the MgH_2 phase[57, 142]. This suggests that uniformity of particle or crystallite size reduction due to ball milling may have a significant influence on reaction kinetics.

With respect to hydrogen desorption, or dehydrogenation, a one-step direct dehydriding path has been determined, where two hydrogen atoms bound to different Mg atoms simultaneously desorb[148]. It has also been shown that desorption can undergo three distinct mechanisms according to one DSC study[143], however, the reason for these mechanisms was not explained. For the reaction to occur, magnesium has to be nucleated and will continue to grow whilst the hydrogen atoms diffuse to the surface and recombine to form H_2 molecules[63]. Each of these steps could be linked to the thermal transitions found in the DSC data but there has been little evidence in the literature to support this theory. Unlike absorption, desorption is not limited by hydrogen disassociation. Desorption reaction mechanisms have more consensus as studies have agreed that nucleation is followed by interface controlled growth[57, 134, 142, 146].

Previous chapters have highlighted the thermodynamic advantage of adding Si to MgH_2 to decrease the stability of dehydrogenation (Eqn. 4.2). When analysing the Mg-Si-H system, H binds with Mg not Si, because SiH_4 is endothermic[67] and is not thermodynamically favourable. Thermodynamic calculations have shown that the addition of silicon, into magnesium hydride significantly reduces thermodynamic stability of the system[64, 67] and that MgH_2 should begin to dehydrogenate at room temperature at 1 bar of pressure. Experimentally, these conditions have never been met, hence the conclusion that reaction kinetics play a more significant role in the desorption reaction. Nano-scale particle sizes and crystallite sizes can overcome slow diffusion rates by reducing overall diffusion distances. A reduction in particle size also enhances net reaction rate by increasing surface area and interfacial contact between different phases[80]. Thus, the crystallite or particle size may determine the rate of diffusion of Mg through the Si atoms obtain Mg_2Si[149]. Our hypothesis is that if the particle sizes of the reactants are small, the kinetic enhancement would allow for hydrogen evolution to proceed at much lower temperatures and may also allow for hydrogen absorption to occur under reasonable pressures and temperatures[7]. The introductory section in Chapter 3 has already highlighted the importance of reaction rates of the Mg-Si-H system giving examples of Bystrzycki *et. al.*[64] and Paskevicius *et. al.*[72]. This was the motivation to synthesise Si nanoparticles.

Eqn. 4.2 $$2MgH_2(s) + Si(s) \rightarrow Mg_2Si(s) + H_2(g)$$

This chapter uses the Si nanoparticles produced *via* mechanochemical ball milling to observe the reaction kinetic behaviour of the system. Presented here is a study involving MgH_2 with Si prepared using different methods to obtain different crystallite sizes (or particle size in the case of amorphous Si nanoparticles). DSC, Sieverts apparatus desorption and temperature programmed desorption were undertaken to obtain reaction kinetic information. A reaction mechanism is proposed to further understand the kinetic behaviour of MgH_2 and Si desorption.

4.2 MgH_2 and Si sample preparation

Six stoichiometric ratios of $2MgH_2$ and Si were mixed together using various preparation methods and are given on the left hand side of Table 4.1. All Si samples were mixed with MgH_2 (Sigma Aldrich, H_2 storage grade, 95%). Samples (A) – (E) were prepared using and Si powder (Sigma Aldrich, − 325 mesh, 99%) and the final sample, (F), using the Si nanoparticles (NP) synthesised in Chapter 3. Sample (A) was the as supplied sample, representing bulk unmilled materials. Sample (A) was prepared by hand mixing $2MgH_2$ + Si in a vial for 5 min. Sample (B) was also placed in a vial with tetrahydrofuran (THF) to undergo mixing *via* ultrasonication. The THF was then evaporated under vacuum. Sample (C) was ball milled for 2 h at a ball to powder ratio (BTP) of 10:1 whilst sample (E) was also ball milled for a longer time of 24 h and a BTP ratio of 24 h. Sample (D) was cryomilled for 2 h at liquid nitrogen temperatures. The NP Si containing sample was mixed for 30 min in the cryomill with MgH2. This MgH_2 was ball milled prior to cryomilling with a BTP ratio of 90:1 for 18 h to obtain the smallest particles possible with limited contamination from the stainless steel milling media.

Table 4.1: Rietveld analysis before dehydrogenation. No primary soller.

$2MgH_2 + Si$	Phase	wt.%	Crystallite Size (nm)
(A) Hand Mixed 5 min	**MgH_2**	**63**	**207 ± 3**
	Mg	**2.1**	**174 ± 33**
R_{wp} = 5%	**Si**	**35**	**173 ± 3**
(B) Ultrasonicated	**MgH_2**	**66**	**201 ± 3**
	Mg	**2.4**	**194 ± 36**
R_{wp} = 5.5%	**Si**	**32**	**169 ± 3**
(C) Ball-milled 2 h	**β-MgH_2**	**61**	**40 ± 0.4**
	γ-MgH_2	**1.0**	**14 ± 7**
R_{wp} = 6.2%	**Mg**	**2.1**	**70 ± 11**
	Si	**36**	**134 ± 2**
(D) Cryomilled 2 h	**β-MgH_2**	**45**	**10 ± 0.1**
	γ-MgH_2	**14**	**5 ± 0.2**
R_{wp} = 4.1%	**Mg**	**2.2**	**72 ± 9.5**
	Si	**35**	**63 ± 0.6**
	Stainless steel 316	**3.5**	**1 ± 0.2**
(E) Ball-milled 30:1 24 h	**β-MgH_2**	**53**	**6 ± 0.1**
	γ-MgH_2	**10**	**3 ± 0.3**
R_{wp} = 3.8%	**Mg**	**0.0**	**0**
	Si	**36**	**46 ± 0.3**
	Stainless steel 316	**1.4**	**3 ± 0.4**
(F) Ball-milled MgH_2 18 h + NP Si	**β-MgH_2**	**67**	**6 ± 0.1**
	γ-MgH_2	**30**	**2 ± 0.2**
	Si	**13 nm amorphous Si**	
R_{wp} = 4.5%	**Stainless steel 316**	**3.0**	**4 ± 0.6**

All of the samples were analysed using X-Ray Diffraction (XRD) to identify the phases present (Figure 4.1) and obtain crystallite size (Table 4.1). In Figure 4.1 the Rietveld refinements for each of the mixtures are shown in colour and the difference between the calculated Rietveld modelling and the raw XRD data are represented by the grey plots beneath. Since there is little variation in the difference plots from a straight line, the accuracy of the Rietveld analysis was high. The R_{wp} value (Table 4.1), or weighted profile *R*-factor value, also gives an indication of the accuracy of the simulated model. This discrepancy index uses an algorithm to optimise the model function that will lead to a minimum of the weighted sum of squares differences

between the experimental and computed intensities[150]. As a general rule, R_{wp} values 5% or less indicates an acceptable goodness of fit[150]. Crystallite size values were taken from the LVol-IB (volume weighted mean column height) that incorporates Lorentzian and Gaussian convolutions varying in 2θ as a function of $\cos(\theta)^{-1}$ and $\tan(\theta)$ respectively. This method provides a volume weighted average crystallite size. Uncertainties were reported from *TOPAS* generated uncertainties using the bootstrap method of error determination.

The samples have been arranged in descending order of crystallite size for MgH_2 and Si from (A) to (F). Since the Si NPs were not crystalline (Chapter 3), the diameter measured from SAXS, 13 nm, is used. The XRD patterns show that as the crystallite size decreased, peak broadening for both MgH_2 and Si peaks became apparent, as expected. Also, the final plot, (F) shows no crystalline Si therefore the wt.% values refer only to the crystalline phases in the sample. This measurement was taken with Al foil rather than the PMMA in an attempt to detect the amorphous Si humps found in Chapter 3. However, the non-crystalline Si structure was masked by the other phases present in the material and was not observed in the diffractogram. Also, this sample is no longer 100% Si which would reduce the intensity of the already weak broad humps for amorphous Si.

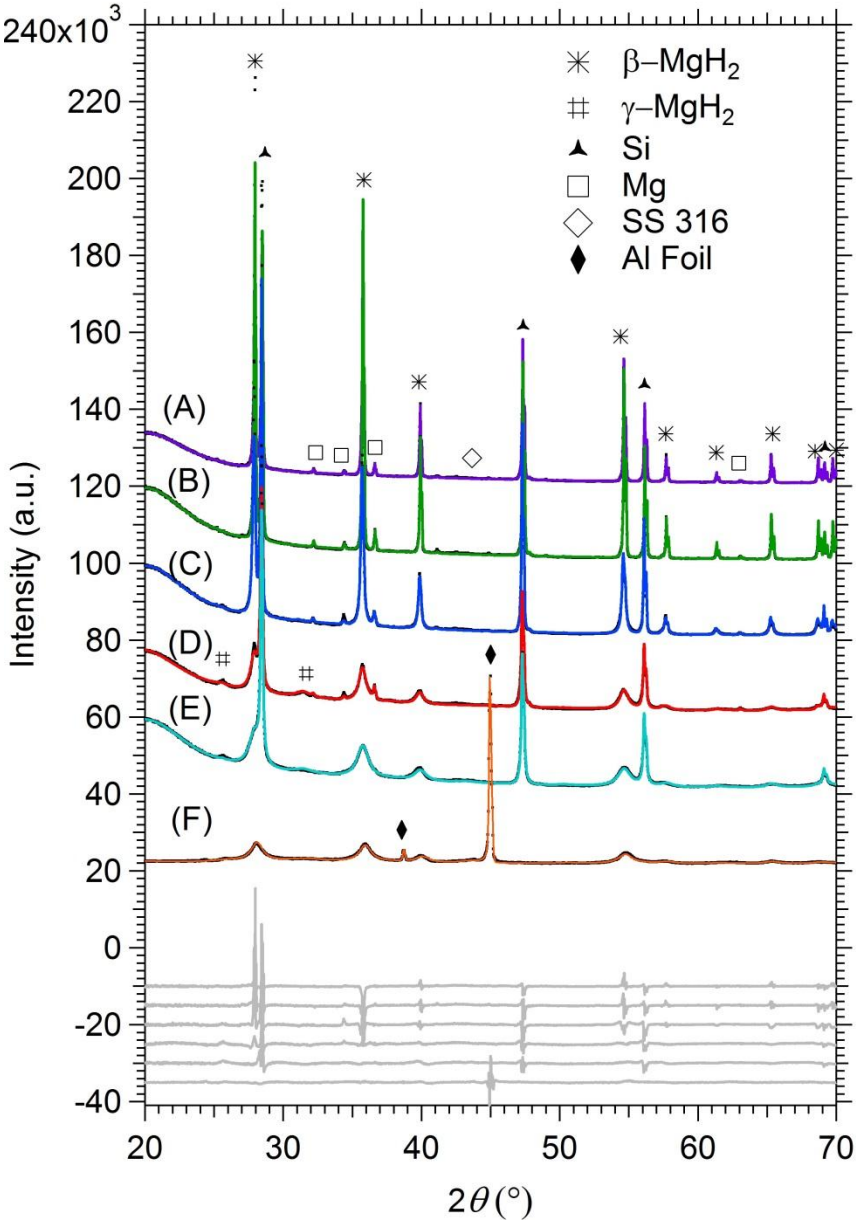

Figure 4.1: XRD patterns of $2MgH_2$ + Si (as supplied from Sigma Aldrich) (A) mixed in a vial by hand for 5 min (B) ultrasonicated in THF (C) ball-milled BTP 10:1 2 h (D) cryomilled for 2 h (E) ball-milled BTP 30:1 24 h (F) ball-milled MgH_2 for 18 h with synthesised Si nanoparticles, 13 nm.

One point to note is the presence of the γ-phase of MgH_2 in the samples that have undergone a milling process. This phase is typically seen in samples that have been subjected to the GPa range of pressures and temperatures up to 900°C although evidence suggests that room temperatures experiments can also result in the formation of this phase[8]. Other phases present in the sample showed minor levels of

contamination. There are two sources of obvious contamination. Firstly, the MgH_2 from Sigma Aldrich is only 95% pure, the remainder being Mg. Secondly, the materials that underwent either ball miling or cryomilling had trace amount of stainless steel 316 (SS 316) present due to their interaction with the milling media; both the canister and balls were made from SS 316. The trace amounts of contamination were taken into account when desorption calculations were done.

Scanning Electron Microscopy (SEM) was done to show the morphology of the ultrasonicated, cryomilled and ball milled for 2 h samples (Figure 4.2). Figure 4.2 (A), (C) and (E) used secondary electrons to give a clear images of the surface morphology particularly particle size and shape. Figure 4.2 (B), (D) and (F) are images using backscattered electrons where darker shades indicate lighter elements. In this case, MgH_2 has a lower molecular weight compared to Si, therefore, MgH_2 is slightly darker in colour than the Si particles[64]. Ultrasonicated particles are the largest with the majority being ≥ 10 μm with a small volume of finer particles. Ball milling at a BTP ratio of 10:1 for 2 h gave significantly smaller particles. Cryomilling for 2 h reduced particle size even further, ≤ 10 μm although some bigger particles are also present.

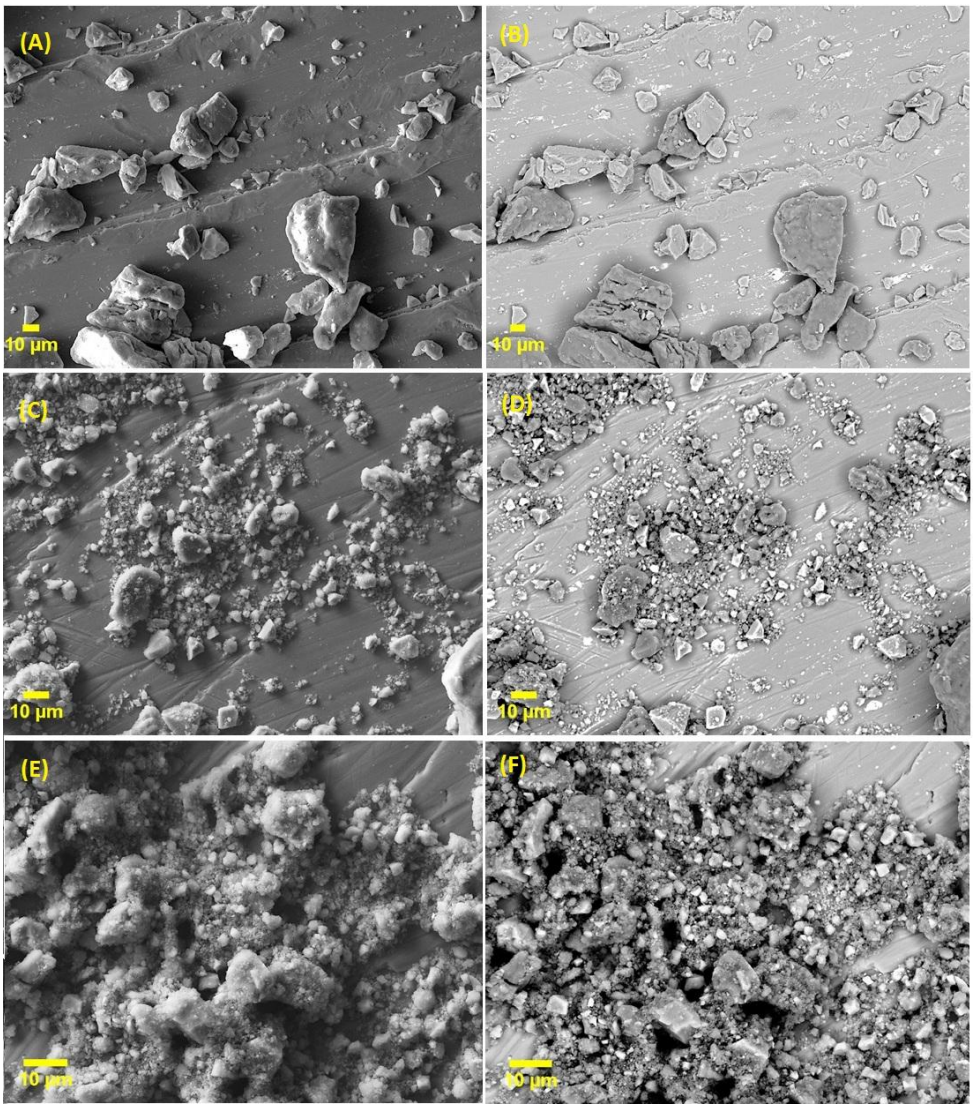

Figure 4.2: SEM micrographs of $2MgH_2$ + Si (A) ultrasonicated in THF, SE (B) ultrasonicated in THF, BSE (C) ball-milled BTP 10:1 2 h, SE (D) ball-milled BTP 10:1 2 h, BSE (E) cryomilled for 2 h, SE (F) cryomilled for 2 h, BSE.

There are several important observations that can be made when comparing the SEM BSE images shown in Figure 4.2 (B), (D) and (F). Ultrasonicated materials show two distinct phases of MgH_2 and Si present. As the particle size undergoes reduction *via* ball milling or cryomilling the distinction between the two phases is less pronounced. For all of the images in general, Si particles (brighter shades in BSE images) are smaller and are more evenly distributed amongst the MgH_2 particles in the ball milled and cryomilled samples. Despite these observations all of the mixing methods show that the two phases are heterogeneously mixed. This behaviour has also been

observed in MgH_2 and Si mixtures that have been ball milled for 20 h[64]. The degree of homogeneity of the reactants is a key feature of the sample as the reaction mechanism is highly dependent on how well the phases are mixed[151].

4.3 Desorption Reaction Kinetics

In order to determine the reaction kinetic parameters of the six MgH_2/Si mixtures, three types of thermal analysis were performed, DSC, Sieverts apparatus and TPD measurements.

DSC was performed at three heating rates, 2°C min^{-1}, 5°C min^{-1} and 10°C min^{-1}, except for the ultrasonicated sample which used 2°C min^{-1}, 5°C min^{-1} and 7°C min^{-1}. The DSC instrument had a maximum operating temperature of 450°C and the thermal peak for the ultrasonicated mixture at 10°C min^{-1} was not resolved. Therefore a lower heating rate had to be used. Thermal transition data for the hand mixed sample was not obtained.

The three different heating rates were used to calculate the activation energies of each of the reactions using the Kissinger method[152, 153]. This method can calculate the activation energy of the rate controlling process based on the thermal transition data obtained from the DSC. The Kissinger method takes the heating rate, β, and the maximum reaction rate peak temperature, T_{max}, to determine reaction rate barrier, otherwise known as the activation energy, E_a (Eqn. 4.3). R is the universal gas constant. A plot of the left hand side of the equation will result in a straight line so that a value for E_a can be obtained.

Eqn. 4.3:
$$\frac{d\ln\left(\frac{\beta}{T_{max}^2}\right)}{d\left(\frac{1}{T_{max}}\right)} = -\frac{E_A}{R}$$

The heating curves for the DSC data are given in Figure 4.3. Different thermal transitions occur for each of the mixtures however several trends are apparent from the data. The DSC data show that each material underwent one or more thermal transitions during the course of constant heating dominated by one thermal event. All the thermal transitions are endothermic and can be related to desorption of MgH_2 in the presence of Si. Below 100°C there are no significant events indicated by the flat baseline. There is also an uncharacteristic line in the data for the 24 h milled sample at 100°C and is a possible software error. Above 100°C the thermal behaviour of all sample display an onset temperature increasing in energy to a peak, resulting in asymmetric peak formation. The onset temperature T_o is strongly related to the nucleation mechanism of the reaction and can also be calculated from the Kissinger method replacing T_{max} with the T_o in Eqn. 4.3[154]. Therefore, the activation energy of nucleation E_n can be obtained[154]. Another observation from the DSC data is that both T_o and T_{max} increase with an increase in heating rate as expected.

The ultrasonicated sample, Figure 4.3 (A) gives a single transition at temperatures > 400°C, the highest of all the samples. The large particle and crystallite sizes can account for this transition occurring at these higher temperatures. Due to the limitations of the DSC (a maximum operating temperature of 450°C), it is possible that larger particles within this sample could desorb at higher temperatures and has not been detected here.

Figure 4.3 (B) displays more than one thermal transition for the 2 h ball milled sample with a BTP ratio of 10:1. The various heating rate curves for this material appear to undergo an initial three phase mechanism similar to that of MgH_2[143] leading up to a double peak between 350°C and 450°C depending on the heating rate. These peaks, in part, are due to the broad range of particle size for MgH_2 within the sample (Figure 4.2 (C)) where the smaller particles desorb at a lower temperature and the larger particles desorb at the higher temperature.

The remaining DSC curves, cryomilled (Figure 4.3 (C)), 24 h ball milled (Figure 4.3 (D)) and NP Si with 18 h ball milled MgH_2 (Figure 4.3 (E)) samples, show a number of overlapping thermal events. Some of this behaviour can be related to the heterogeneous particles sizes of MgH_2 in the samples, however, it is more likely due

to the different crystalline phases present, as detected by the XRD, γ-MgH_2 and β-MgH_2. The cryomilled sample (Figure 4.3 (C)) as well as the sample containing Si NPs (Figure 4.3 (E)) show a small thermal event at 270°C and 210°C respectively, almost masked by the onset rise in temperature of the desorption reaction. A previous study showed that γ-MgH_2 completely desorbs at lower temperatures than β-MgH_2[155]. Partial decomposition of β-MgH_2 does occur at this lower temperature, however, this structure is not completely desorbed until higher temperatures are reached[155]. The 24 h ball milled sample (Figure 4.3 (D)) has a less obvious transition occurring at 200°C and 250°C for the 5°C min^{-1} and 10°C min^{-1} heating rates respectively. This is due to the lower concentration of γ-MgH_2 present in these samples (Table 4.1).

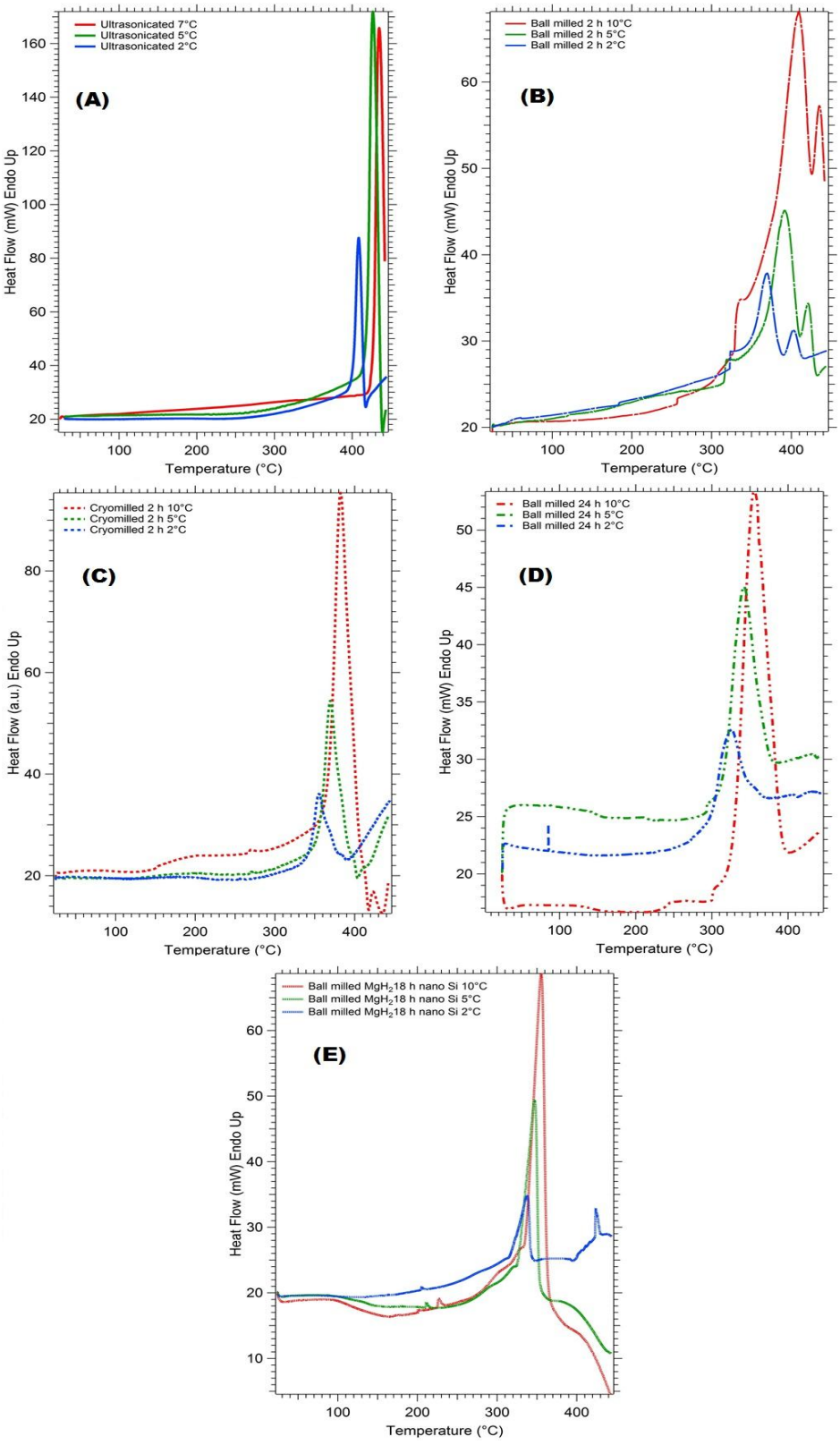

Figure 4.3: DSC curves indicating different heating rates for MgH_2 + Si. (A) Ultrasonicated (B) Ball milled 2h (C) Cryomilled 2 h (D) Ball milled 24 h (E) Ball milled 18 h MgH_2 + NP Si.

The graphs with the slopes used to obtain E_n and E_a are shown in Figure 4.4 and Figure 4.5. The regression value, R^2, was > 0.95 for all samples indicating a reasonable goodness of fit to the data. The calculated activation energy values are given in the summary table (Table 4.5). There is no apparent trend that correlates the nucleation activation energy values to crystallite/particle size. The highest E_n value was not the bulk sized ultrasonicated particles; rather the 2 h ball milled sample gave a value of 355.6 kJ mol^{-1}. However, the lowest value for E_n was 133.5 kJ mol^{-1} for the 24 h ball milled sample. This suggests that nucleation of Mg_2Si formation is not correlated to crystallite/particle size.

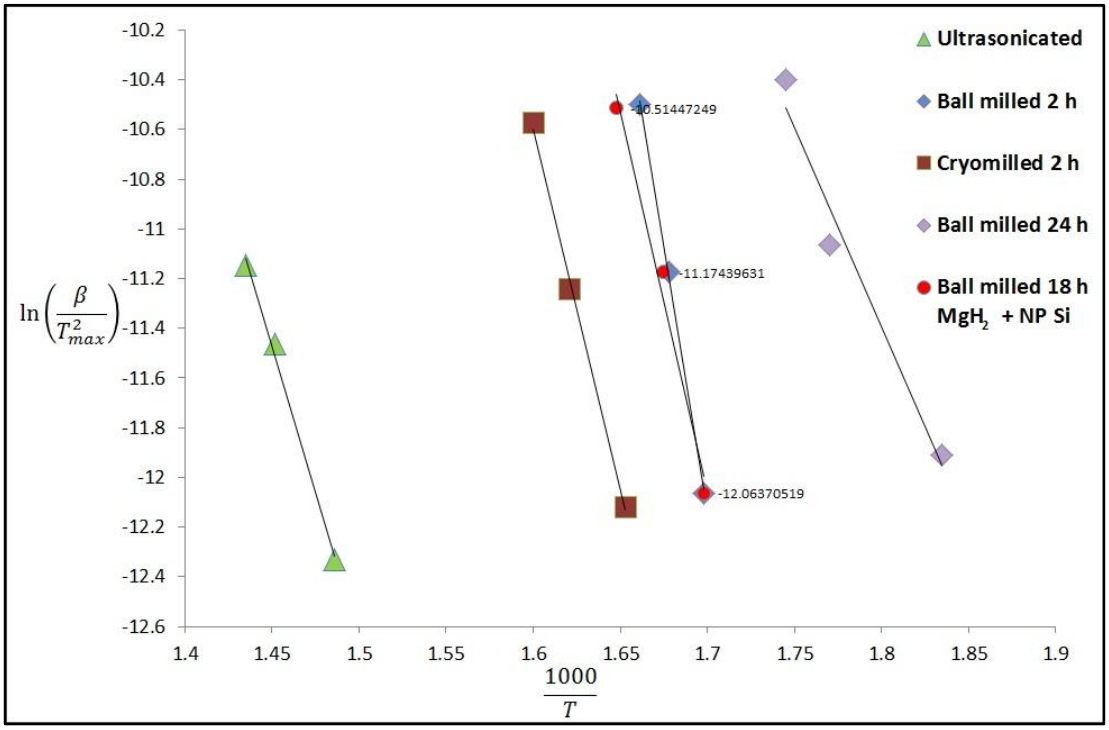

Figure 4.4: DSC data plotted to obtain Mg_2Si nucleation activation energy, E_n.

Growth activation energy values, on the other hand, give an overwhelming correlation between crystallite sizes determined from XRD (Figure 4.6) with the exception of the Si NP sample. Figure 4.6 shows a linear relationship between E_a and crystallite size with an R^2 value of 0.96. Although the relationship can be fit to a

straight line, more data is required for a larger range of crystallite sizes to confirm this relationship.

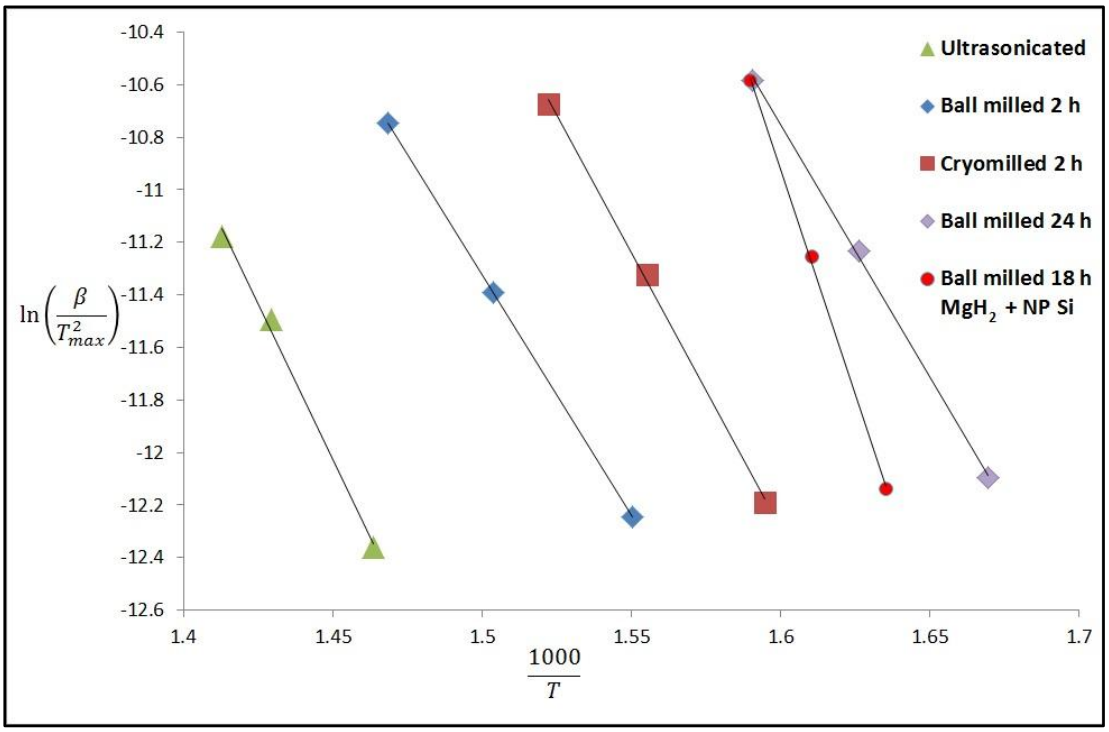

Figure 4.5: DSC data plotted to obtain Mg_2Si growth activation energy, E_a.

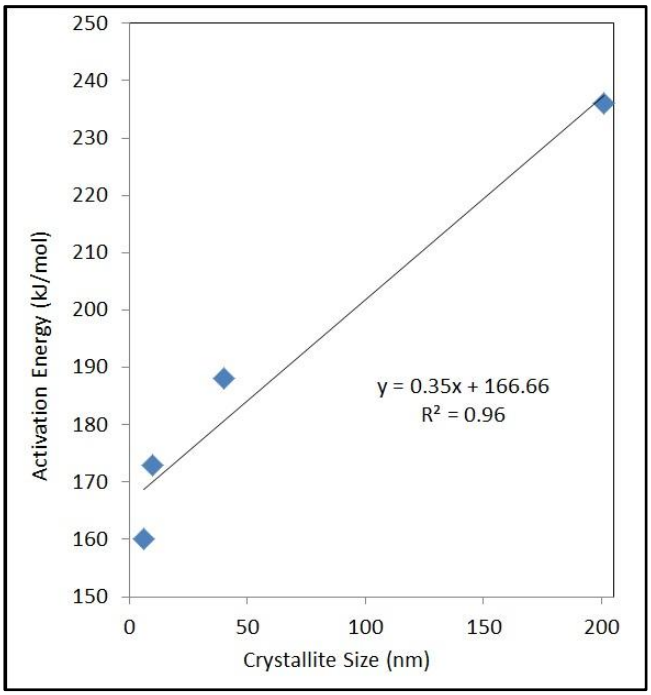

Figure 4.6: Relationship between crystallite size and activation energy, E_a.

In order to obtain the reaction rate constant, k, the experimental data can be expressed as a function of the transformed fraction, α, from established reaction kinetic models. The models described in this chapter relate to solid state reactions. Solid state kinetic models are a mathematical description of what occurs experimentally and can describe a particular reaction type[156]; in this case, the rate limiting step.

The rate limiting step can be determined from the best fit between the experimental data and the proposed models. This method of analysis is detailed in Barkhordarian *et. al.*[157] and will only be briefly explained here. There are three single particle models that can describe kinetic reaction behaviour, surface reaction[158], Johnson-Mehl-Avrami (JMA)[49, 134, 135] and Carter-Valensi (CV)[142, 159] models. The surface controlled mechanism assumes that chemisorption is the slowest step of desorption with α linearly changing with time, t. The JMA model applies to nucleation and growth mechanisms occurring both at the surface as well as in the bulk phase. The assumption for the JMA model is that hydrogen diffusion is relatively fast. JMA modelling also accounts for the dimensionality of growth, either two dimensional (2D) or three dimensional (3D). The CV model is different in that it provides for a mechanism which begins with nucleation at the surface of the particle and growth continues from the surface into the bulk. The CV model assumes that nucleation on the surface is fast and the rate limiting step is either 2D or 3D interfacial growth. This model can also be expressed in terms of 3D diffusional growth. Table 4.2 gives the equations used for each of these models.

Table 4.2: Reaction kinetic model equations.

Model Equation	Description
$\alpha = kt$	Surface controlled mechanism [158] or chemisorption
$[-\ln(1-\alpha)]^{1/2} = kt$	JMA [160, 161, 162] 2D interfacial growth
$[-\ln(1-\alpha)]^{1/3} = kt$	JMA [160, 161, 162] 3D interfacial growth
$1-[1-\alpha]^{1/2} = kt$	CV [163, 164] 2D interfacial growth
$1-[1-\alpha]^{1/3} = kt$	CV [163, 164] 3D interfacial growth
$1-\left(\frac{2\alpha}{3}\right)-(1-\alpha)^{2/3} = kt$	CV [163, 164] 3D diffusional growth

Reaction rate experimental data was obtained using the manometric Sieverts apparatus described in Chapter 2. The sample was held isothermally in a furnace at 300°C and hydrogen release was measured over time (24 h). The resultant kinetic data is given in Figure 4.7 (A) for each of the six samples. An immediate observation is that the reaction proceeds at a faster rate as crystallite size decreases. Again, the only exception being the Si NP sample with ball milled MgH_2. Another interesting point to note is that the 24 h ball milled sample is the only sample that approaches complete desorption in the 24 h time period. The amount of H_2 desorbed from each sample is given in Table 4.5. As expected, the bulk samples (hand mixed and ultrasonicated) are the slowest due to their larger particle size and they release the least amount of hydrogen. Milled materials contain a lot of crystallite boundaries which can act as fast diffusion paths for hydrogen atoms[76] hence the faster reaction rates.

A zoom of the reaction data showing the first hour is given in Figure 4.7 (B). This plot shows that the 24 h ball milled sample starts at an extremely slow rate similar to that of the 2 h ball milled sample. There is a rapid change in the reaction rate 45 min after the reaction is initiated. This implies that there is a kinetic barrier present for this sample possibly due to the presence of an oxidation layer on the MgH_2. All other samples have a constant rate from the beginning. Si NP + ball milled MgH_2 has the

fastest rate followed by the 2 h cryomilled and 2 h ball milled samples. In order to compare each of the samples with the kinetic models given in the summary table, Table 4.5, the data was normalised to give the transformed fraction, α, Figure 4.7 (C). The hydrogen concentration (wt.%) from the desorption reaction was normalised by dividing by the maximum possible hydrogen release, that is, 5 wt.% to obtain value ranges for α over 24 h.

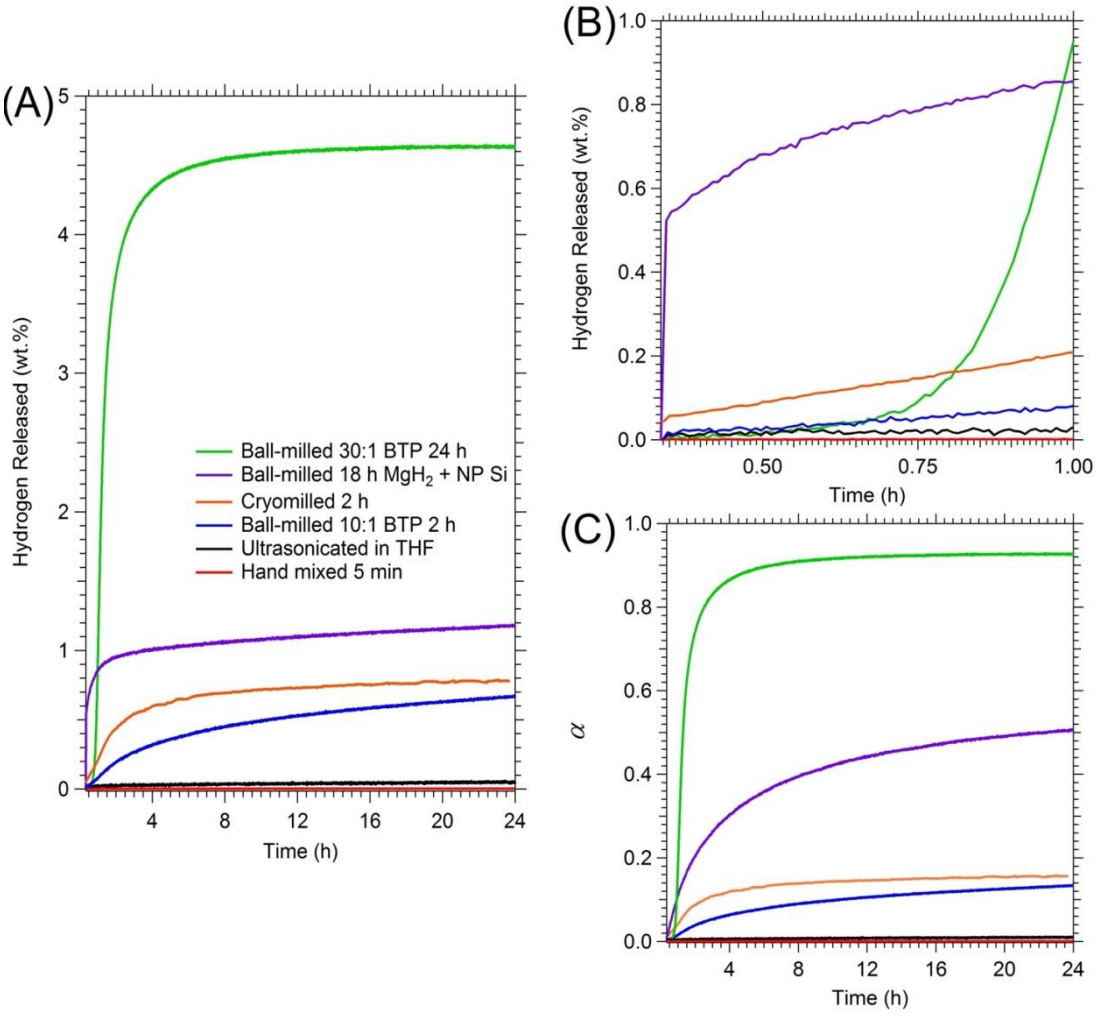

Figure 4.7: Rate of reaction curves for MgH_2 + Si of varying crystallite/particle sizes (A) Rate of desorption over 24 h (B) Rate of desorption over 1 h (zoom of (A)) (C) Rates of reaction normalised to α values.

The equations in Table 4.2 were applied to the normalised data for each of the mixtures and the results are given in the following figures, Figure 4.8 - Figure 4.13.

The model equation that gives the best linear fit with time is considered to be the rate limiting step of the overall desorption kinetic reaction. For the hand mixed, ultrasonicated, 2 h ball milled, cryomilled and NP Si containing samples a straight line fit to the CV 3D diffusion growth controlled model had the highest regression values of > 0.8. For ease of comparison between each of the samples, Figure 4.8 (A), Figure 4.9 (A), Figure 4.10 (A), Figure 4.11 (A), Figure 4.12 and Figure 4.13 (A) have been displayed on the same scale. As it was difficult to get a view of the straight line in these figures, Figure 4.8 (B), Figure 4.9 (B), Figure 4.10 (B) and Figure 4.11 (B) show the line of best fit on more clearly on a different scale. It can be seen from the line of best fit for each of the models, the best model to describe the rate limiting step for the hand mixed, ultrasonicated, 2 h ball milled, cryomilled and NP Si containing samples is the CV 3D diffusion growth model. This model assumes that nucleation is relatively fast and occurs at surface boundaries[157] between Mg and Si atoms. The diffusional growth then continues from these boundaries to form bulk Mg_2Si particles. This is in agreement with Kelly *et. al.*[71] where the kinetic barrier of absorption was found to be the mass transport of Mg and Si between the Mg_2Si phase and the individual elemental phases.

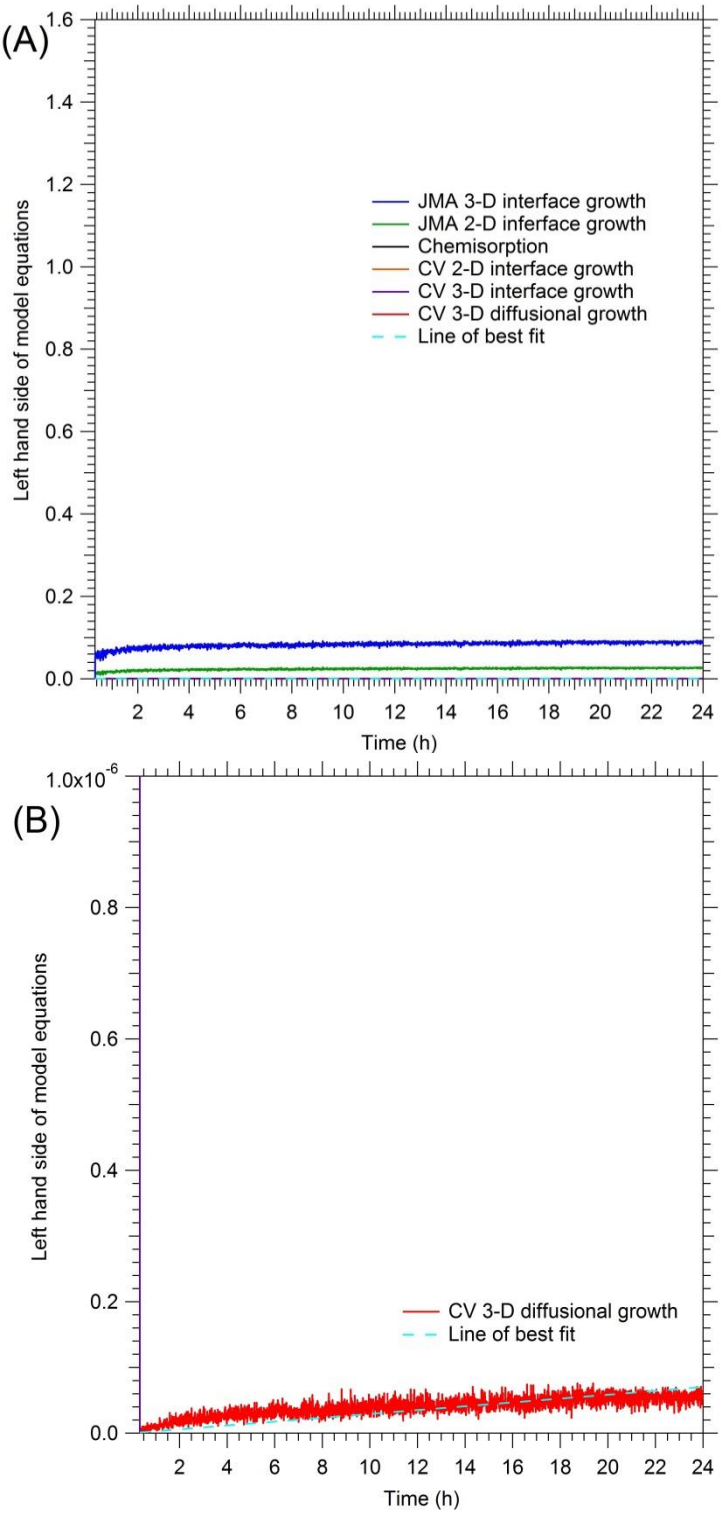

Figure 4.8: (A) Curves from different kinetic equations applied to the desorption data at 300°C of $2MgH_2$ + Si hand mixed for 5 min. (B) The slope of the line of best fit equates to the rate constant, *k*.

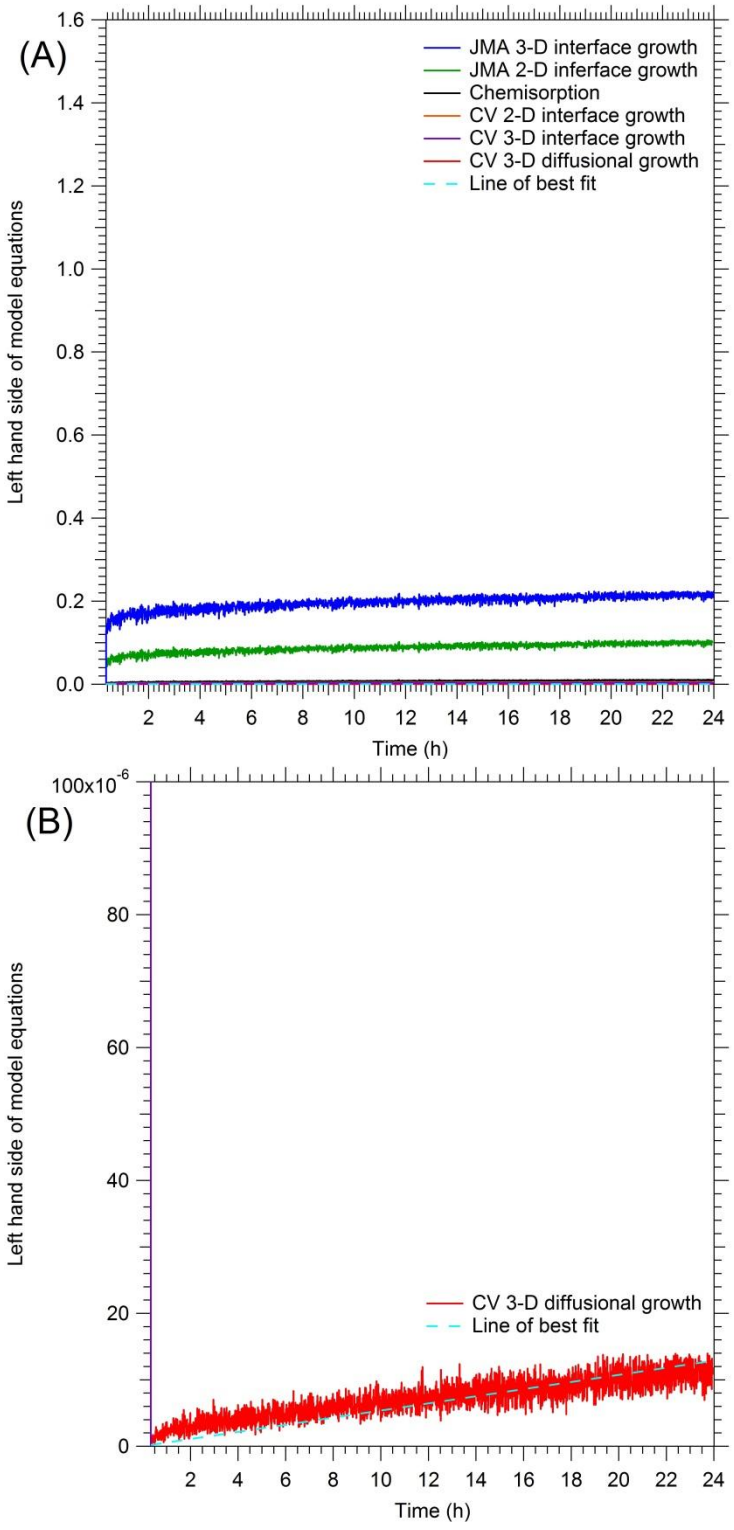

Figure 4.9: (A) Curves from different kinetic equations applied to the desorption data at 300°C of $2MgH_2$ + Si ultrasonicated in THF. (B) Lines represent a linear fit to the experimental data with the slope value equal to the rate constant, *k*.

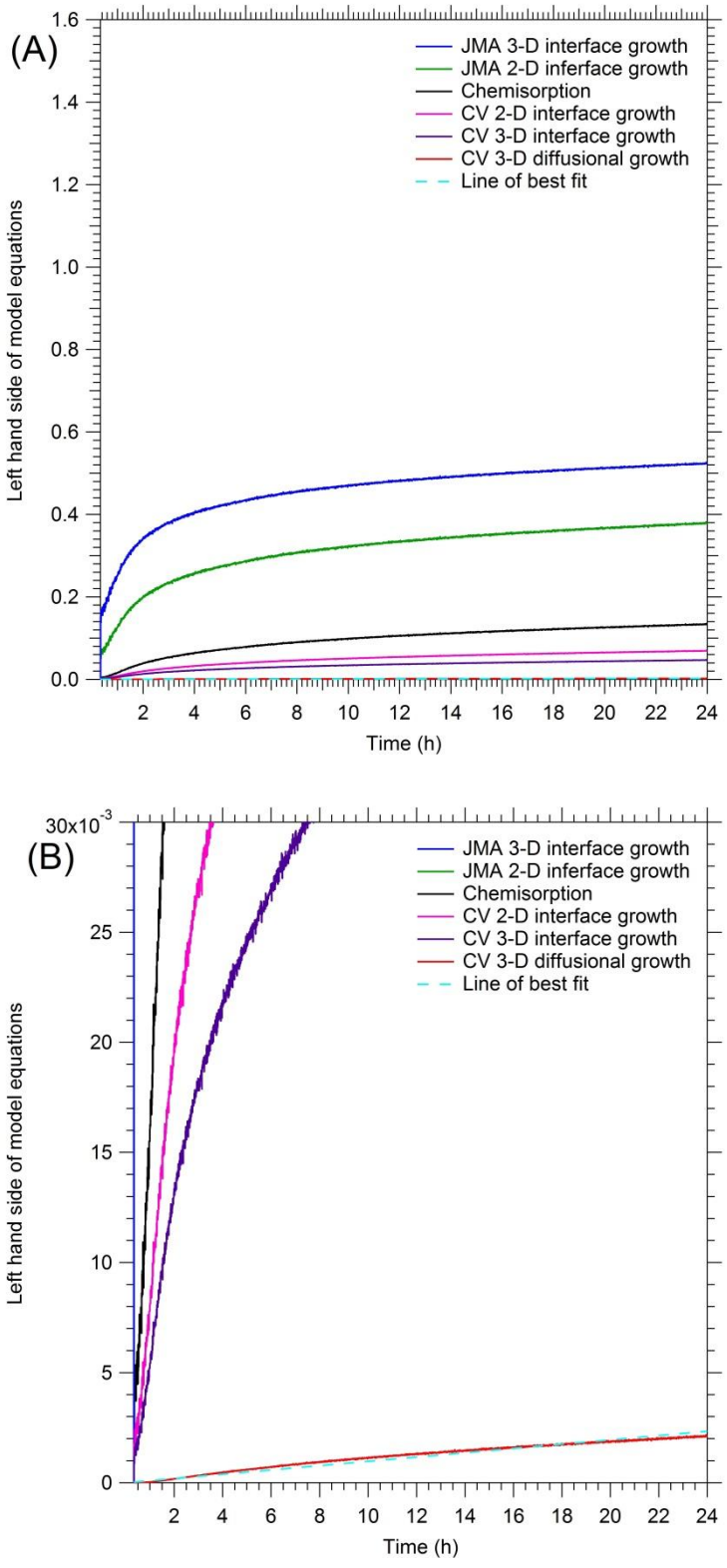

Figure 4.10: (A) Curves from different kinetic equations applied to the desorption data at 300°C of $2MgH_2$ + Si ball-milled for 2 h. (B) The slope of the line of best fit equates to the rate constant, *k*.

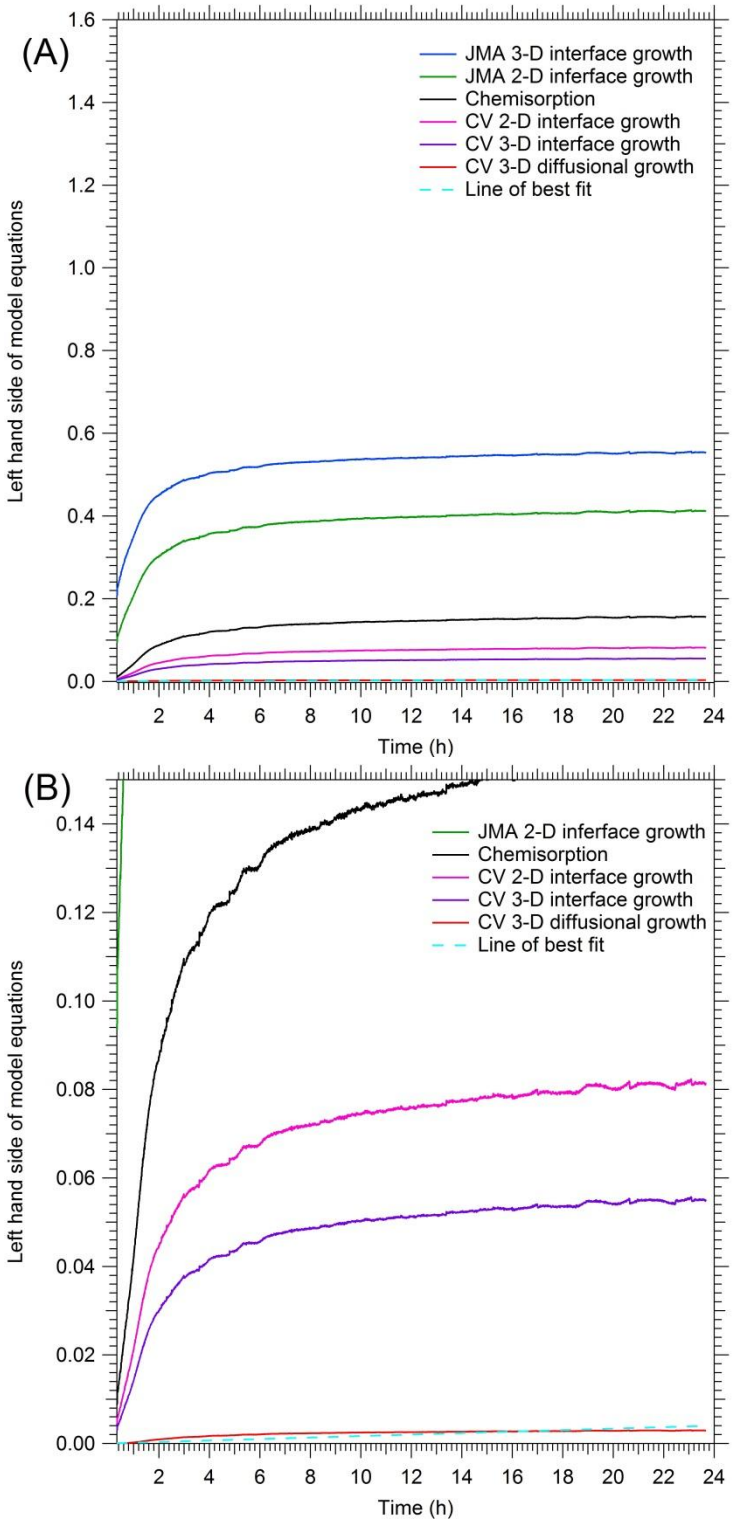

Figure 4.11: (A) Curves from different kinetic equations applied to the desorption data at 300°C of $2MgH_2$ + Si cryomilled for 2 h. (B) The slope of the line of best fit equates to the rate constant, *k*.

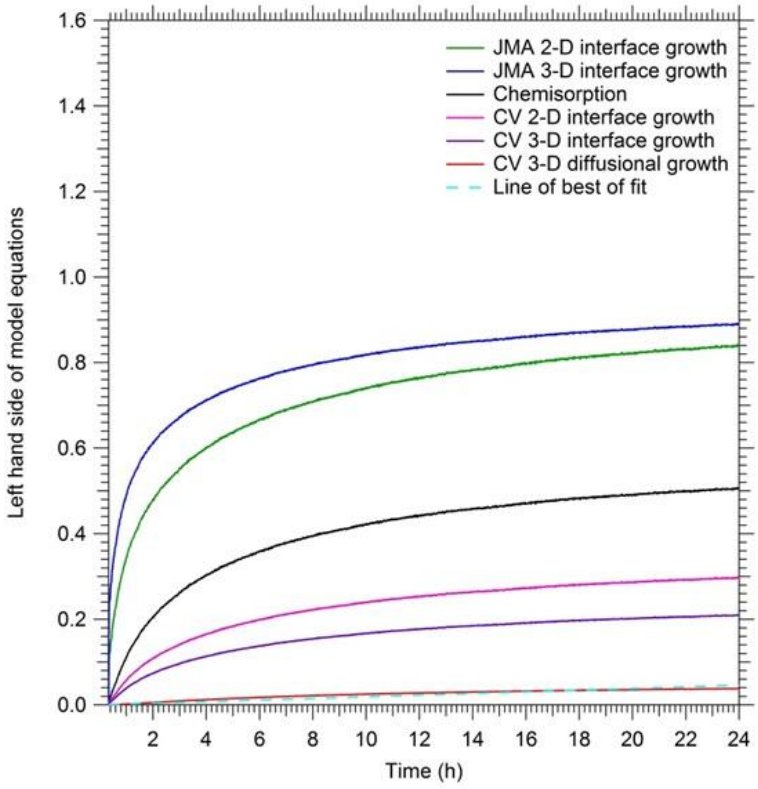

Figure 4.12: (A) Curves from different kinetic equations applied to the desorption data at 300°C of $2MgH_2$ ball-milled for 18 h + Si nanoparticles. The slope of the line of best fit equates to the rate constant, *k*.

The 24 h ball milled sample, however, does not fit any of the models from Table 4.1 with such accuracy (Figure 4.13 (A)). The discrepancy between the experimental data and mathematical models appear to be related by the aforementioned rapid change in reaction rate at 45 min (Figure 4.7 (B)) possibly due to a layer of oxidised Mg at the surface of the MgH_2 particles. If rate of reaction is not constant with time, other variables such as rate constant can be used as an indication of reaction behaviour[165]. However, in the case of this study, *k* is determined directly from the best fit model and cannot be used in this way. Instead, a wider range of mathematical models were employed to analyse the data and are given in Table 4.3. The results of applying these models to the experimental data are given in Figure 4.13 (B). Once again, none of the models gave a straight line fit to the data. Therefore, none of the models fit the data, indicating that the reaction model for this data is more complicated than simple homogenous kinetic behaviour. As a result the reaction constant, *k*, could not be calculated for the sample that had been ball milled for 24 h.

Table 4.3: Second set of reaction kinetic model equations[156].

Model Equation	Description
$\alpha^{1/2} = kt$	Power law (P2)
$\alpha^{1/3} = kt$	Power law (P3)
$\alpha^{1/4} = kt$	Power law (P4)
$[-\ln(1-\alpha)]^{1/4} = kt$	JMA interfacial growth (A4)
$\alpha^2 = kt$	1D diffusion (D1)
$[(1-\alpha)ln(1-\alpha)] + \alpha = kt$	2D diffusion (D2)
$[1-(1-\alpha)^{1/3}]^2 = kt$	Jander 3D diffusion (D3)
$1 - (2/3)\alpha - (1-\alpha)^{2/3}$	Ginstling-Brounshtein (D4)
$\alpha = kt$	Zero order or surface controlled [158] (F0)
-ln$(1-\alpha) = kt$	First order (F1)
$\frac{1}{(1-\alpha)} - 1 = kt$	Second order (F2)
$\frac{1}{2}[(1-\alpha)^{-2} - 1] = kt$	Third order (F3)

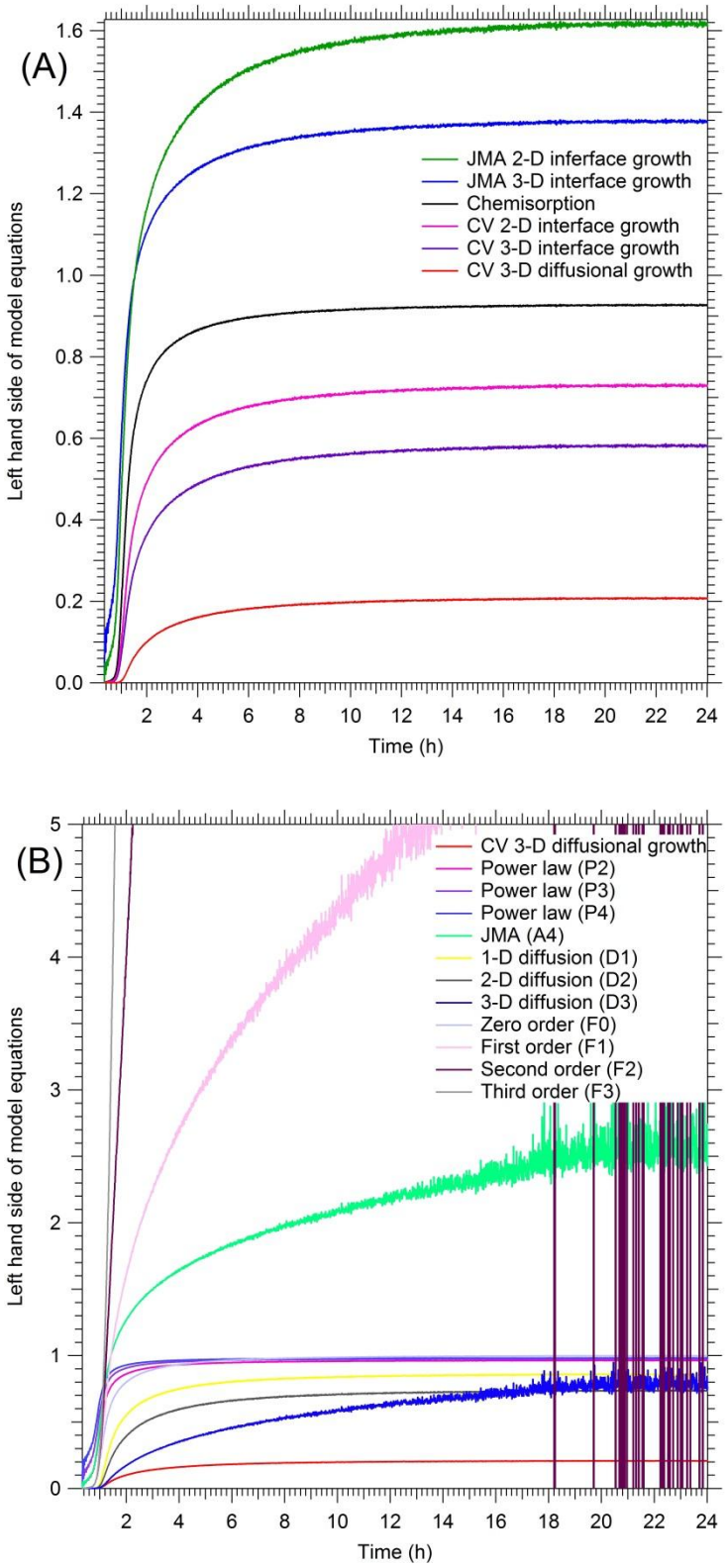

Figure 4.13: (A) Curves from Table 4.2 kinetic equations applied to the desorption data at 300°C of $2MgH_2$ + Si ball-milled for 24 h. (B) Curves from Table 4.3 kinetic equations applied to the desorption data at 300°C of $2MgH_2$ + Si ball-milled for 24 h.

The reaction rate constant values that were calculated for the other samples are given in the summary Table 4.5. These were calculated using the Igor Pro (Version 6.02A, Wavemetrics, Oregon, 2007) linear fit function. The error is automatically reported at a 95% confidence interval from this function. The hand mixed sample and ultrasonicated sample have similar *k* values within error and the reaction rate increases with a decrease in crystallite size. This type of reaction kinetic improvement has been highlighted in the introduction of this chapter as it has been widely studied[58, 159, 166, 167].

The relationship between the activation energy, E_a and the rate constant *k* is given by the Arrhenius equation (Eqn. 4.4). Since E_a was determined using the Kissinger method and *k* from fitting model equations to isothermal kinetic data, the final kinetic parameter in the Arrhenius equation, the pre-exponential factor, *A*, can be calculated. The pre-exponential factor, *A*, is a value that relates to the frequency of collisions and is closely linked with collision theory[168]. *A* is determined at the same temperature at which kinetic data were obtained, 300°C and the resulting values are also in Table 4.5 and as expected show the same relationship to crystallite/particle size as the other parameters, E_a and *k*.

Eqn. 4.4 $$k = Ae^{-\frac{E_a}{RT}}$$

Each of the reactions shown in Figure 4.7 (A) were continued beyond 24 h for a total of 72 h at 300°C to allow the desorption reaction to go as close to completion as possible (Table 4.5). Again, XRD was performed to identify the phases present and to calculate crystallite size for the crystalline materials. The diffractograms for the desorbed samples are given in Figure 4.14 and the results from Rietveld analysis for crystallite size are in Table 4.4. The results show that the hand mixed sample suffered kinetically due to the larger particle and crystallite size of the reactants and with only 10% Mg_2Si conversion. Surprisingly, no Mg_2Si was present for the ultrasonicated sample. This could be due to the presence of a THF coating over the

particles during mixing limiting the reaction. Desorption kinetic data showed a release of 0.06 wt.% H_2 and this was more likely to be the influence of THF vaporisation since no Mg_2Si was formed. The sample that was ball milled for 2 h contained approximately 38% Mg_2Si which correlates well with the desorption data.

Table 4.4: Rietveld analysis after dehydrogenation. No primary soller.

$2MgH_2 + Si$	Phase	wt.%	Crystallite Size (nm)
(A) Hand Mixed 5 min	**Mg_2Si**	**10.3**	**58 ± 2**
	β-MgH_2	**53.6**	**212 ± 4**
R_{wp} = 6.1%	**Mg**	**4.9**	**126 ± 11**
	Si	**31.2**	**180 ± 4**
(B) Ultrasonicated 2 h	**Mg_2Si**	**0**	
	β-MgH_2	**67**	**178 ± 3**
	Mg	**3.3**	**125 ± 17**
R_{wp} = 6.1%	**Si**	**28.7**	**150 ± 3**
(C) Ball-milled 2 h	**Mg_2Si**	**38**	**66 ± 0.7**
	β-MgH_2	**33.3**	**98 ± 1.5**
R_{wp} = 5%	**Mg**	**0**	
	Si	**17.7**	**133 ± 3**
	MgO	**10.9**	**1.8 ± 0.1**
(D) Cryomilled 2 h	**Mg_2Si**	**7.7**	**34 ± 0.8**
	β-MgH_2	**34.5**	**28 ± 0.2**
R_{wp} = 3%	**Mg**	**3.4**	**51 ± 3**
	Si	**26.4**	**58 ± 0.5**
	MgO	**24.5**	**2.4 ± 0.1**
	SS 316	**3.5**	**1 ± 0.2**
(E) Ball-milled 30:1 24 h	**Mg_2Si**	**80.2**	**57 ± 0.4**
	Mg	**3.4**	**1 ± 0.6**
R_{wp} = 4.5%	**Si**	**1.4**	**63 ± 9**
	MgO	**9.4**	**2.6 ± 0.2**
	SS 316	**5.6**	**1 ± 0.2**
(F) Ball-milled MgH_2 18 h	**β-MgH_2**	**15.1**	**12 ± 0.4**
+ NP Si	**Mg_2Si**	**24.3**	**6 ± 0.2**
	Si	**13 nm amorphous Si**	
R_{wp} = 4.7%	**MgO**	**60.6**	**3 ± 0.1**

Cryomilled samples, 2 h and NP Si mixture, shows a high wt.% of MgO present after dehydrogenated. This implies that this method of mixing exposes the sample to O_2 at some stage. The presence of MgO can also account for the initial fast reaction kinetics as MgO is formed during the early stages of the desorption reaction. Here Mg bonds with the O_2 as it releases the H_2. This reaction does not have high thermodynamic stability and therefore requires only a small amount of energy to occur. This is the reason this reaction does not show any significant thermal transitions in the DSC data. MgO in these samples also account for the samples not releasing 5 wt.% H_2 as predicted from thermodynamic calculations[67].

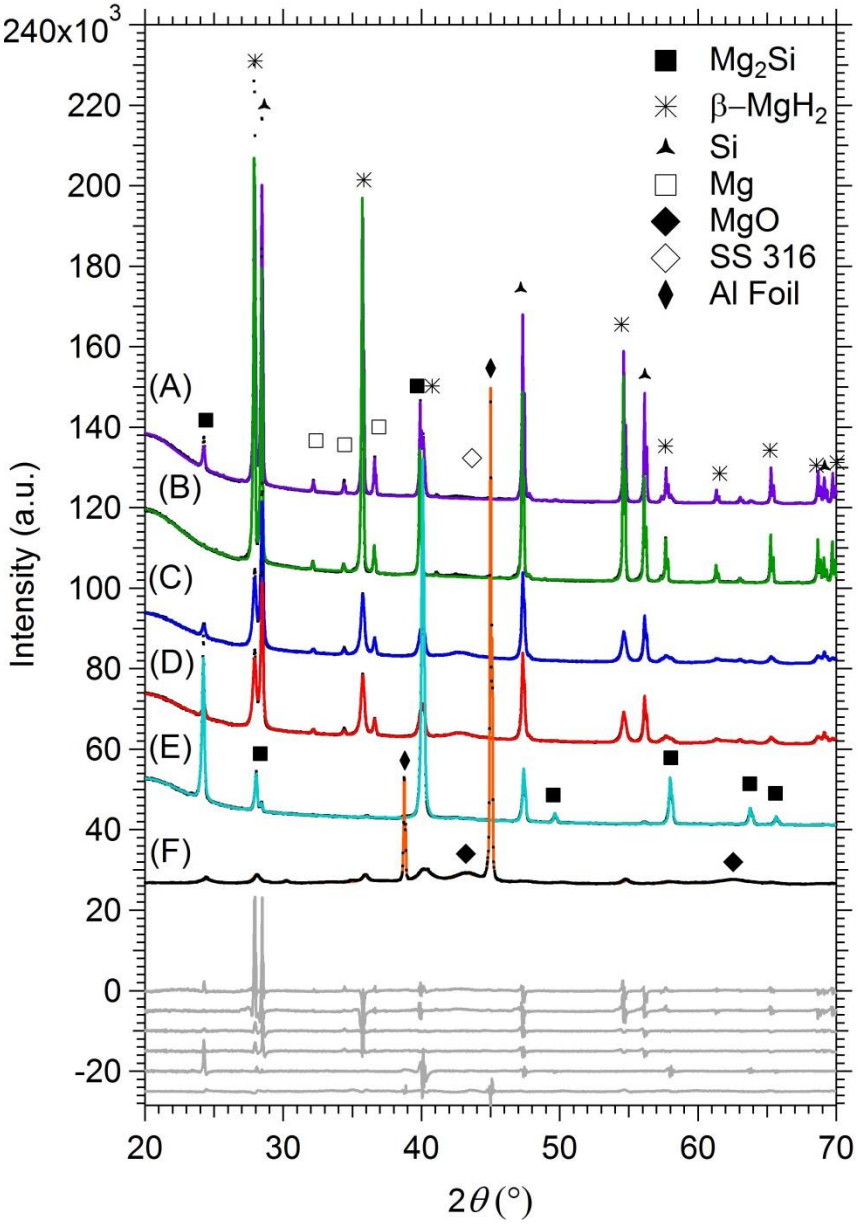

Figure 4.14: XRD patterns after desorption of $2MgH_2$ + Si (A) mixed in a vial by hand for 5 min (B) ultrasonicated in THF for 1 h (C) ball-milled BTP 10:1 2 h (D) cryomilled for 2 h (E) ball-milled BTP 30:1 24 h (F) ball-milled MgH_2 for 18 h with synthesised Si nanoparticles, 13 nm.

It can be seen from the XRD pattern for the 24 ball milled sample that no MgH_2 remains. There is a small amount of MgO in the sample after desorption together with trace amounts of Si, Mg and SS 316. This accounts for the sample releasing 4.63 wt.% instead of the theoretical value of 5 wt.% H_2. This sample also underwent complete desorption in the fastest time of under 16 h.

Table 4.5: Summary of desorption reaction parameters and total wt.% desorbed.

Process	Crystallite size (nm)	Nucleation Activation Energy E_n (kJ mol^{-1})	Growth Activation Energy E_a (kJ mol^{-1})	Rate limiting step	Rate constant, k (h^{-1})	Pre-exponential factor, A (h^{-1})	Total H_2 wt.% desorbed (72 h)
Pure MgH_2[159]	**Ball milled**			**JMA 3D growth**	18×10^{-5} $(\pm 2 \times 10^{-5})$		
Hand mixed 5 min	***β*-MgH_2 = 207 (± 3) Si = 173 (± 3)**	-	-	**CV 3D diffusion**	2.90×10^{-9} $(\pm 0.02 \times 10^{-9})$	-	0.070 (± 0.003)
Ultrasonicated 1 h	***β*-MgH_2 = 201 (± 3) Si = 169 (± 3)**	**194.8 (± 4.9)**	**235.9 (± 5.9)**	**CV 3D diffusion**	5.4×10^{-7} $(\pm 0.02 \times 10^{-7})$	5.7×10^{-7} $(\pm 0.02 \times 10^{-7})$	0.160 (± 0.008)
Ball-milled 2 h	***β*-MgH_2 = 40 (± 0.4) Si = 134 (± 2)**	**355.6 (± 8.9)**	**187.6 (± 4.7)**	**CV 3D diffusion**	9.7×10^{-5} $(\pm 0.02 \times 10^{-5})$	1.0×10^{-4} $(\pm 0.2 \times 10^{-4})$	0.670 (± 0.03)
Cryomilled 2 h	***β*-MgH_2 = 10 (± 0.1) Si = 63 (± 0.6)**	**241.4 (± 6.0)**	**173.3 (± 4.3)**	**CV 3D diffusion**	1.7×10^{-4} $(\pm 0.009 \times 10^{-4})$	1.8×10^{-4} $(\pm 0.009 \times 10^{-4})$	0.89 (± 0.04)
Ball-milled 24 h	***β*-MgH_2 = 6 (± 0.1) Si = 46 (± 0.3)**	**133.5 (± 3.3)**	**159.8 (± 4.0)**	-	-	-	4.63 (± 0.23)
Ball- milled 18 hr MgH_2 NP Si	***β*-MgH_2 = 6 (± 0.1) Si = 13 (diameter)**	**253.9 (± 6.3)**	**234.8 (± 5.9)**	**CV 3D diffusion**	1.9×10^{-3} $(\pm 0.006 \times 10^{-3})$	2.0×10^{-3} $(\pm 0.006 \times 10^{-3})$	2.94 (± 0.14)

4.4 Conclusion

The desorption kinetics of MgH_2 and Si have been studied for a range of crystallite/particle sizes. The kinetic parameters for this reaction have been determined and include nucleation activation energy, E_n, growth activation energy, E_a, the rate constant, k, and the pre-exponential factor, A. The Kissinger method was used to calculate the activation energies and it was found that E_a strongly correlates with crystallite size of the reactants. However, no such trend was evident for E_n. The rate limiting mechanism for the reaction was found to CV 3D diffusion. This indicates that nucleation occurs at the surface at fast rate followed by slow diffusion of H_2 out of the Mg matrix whilst Si bonds with the Mg simultaneously to form Mg_2Si. Oxygen contamination played a large role in the early stages of the reaction and can account for reaction behaviour as well as the low conversion rate, especially for the samples that had been cryomilled. It appears that the relationship between the reaction kinetic parameters and crystallite size could be directly proportional, that is, linear; however, more work is required to confirm these preliminary results.

Chapter 5: Synthesising Mg_2Si Nanoparticles for High Pressure Hydrogenation

"There is only one thing worse than coming home from the lab to a sink full of dirty dishes, and that is not going to the lab at all!"

Chien Shiung Wu (1912 – 1997)

This chapter focuses on the absorption reaction of the Mg-Si-H system. Here Mg_2Si nanoparticles are synthesised using mechanochemical methods, similar to those used in Chapter 3. A range of characterisation techniques were employed to ensure Mg_2Si was achieved *via* this reaction process. Nanoparticles were synthesised to give the absorption reactants the shortest diffusion distances possible to overcome the reaction barriers associated with this reaction. Partial hydrogenation was achieved and the high pressure conditions to obtain this outcome are explained in detail towards the latter half of the chapter.

5.1 Introduction

Magnesium silicide, Mg_2Si, is a light weight, environmentally benign[169], economically profitable and indirect gap narrow band semiconductor[170] that has properties relevant to a range of applications. For example, nano-films of Mg_2Si are used in thermoelectric applications due to its efficient thermoelectric energy conversion[171] and its compatibility with modern silicon microelectronics[172]. Good mechanical properties and wear resistance have led to Mg_2Si being used as a reinforcement material for aluminium and magnesium alloys[173]. Other uses include anticorrosive coatings[174], the creation of ohmic contacts[175], interconnections in silicon planar technology[176], infrared optical devices[177], photovoltaic applications[178] and an as alternative for anode materials in rechargeable lithium batteries[179]. A more recent application is the use of Mg_2Si as a hydrogen storage material to improve the thermodynamic limitations of pure magnesium (Mg)[67].

Already mentioned in Chapter 3, Vajo *et. al.*[67] first reported that the stoichiometric addition of Si to MgH_2 (Eqn. 5.1) significantly lowered the thermodynamics of MgH_2 dehydrogenation (ΔH = 38.9 kJ mol^{-1} H_2)[67] without dramatically altering the hydrogen storage capacity (5.0 wt.%). In theory, Mg_2Si is an ideal material for hydrogen storage applications as it is predicted to have a hydrogen equilibrium pressure of 1 bar at 20°C or 100 bar at 150°C (*HSC Chemistry* 6.12 software, Outotech Research). Despite this, kinetic limitations prevent rehydrogenation from

occurring and the most vigorous attempt to directly rehydrogenate Mg_2Si, up to 350°C and 1850 bar, was unsuccessful[72].

Eqn. 5.1 $$2MgH_2 + Si \rightarrow Mg_2Si + H_2$$

Mechanical activation of Mg_2Si by ball-milling under high pressure hydrogen over 48 h at 50 bar[67] and 20 bar[76] showed only 0.8 wt.% hydrogen absorption in the case of 50 bar. Although the weight percentage of H was not reported at 20 bar, XRD results indicated that some absorption took place[76]. The fact that it took 48 h for minor hydrogen absorption to occur further emphasizes the kinetic limitations to hydrogenation in the Mg-Si-H system. The problems with hydrogen reversibility in the Mg-Si-H system were investigated further using Density Functional Theory (DFT) modelling[70]. The DFT results found that the energy barriers for hydrogen dissociation (39.8 and 47.2 kJ mol^{-1} H_2 along two different pathways) were sufficiently low enough for dissociation to occur at room temperature[70], however, dissociation on Mg_2Si was strongly impeded once an oxide layer was formed on the surface.

Kelly *et. al.*[71] studied the kinetic limitations of the Mg-Si-H system using thin films and also showed that H_2 dissociation was not the limiting factor, neither was the diffusion of hydrogen through the Mg_2Si matrix. Instead, Kelly *et. al.*[71] realised that the slow diffusion rate of Mg and Si away from each other in Mg_2Si to separate phases inhibits the hydrogenation pathway. The thin film study suggested that a reaction depth of 1 nm was necessary to facilitate complete hydrogenation of Mg_2Si[71], thus making the system highly impractical. However, thin films introduce interfacial clamping effects that can affect the hydrogen equilibrium pressure of the hydride in question[180] and the possibility of such an effect cannot be excluded. Clamping effects actually destabilize the thin-film hydride and further increase the equilibrium pressure[180]. In addition, based on the predicted thermodynamics of the Mg-Si-H, Kelly *et. al.*[71] applied only 200 bar of hydrogen which means that the

sample would only absorb at 165°C (*HSC Chemistry* 6.12 software, Outotech Research) where the kinetics would be slow.

Overcoming reaction kinetic barriers is a key factor to H_2 storage in the Mg-Si-H system. Crystallites and more importantly particles in the nano-scale range would reduce diffusion distances of Mg through Si[149] to accommodate H_2 storage under viable conditions. Paskevicius *et. al.*[72] ball milled $2MgH_2$ + Si to reduce the crystallite size from bulk to the range of 2 – 30 nm (with significantly larger particle size). Upon dehydrogenation, neutron diffraction showed the formation of nanoscopic crystallites of Mg_2Si (~ 15 – 30 nm). Rehydrogenation of these nanosized crystallites was not successful, even at pressures close to 2 kbar and 290°C[72]. This suggests that the kinetic limitations for this system could be due to particle size and not just crystallite size. The aim of this chapter, therefore, is to synthesize small Mg_2Si nanoparticles to observe if it is indeed possible for hydrogenation to proceed under modest conditions to form MgH_2 and Si.

This chapter focuses on synthesizing nanoparticles of Mg_2Si using mechanochemical ball milling and a LiCl buffer phase to control the size of the particles. The hypothesis of improved reaction kinetics through small particles size is explored by using suitable salt separation techniques and high pressure hydrogenation of the nanoparticles.

5.2 Nanoparticle Synthesis

The synthesis of magnesium silicide in an inert salt matrix (Eqn. 5.2) was first explored using thermodynamic calculations (*HSC Chemistry* 6.12 software, Outotech Research). The Gibbs free energy of formation at room temperature was strongly negative ($\Delta_r G_{298K} = -1335$ kJ mol^{-1}) indicating that the reaction was energetically favourable. The reactants were first ball milled at various processing conditions, including ball to powder (BTP) ratios and milling times without additional LiCl buffer to gauge the optimal conditions for 100% reaction conversion. X-ray diffraction (XRD) (Figure 5.1) showed that no reactants were present when a BTP

ratio of 90:1 and a milling time of 24 h was used, indicating that the reaction appeared to have gone to completion. XRD however, would not be able to detect small fractions of low atomic mass Li, where present, nor is it able to detect amorphous Li and $MgCl_2$ that may have changed structure due to the ball milling process.

Eqn. 5.2 $$SiCl_4\ (l) + 8Li\ (s) + 2MgCl_2\ (s) \rightarrow Mg_2Si\ (s) + 8LiCl\ (s)$$

Once it was determined that Eqn. 5.2 would proceed; LiCl was added to the reactants in order to control the particle size of Mg_2Si formed during milling (Eqn. 5.3). In order to manufacture the smallest possible particles, the solid reactants including the LiCl buffer were individually premilled for a period of time (

Table 5.1) to reduce their particle size. It was determined that the buffer to product ratio (LiCl:Mg_2Si, by volume) of 15:1 and a premilling time of 3 h for each reactant could obtain the smallest particle size whilst still achieving full reaction conversion according to the XRD phase identification (Figure 5.1). Milling times were not taken beyond 24 h to minimise milling medium contamination (stainless steel 316) that was inevitable during the long ball milling process.

Eqn. 5.3 $$SiCl_4\ (l) + 8Li\ (s) + 2MgCl_2\ (s) + xLiCl\ (s) \rightarrow Mg_2Si\ (s) + (8+x)LiCl\ (s)$$

Table 5.1: Ball milling conditions used to produce Mg_2Si nanoparticles.

Ball to Powder Ratio (by weight)	Pre milling time (h)	Reaction milling time (h)
30:1	0	12
60:1	3	18
90:1	6	24

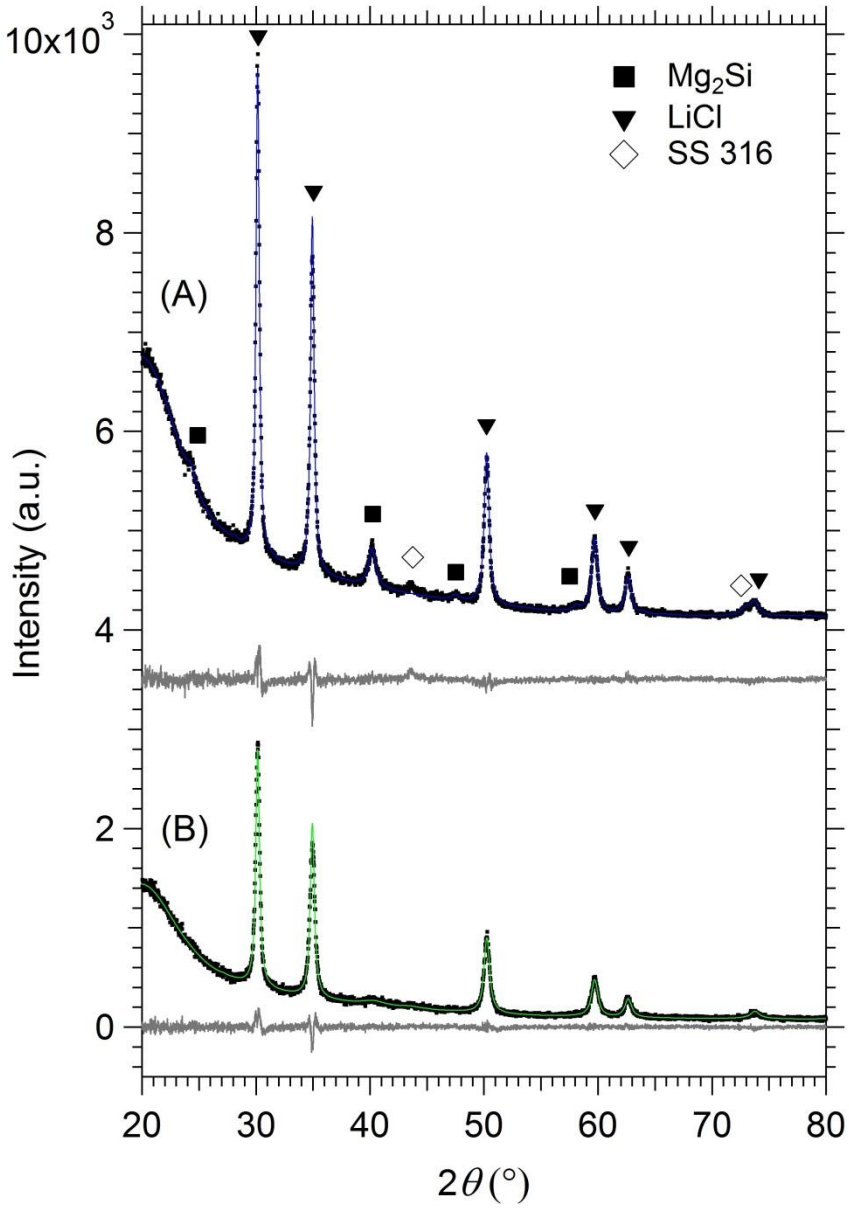

Figure 5.1: XRD diffractograms showing (A) Products from Eqn. 5.2 without additional LiCl added to the reactants (B) Products from Eqn. 5.3 with LiCl added to the reactants in a buffer to Mg_2Si volume ratio 15:1. Grey plots are the difference between the collected data and the Rietveld refinement.

The XRD patterns from Eqn. 5.2 (Figure 5.1 (A)) predominately show the presence of LiCl with only two main peaks from Mg_2Si particles with very small crystallites. A reduction in Mg_2Si crystallite size from 8 nm (without LiCl buffer added) to 2 nm (with LiCl buffer added) was observed when Rietveld analysis was done on the

patterns containing LiCl. The crystallite size calculations from the Rietveld analysis are also given in Table 5.2. As a general rule, an R_{wp} value of 5% or less indicates an acceptable goodness of fit[150]. Note that the particle size is also reduced as shown below by SAXS measurements.

Table 5.2: Crystallite size from Rietveld Refinement for Mg_2Si embedded in LiCl.

Sample	Phase	wt.%	Crystallite Size (nm)
(A) No additional LiCl with reactants	**Mg_2Si**	**13**	**8.0 ± 0.3**
R_{wp} = 4.4%	**LiCl**	**86**	**53 ± 3**
(B) 15:1 LiCl added to reactants	**Mg_2Si**	**10**	**2.0 ± 0.2**
R_{wp} = 5.7%	**LiCl**	**88**	**40 ± 2**
	Stainless steel 316	**2.4**	**2.0 ± 0.5**

Although the XRD results show that there are no residual reactants in the final product, it is difficult to assess a complete salt metathesis reaction, especially when such a high LiCl buffer to product volume ratio (15:1) is used. Two examples of this are show in Sheppard *et. al.*[89] and Tsuzuki *et. al.*[181]. The first study, Sheppard *et. al.*[89], synthesised MgH_2 nanoparticles using mechanochemical ball milling methods and found that the reaction was only ~ 95% complete without the salt buffer and ~ 78% complete when a 10:1 volume ratio of buffer was used. Similarly, Tsuzuki *et. al.*[181] used mechanochemical ball milling to produce ZnS nanoparticles with a 10:1 volume ratio of buffer and it took 36 h and 80 h to achieve complete conversion of the reactants; much longer than the 24 h used to produce the Mg_2Si nanoparticles in this chapter. These two studies used only two reagents to form the final product whereas this study uses three. This also reduces the likelihood of the reaction going to completion. These issues are addressed in the future work section of Chapter 7.

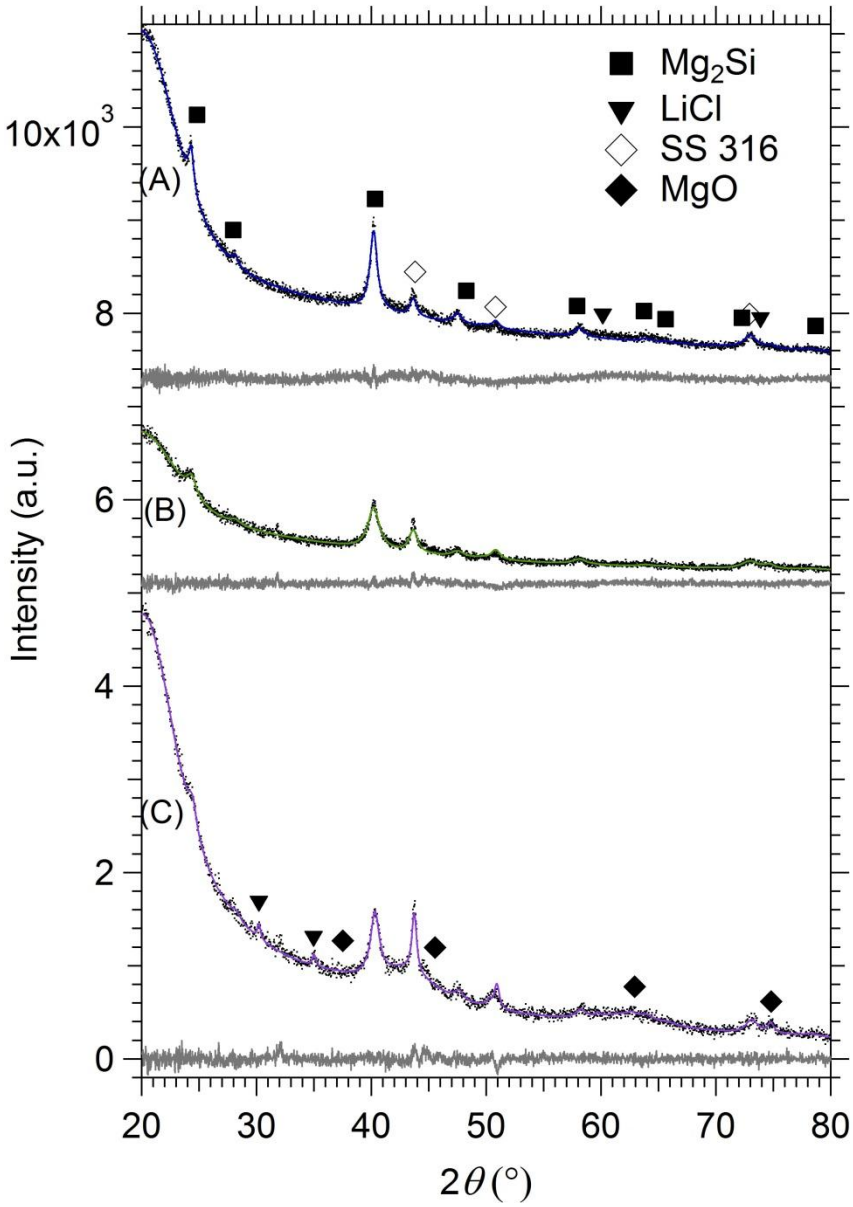

Figure 5.2: XRD diffractograms showing (A) THF washed Eqn. 5.2 (B) THF washed Eqn. 5.3 (C) Sample (B) Mg_2Si heated to 140°C for minimum 12 h to evaporate all THF. Grey plots are the difference curves between the collected data and calculated Rietveld models.

The presence of LiCl slows sorption reaction kinetics as the salt acts as a barrier impeding hydrogen flow in and out of the storage material[7]. Therefore LiCl was removed with tetrahydrofuran (THF) by washing, centrifuging, and decanting three times before drying under vacuum. The resulting powder was then analysed using XRD as shown in Figure 5.2 and Table 5.3. The Rietveld analysis confirmed that the Mg_2Si crystallite size reduced, from 21.0 ± 0.3 nm to 7.0 ± 0.6 nm when LiCl was

used as a synthesis buffer. These values are higher than the earlier reported values (8 nm and 2 nm) that had LiCl present during the XRD. This is due to the Mg_2Si being the dominant phase after washing. Therefore, the parameters extracted from the Rietveld profile analysis after washing with THF are regarded as the more reliable.

Table 5.3: Crystallite size from Rietveld Refinement of the Mg_2Si washed samples (Figure 5.2).

Sample	Phase	wt.%	Crystallite Size (nm)
(A) Washed no additional LiCl	**Mg_2Si**	**91**	**21 ± 3**
R_{wp} = 4.7%	**SS 316**	**10**	**9.0 ± 0.7**
(B) Washed 15:1 additional LiCl	**Mg_2Si**	**82**	**7.0 ± 0.6**
R_{wp} = 4.7%	**Stainless steel**	**18**	**7.0 ± 0.3**
(C) Washed 15:1 additional LiCl heated to 150°C	**Mg_2Si**	**20**	**7.0 ± 0.7**
R_{wp} = 2.6%	**Stainless steel**	**5**	**14.0 ± 0.8**
	MgO	**73**	**1.0 ± 0.1**
	LiCl	**2**	**19 ± 4**

In order to characterise the structure of the Mg_2Si particles they were further investigated using scanning electron microscopy (SEM), transmission electron microscopy (TEM) and small angle x-ray scattering (SAXS). The SEM image for the unbuffered sample before washing (Eqn. 5.2), given in Figure 5.3 (A), shows a conglomerate of material where smaller particles less than 100 nm in size exist within a larger aggregate. It was difficult to differentiate between the LiCl matrix and the Mg_2Si particles, even when energy dispersive x-ray spectroscopy (EDS) mapping was performed (data not shown). After washing with THF, the morphology of the particles is revealed and individual sphere-like particles approximately 30 nm in size are abundant in the SEM micrograph (Figure 5.3 (B)) with some aggregation. There is also evidence of smaller particles, under 10 nm in diameter. As Eqn. 5.2 did not have a LiCl buffer added to the reactants, it is expected that larger particles would form at the beginning of the reaction. As the reaction proceeds LiCl begins to form,

and limit growth of the newly formed Mg_2Si thus producing smaller particles compared to the beginning of the reaction.

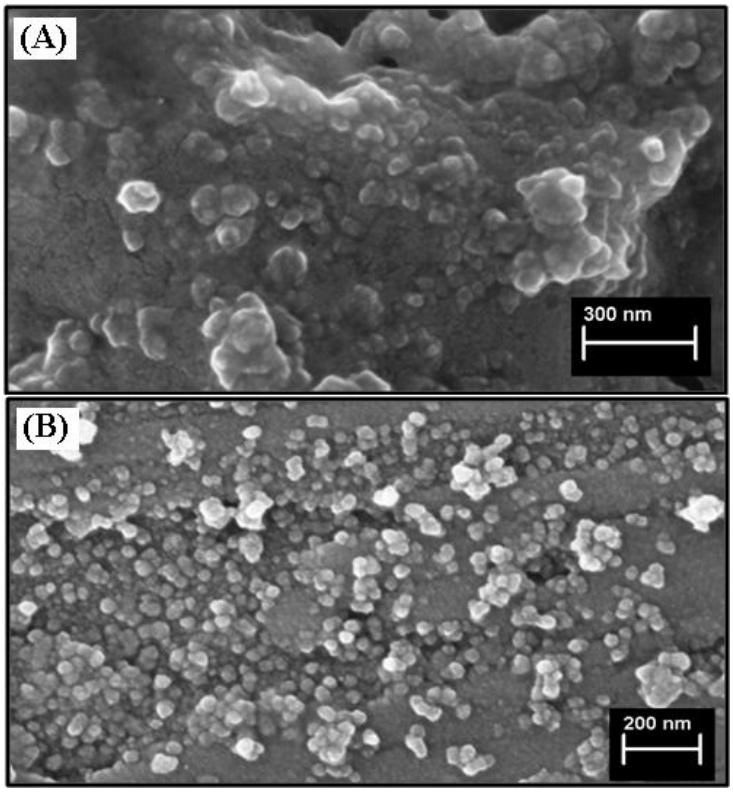

Figure 5.3: SEM micrographs of Mg_2Si (A) embedded in LiCl and (B) after the LiCl was removed with THF.

To confirm that the bimodal particle distribution was an average representation of the sample, a larger sample size was analysed using Small Angle X-ray Scattering (SAXS) (Figure 5.4 (A)). Taking the evidence from the SEM of spherical morphology, a least squares fit of a volume distribution (Unified Fit Model)[103] was calculated. The Unified Fit Model was used to determine average bulk particle size. This model is described in detail in Beaucage [103] and divides the raw data into the Guinier part and the power law tail in order to calculate the radius of gyration. The resulting volume distribution showed that the mean diameter for the small and large distributions were 5.5 nm and 42.5 nm respectively. On the other hand, the sample produced from the LiCl buffer reaction produced a more mono-dispersed size

distribution from the SAXS analysis (Figure 5.4 (B)). The diameter for this sample was calculated from the Unified Fit Model and was determined to be 13 nm on average. The shape of the data between the q value of 0.2 and 0.3 $Å^{-1}$ is an artefact that arises due to the incomplete subtraction of the background from the capillary. Each capillary is slightly different and it is almost impossible to ensure that the beam passes through the same part of the capillary of both the one containing the sample and the blank. As a result, the data above q = 0.2 $Å^{-1}$ has been excluded from the model.

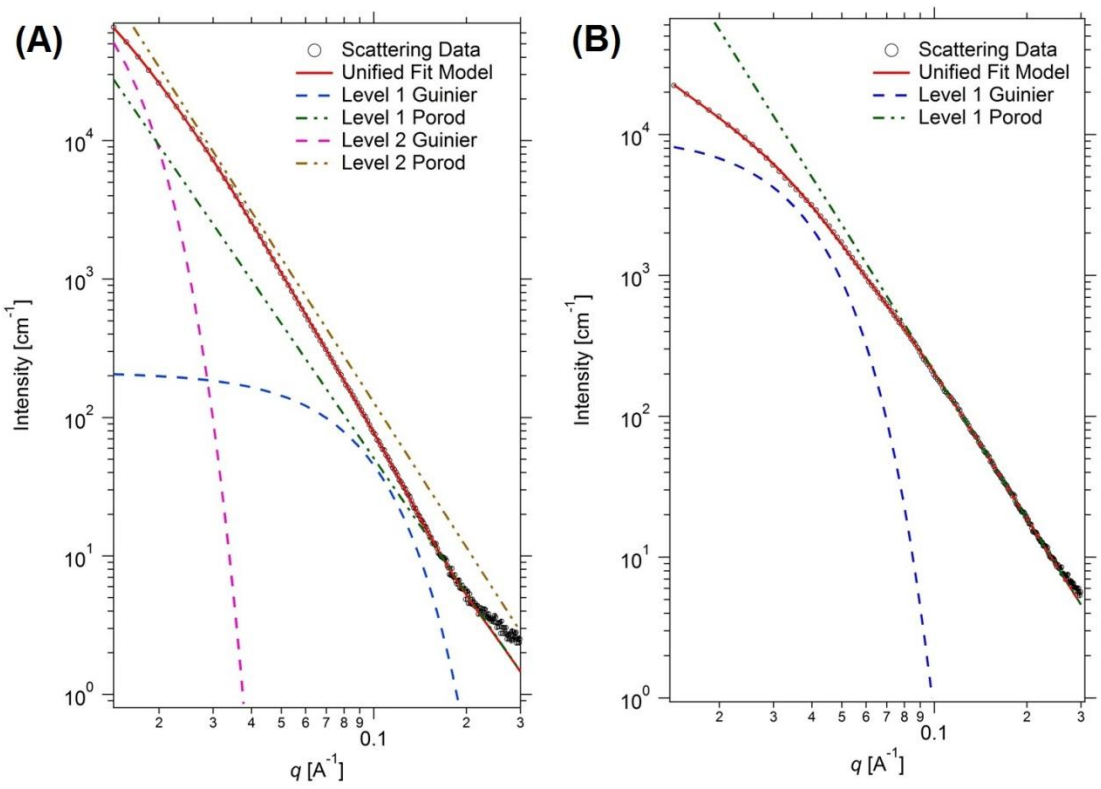

Figure 5.4: SAXS modelling of Mg_2Si particles synthesised (A) Numerical modelling for the two size distributions for the sample with no LiCl buffer (Eqn. 5.2) (B) Unified Fit Model to experimental data for sample with LiCl buffer (Eqn. 5.3).

A TEM micrograph for the Mg_2Si particles produced with buffer (15:1 LiCl to Mg_2Si ratio) from Eqn. 5.3 is given in Figure 5.5. Ultrasonication was able to separate the particles effectively in toluene before dropping onto a TEM grid, confirmed by the individual particles visible in Figure 5.5 (red circles). Despite this, there is also

evidence of clusters of particles as seen by the dark group of particles towards the centre of the image. This may be aggregated small particles or an agglomeration with a bigger particle size. EDS did not detect any of the contaminants such as SS 316 or LiCl. The typical particle size from TEM gives similar results to the SAXS analysis showing that there are particles from less than 10 nm through to larger particles approximately 20 nm in diameter. The large dark shadow in the micrograph was a result of the toluene, used to suspend the particles, reacting with the holey carbon film on the copper TEM grid. High resolution TEM on several of the particles showed lattice planes at a *d*-spacing of 2.26 Å (Figure 5.5 insert). This corresponds to the (0 2 2) *hkl* reflection of Mg_2Si at d = 2.26 Å.

One noticeable difference between the TEM image of the particles and the modelling to calculate particle size is that the TEM shows smaller sized particles. This is because the TEM uses a very small amount of sample compared to the SAXS and also the SAXS distribution is volume weighted, not number weighted as for the TEM. This results in a size distribution from SAXS being skewed by larger particles in the sample. The Mg_2Si particles produced here from the SAXS Unified Fit [103] method resulted in 13 nm diameter nanoparticles, the smallest reported in the literature[64, 72, 83].

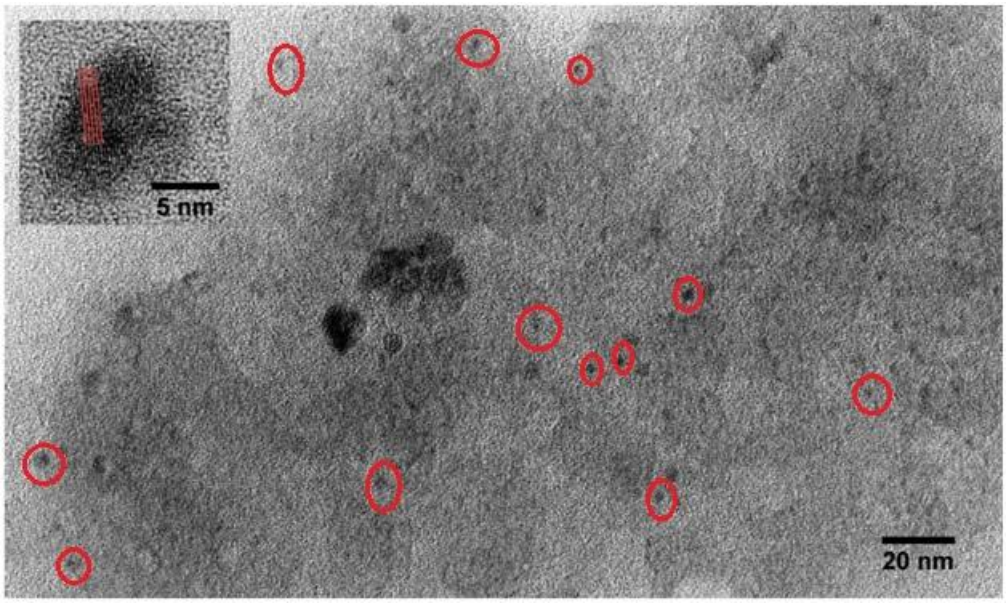

Figure 5.5: High Resolution TEM of washed Mg_2Si nanoparticles synthesised with a LiCl buffer. The inset displays lattice fringing from d = 2.26 Å.

5.3 Hydrogenation of Mg_2Si Nanoparticles

Reaction kinetics are regarded as the limiting factor with respect to the hydrogenation of magnesium silicide[71, 72]. Therefore, 13 nm Mg_2Si nanoparticles stand the best chance to date of overcoming these kinetic barriers and give the Mg-Si-H system an optimum chance of absorbing hydrogen. Thermodynamic equilibrium conditions were first determined for Eqn. 5.1 from calculations using the same software used for the synthesis process, *HSC Chemistry* 6.12 software, Outotech Research. The compressibility of hydrogen has a significant effect on the thermodynamic calculations at high pressures, hence fugacity is used in the equation[85]. The fugacity values [182] (per mole of hydrogen gas) were calculated for a set range of temperatures and the corresponding equilibrium pressures were also calculated (Table 5.4).

Table 5.4: Calculated [182] values of fugacity and equilibrium pressure at specific temperatures for Eqn. 5.1.

Temperature (°C)	Equilibrium Fugacity (bar)	Equilibrium Pressure (bar)
0	0.45	0.45
50	5.48	5.44
100	35.8	35.2
150	155	145
200	504	423
250	1330	939
300	3000	1709

The manometric Sieverts apparatus used at Curtin and Griffith universities were able to achieve maximum pressures of approximately 1 kbar and 2 kbar respectively. Mg_2Si synthesised with 15:1 LiCl buffer washed with THF was used for all high pressure experiments. Measurements were taken incrementally from room temperature to a maximum of 200°C to remain above the thermodynamic equilibrium pressure at all times and prevent the possibility of desorption. Initially,

the Mg_2Si nanoparticles were tested at Curtin University. After pressurizing to 750 bar at room temperature, the temperature was ramped incrementally by 50°C, to a maximum of 200°C, and was held for 24 h for each of these temperatures. Simultaneously, a portion of Mg_2Si from the same batch of material was loaded under 1.8 kbar at room temperature in the Sieverts apparatus at Griffith University. The temperature was incremented and held at each new temperature for a minimum of 24 h. Once each of the systems had reached thermal equilibrium, changes in pressure and time were measured. A change in pressure can be directly related to the number of moles of hydrogen absorbed according to the method described by Gross *et. al.*[44]. There was no detectable pressure drop in the sample held at 200°C, 850 bar indicating that absorption had not taken place. There was also no evidence of either absorption product of MgH_2 or Si in the resultant XRD pattern (Figure 5.6 (B)).

On the other hand, the sample held at 1.8 kbar showed a reduction in pressure equating to absorption of 1.68 ± 0.5 wt.%. However, the resultant XRD pattern (Figure 5.6 (C)) did not display peaks from either MgH_2 or Si indicating that absorption of hydrogen into the Mg_2Si nanoparticles had not taken place. The drop in pressure could be a result of an extremely slow gas leak over the time of the experiment, a notorious problem with high pressure experiments[72]. The appearance of peaks at 30° and 35° 2θ were due to the presence of LiCl. Although these peaks were not evident in XRD of the washed samples (Figure 5.2), upon heating the residual LiCl from the washing process became more apparent as the crystallites grew at temperatures above room temperature. There was also some evidence of very broad magnesium oxide humps (MgO) centred on 2θ values of 43° and 63° which indicated a small amount of MgO present with very small crystallite size.

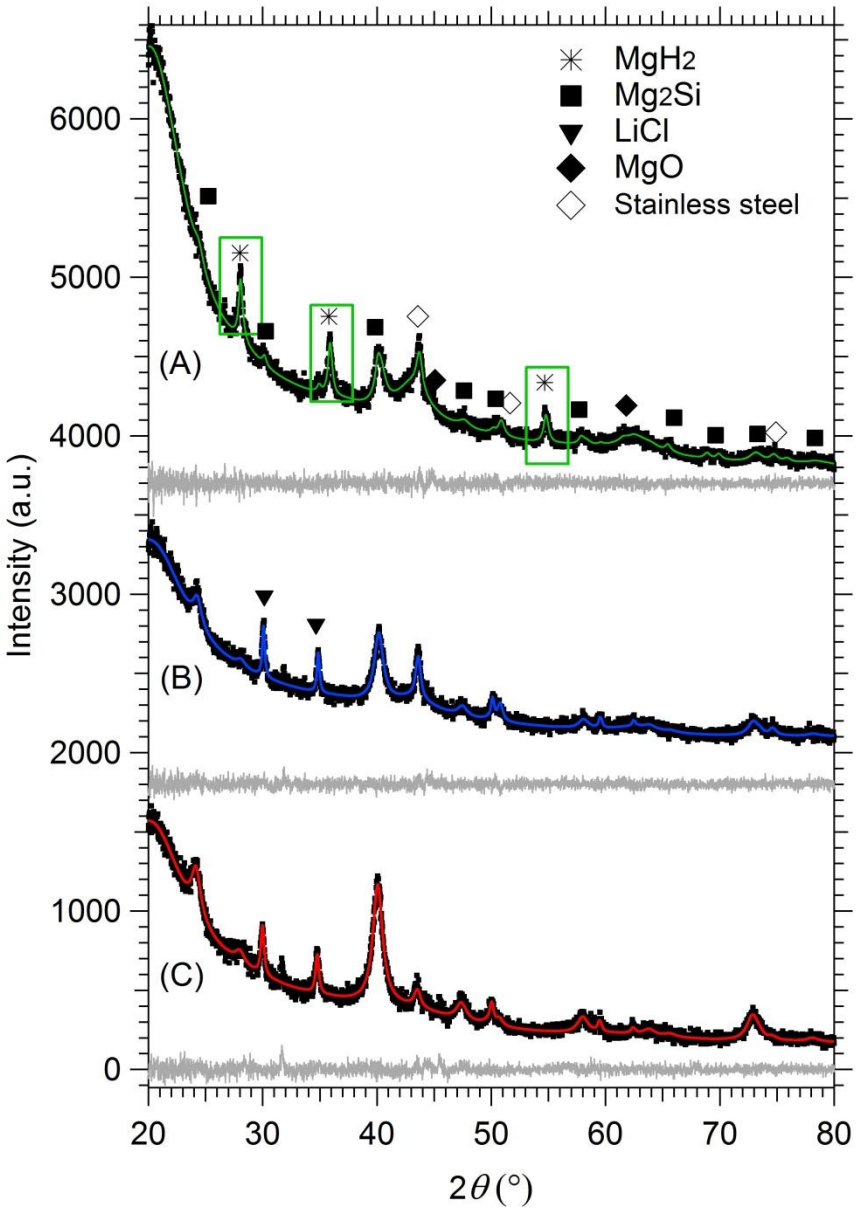

Figure 5.6: XRD diffractograms of (A) Curtin 1.2 kbar without THF (B) Curtin 850 bar with THF (C) Griffith 1.8kbar with THF. Grey plots are the difference curves between the collected data and calculated Rietveld models.

As a result of the unsuccessful attempt of the Mg_2Si nanoparticles to absorb hydrogen at 850 bar and 1.8 kbar of pressure, the procedure to wash the LiCl from the nanoparticles was further investigated. To reduce the LiCl content in the sample, further washes with THF were done. The sample was then placed under vacuum ($11.2 \times 10^{-8}\ mbar$) for at least 18 h. Thermal stability of the washed Mg_2Si from Eqn. 5.3 was then assessed by heating at a constant rate to 500°C whilst measuring

the partial pressure at specific atomic mass units (residual gas analysis (RGA)) to identify any gases released (Figure 5.8 (A)). This experiment gave two unexpected results; 1) THF was still present even after evacuating the sample for 18 h in dynamic vacuum at room temperature, and 2) A significant amount of H_2 was released from the sample at 70°C and again at 100°C, 150°C and 220°C (Figure 5.8(A)). The behaviour of the gas released from the washed Mg_2Si specimen can be explained by the presence of THF. The first peak can be associated with the low boiling point of THF (66°C) and subsequent peaks are related to the thermal decomposition of THF under vacuum[183]. The decomposition products of THF are usually hydrogen, carbon monoxide and hydrocarbons[183]. However, XRD analysis (not shown) showed significant amounts of magnesium oxide (MgO) after heating the sample to 500°C. The presence of MgO was most likely due to magnesium's strong affinity to oxygen; hence, instead of forming carbon monoxide, as the THF decomposed at higher temperatures, MgO was formed. There is also the possibility of the cell leaking at temperatures above 400°C under the $11.2 \times 10^{-8}\, mbar$ vacuum. Rietveld refinement on the washed samples took into account the presence of SS 316 and MgO contamination and the calculated crystallite sizes are given in Table 5.3.

To minimize the THF present in the Mg_2Si nanoparticles, an added step of THF evaporation was incorporated into the synthesis process. The sample was heated (also under vacuum) to 140°C and the gases monitored using RGA until the spectrum showed no signs of residual THF. The XRD diffractogram for the THF 'free' sample can be seen in Figure 5.2 (C). This process still led to the development of MgO in the sample, however, the broad peak Rietveld refinement showed that the crystallites were 1 nm, possibly due to the formation of an MgO shell around the Mg_2Si nanoparticles.

The high pressure experiment was then repeated at Curtin University using the same method described earlier. Again, the sample was ramped in 50°C increments from room temperature to 200°C, while holding each temperature for 24 h. The maximum pressure reached during this experiment was 1.2 kbar at 200°C which is still above the predicted equilibrium pressure (Table 5.4). Figure 5.7 shows the amount of H_2

absorbed with time for the 1.2 kbar experiment for each incremental temperature. The graph shows an irregular absorption curve that does not have a smooth kinetic pattern for each temperature. There are several reasons for the irregularities highlighted in the data (Figure 5.7) including: subtle temperature variation of the sample cell at room temperature, the small quantity of hydrogen absorbed compared to the overall volume of the sample cell (4.84 cm^3) and subtle errors in volume calibration. It also gives a total absorption of 3.4 wt.%. This would indicate that a high percentage of the Mg_2Si nanoparticles absorbed hydrogen under these high pressure conditions. However, the XRD shown in Figure 5.6 (A) does not show a considerable reduction in peak intensity to corroborate this high absorption result. To obtain a more accurate H_2 absorption result, the valve of the sample cell was closed and the cell cooled to room temperature. This drop in pressure from the start of the experiment at room temperature to the final cooled pressure was used to calculate the amount of H_2 absorbed.

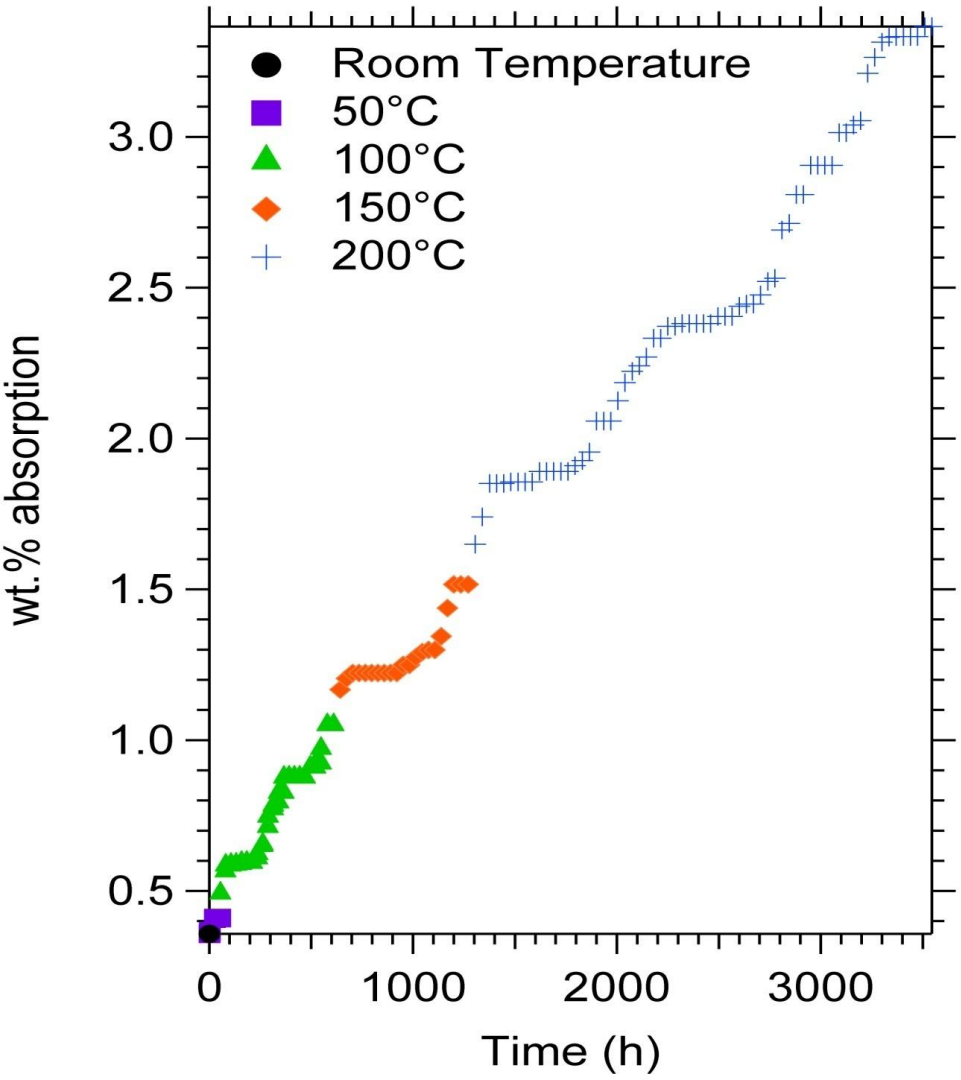

Figure 5.7: Plot of Mg_2Si absorption data showing wt.% of H_2 absorbed with time.

A pressure drop correlating to an absorption of 1.63 ± 0.2 wt.% was observed by comparing the room temperature pressure before and after the temperature increments. The wt.% reported here uses the weight of the sample including the impurities, MgO, SS 316 and LiCl reported in Table 5.3. Since approximately 20% of the original sample weight was Mg_2Si, this absorption wt.% for hydrogen correlates well with the formation of magnesium hydride as shown by the appearance of XRD peaks at 2θ values of 27.9°, 35.7° and 54.6° (Figure 5.6 (A)). The silicon product from Eqn. 5.1, however, was not observed. This indicates that crystalline silicon was not formed under these high pressure conditions, rather amorphous

silicon may have been created. The amorphous silicon phase typically shows broad halos centred at 28° and 50° 2θ in an XRD pattern[131], however this non-crystalline Si structure was masked by the other phases present in the material. In order to corroborate that hydrogen had been absorbed, temperature program desorption (TPD) was carried out using RGA and a heating rate of 2°C min^{-1}. The results are given in the partial pressure plot (Figure 5.8 (B)). Additionally, the single desorption peak (solid line in Figure 5.8) occurred at a temperature of 240°C, higher than THF reaction implying that the H_2 gas exiting the system is due to the hydrided Mg_2Si phase rather than from any reaction with THF (indicated by the dotted line in Figure 5.8 (A)).

The results also show that H_2 gas started leaving the system from as low as 100°C and peaked at 240°C. This temperature is much lower than pure bulk (unmilled) and 14 h milled MgH_2 dehydrogenation, which desorbs at a TPD value of 430°C and 400 °C.[184] The TPD peak shape is the same as ball milled MgH_2 with Si [184] that had a maximum decomposition temperature of 275°C. The reduced value of 240°C (Figure 5.8 (B)) is most likely due to the reduced particle size thus improving reaction kinetics of the Mg-Si-H system.

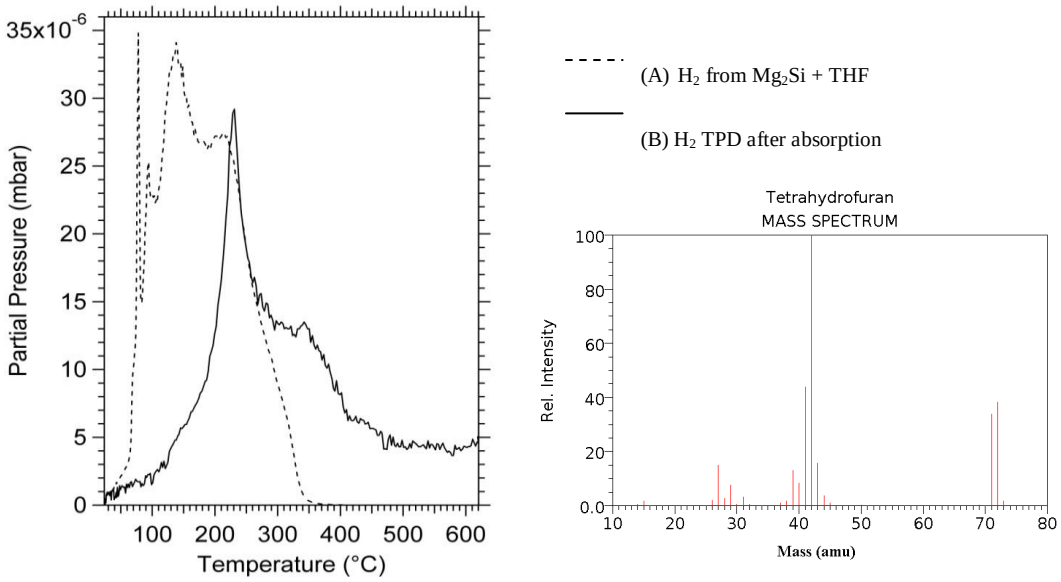

Figure 5.8: RGA data (A) from the Mg_2Si nanoparticles after washing with THF and (B) TPD of the absorbed Mg_2Si nanoparticles from RT to 600°C at 2°C min^{-1}. The fractionation mass spectroscopy pattern for THF is also displayed.

Despite the long reaction time, Mg_2Si was still detected in the diffraction pattern, indicating that the hydrogenation reaction had not gone to completion. This is possibly due to impurities present (MgO and SS 316) in the sample. Dai *et. al.*[70] used Density Functional Theory (DFT) to theoretically show that impurities such as an oxidised surface can impede the hydrogenation of Mg_2Si.

To eliminate the effect of THF on the hydrogenation of Mg_2Si nanoparticles, a final set of experiments were done on Mg_2Si within the LiCl salt matrix. In order to observe any change in Mg_2Si, the sample produced from the no buffer reaction (Eqn. 5.2) was used, as the Mg_2Si peaks were more prominent in the XRD in that sample.

To explore the possibility of amorphous Si forming during hydrogenation, the XRD holder was changed from the PMMA bubble holder to a single crystal Low Background Holder (LBH). Oxygen and moisture contamination was avoided by placing a 300 nm layer of aluminium over the sample on the LBH. This technique eliminates the amorphous humps seen in Figure 5.1 from the PMMA bubble and instead gives sharp crystalline Al peaks (Figure 5.9).The Al barrier was not completely air-tight, hence the appearance of the $LiCl{\cdot}H_2O$ phase in the XRD patterns. Again, the non-crystalline Si structure was masked by the other phases present in the material and was not observed in the diffractograms.

In another high pressure experiment using THF free Mg_2Si produced with LiCl buffer, at Curtin University, a maximum pressure of 650 bar was achieved, therefore the sample was only heated to 175°C for 24 h to ensure the conditions for hydrogenation were above thermodynamic equilibrium. As the XRD patterns in Figure 5.9 indicate, there is no evidence of MgH_2 formation, indicating that the sample did not undergo hydrogenation. The sample was then evacuated, heated to 300°C and the changes in pressure measured to observe any dehydrogenation. As expected, there was little change in pressure (equivalent to 0.18 wt.% hydrogen desorbed).

Prior to the high pressure conditions of 650 bar H_2 at 175°C the sample was heated to 440°C may have completed the synthesis reaction as mentioned earlier in section 5.2. The XRD may not have detected small quantities of reactants including residual Mg

thus the possibility of Mg hydrogenation in the earlier experiment (Figure 5.6 (A)) cannot be ruled out. If the sample in LiCl did go to completion, this would indicate that there is no Mg to hydride when placed under 650 bar of H_2.

Another possibility for the lack of MgH_2 formation is the lower reaction pressure, 650 bar rather than 1.2 kbar and temperature, 175°C instead of 200°C compared to the earlier experiment. These conditions mean that the absorption kinetics were slower and this would have been further compounded by the presence of LiCl limiting hydrogen diffusion. The lack of absorption observed during these experiments was not unexpected as previous studies[7] showed that LiCl greatly reduces the sorption reaction kinetics. Since the presence of the LiCl matrix slows the diffusion of hydrogen into the Mg_2Si phase, it would also slow the formation of MgH_2 and Si from Mg_2Si.

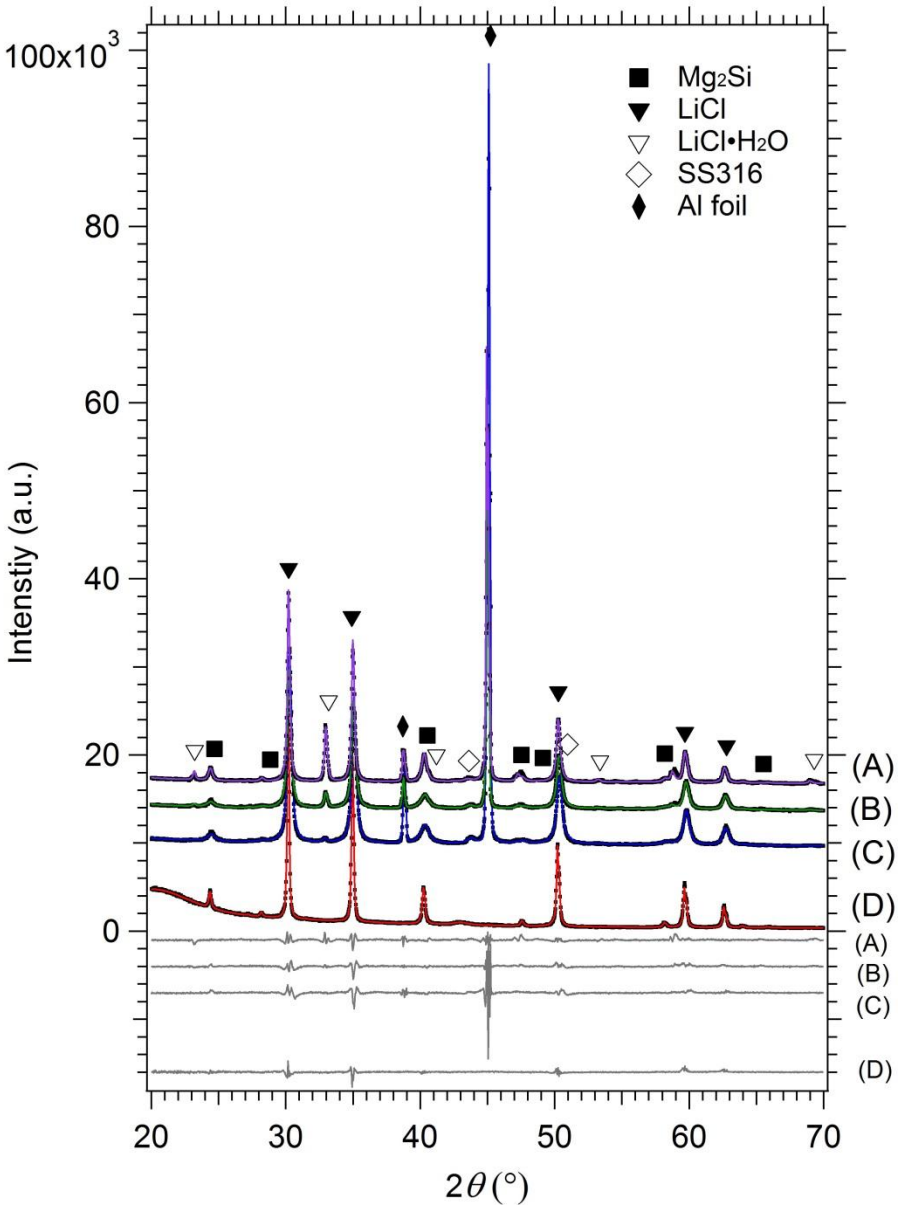

Figure 5.9: XRD diffratograms of the experiments where the Mg_2Si remained in the LiCl salt matrix. (A) Mg_2Si in LiCl after absorption (650 bar H_2, 175°C) and TPD (vaccum, 300°C). (B) Mg_2Si in LiCl, 175°C, 650 bar H_2, 24 h. (C) Mg_2Si in LiCl from Eqn. 5.2. (D) Mg_2Si in LiCl from Eqn. 5.2 heated to 440°C. Grey plots are the difference curves between the collected data and calculated Rietveld models.

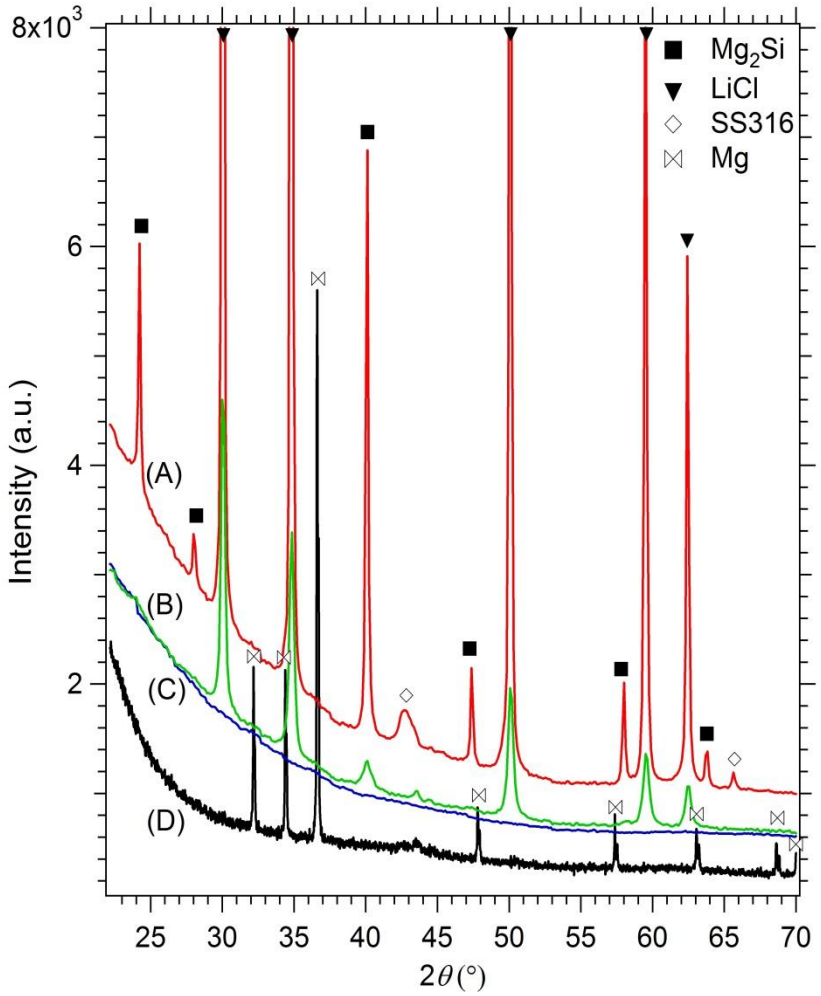

Figure 5.10: Data from the Powder Diffraction Beamline at the Australian Synchrotron (λ = 1.000026 Å): (A) Mg_2Si in LiCl heated to 440°C (B) Mg_2Si as synthesized in LiCl (C) Background (borosilicate capillary) (D) Mg standard.

To confirm the source of hydrogen absorption shown in the XRD pattern of Figure 5.9 (A), was Mg_2Si and not unreacted Mg from the mechanochemical synthesis reaction, samples of Mg_2Si in LiCl were taken to the Australian Synchrotron Facility. The as synthesised and heated samples were placed into borosilicate capillaries and diffraction data from the powder diffraction beamline obtained (Figure 5.10). A Mg standard has been included with the beamline data to attempt to match peaks at these intensities to a known Mg pattern. According to these patterns there is little evidence to suggest that residual Mg is present after synthesis. Therefore, it is most likely that the absorption of the synthesised Mg_2Si nanoparticles took place to produce the MgH_2 peaks given in Figure 5.6 (A). The ultimate test to prove it was the Mg_2Si

nanoparticles that absorbed hydrogen would be to repeat the experiment at the high pressure of 1.2 kbar. This could not be repeated since the high pressure cell could no longer achieve pressures above 1 kbar after conducting the initial experiments.

5.4 Conclusion

Mg_2Si nanoparticles were synthesised and separated from the LiCl matrix in which it was formed. The Mg_2Si phase was identified using XRD and HRTEM measured (0 2 2) *hkl* lattice plane. The bulk average particle size was measured using SAXS and was found to be 13 nm. XRD analysis showed that these small Mg_2Si nanoparticles reacted with high pressure H_2 to produce the MgH_2 phase, however, slow kinetic limitations did not allow the reaction to go to completion. Without repeating the 1.2 kbar experiment the certainty of Mg_2Si nanoparticle absorption cannot be confirmed. However, the results from this chapter indicate that it may be physically possible to overcome the kinetic barriers. The combination of the drop in pressure equating to 1.63 ± 0.2 wt.% H_2 absorbed, together with the presence of MgH_2 in the XRD pattern, indicates that the transport of hydrogen into the Mg_2Si crystalline structure and the separation of the Si phase from the Mg may have occurred. Despite these promising results, complete absorption was not achieved, therefore the reaction kinetic limitations still play a big role in absorption even at high pressures above 1 kbar.

Chapter 6: Destabilising MgH_2 and $NaMgH_3$ using group IV elements Si, Ge and Sn

"Science and everyday life cannot and should not be separated. Science, for me, gives partial explanation for life. In so far as it goes, it is based on fact, experience and experiment."

Rosalind Franklin (1920 – 1958, England)

This chapter introduces Ge and Sn to the Mg-H system for thermodynamic destabilisation to compare the aforementioned Mg-Si-H system. In addition $NaMgH_3$ destabilised with Si will also be discussed. The addition of group IV elements, Si, Ge and Sn to Mg-based hydrides has led to the successful destabilisation of MgH_2 and $NaMgH_3$ resulting in hydrogen release at lower temperatures. The extent that these group IV elements affect desorption properties of MgH_2 and the effect of Si on $NaMgH_3$ is explored using isothermal and temperature programmed desorption techniques. The aim of this study is to thermodynamically destabilise MgH_2 through the addition of group IV metals causing the formation of intermetallic phases upon hydrogen desorption. A discussion of thermodynamic equilibrium conditions and the difficulty in obtaining these conditions due to kinetic limitations is also included.

6.1 Introduction

As mentioned in Chapters 1 and 3, magnesium is an attractive choice of material to store hydrogen (Eqn. 6.1). A drawback has been the slow reaction kinetics due to the strong binding energy between magnesium and hydrogen[185]. The reaction kinetics can be significantly enhanced through the use of particle size refinement agents during ball milling[52]. Another disadvantage of magnesium has been the high thermodynamic stability, where the thermodynamics are known to be: ΔH = 74 kJ mol^{-1} H_2 and ΔS = 133.4 J mol^{-1} H_2 K^{-1} [7]. At thermodynamic equilibrium these thermodynamic parameters equate to a 1 bar H_2 desorption temperature of 282°C, too high for most practical applications.

Eqn. 6.1 $$\boldsymbol{MgH_2(s) \rightarrow Mg(s) + H_2(g)}$$

Figure 6.1 (red plot) shows the calculated equilibrium pressures converted from fugacity values obtained from *HSC Chemistry* 6.12 software, Outotech Research for

MgH_2 across a range of temperatures. $NaMgH_3$ is another viable hydrogen storage material with a storage capacity of 6 wt.% H_2. $NaMgH_3$ undergoes a two-step desorption process that releases *ca.* 4 wt.% and 2 wt.% of hydrogen gas in each step. The first step (Eqn. 6.2) is the most relevant to practical applications because of its lower operating temperature and the benefit of restricting molten Na metal formation. Similar to MgH_2, $NaMgH_3$ also contains strongly bound hydrogen[186]. A recent study measured the thermodynamic properties of $NaMgH_3$ as ΔH = 86.6 kJ mol^{-1} H_2 and ΔS = 132.2 J mol^{-1} H_2 K^{-1} giving an operational temperature of 382°C at 1 bar H_2 [187]. The heat capacity of $NaMgH_3$ has not been determined, therefore, the equilibrium plot is not shown in Figure 6.1.

Eqn. 6.2 $$\boldsymbol{NaMgH_3 \rightarrow Mg + NaH + H_2(g)}$$

Thermodynamic destabilisation of MgH_2 can be achieved by introducing another element to allow for the formation of a more energetically favourable intermetallic upon hydrogen desorption. Si is a well-known additive that has been used to destabilize MgH_2 [67, 72, 188, 189] (Eqn. 6.3), significantly reducing the enthalpy of reaction to 38.9 kJ mol H_2^{-1} [67]. This reduction in enthalpy results in a theoretical desorption temperature of 25°C at 1 bar with a H capacity of 5 wt.% (Figure 6.1, yellow plot). Despite these ideal conditions, attempts to achieve this experimentally have been extremely limited by reaction kinetics[72]. The destabilisation of $NaMgH_3$ is also achieved with the addition of Si to the system (Eqn. 6.6), with desorption of pure $NaMgH_3$ temperature from 350 – 250°C reported in the literature[186]. Equilibrium conditions for $NaMgH_3$ and Si are slightly higher than MgH_2 + Si however gives lower enthalpy values of than $NaMgH_3$ alone. The theoretical hydrogen capacity is also reduced from 4 wt.% to 3.13 wt.% once Si is added. A direct comparison between $NaMgH_3$ + Si with MgH_2 + Si shows that the equilibrium pressure for the former is much lower than the latter at higher temperatures. This indicates that reaction kinetics limitation could be overcome with an increase in temperature without thermodynamic restrictions coming into effect. This would also

lead to better reabsorption of Mg_2Si by this change in the reaction pathway. The present study investigates the use of Si as a thermodynamic destabilisation agent to reduce the operating temperature of $NaMgH_3$ into a more practical range for most applications.

After Si, the next group IV elements in the period are Ge and Sn, which also form intermetallics with Mg[190, 191, 192]. For direct comparison with MgH_2 with Si reactions, theoretical equilibrium pressures of MgH_2 with Ge and Sn have been included in Figure 6.1. With respect to Ge, it has similar properties to Si and has also been studied as a destabilising additive to MgH_2 [193] (Eqn. 6.4). Adding Ge to the system has a reduced theoretical storage capacity of 3.22 wt.% H_2. Walker *et. al.*[193] found that the enthalpy of desorption with the addition of Ge was reduced by 60 kJ mol^{-1} H_2 to a value of ΔH = 14 kJ mol^{-1} H_2. The Mg-Ge-H system is investigated further herein by directly comparing changes in dehydrogenation properties with Si. In addition, the next group IV element, Sn, is also added to MgH_2 (Eqn. 6.5) to provide a comprehensive investigation of the kinetic difficulties that persist in these systems. The increase in molecular mass with the addition of Sn gives a stoichiometric reduction in hydrogen storage capacity of 2.36 wt.% H_2. Experimentally, the addition of Sn to MgH_2 has already proven to be an effective destabilising element for MgH_2[138, 194, 195] however, there has been no direct comparison made between Si, Ge and Sn with consistent preparation and characterisation techniques. Therefore, this study aims to destabilise MgH_2 desorption using these group IV elements using the same mixing process and desorption experimentation. Destabilisation of $NaMgH_3$ will also be investigated by the same processes by adding Si.

Eqn. 6.3 $$2MgH_2(s) + Si\ (s) \leftrightarrow Mg_2Si(s) + 2H_2(g)$$

Eqn. 6.4 $$2MgH_2(s) + Ge\ (s) \leftrightarrow Mg_2Ge(s) + 2H_2(g)$$

Eqn. 6.5 $$2MgH_2(s) + Sn\ (s) \leftrightarrow Mg_2Sn(s) + 2H_2(g)$$

Eqn. 6.6 $$2Na\,MgH_3 + Si \rightarrow Mg_2Si + 2\,NaH + 2H_2(g)$$

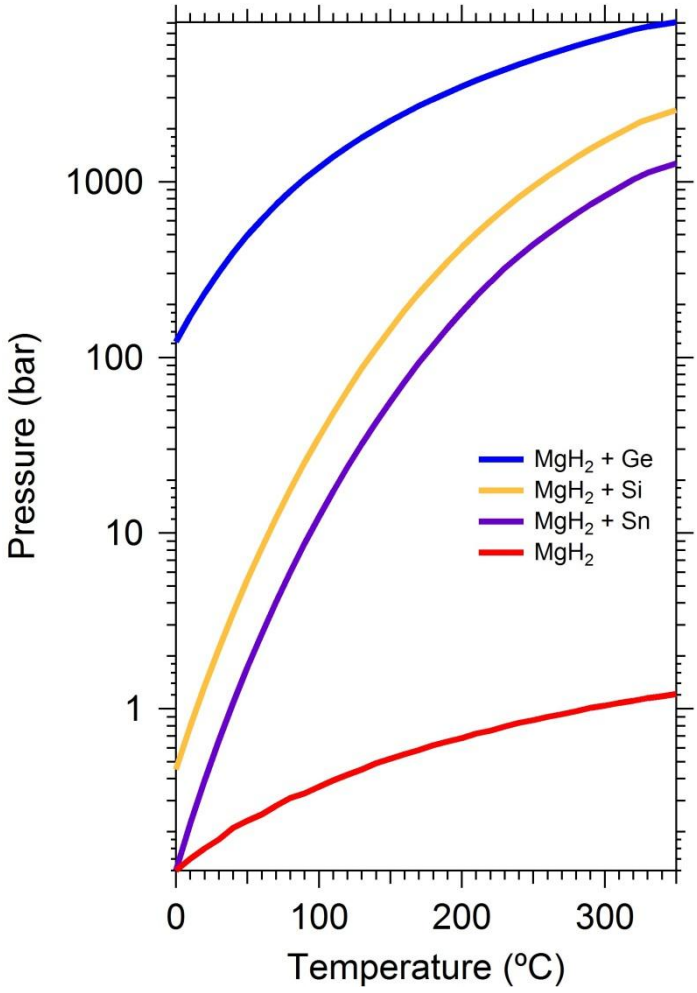

Figure 6.1: Calculated equilibrium pressures for MgH_2 pure and with Group IV elements (*HSC Chemistry* 6.12 software, Outotech Research).

6.2 Group IV (Si, Ge and Sn) Mixing

Prior to all desorption experiments, the materials as supplied by the manufacturer were characterised in terms of phases present and crystallite size. XRD and Rietveld refinement results show that the MgH_2 contained a 3.7 wt.% Mg phase (Figure 6.2

(A)) which would result in a lower than expected H wt.% desorption. The remainder of the material was MgH_2 with tetragonal, 136, P42/mnm structure and a crystallite size of 85 nm ± 0.9 (Table 6.1). The raw Si material had no detectable contaminates and was found to have a cubic, 227, Fd-3m structure and a large crystallite size of 211 nm ± 3 (Table 6.1, Figure 6.2 (B)). Ge (cubic, 227, Fd-3m, crystallite size 227 nm ± 3.5) also had a small percentage of contamination, GeO_2, 2.6 wt.% (Table 6.2), Figure 6.3 (A)). However, there was little evidence of this phase in subsequent analysis as Mg/MgH_2 will reduce GeO_2 to form Ge and MgO. Sn, like Si, had no detectable contamination and had a different crystallite structure to both Si and Ge (tetragonal, 141, I41/amd) with a much larger crystallite size of 547 nm ± 15. The synthesized $NaMgH_3$ (Orthorhombic, 62, Pnma, crystallite size 30 nm ± 0.3) had a similar oxidation occurrence to Sheppard *et. al.*[187] with MgO forming during the process (Table 6.3, Figure 6.4 (A)), however the majority of the material being the intended product, $NaMgH_3$ (76.3 wt.%). It should be noted that the grey plots at the bottom of each figure (Figure 6.2 - Figure 6.5) are an indication of the difference between the raw data collected on the XRD equipment and Rietveld refinement used to identify phases and calculate crystallite size of these phases. The R_{wp} values (Table 6.1 - Table 6.4), or weighted profile *R*-factor value, also gives an indication of the accuracy of the simulated model. This discrepancy index uses an algorithm to optimize the model function so that a minimum of the weighted sum of squares differences between the experimental and computed intensities is calculated[150]. As a general rule, R_{wp} values 5% or less indicates an acceptable goodness of fit[150], however, this value largely depends on an over estimation of uncertainties and should only be used as a guide[150].

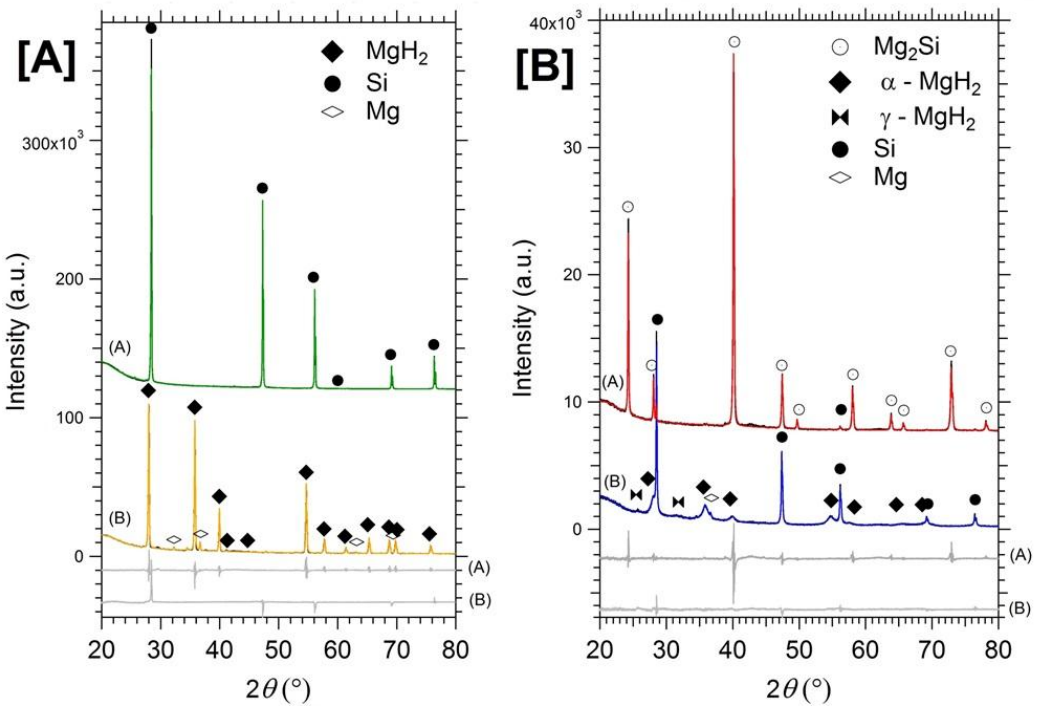

Figure 6.2: [A] XRD of materials as supplied from Sigma Aldrich (A) Si (B) β-MgH_2 [B] XRD of (A) Desorbed MgH_2 and Si producing Mg_2Si, 24 h in 50 - 350°C increments (B) β-MgH_2, γ- MgH_2 and Si cryomilled for 30 min.

Table 6.1: Pure MgH_2 and Si addition to MgH_2 crystallite size from Rietveld Refinement.

Sample	Phase	Structure	wt.%	Crystallite Size (nm)
[A] (B) MgH_2 R_{wp} = 8.1%	**β-MgH_2**	**Tetragonal, 136, P42/mnm**	**96.3**	**85.6 ± 0.9**
(as supplied)	**Mg**	**Hexagonal, 194, P63/mmc**	**3.7**	**93.2 ± 12.5**
[A] (A) Si R_{wp} = 7% (as supplied)	**Si**	**Cubic, 227,Fd-3m**	**100**	**211 ± 3.0**
[B] (B) $2MgH_2$ + Si R_{wp} = 4.8%	**β-MgH_2**	**Tetragonal, 136, P42/mnm**	**45.2**	**7.6 ± 0.1**
(cryomilled 30 min)	**γ-MgH_2**	**Orthorhombic, 60,Pbcn**	**21.6**	**2.4 ± 0.2**
	Mg	**Hexagonal, 194, P63/mmc**	**1.0**	**58 ± 13**
	Si	**Cubic, 227, Fd-3m**	**32.2**	**67.3 ± 0.3**
[B] (A) Mg_2Si R_{wp} =7.9 % (desorbed)	**Mg_2Si**	**Cubic, 225, Fm-3m**	**97.1**	**62.3 ± 0.5**
	Si	**Cubic, 227, Fd-3m**	**2.4**	**99.8 ± 13**
	MgO	**Cubic, 225, Fm-3m**	**0.5**	**2.3 ± 0.1**

After cryomilling each of the reactants in the correct stoichiometric ratios (Eqn. 6.3 - Eqn. 6.6), XRD was again used to identify the phases present as well as the new crystallite size. These results can be found in Figure 6.2 - Figure 6.5 and Table 6.1 - Table 6.4. From an initial crystallite size of 85 nm ± 0.9, the size of β-MgH_2 greatly reduced once cryomilled with Si, Ge and Sn giving sizes of 7.6 nm ± 0.1, 5.6 nm ± 0.2 and 7.0 nm ± 0.6 respectively and pure β-MgH_2 cryomilled under the same conditions gave a crystallite size of 6.3 nm ± 0.1. Each of the group IV elements also reduced in crystallite size but not to the same extent as MgH_2. It was interesting to observe that the cyromilling of MgH_2 with Si lead to the formation of γ-phase MgH_2, however, this phase was not evident with either Ge or Sn mixing. Orthorhombic 60, Pbcn γ-MgH_2 usually occurs when MgH_2 is subjected to high pressure within the GPa range[8]. One explanation for this phase to occur with Si addition is that Si has a higher hardness value (6.5 Mohs Scale) compared to Ge (6 Mohs Scale) and Sn (4 Mohs) and at 77 K the hardness increases the impact on the MgH_2 particles thus producing γ-MgH_2. Cryomilling $NaMgH_3$ with Si reduced crystallite size as expected without effecting the structure of either $NaMgH_3$ or Si. MgO remained constant in terms of wt.% and crystallite size throughout the course of cryomilling and hydrogen desorption (Table 6.4).

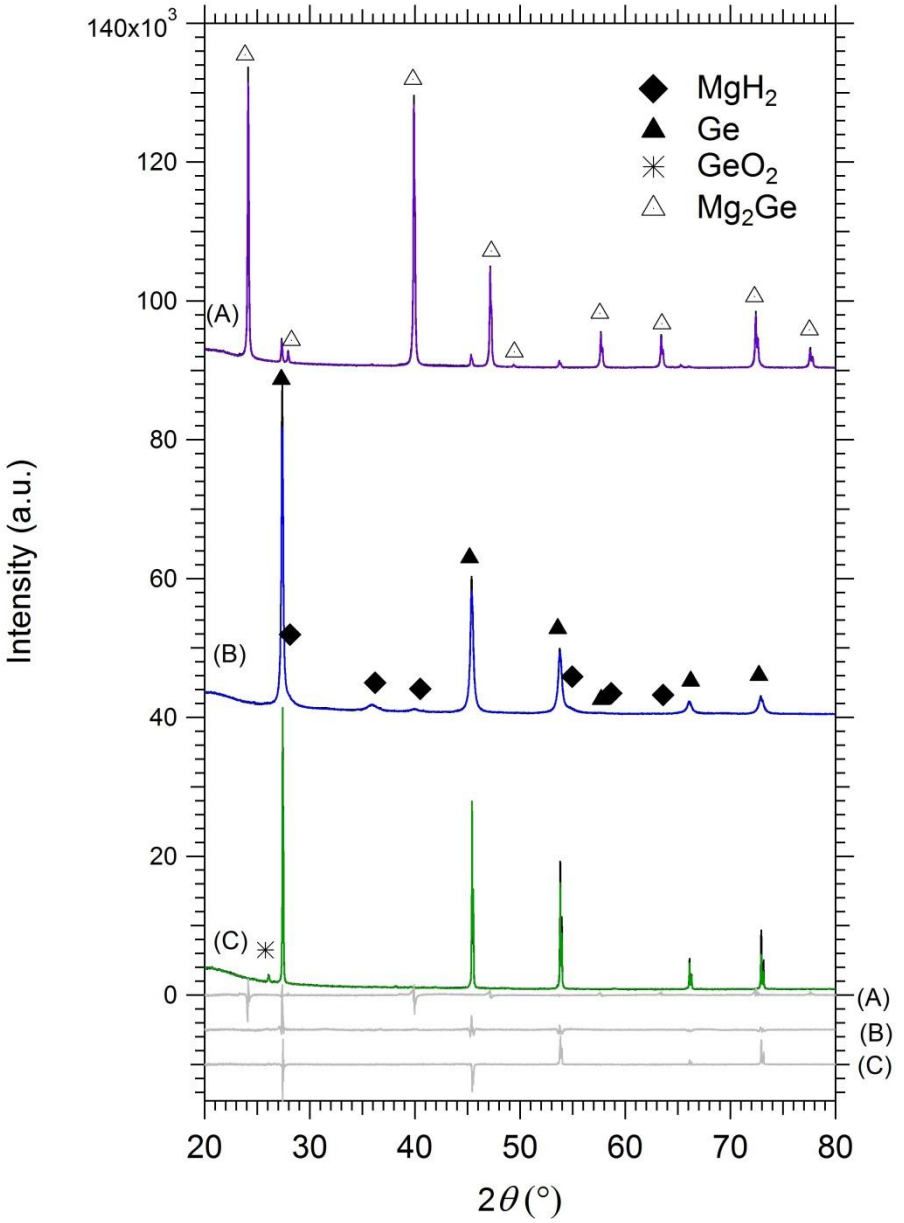

Figure 6.3: XRD patterns of Ge based experiments (A) MgH_2 and Ge desorbed to form Mg_2Ge, 24 h in 50 - 350°C increments (B) Cryomilled with MgH_2 for 30 min (C) Ge as supplied from Sigma-Aldrich.

Table 6.2: Ge addition to MgH_2, crystallite size from Rietveld Refinement.

Sample	Phase	Structure	wt.%	Crystallite Size (nm)
(A) Ge R_{wp} = 8.7%	Ge	Cubic, 227, Fd-3m	97.4	227 ± 3.5
(as supplied)	GeO_2	Trigonal, 152, P3121	2.6	58.2 ± 8.1
(B) $2MgH_2$ + Ge R_{wp} = 9%	β-MgH_2	Tetragonal, 136, P42/mnm	38.1	5.6 ± 0.2
(cryomilled 30 min)	Ge	Cubic, 227, Fd-3m	61.9	35 ± 0.6
(C) Mg_2Ge R_{wp} = 6.7%	Mg_2Ge	Cubic, 225, Fm-3m	95.9	73 ± 0.4
(desorbed)	Ge	Cubic, 227, Fd-3m	4.1	78 ± 3.4

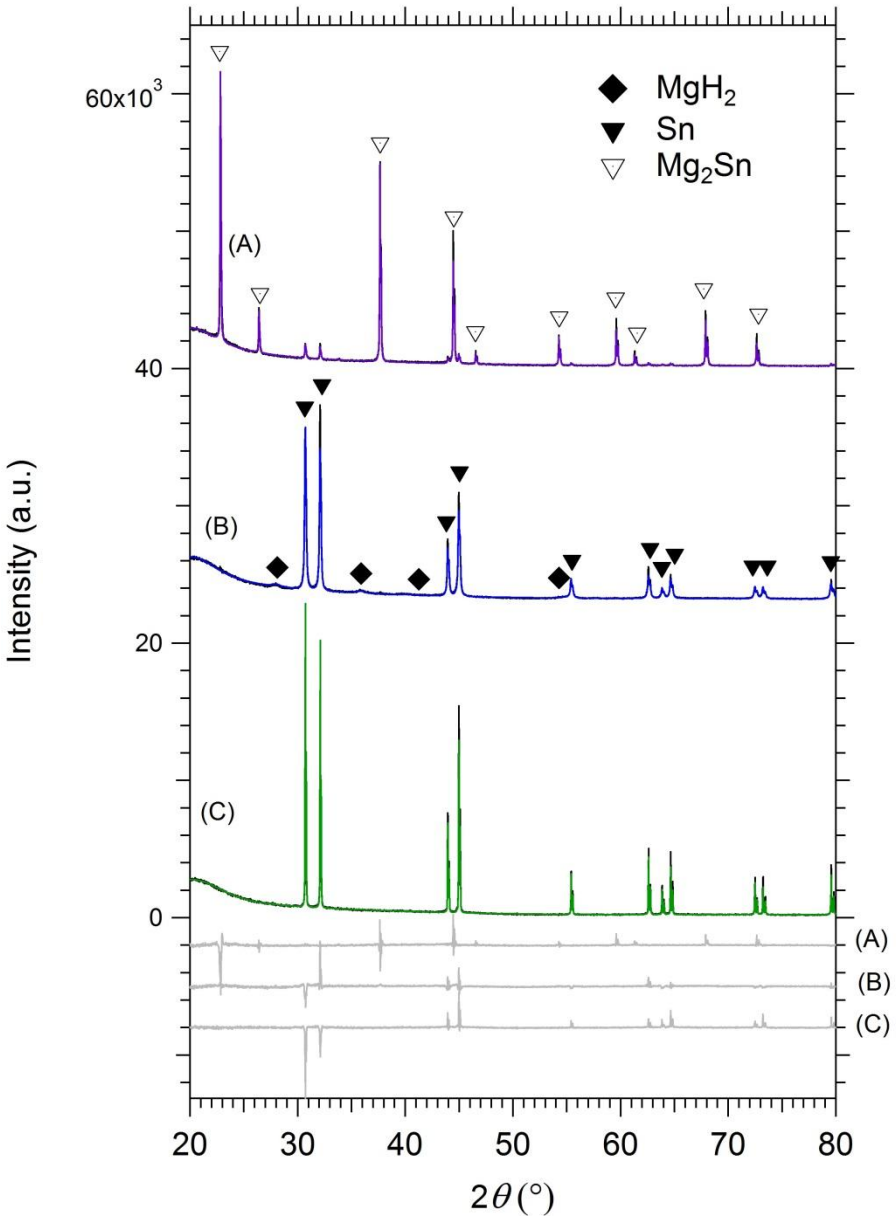

Figure 6.4: XRD patterns of Sn based experiments (A) MgH_2 and Sn desorbed to form Mg_2Sn, 24 h in 50 - 350°C increments (B) Cryomilled with MgH_2 for 30 min (C) Sn as supplied from Sigma-Aldrich.

Table 6.3: Sn addition to MgH_2, crystallite size from Rietveld Refinement.

Sample	Phase	Structure	wt.%	Crystallite Size (nm)
(A) Sn	**Sn**	**Tetragonal, 141, I41/amd**	**100**	**547 ± 16.0**
R_{wp} = 8.1%				
(B) $2MgH_2$ + Sn	**β-MgH2**	**Tetragonal, 136, P42/mnm**	**26.4**	**7.0 ± 0.6**
R_{wp} =6.2%				
(cryomilled 30 min)	**Sn**	**Tetragonal, 141, I41/amd**	**73.6**	**85 ± 3.0**
(C) Mg_2Sn	**Mg_2Sn**	**Cubic, 225, Fm-3m**	**93.6**	**147 ± 5.2**
R_{wp} = 7.8%				
(desorbed)	**Sn**	**Tetragonal, 141, I41/amd**	**6.4**	**94 ± 7.1**

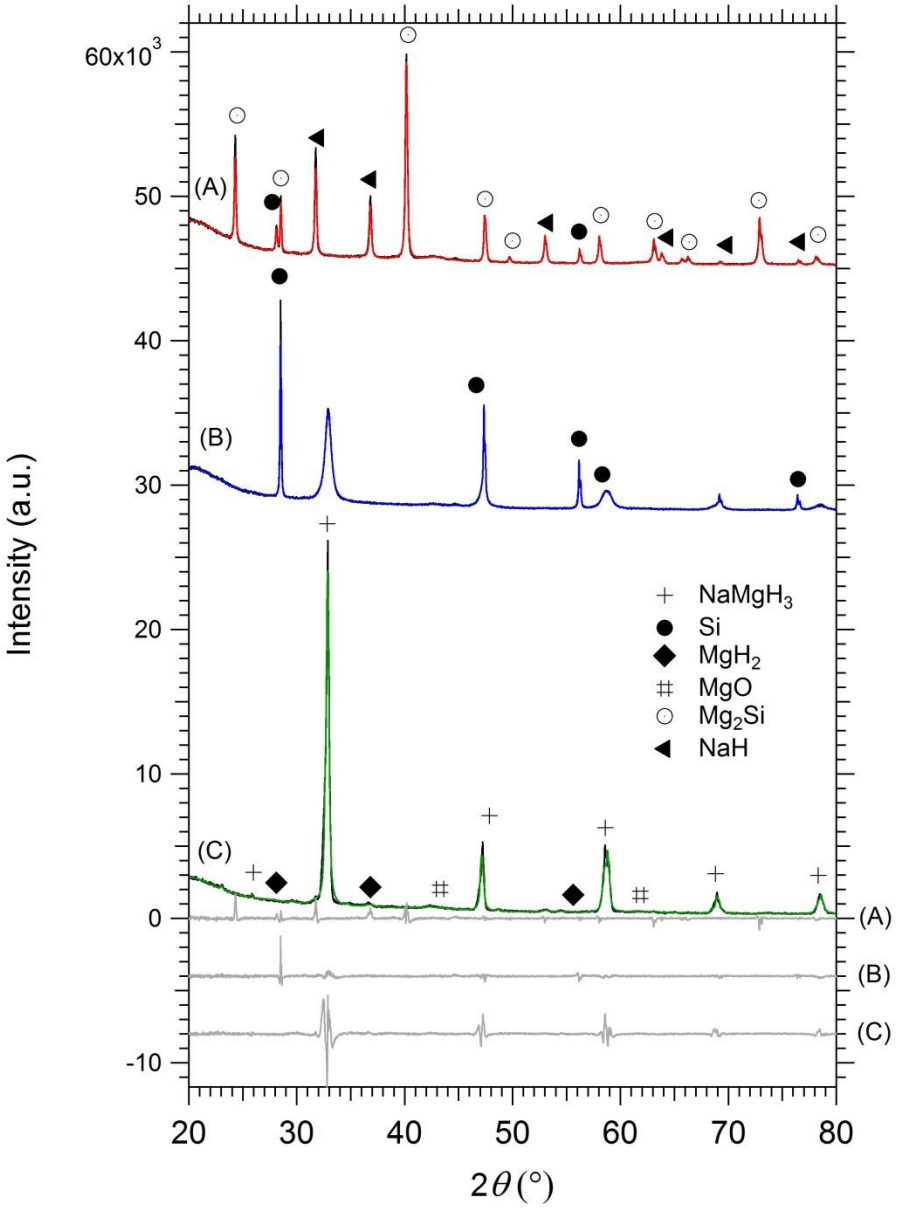

Figure 6.5: XRD patterns of $NaMgH_3$ based experiments (A) $NaMgH_3$ and Si desorbed to form Mg_2Si and NaH, 24 h in 50 - 350°C increments (B) Cryomilled with Si for 30 min (C) $NaMgH_3$ synthesised from MgH_2 and NaH.

Table 6.4: Si addition to $NaMgH_3$, crystallite size from Rietveld Refinement.

Sample	Phase	Structure	wt.%	Crystallite Size (nm)
(A) $NaMgH_3$ R_{wp} = 9.3% (synthesised from MgH_2 + NaH)	**$NaMgH_3$**	**Orthorhombic, 62, Pnma**	**76.3**	**30.7 ± 0.3**
	NaH	**Cubic, 225, Fm-3m**	**2.2**	**7.7 ± 1.4**
	MgH_2	**Tetragonal, 136, P42/mnm**	**3.7**	**2.5 ± 0.7**
	MgO	**Cubic, 225, Fm-3m**	**17.8**	**1.3 ± 0.1**
(B) $2NaMgH_3$ + Si R_{wp} = 4.5% (cryomilled 30 min)	**$NaMgH_3$**	**Orthorhombic, 62, Pnma**	**60.9**	**10.7 ± 0.1**
	Si	**Cubic, 227, Fd-3m**	**21.4**	**80.9 ± 0.9**
	MgO	**Cubic, 225, Fm-3m**	**17.7**	**1.4 ± 0.1**
(C) Mg_2Si, NaH R_{wp} = 6.2% (desorbed)	**Mg_2Si**	**Cubic, 225, Fm-3m**	**47.7**	**43.9 ± 0.4**
	NaH	**Cubic, 227, Fd-3m**	**27.4**	**40.2 ± 0.6**
	Si	**Cubic, 227, Fd-3m**	**7.7**	**76.4 ± 2.7**
	MgO	**Cubic, 225, Fm-3m**	**17.2**	**2.2 ± 0.1**

In order to gauge homogeneity of mixing and morphological information of the cryomilled powders, each sample containing MgH_2 and group IV elements was analysed with the SEM. Backscattered electron (BSE) images of these samples are shown in Figure 6.6 (A), (B) and (C). The BSE technique allowed electrons to interact with the specimens in such a way that the lighter regions show elements of heavier atomic mass. All samples were viewed under similar conditions (magnification, spot size, electron voltage and working distance) to easily compare differences or similarities. Figure 6.6 (A) shows that there is little difference in shade variation as MgH_2 and Si have similar atomic mass. However, the slightly lighter shade can be attributed to Si particles. Si particles appear to be slightly larger in size to MgH_2. As the atomic mass increases, the difference between MgH_2 and Ge (Figure 6.6 (B)) and Sn (Figure 6.6 (C)) are more apparent. The micrographs show that each of the phases is well dispersed after mixing with the cryomill. Similar to Si, Ge and Sn particle size correlates well with crystallite size in that they are larger than MgH_2. All the micrographs of the cryomilled materials show a large spread for particle size distribution ranging from 100 nm through to a few microns. This result is similar to another publication that mixed MgH_2 with Ge *via* ball milling. The

authors also found a large particle size distribution ranging from 10 μm particles in the sub-micron range[193].

During the course of capturing the SEM images, Energy Dispersive X-ray Spectroscopy (EDS) was done in order to map the group IV element location with that of MgH_2. It was found that there was there was little difference between each elemental map; therefore, it was not easy to distinguish where each phase was located. In order to determine why BSE images gave distinct phases (according to atomic weight) and EDS gave no distinction, accelerating voltage was adjusted and BSE images taken (Figure 6.7). The results showed that as the interaction volume increased the distinction between the phases became less obvious. This implies that the mixes were more homogeneous than first assumed; therefore the reaction should proceed easily.

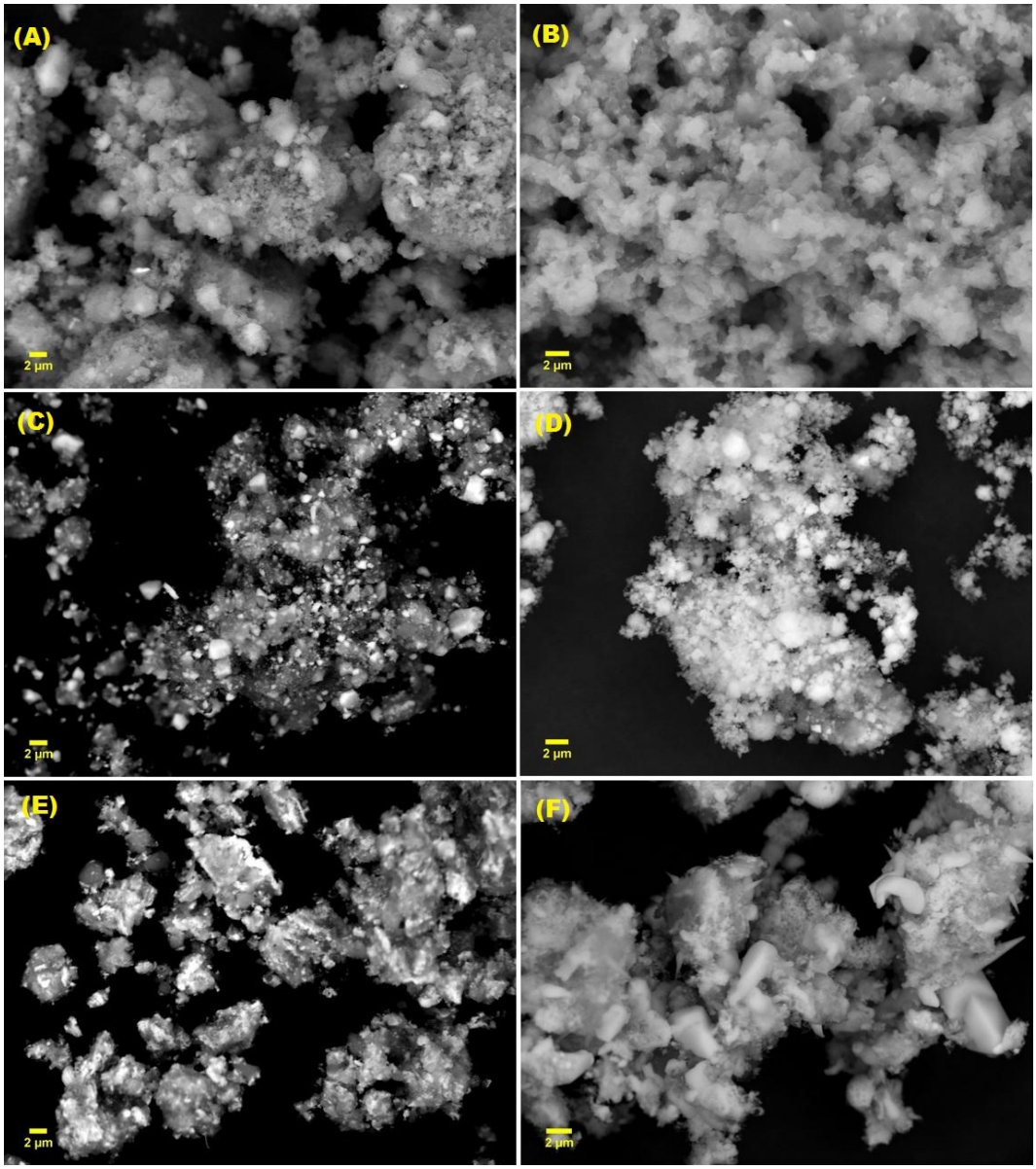

Figure 6.6: SEM BSE images (accelerating voltage 20 kV) of (A) $2MgH_2$+Si (B) $2MgH_2$+Ge (C) $2MgH_2$+Sn (D) Mg_2Si (E) Mg_2Ge (F)Mg_2Sn.

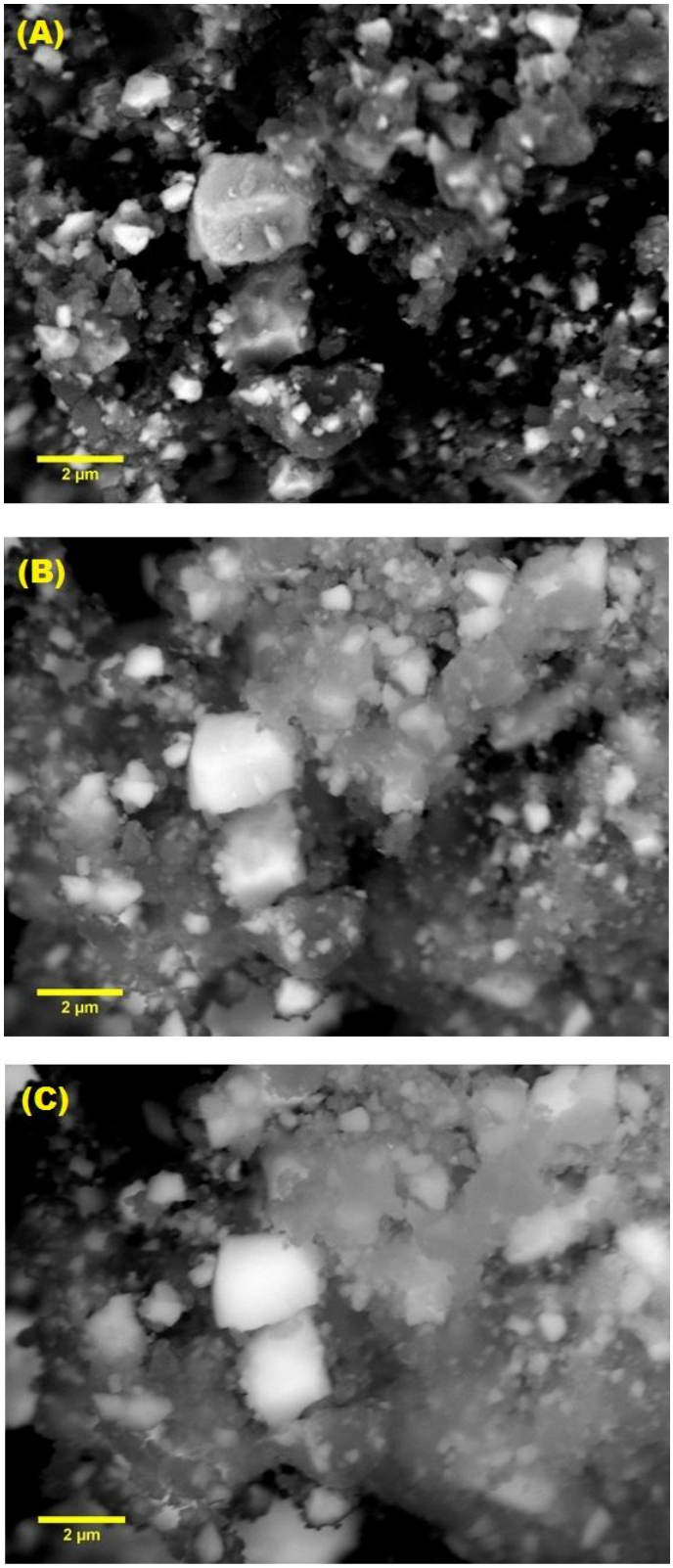

Figure 6.7: SEM images of MgH_2 + Ge with different accelerating voltages (A) 10 kV (B) 20 kV (C) 30 kV.

6.3 Group IV Absorption and Analysis

MgH_2 and $NaMgH_3$ desorption behaviour was observed using manometric Sieverts apparatus (Figure 6.8) and temperature programmed desorption (TPD) (Figure 6.9) once the group IV elements were added. Initially, samples were analysed using a manometric Sieverts apparatus where the sample cell was placed in a furnace and isothermal measurements taken over time. Each sample was held for 24 h at 50°C increments through to a maximum temperature of 350°C. If there was no desorption detected after 2 h at 350°C, the run was stopped. All of the mixtures showed little or no hydrogen desorption at the lower temperatures of 50°C and 100°C.

MgH_2 with Ge was the first mixture to begin hydrogen release at 150°C; although this step was kinetically slow, as indicated by the shallow incline at 150°C in Figure 6.8 (B). The majority of this mixture desorbed at higher temperatures (200°C - 250°C) and faster reaction rates (steeper inclines Figure 6.8 (B)) until it completely desorbed over the 300°C time period. XRD from the completed reaction is given in Figure 6.3 (C) and shows 96% face centred cubic (FCC) structure Mg_2Ge. No evidence of MgH_2 peaks could be detected using XRD, however, traces of Ge still remained. The final wt.% calculated from the Sieverts desorption resulted in a 2.91 wt.%, slightly lower than the value calculated from constituent composition of 3.22 wt.%. The marginally lower experimental value is attributed to both Ge and MgH_2 containing small amounts of Mg and GeO_2, as indicated by the XRD prior to desorption (Figure 6.2 (A), Figure 6.3 (A)). MgH_2 has a purity of ~ 95% therefore all desorption reactions would not reach theoretical desorption values due to the presence of impurities. The BSE image from SEM (Figure 6.6 (E)) after desorption has taken place also shows homogeneous morphology of smaller particles when compared to pre-desorption images. Also, there is no significant difference in light and dark shades indicating that full conversion has almost taken place as differences in the atomic mass are not observed.

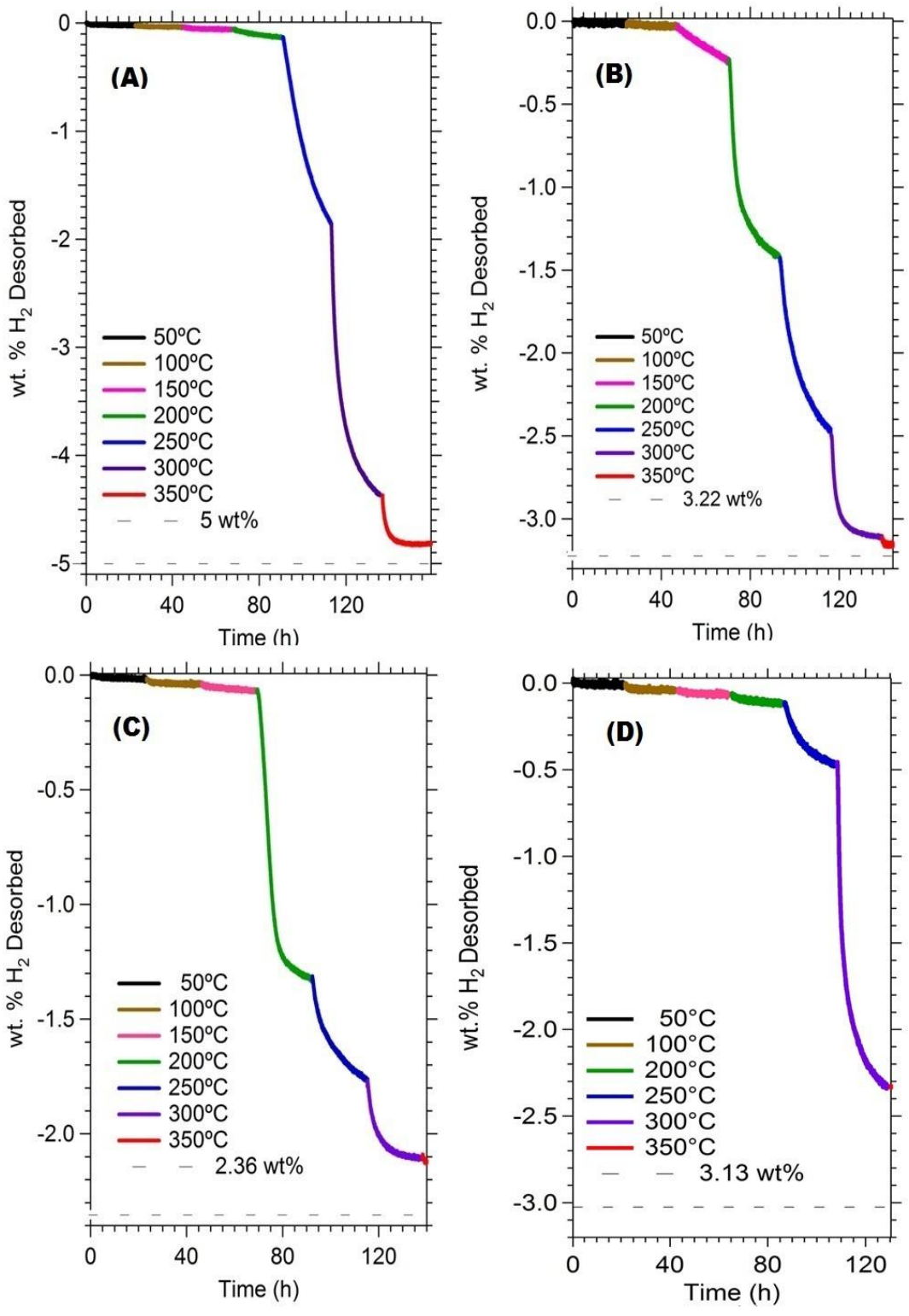

Figure 6.8: Time and temperature relationship with wt.% of H_2 desorbed from (A)2 MgH_2 + Si (B) 2MgH_2 + Ge (C) 2MgH_2 + Sn (D) 2$NaMgH_3$ + Si.

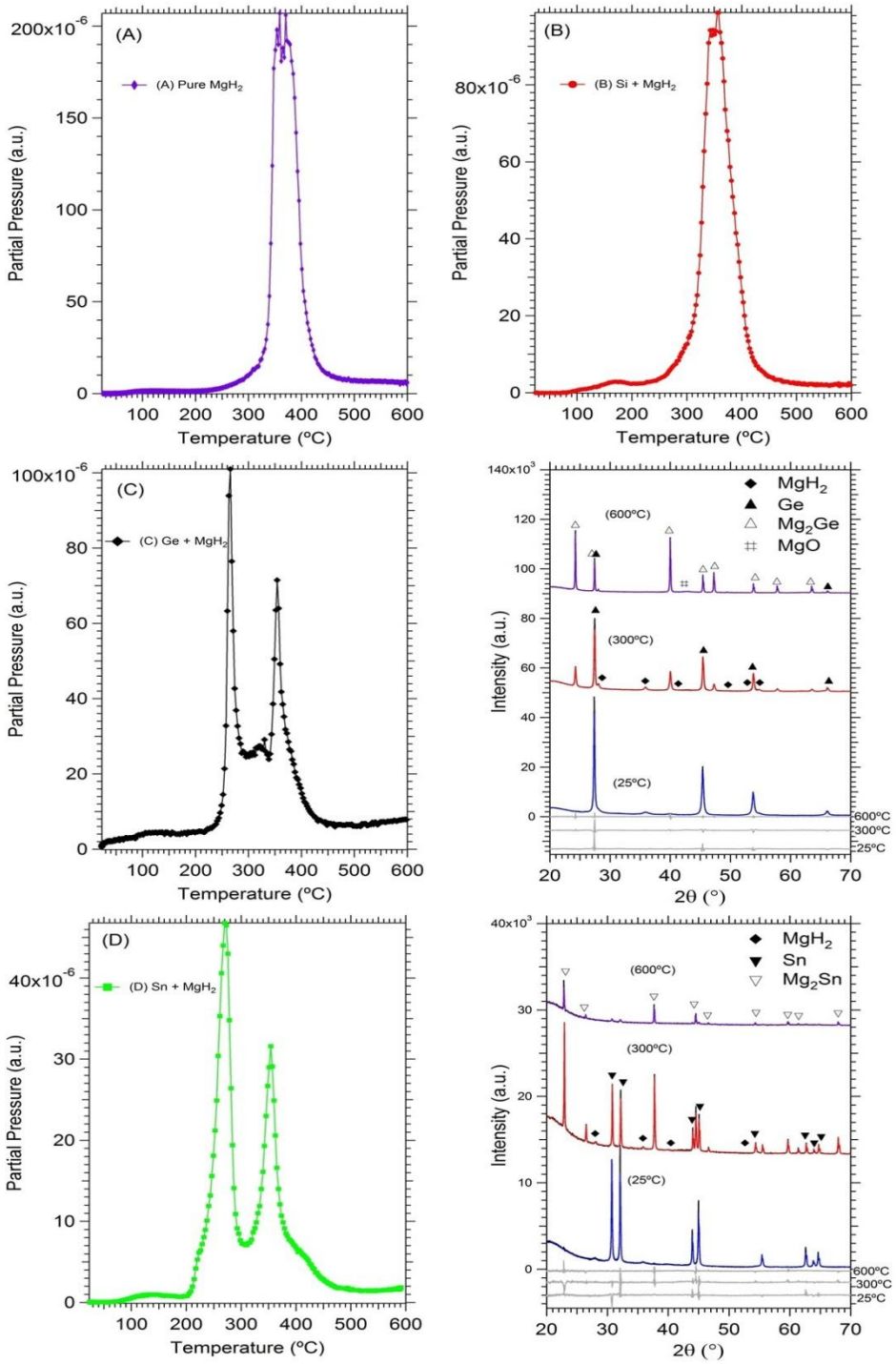

Figure 6.9: Mass spectra of desorbed gases from: (A) Pure MgH_2 (B) $2MgH_2$ + Si (C) $2MgH_2$ + Ge with Si XRD taken at 25°C, 300°C and 600°C (D) $2MgH_2$ + Sn with XRD taken at 25°C, 300°C and 600°C.

The MgH_2 and Ge mixture desorption process also began at a lower temperature of 260°C compared to all other materials in the (TPD) results (Figure 6.9 (B)). An

unexpected result from the TPD containing Ge was the second desorption peak occurring at 350°C. To understand this phenomenon, a second experiment was done and the TPD halted at 300°C (after the first peak was fully resolved) and the sample cell placed in liquid nitrogen to prevent any further reaction. The resultant XRD is shown in the inset of Figure 6.9 (C). All peaks indicated partial conversion of MgH_2 and Ge to Mg_2Ge. Since there were no unknown phases other than MgH_2, Ge and Mg_2Ge, that is, no intermetallic phase present such as MgGe, the second desorption peak can be explained by the wide range in particle size. The particles must be significantly different enough such that diffusion of Mg and Ge occurs in two stages, one temperature (260°C) for the smaller particle range, approximately 100 nm or below, and a higher temperature of 350°C for the larger (micron sized) particles. This is in contradiction with Walker *et. al.*[193] who attributed a single peak found in DSC measurements to be the thermodynamic event of MgH_2 dehydrogenation despite a large variation in particle size.

Sn with MgH_2 began desorption at 200°C as detected using the Sieverts apparatus. The steep incline at this temperature in Figure 6.8 (C) indicates faster reaction kinetics however, full desorption did not occur after 24 h. Once the temperature increased to 250°C and then 300°C the rate of reaction slowed and by 350°C was fully desorbed. Figure 6.4 (C) shows the resultant XRD after desorption with a conversion of 93.6 wt.% FCC structure Mg_2Sn. Again the Sieverts measurements gave a slightly lower conversion of 2.15% when compared to the theoretical storage capacity of 2.36 wt.%. SEM results give an interesting change in morphology of the reacted Mg_2Sn that was not seen in any other sample (Figure 6.6 (F)). Although largely homogenous in atomic mass (no differences in light and dark shades), well defined obelisk shaped particles of various sizes were detected. This is in contrast to Mg_2Sn morphology synthesised during reactive ball milling which is more spherical in structure[196]. Similar to the reaction containing Ge, Sn with MgH_2 also resulted in a double peak during the TPD experiment due to the wide particle size distribution. The initial peak occurred at 270°C with the second at 360°C as shown in Figure 6.9 (D). A double desorption peak was also displayed during a TPD experiment[194] with balled milled MgH_2 and Sn with the addition of cyclohexane. This different

preparation technique of ball milling with cyclohexane reduced the temperature of the peaks to 217°C and 257°C[194]. The authors of this study[194] concluded that the formation of the two desorption thermodynamic events was due to the existence of two types of hydrogen species in the Sn/MgH_2 composite, however, our XRD results contradict this statement. Similar to the Ge sample, the experiment was repeated and stopped at 300°C and the XRD (Figure 6.9 (C)) showed no unexpected phases. Therefore, the double peak can be attributed to variation in particle size resulting in different diffusion rates for Mg and Sn to form Mg_2Sn.

Both Ge and Sn samples mixed with MgH_2 appeared to have less kinetic limitations than Si with MgH_2. As indicated in Figure 6.8 (A) desorption of this mixture began at 250°C and as expected, an increase in temperature lead to an increase in reaction kinetics although the sample was not fully desorbed until 350°C. These results are in agreement with Paskevicius *et. al.*[72] where MgH_2 ball milled with Si for 24 h desorbed in the range of 250°C and 350°C. XRD post reaction resulted in the presence of FCC structured Mg_2Si with 97.1 wt.% (Figure 6.2 II (B)). Again the theoretical value of 5 wt.% was not reached due to the impurity of Mg detected in the MgH_2. Sieverts apparatus desorption obtained a final H_2 release of 4.81 wt.%, 96% of the theoretical value. This experimental value was also in agreement with Paskevicius *et. al.*[72] where 4.56 wt.% of hydrogen was released for the same reaction when taking impurities in the starting reagents into account. BSE SEM on the sample after Sieverts apparatus desorption Figure 6.6 (D) correlates with near full conversion of the desorption reaction showing a homogenous mixture in terms of atomic weight (no variation in light and dark shades) as well as particle size (average size less than 1 μm).The desorption temperature during TPD measurements was also higher for Si than either Ge or Sn, where desorption occurred as a single event at a maximum temperature of 350°C. This value was marginally lower than MgH_2 that had been cryomilled under the same conditions (desorption temperature of 370°C) again reinstating the fact that this reaction is kinetically limited despite the thermodynamic destabilisation effect of Si addition. The single peak due to Mg diffusion into the Si matrix occurs in one transition implying that the particle size distribution was narrower. Another study that involved TPD also gave single peak

desorption however, at a lower temperature (290°C), as a different heating rate was used and the sample was under helium atmosphere, not under vacuum[188]. The TPD data correlated well with the Sieverts desorption kinetic data as they both showed slow H_2 release at lower temperatures with increased rate when temperatures were increased. Since the Sieverts experiment was not possible with pure MgH_2 due to it reaching equilibrium and possibly reabsorbing H_2 above 1 bar of pressure at temperatures higher than 282°C then TPD was the only method where a comparison could be made between pure MgH_2 behaviour with the other mixtures. An important point to note for the group IV element samples added to MgH_2 was that all desorption temperatures were lower than pure MgH_2 (365°C).

Si addition to $NaMgH_3$ Sieverts apparatus desorption results are shown in Figure 6.8 (D). Initially, desorption occurred at a consistently slow rate until 250°C, where the rate increased. The majority of desorption however, occurred at 300°C, 80°C lower than pure $NaMgH_3$[187]. Similar, to the previous mixtures, a lower experimental value was reached for hydrogen desorption, 2.34 wt.%, compared to the first stage desorption (Figure 6.8) theoretical value of 3.13 wt.%. This larger discrepancy was due to the inherent formation of MgO during the synthesis process which remained constant at approximately 17 wt.% (Table 6.4). TPD results gave the appearance of overlapping peaks occurring at maximum temperatures of 320°C and 340°C. As with Ge and Sn addition to MgH_2 this could be the result of differing particle sizes.

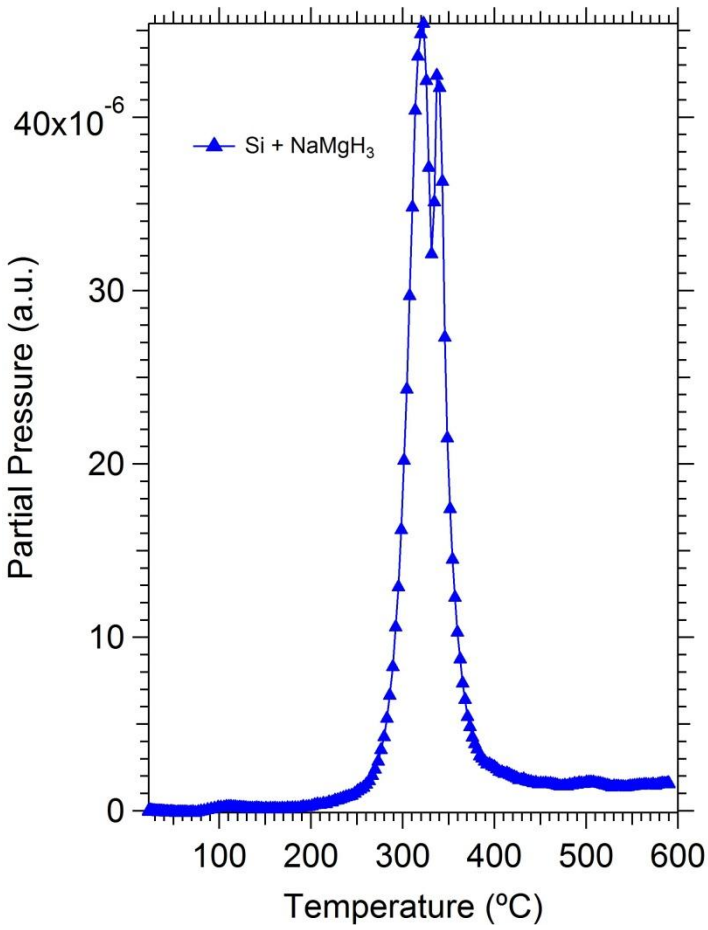

Figure 6.10: Mass spectra of desorbed gases from $2NaMgH_3$ + Si.

6.4 Conclusion

Each of the Group IV elements added to either MgH_2 or $NaMgH_3$ successfully destabilized desorption thermodynamics, however, reaction kinetics plays a larger role in the reaction. This conclusion has been made as none of the materials were able to reach theoretical thermodynamic equilibrium values (Figure 6.1) during the experiments. XRD showed that crystallites size for MgH_2 for each of the mixtures were similar, however, crystallite sizes for Si, Ge and Sn varied greatly. On the other hand, the SEM showed that particle size was relatively similar for each of the mixtures. SEM also showed that heterogeneous particle sizes of the reactants become

smaller and more uniform in size once Mg_2Si, Mg_2Ge and Mg_2Sn are formed after dehydrogenation. Therefore, dependency on crystallite size for MgH_2 was not considered significant enough to affect kinetic behaviour. It appears that the system that contained Ge and MgH_2 had the fastest reaction kinetics since it started desorption at the lowest temperature of 150°C. Sn also had a significant effect on MgH_2 with desorption occurring at 200°C. Si, with comparison to the other group IV elements, had a lesser effect on MgH_2 with desorption initiated at 250°C. This study also provided information on the influence of Si on the $NaMgH_3$ compound. Reduction in desorption temperatures for all materials was observed, however, kinetic limitations ensured that thermodynamic equilibrium conditions were never achieved. This indicates that kinetics have a greater role to play in each of the systems studied. Since differences in particle size were considered significant, the difference in kinetics is most likely due to different order of reaction for nucleation and possibly growth due to these differences. Reaction kinetics play a big role in these systems and it is recommended that further analysis be done on parameters such as activation energy, reaction order values for both nucleation and growth mechanisms.

Chapter 7: Conclusions and Future Work

"If we assume we've arrived: we stop searching, we stop developing."

Jocelyn Bell Burnell (1943 – Present, Northern Ireland)

This is the final chapter of this Ph.D. thesis. Here is an overall summary of the hypotheses, experimentation and conclusions presented in each of the previous chapters. Included here is also a section on future work that could be done to further enhance the scientific knowledge gained from this research.

7.1 Conclusions

Worldwide energy demand has led the scientific community into alternative energy research including the use of renewable energy combined with hydrogen storage systems. This type of system includes electrolysis *via* renewable sources to produce hydrogen from water, then storing the hydrogen in an appropriate medium. This would ensure energy on demand rather than depend on the availability of the renewable source. The hydrogen storage system would then be linked with a compatible fuel cell to convert the hydrogen into clean energy.

This thesis has focused on hydrogen storage solutions through an investigation into magnesium hydride based materials. Magnesium is an attractive medium to store hydrogen; however, there are some key areas that do not meet the requirements for a practical system, thermodynamic stability and reaction kinetic issues. Combining magnesium with group IV elements such as Si, Ge and Sn have been shown to reduce the thermodynamic stability to some extent. Therefore, experimentation was undertaken using each of these elements with either MgH_2 or $NaMgH_3$.

The first issue addressed was the kinetic reaction limitations in the MgH_2 + Si desorption reaction. The objective of this chapter was to produce nanoparticles to reduce diffusion distances between MgH_2 and Si and in turn encourage fast reaction rates during hydrogen release. Si nanoparticles were synthesised (Chapter 3) using mechanochemical ball milling methods. These Si nanoparticles were difficult to characterise due to the amorphicity of the particles during the ball milling process. Specialist experimental techniques such as EELS and EFTEM in combination with XRD were used to identify the Si phase present in the products from the synthesis reaction. SAXS analysis showed that these particles had an average size of 13 nm.

These particles were used to compare crystallite size with the small particles size with respect to reaction rates (Chapter 4). Kinetic modelling showed that the MgH_2 + Si desorption reaction was limited by 3Dimensional diffusion according to the Carter-Valensi model. This implies that nucleation of Mg_2Si was relatively quick and diffusion of Mg through the metallic matrix, during the growth of Mg_2Si, controlled the reaction rate. The kinetic parameters nucleation activation energy, E_n, growth activation energy, E_a, the rate constant, k, and the pre-exponential factor, A were calculated from experimental data. The Kissinger method was used to calculate the activation energies and it was found that E_a strongly correlates with crystallite size of the reactants but no such trend was evident for E_n. Oxygen contamination was found to be a hindering factor for complete H_2 desorption and this issue would need to be addressed in future experimentation. It was therefore difficult to conclude whether the nanoparticles made a significant difference to desorption kinetics due to the high level of O_2 contamination.

The next section of work (Chapter 5) investigated the absorption process. Again, similar to Chapter 3, the objective was to reduce reactant diffusion distances. This time the focus was on the prospect of improving reaction kinetic limitations and hydriding Mg_2Si. Therefore, Mg_2Si nanoparticles were synthesised using the same mechanochemical method as the Si nanoparticles. The nanoparticles had an average particle size of 13 nm and were subjected to high pressure conditions (abover 1 kbar, 200°C) significantly greater than thermodynamic equilibrium to attempt absorption. Initial attempts were found to be unsuccessful due to the presence of THF on the surface of the particles. Once this was removed, partial hydrogenation was achieved. This indicates that nanoparticles can possibly overcome kinetic barriers however, as the reaction did not go to completion, this kinetic limitation continues to hinder the reaction.

The final chapter in this thesis focussed on incorporating other group IV elements into Mg based systems, MgH_2 and $NaMgH_3$ to destabilise the respective desorption reactions. Theoretically, Si, Ge and Sn addition will reduce thermodynamic stability, however, once again reaction kinetic limitations showed that the equilibrium conditions were difficult to obtain. A direct comparison was made between the three

group IV elements and systematically analysed to give a complete set of data. It was found that Ge addition allowed desorption to start at 150°C, Sn at 200°C and Si 250°C, all of which are lower temperatures than that of pure MgH_2. This indicates that when prepared under the same conditions all materials destabilised MgH_2, but kinetics played a more significant role to the extent that thermodynamic equilibrium was not achieved.

7.2 Recommendations for Future Work

To further the work presented here in this thesis, several recommendations for future experimentation and analysis can be made.

1. The high affinity of Mg to O_2 was found to be one of the major hurdles in this project. To overcome this issue the solvent used to wash the nanoparticles from the LiCl should be changed for an alternative that does not contain any oxygen. Different separation techniques should also be explored.
2. In order to accurately determine the relationship between crystallite/particle size and activation energy, more samples of different sizes should undergo the same experimental procedure given in Chapter 4.
3. Confirmation as to whether or not the Mg_2Si nanoparticles absorbed hydrogen at high pressures and temperatures is also recommended. Firstly, to show that the mechanochemical ball milling reaction went to completion, differential thermal analysis (DTA) or differential scanning calorimetry (DSC) up to a temperature of 600°C. If a thermal transition is not detected during a constant temperature ramp, this would suggest that the reaction was completed during milling[181].
4. Also, systematic testing of the Mg_2Si synthesis reaction is recommended. This would involve synthesising Mg_2Si, where the final volume fraction of buffer is always 15:1 and concentrations of the starting reagents varied. The aim would be to find the upper limit for which Mg can be in the sample but not detectable by XRD. One way to do this would be to keep the $SiCl_4$ concentration constant and incrementally increase Li and $MgCl_2$

concentrations to produce excess Mg. After each increment XRD would be performed until the point where Mg is detectable by XRD.

References

Every reasonable statement has been made to acknowledge the owners of copyright material. I would be pleased to hear from any copyright owner who has been omitted or incorrectly acknowledged.

1. Abrams, D. M.; Wiener, R. J., A model of peak production in oil fields. *Am J Phys* **2010,** *78* (1), 24 – 27.
2. Arent, D. J.; Wise, A.; Gelman, R., The status and prospects of renewable energy for combating global warming. *Energ Econ* **2011,** *33* (4), 584 – 593.
3. Kelly, N. A.; Gibson, T. L.; Cai, M.; Spearot, J. A.; Ouwerkerk, D. B., Development of a renewable hydrogen economy: Optimization of existing technologies. *International Journal of Hydrogen Energy* **2010,** *35* (3), 892 – 899.
4. Department Of Energy, USA *Targets for OnBoard Hydrogen Storage Systems for Light-Duty Vehicles*; Office of Energy Efficiency and Renewable Energy and The FreedomCAR and Fuel Partnership: 2009.
5. Hirscher, M., *Handbook of Hydrogen Storage: New Materials for Future Energy Storage*. Wiley-VCH: Weinheim, 2010.
6. Rand, D. A. J., Dell, R. M. , *Hydrogen energy : challenges and prospects*. Cambridge : Royal Society of Chemistry: Cambridge, 2008.
7. Paskevicius, M.; Sheppard, D. A.; Buckley, C. E., Thermodynamic changes in mechanochemically synthesized magnesium hydride nanoparticles. *Journal of the American Chemical Society* **2010,** *132* (14), 5077 – 83.
8. Manchester, F. D. a. S.-M., A., *Phase diagrams of binary hydrogen alloys*. ASM International: Materials Park, OH, **2000**.
9. Cuevas-Cubria, C., Schultz, Andrew., Petchey, Rebecca., Maliyasena, Apsara., Sandu, Suwin. *Energy in Australia 2010*; Commonweath of Australia: Canberra, 2010.
10. *World Energy Outlook*. International Energy Agency: Paris, 2009.
11. Rockstrom, J.; Steffen, W.; Noone, K.; Persson, A.; Chapin, F. S.; Lambin, E. F.; Lenton, T. M.; Scheffer, M.; Folke, C.; Schellnhuber, H. J.; Nykvist, B.; de Wit, C. A.; Hughes, T.; van der Leeuw, S.; Rodhe, H.;

Sorlin, S.; Snyder, P. K.; Costanza, R.; Svedin, U.; Falkenmark, M.; Karlberg, L.; Corell, R. W.; Fabry, V. J.; Hansen, J.; Walker, B.; Liverman, D.; Richardson, K.; Crutzen, P.; Foley, J. A., A safe operating space for humanity. *Nature* **2009,** *461* (7263), 472 – 475.
12. Accredited Renewable Sites. In *http://www.ga.gov.au/map/orer/*, Office of the Renewable Energy Regulator: Canberra, 2011.
13. Mountain, B. *Electricity Prices in Australia: An International Comparison*; Carbon + Energy Markets: Melbourne, 2012.
14. Hepworth, A., Maher, Sid., Energy prices 'to keep rising'. *The Australian* 2012.
15. Hardman, C., C., Folser, George, R.,, Energy efficient electrolyzer for the production of hydrogen. *International Journal of Hydrogen Energy* **1983,** *8* (4), 310 – 310.
16. Lehman, P. A.; Chamberlin, C. E., Design of a photovoltaic-hydrogen-fuel cell energy system. *International Journal of Hydrogen Energy* **1991,** *16* (5), 349 – 352.
17. Crockett, R. G. M.; Newborough, M.; Highgate, D. J.; Probert, S. D., Electrolyser-based electricity management. *Applied Energy* **1995,** *51* (3), 249 – 263.
18. Vanhanen, J. P.; Lund, P. D.; Tolonen, J. S., Electrolyser-metal hydride-fuel cell system for seasonal energy storage. *International Journal of Hydrogen Energy* **1998,** *23* (4), 267 – 271.
19. Santarelli, M.; Calì, M.; Macagno, S., Design and analysis of stand-alone hydrogen energy systems with different renewable sources. *International Journal of Hydrogen Energy* **2004,** *29* (15), 1571 – 1586.
20. Zoulias, E. I.; Lymberopoulos, N., Techno-economic analysis of the integration of hydrogen energy technologies in renewable energy-based stand-alone power systems. *Renewable Energy* **2007,** *32* (4), 680 – 696.
21. Bilgen, E., Domestic hydrogen production using renewable energy. *Sol Energy* **2004,** *77* (1), 47 – 55.
22. Turner, J.; Sverdrup, G.; Mann, M. K.; Maness, P.-C.; Kroposki, B.; Ghirardi, M.; Evans, R. J.; Blake, D., Renewable hydrogen production. *International journal of energy research* **2008,** *32* (5), 379 – 407.
23. Zuttel, A., Materials for hydrogen storage. *Materials Today* **2003,** *6* (9), 24 – 33.

24. Ram, G.; Pant, K., Hydrogen Storage in Metal Hydrides. In *Hydrogen Fuel*, CRC Press: 2008; pp 381 – 407.
25. Ram, G.; Pant, K., Hydrogen Storage in Carbon Materials. In *Hydrogen Fuel*, CRC Press: 2008; pp 409 – 436.
26. Corbo, P.; Migliardini, F.; Veneri, O., Experimental analysis and management issues of a hydrogen fuel cell system for stationary and mobile application. *Energy Conversion and Management* **2007,** *48* (8), 2365 – 2374.
27. Kothari, R.; Buddhi, D.; Sawhney, R. L., Comparison of environmental and economic aspects of various hydrogen production methods. *Renewable and Sustainable Energy Reviews* **2008,** *12* (2), 553 – 563.
28. Srinivasan, S., *Fuel Cells: From Fundamentals to Applications*. Springer: 2006.
29. Levene, J. I.; Mann, M. K.; Margolis, R. M.; Milbrandt, A., An analysis of hydrogen production from renewable electricity sources. *Sol Energy* **2007,** *81* (6), 773 – 780.
30. Akyuz, E.; Coskun, C.; Oktay, Z.; Dincer, I., Hydrogen production probability distributions for a PV-electrolyser system. *International Journal of Hydrogen Energy* **2011,** *36* (17), 11292 – 11299.
31. Verbruggen, A.; Fischedick, M.; Moomaw, W.; Weir, T.; Nadaï, A.; Nilsson, L. J.; Nyboer, J.; Sathaye, J., Renewable energy costs, potentials, barriers: Conceptual issues. *Energy Policy* **2010,** *38* (2), 850 – 861.
32. DOE US Department of Energy. http://www.doe.gov (accessed 05/02/08).
33. Cellex-powered forklifts complete Wal-Mart trials. *Fuel Cells Bulletin* **2007,** (3), 10.
34. Hydrogenics, LiftOne link to deploy forklifts. *Fuel Cells Bulletin* **2007,** (3), 5.
35. Praxair, Powertech ally on hydrogen fueling for fuel cell forklifts. *Fuel Cells Bulletin* **2010,** (5), 8.
36. Fuel cell forklifts for Walmart Canada distribution center. *Fuel Cells Bulletin* **2010,** (3), 3 – 4.
37. McConnell, V. P., Fuel cells in forklifts extend commercial reach. *Fuel Cells Bulletin* **2010,** (9), 12 – 19.
38. Agbossou, K.; Chahine, R.; Hamelin, J.; Laurencelle, F.; Anouar, A.; St-Arnaud, J. M.; Bose, T. K., Renewable energy systems based on hydrogen for remote applications. *J Power Sources* **2001,** *96* (1), 168 – 172.

39. Gray, E. M.; Webb, C. J.; Andrews, J.; Shabani, B.; Tsai, P. J.; Chan, S. L. I., Hydrogen storage for off-grid power supply. *International Journal of Hydrogen Energy* **2011,** *36* (1), 654 – 663.
40. Paul, B.; Andrews, J., Optimal coupling of PV arrays to PEM electrolysers in solar-hydrogen systems for remote area power supply. *International Journal of Hydrogen Energy* **2008,** *33* (2), 490 – 498.
41. Young, D. C.; Mill, G. A.; Wall, R., Feasibility of renewable energy storage using hydrogen in remote communities in Bhutan. *International Journal of Hydrogen Energy* **2007,** *32* (8), 997 – 1009.
42. Walker, G., *Solid State Hydrogen Storage Materials and Chemistry*. Woodhead Publishing Limited: Cambridge England, 2008.
43. Zuttel, A., *Hydrogen as a future energy carrier*. Weinheim : Wiley-VCH: Weinheim, 2008.
44. Gross, K. J., Carrington, R.K., Barcelo, S., Karkamkar, A., Purewal, Ma, S., Zhou, H-C., Dantzer, P., Ott, K., Burrell, T., Semeslberger, T., Pivak, Y., Dam, B., Chandra, D., and Parilla, P. *Recommended Best Practices for the Characterization of Storage Properties of Hydrogen Storage Materials*; U.S. D.O.E. Hydrogen Program: 2011.
45. Murshidi, J. A.; Paskevicius, M.; Sheppard, D. A.; Buckley, C. E., Structure, morphology and hydrogen storage properties of a $Ti_{0.97}Zr_{0.019}V_{0.439}Fe_{0.097}Cr_{0.045}Al_{0.026}Mn_{1.5}$ alloy. *International Journal of Hydrogen Energy* **2011,** *36* (13), 7587 – 7593.
46. Stander, C. M.; Pacey, R. A., The lattice energy of magnesium hydride. *Journal of Physics and Chemistry of Solids* **1978,** *39* (8), 829 – 832.
47. Kisi, E. H.; Buckley, C. E.; Gray, E. M., The Hydrogen Activation of $LaNi_5$. *Journal of Alloys and Compounds* **1992,** *185* (2), 369 – 384.
48. Imamura, H.; Sakasai, N.; Kajii, Y., Hydrogen absorption of Mg-based composites prepared by mechanical milling: Factors affecting its characteristics. *Journal of Alloys and Compounds* **1996,** *232* (1 – 2), 218 – 223.
49. Zaluska, A.; Zaluski, L.; Strom-Olsen, J. O., Nanocrystalline magnesium for hydrogen storage. *Journal of Alloys and Compounds* **1999,** *288* (1 – 2), 217 – 225.
50. Zuttel, A., Hydrogen storage methods. *Naturwissenschaften* **2004,** *91* (4), 157 – 172.

51. Sakintuna, B.; Lamari-Darkrim, F.; Hirscher, M., Metal hydride materials for solid hydrogen storage: A review. *International Journal of Hydrogen Energy* **2007,** *32* (9), 1121 – 1140.
52. Pitt, M. P., Paskevicius, M., Webb, C. J., Sheppard, D. A., Buckley, C. E., Gray, E. M.,, The synthesis of nanoscopic Ti based alloys and their effects on the MgH_2 system compared with the MgH_2 + $0.01Nb_2O_5$ benchmark. *International Journal of Hydrogen Energy* **2012,** *37* (5), 4227 – 4237.
53. Mueller, W. M.; Blackledge, J. P.; Libowitz, G. G.; Commission, U. S. A. E., *Metal hydrides*. Academic Press: 1968.
54. Koeneman, J., and Metcalfe, A.G.,, Solubility of Hydrogen in Magnesium. *Trans. Amer. Soc. Metals* **1959,** *78*.
55. Bystrzycki, J.; Czujko, T.; Varin, R. A.; Mizera, J., The effect of milling mode on the hydriding properties of nanocrystalline Mg_2Ni. *Functional Nanomaterials for Optoelectronics and Other Applications* **2004,** *99 – 100*, 137 – 140.
56. Hanada, N.; Ichikawa, T.; Fujii, H., Hydrogen absorption kinetics of the catalyzed MgH_2 by niobium oxide. *Journal of Alloys and Compounds* **2007,** *446 – 447*, 67 – 71.
57. Huot, J.; Liang, G.; Boily, S.; Van Neste, A.; Schulz, R., Structural study and hydrogen sorption kinetics of ball-milled magnesium hydride. *Journal of Alloys and Compounds* **1999,** *293 – 295* (0), 495 – 500.
58. Imamura, H.; Kitazawa, I.; Tanabe, Y.; Sakata, Y., Hydrogen storage in carbon/Mg nanocomposites synthesized by ball milling. *International Journal of Hydrogen Energy* **2007,** *32* (13), 2408 – 2411.
59. Oelerich, W., Klassen, T., Bormann, R., Comparison of the catalytic effects of V, V_2O_5, VN, and VC on the hydrogen sorption of nanocrystalline Mg. *Journal of Alloys and Compounds* **2001,** *322* (1 – 2), L5 – L9.
60. Taylor, S. R., Abundance of chemical elements in the continental crust: a new table. *Geochimica et Cosmochimica Acta* **1964,** *28* (8), 1273 – 1285.
61. Kramer, D., A.,. Magnesium Recycling in the United States 1998.
62. Pozzo, M.; Alfe, D., Structural properties and enthalpy of formation of magnesium hydride from quantum Monte Carlo calculations. *Physical Review B* **2008,** *77* (10).
63. Dornheim, M.; Doppiu, S.; Barkhordarian, G.; Boesenberg, U.; Klassen, T.; Gutfleisch, O.; Bormann, R., Hydrogen storage in

magnesium-based hydrides and hydride composites. *Scripta Materialia* **2007,** *56* (10), 841 – 846.
64. Bystrzycki, J.; Polanski, M.; Plocinski, T., Nano-Engineering Approach to Destabilization of Magnesium Hydride (MgH_2) by Solid-State Reaction with Si. *Journal of Nanoscience and Nanotechnology* **2009,** *9* (6), 3441 – 3448.
65. Mackay, D., Paterson, Sally,. Calculating fugacity. *Environmental science & technology* **1981,** *15* (9), 1006 – 1014.
66. Tunell, G., The Definition and Evaluation of the Fugacity of an Element or Compound in the Gaseous State. *The Journal of Physical Chemistry* **1930,** *35* (10), 2885 – 2913.
67. Vajo, J. J.; Mertens, F.; Ahn, C. C.; Bowman, R. C.; Fultz, B., Altering Hydrogen Storage Properties by Hydride Destabilization through Alloy Formation: LiH and MgH_2 Destabilized with Si. *The Journal of Physical Chemistry B* **2004,** *108* (37), 13977 – 13983.
68. Alapati, S. V.; Johnson, J. K.; Sholl, D. S., Identification of destabilized metal hydrides for hydrogen storage using first principles calculations. *The journal of physical chemistry. B* **2006,** *110* (17), 8769 – 8776.
69. Züttel, A.; Wenger, P.; Rentsch, S.; Sudan, P.; Mauron, P.; Emmenegger, C., $LiBH_4$ a new hydrogen storage material. *J Power Sources* **2003,** *118* (1 – 2), 1 – 7.
70. Dai, B.; Sholl, D. S.; Johnson, J. K., First-principles investigation of adsorption and dissociation of hydrogen on Mg_2Si surfaces. *Journal of Physical Chemistry C* **2007,** *111*, 6910 – 6916.
71. Kelly, S. T.; Van Atta, S. L.; Vajo, J. J.; Olson, G. L.; Clemens, B. M., Kinetic limitations of the Mg_2Si system for reversible hydrogen storage. *Nanotechnology* **2009,** *20* (20), 204017.
72. Paskevicius, M.; Sheppard, D. A.; Chaudhary, A. L.; Webb, C. J.; Gray, E. M. A.; Tian, H. Y.; Peterson, V. K.; Buckley, C. E., Kinetic limitations in the Mg–Si–H system. *International Journal of Hydrogen Energy* **2011,** *36* (17), 10779-10786.
73. Stioui, M.; Stioui, A.; Grayevsky, A.; Moran, S.; Kreitzman, N.; Kaplan, D.; Shaltiel, Proton magnetic resonance study of diffusion-related properties in magnesium-rich compounds. *Journal of the less-common metals* **1984,** *104* (1), 119 – 124.
74. Spatz, P.; Aebischer, H.; Krozer, A.; Schlapbach, L., The Diffusion of H in Mg and the Nucleation and Growth of MgH_2 in Thin Films. *Zeitschrift für Physikalische Chemie* **1993,** *181* (Part_1_2), 393 – 397.

75. Wronski, Z.; Varin, R. A.; Chiu, C.; Czujko, T.; Calka, A., Mechanochemical synthesis of nanostructured chemical hydrides in hydrogen alloying mills. *Journal of Alloys and Compounds* **2007,** *434 – 435*, 743 – 746.
76. Janot, R.; Cuevas, F.; Latroche, M.; Percheron-Guegan, A., Influence of crystallinity on the structural and hydrogenation properties Of Mg_2X phases (X = Ni, Si, Ge, Sn). *Intermetallics* **2006,** *14* (2), 163 – 169.
77. Gross, K. J.; Spatz, P.; Zuttel, A.; Schlapbach, L., Mechanically milled Mg composites for hydrogen storage - The transition to a steady state composition. *Journal of Alloys and Compounds* **1996,** *240* (1 – 2), 206 – 213.
78. Oelerich, W.; Klassen, T.; Bormann, R., Metal oxides as catalysts for improved hydrogen sorption in nanocrystalline Mg-based materials. *Journal of Alloys and Compounds* **2001,** *315* (1 – 2), 237 – 242.
79. Schulz, R.; Huot, J.; Liang, G.; Boily, S.; Lalande, G.; Denis, M. C.; Dodelet, J. P., Recent developments in the applications of nanocrystalline materials to hydrogen technologies. *Materials Science and Engineering a-Structural Materials Properties Microstructure and Processing* **1999,** *267* (2), 240 – 245.
80. Vajo, J. J.; Salguero, T. T.; Gross, A. F.; Skeith, S. L.; Olson, G. L., Thermodynamic destabilization and reaction kinetics in light metal hydride systems. *Journal of Alloys and Compounds* **2007,** *446 – 447*, 409 – 414.
81. Jeon, K. J.; Theodore, A.; Wu, C. Y., Enhanced hydrogen absorption kinetics for hydrogen storage using Mg flakes as compared to conventional spherical powders. *J Power Sources* **2008,** *183* (2), 693 – 700.
82. Montone, A.; Grbovic, J.; Bassetti, A.; Mirenghi, L.; Rotolo, P.; Bonetti, E.; Pasquini, L.; Antisari, M. V., Microstructure, surface properties and hydrating behaviour of Mg-C composites prepared by ball milling with benzene. *International Journal of Hydrogen Energy* **2006,** *31* (14), 2088 – 2096.
83. Niu, X. P.; Lu, L., Formation of magnesium silicide by mechanical alloying. *Advanced Performance Materials* **1997,** *4* (3), 275 – 283.
84. Dodd, A. C.; McCormick, P. G., Synthesis of nanoparticulate zirconia by mechanochemical processing. *Scripta Materialia* **2001,** *44* (8 – 9), 1725 – 1729.

85. Paskevicius, M.; Webb, J.; Pitt, M. P.; Blach, T. P.; Hauback, B. C.; Gray, E. M.; Buckley, C. E., Mechanochemical synthesis of aluminium nanoparticles and their deuterium sorption properties to 2 kbar. *Journal of Alloys and Compounds* **2009,** *481* (1 – 2), 595 – 599.
86. Dornheim, M.; Eigen, N.; Barkhordarian, G.; Klassen, T.; Bormann, R., Tailoring hydrogen storage materials towards application. *Advanced Engineering Materials* **2006,** *8* (5), 377 – 385.
87. Paskevicius, M. A nanostructural investigation of mechnaochemically synthesised hydrogen stroage materials. Curtin University of Technology, Perth, 2009.
88. Sandu, I.; Moreau, P.; Guyomard, D.; Brousse, T.; Roue, L., Synthesis of nanosized Si particles via a mechanochemical solid-liquid reaction and application in Li-ion batteries. *Solid State Ionics* **2007,** *178*, 1297 – 1303.
89. Sheppard, D. A.; Paskevicius, M.; Buckley, C. E., The Mechanochemical synthesis of magnesium hydride nanoparticles. *Journal of Alloys and Compounds* **2010,** *492* (1 – 2), L72 – L74.
90. Wu, H. P.; Liu, J. F.; Wang, Y. W.; Zeng, Y. W.; Jiang, J. Z., Preparation of Ge nanocrystals via ultrasonic solution reduction. *Materials Letters* **2006,** *60* (7), 986 – 989.
91. Mendez-Vilas, A., Diaz, J., *Microscopy: Science, Technology, Applications and Educaton*. Fromatex Research Center: Badajoz, Spain, 2010; Vol. 2.
92. Cheary, R. W.; Coelho, A., A fundamental parameters approach to X-ray line-profile fitting. *Journal of Applied Crystallography* **1992,** *25* (2), 109 – 121.
93. Dinnebier, R. E.; Billinge, S. J. L., Chapter 1 Principles of Powder Diffraction. In *Powder Diffraction: Theory and Practice*, The Royal Society of Chemistry: 2008; pp 1 – 19.
94. X-ray powder diffractometer. http://peggy.uni-mki.gwdg.de/Docs/ausstattung/puldiff.html (accessed 23/05/12).
95. Warren, B., *X-ray diffraction*. Addison-Wesley Pub. Co: Reading, Mass, 1969.
96. Finger, L.; Cox, D.; Jephcoat, A., A correction for powder diffraction peak asymmetry due to axial divergence. *Journal of Applied Crystallography* **1994,** *27* (6), 892 – 900.
97. Coelho, A. A., Topas User Manual. 3.0 ed. ed.; Bruker AXS GmbH: Karlsruhe, Germany, 2003.
98. Schnablegger, H. a. S., Y., *The SAXS Guide: Getting acquainted with the principles*. 2nd ed.; Anton Paar GmbH: Austria, 2011.

99. Glatter, O., *Small angle x-ray scattering*. London : Academic Press: London, 1982.
100. Brumberger, H., *Modern aspects of small-angle scattering*. Kluwer Academic Publishers: Dordrecht Boston, 1995.
101. Buckley, C. E., Small Angle Scattering Data Collection. Curtin University of Technology: Perth, Australia, 2006.
102. Wignall, G., D., *Advantages of Absolute Calibration in Small Ange X-ray and Neutron Scattering Studies of Polymers and Colloids*; Solid State Division Oak Ridge National Laboratory: Oak Ridge, Tennessee, 1996.
103. Beaucage, G.; Schaefer, D. W., Structural studies of complex systems using small-angle scattering: a unified Guinier/power-law approach. *Journal of Non-Crystalline Solids* **1994,** *172 – 174, Part 2*, 797 – 805.
104. Terasawa, M., Kihara, M., Basic Characteristics of Synchrotron Radiation and Its Related Facilities and Instrumentation. In *Applications of Synchrotron Radiation to Materials Analysis*, Saisho H., G., Y., Ed. Elsevier Science: Tsukuba, 1996; pp 1 – 78.
105. Williams, D. B., Carter, C. Barry, , *Transmission Electron Microscopy A Textbook for Materials Science* Boston, MA : Springer US: Boston, MA, 2009.
106. Varsani, R. 2D and 3D Composition and Chemistry of Nanomaterials. The University of Western Australia, Perth, 2009.
107. Wittke, J., H., Types of Signals. http://www4.nau.edu/microanalysis/Microprobe-SEM/Signals.html (accessed Accessed 17/03/2013).
108. Goldstein, J., *Scanning electron microscopy and X-ray microanalysis*. Springer: New York, 2003.
109. Nieto de Castro, C. A.; Lourenço, M. J. V.; Sampaio, M. O., Calibration of a DSC: its importance for the traceability and uncertainty of thermal measurements. *Thermochimica Acta* **2000,** *347* (1 – 2), 85 – 91.
110. Reilly, J. J.; Adzic, G. D.; Johnson, J. R.; Vogt, T.; Mukerjee, S.; McBreen, J., The correlation between composition and electrochemical properties of metal hydride electrodes. *Journal of Alloys and Compounds* **1999,** *293 – 295*, 569 – 582.
111. Gorra, X. Residual Gas Analysis. http://x-tronix.info/2011/10/26/residual-gas-analysis-rga.aspx (accessed 17/03/2013).

112. Wong, H., Recent developments in silicon optoelectronic devices. *Microelectronics reliability* **2002,** *42* (3), 317 – 326.
113. Reindl, A.; Voronov, A.; Gorle, P.; Rauscher, M.; Roosen, A.; Peukert, W., Dispersing and stabilizing silicon nanoparticles in a low-epsilon medium. *Colloids and Surfaces A: Physicochemical and Engineering Aspects* **2008,** *320* (1), 183 – 188.
114. Meillaud, F.; Feltrin, A.; Despeisse, M.; Haug, F.; Domine, D.; Python, M.; Söderström, T.; Cuony, P.; Boccard, M.; Nicolay, S., Realization of high efficiency micromorph tandem silicon solar cells on glass and plastic substrates: Issues and potential. *Solar Energy Materials and Solar Cells* **2011,** *95* (1), 127 – 130.
115. Moulin, E.; Sukmanowski, J.; Schulte, M.; Gordijn, A.; Royer, F.; Stiebig, H., Thin-film silicon solar cells with integrated silver nanoparticles. *Thin Solid Films* **2008,** *516* (20), 6813 – 6817.
116. Klein, S.; Dell'Arciprete, M. L.; Wegmann, M.; Distel, L. V.; Neuhuber, W.; Gonzalez, M. C.; Kryschi, C., Oxidized silicon nanoparticles for radiosensitization of cancer and tissue cells. *Biochemical and biophysical research communications* **2013**.
117. Gangal, A. C.; Kale, P.; Edla, R.; Manna, J.; Sharma, P., Study of kinetics and thermal decomposition of ammonia borane in presence of silicon nanoparticles. *International Journal of Hydrogen Energy* **2012,** *37* (8), 6741 – 6748.
118. Feng, S.; Yu, D.; Zhang, H.; Bai, Z.; Ding, Y., The growth mechanism of silicon nanowires and their quantum confinement effect. *Journal of crystal growth* **2000,** *209* (2), 513 – 517.
119. Kanemitsu, Y., Efficient light emission from crystalline and amorphous silicon nanostructures. *Journal of luminescence* **2002,** *100* (1), 209 – 217.
120. Flagan, R. C.; Lunden, M. M., Particle structure control in nanoparticle synthesis from the vapor phase. *Materials Science and Engineering: A* **1995,** *204* (1), 113 – 124.
121. Scheier, P.; Marsen, B.; Lonfat, M.; Schneider, W.-D.; Sattler, K., Growth of silicon nanostructures on graphite. *Surface science* **2000,** *458* (1), 113 – 122.
122. Hryciw, A.; Meldrum, A.; Buchanan, K.; White, C., Effects of particle size and excitation spectrum on the photoluminescence of silicon nanocrystals formed by ion implantation. *Nuclear Instruments and Methods in Physics Research Section B: Beam Interactions with Materials and Atoms* **2004,** *222* (3), 469 – 476.

123. Lam, C.; Zhang, Y.; Tang, Y.; Lee, C.; Bello, I.; Lee, S., Large-scale synthesis of ultrafine Si nanoparticles by ball milling. *Journal of Crystal Growth* **2000,** *220* (4), 466 – 470.
124. Heath, J. R.; Shiang, J. J.; Alivisatos, A. P., Germanium quantum dots: Optical properties and synthesis. *The Journal of Chemical Physics* **1994,** *101* (2), 1607 – 1615.
125. Qian, D.; Jiang, J. Z.; Hansen, P. L., Preparation of ZnO nanocrystals via ultrasonic irradiation. *Chem Commun (Camb)* **2003,** *0* (9), 1078 – 9.
126. Paskevicius, M.; Sheppard, D. A.; Buckley, C. E., Characterisation of mechanochemically synthesised alane (AlH_3) nanoparticles. *Journal of Alloys and Compounds* **2009,** *487* (1 – 2), 370 – 376.
127. Zakharov, L. N., Antipin, M.Yu., Struchkov, Yu.T., Gusev, A.V., Gibin, A.M., Zhernenkov, N.V., Molecular and crystal structures of $SiCl_4$ at 163 K. *Kristallografiya, Soviet Physics, Crystallography* **1986,** *31* (99 – 100), 171 – 172.
128. Zhou, E. H.; Suryanarayana, C.; Fores, F. H., Effect of Premilling in Elemental Powders on Solid Solubility Extention of Magnesium in Titanium by Mechanical Alloying. *Materials Letters* **1995,** *23* (1 – 3), 27 – 31.
129. Poffo, C. M.; de Lima, J. C.; Souza, S. M.; Triches, D. M.; Grandi, T. A.; de Biasi, R. S., Structural, thermal and optical study of nanocrystalline silicon produced by ball milling. *J Raman Spectrosc* **2010,** *41* (12), 1606 – 1609.
130. Shen, T. D.; Koch, C. C.; McCormick, T. L.; Nemanich, R. J.; Huang, J. Y.; Huang, J. G., The structure and property characteristics of amorphous/nanocrystalline silicon produced by ball milling. *Journal of Materials Research* **1995,** *10* (1), 139 – 148.
131. Wang, J.; Ganguly, S.; Sen, S.; Browning, N. D.; Kauzlarich, S. M., Synthesis and characterization of P-doped amorphous and nanocrystalline Si. *Polyhedron* **2013,** *58*, 156-161.
132. Rumpf, H., Physical Aspects of Comminution and New Formulation of a Law of Comminution. *Powder Technology* **1973,** *7* (3), 145 – 159.
133. Ahn, C.; Krivanek, O., *EELS atlas*. Gatan: 1983.
134. Vigeholm, B.; Vigeholm, K.; Jensen, B.; Larsen, A. S.; Pedersen, Elements of hydride formation mechanisms in nearly spherical magnesium powder particles. *Journal of the less-common metals* **1987,** *131* (1), 133 – 141.

135. Borgschulte, A.; Gremaud, R.; Griessen, R., Interplay of diffusion and dissociation mechanisms during hydrogen absorption in metals. *Physical Review B* **2008,** *78* (9).
136. Ingason, A. S.; Olafsson, S., Influence of MgO nano-crystals on the thermodynamics, hydrogen uptake and kinetics in Mg films. *Thin Solid Films* **2006,** *515* (2), 708 – 711.
137. Mintz, M. H.; Mintz, Z.; Gavra, Z.; Hadari, Kinetic study of the reaction between hydrogen and magnesium, catalyzed by addition of indium. *Journal of inorganic and nuclear chemistry* **1978,** *40* (5), 765 – 768.
138. Imamura, H.; Tanaka, K.; Kitazawa, I.; Sumi, T.; Sakata, Y.; Nakayama, N.; Ooshima, S., Hydrogen storage properties of nanocrystalline MgH_2 and MgH_2/Sn nanocomposite synthesized by ball milling. *Journal of Alloys and Compounds* **2009,** *484* (1 – 2), 939 – 942.
139. Ryden, J.; Hjörvarsson, B.; Ericsson, T.; Karlsson, E.; Krozer, A.; Kasemo, B., Unusual kinetics of hydride formation in Mg-Pd sandwiches, studied by hydrogen profiling and quartz crystal microbalance measurements. *Journal of the Less Common Metals* **1989,** *152* (2), 295 – 309.
140. He, Y. P.; Zhao, Y. P.; Huang, L. W.; Wang, H.; Composto, R. J., Hydrogenation of Mg film and Mg nanoblade array on Ti coated Si substrates. *Applied Physics Letters* **2008,** *93* (16).
141. Nørskov, J.; Houmøller, A.; Johansson, P.; Lundqvist, B., Adsorption and Dissociation of H_2 on Mg Surfaces. *Physical Review Letters* **1981,** *46* (4), 257 – 260.
142. Fernández, J. F.; Sánchez, C. R., Rate determining step in the absorption and desorption of hydrogen by magnesium. *Journal of Alloys and Compounds* **2002,** *340* (1 – 2), 189 – 198.
143. Bohmhammel, K.; Christ, B.; Wolf, G., Kinetic investigations on the basis of isothermal DSC measurements of hydrogenation and dehydrogenation of magnesium hydride. *Thermochimica Acta* **1998,** *310* (1 – 2), 167 – 171.
144. Mintz, M. H.; Zeiri, Y., Hydriding kinetics of powders. *Journal of Alloys and Compounds* **1995,** *216* (2), 159 – 175.
145. Hanada, N.; Ichikawa, T.; Orimo, S.-I.; Fujii, H., Correlation between hydrogen storage properties and structural characteristics in mechanically milled magnesium hydride MgH_2. *Journal of Alloys and Compounds* **2004,** *366* (1 – 2), 269 – 273.

146. Gerasimov, K. B.; Konstanchuck, I. G.; Chizhik, S. A.; Bobet, J. L., "Hysteresis" in interaction of nanocrystalline magnesium with hydrogen. *International Journal of Hydrogen Energy* **2009,** *34* (4), 1916 – 1921.
147. Ma, T.; Isobe, S.; Morita, E.; Wang, Y. M.; Hashimoto, N.; Ohnuki, S.; Kimura, T.; Ichikawa, T.; Kojima, Y., Correlation between kinetics and chemical bonding state of catalyst surface in catalyzed magnesium hydride. *International Journal of Hydrogen Energy* **2011,** *36* (19), 12319 – 12323.
148. Kelkar, T.; Pal, S., A computational study of electronic structure, thermodynamics and kinetics of hydrogen desorption from Al- and Si-doped alpha-, gamma-, and beta-MgH_2. *Journal of Materials Chemistry* **2009,** *19* (25), 4348 – 4355.
149. Chu, W. K.; Lau, S. S.; Mayer, J. W.; Müller, H.; Tu, K. N., Implanted noble gas atoms as diffusion markers in silicide formation. *Thin Solid Films* **1975,** *25* (2), 393 – 402.
150. Toby, B. H., R factors in Rietveld analysis: How good is good enough? *Powder Diffraction* **2006,** *21* (1), 67 – 70.
151. Machida, M.; Eguchi, K.; Arai, H., Analytical Electron Microscope Analysis of the Formation of BaO · 6Al2O3. *Journal of the American Ceramic Society* **1988,** *71* (12), 1142 – 1147.
152. Kissinger, H. E.; Kissinger, Reaction Kinetics in Differential Thermal Analysis. *Analytical chemistry* **1957,** *29* (11), 1702 – 1706.
153. Boswell, P. G., On the calculation of activation energies using a modified Kissinger method. *Journal of Thermal Analysis* **1980,** *18* (2), 353 – 358.
154. Wang, H.-R.; Gao, Y.-L.; Ye, Y.-F.; Min, G.-H.; Chen, Y.; Teng, X.-Y., Crystallization kinetics of an amorphous Zr–Cu–Ni alloy: calculation of the activation energy. *Journal of Alloys and Compounds* **2003,** *353* (1 – 2), 200 – 206.
155. Gennari, F. C.; Castro, F. J.; Urretavizcaya, G., Hydrogen desorption behavior from magnesium hydrides synthesized by reactive mechanical alloying. *Journal of Alloys and Compounds* **2001,** *321* (1), 46 – 53.
156. Khawam, A.; Flanagan, D. R., Solid-state kinetic models: basics and mathematical fundamentals. *The Journal of Physical Chemistry B* **2006,** *110* (35), 17315 – 17328.
157. Barkhordarian, G.; Klassen, T.; Bormann, R., Kinetic investigation of the effect of milling time on the hydrogen sorption

reaction of magnesium catalyzed with different Nb_2O_5 contents. *Journal of Alloys and Compounds* **2006,** *407* (1 – 2), 249 – 255.
158. Jacobs, P.; Tompkins, F., Classification and theory of solid reactions. *Chemistry in the solid state* **1955,** *184*, 212.
159. Dal Toè, S.; Lo Russo, S.; Maddalena, A.; Principi, G.; Saber, A.; Sartori, S.; Spataru, T., Hydrogen desorption from magnesium hydride–graphite nanocomposites produced by ball milling. *Materials Science and Engineering: B* **2004,** *108* (1), 24 – 27.
160. Avrami, M., Kinetics of Phase Change. I General Theory. *The Journal of Chemical Physics* **1939,** *7* (12), 1103.
161. Avrami, M., Kinetics of phase change. II transformation-time relations for random distribution of nuclei. *The Journal of Chemical Physics* **1940,** *8*, 212.
162. Avrami, M., Granulation, phase change, and microstructure kinetics of phase change. III. *The Journal of Chemical Physics* **1941,** *9*, 177.
163. Carter, R. E., Kinetic Model for Solid-State Reactions. *The Journal of Chemical Physics* **1961,** *34*, 2010.
164. Valensi, G., Kinetics of oxidation of metallic spherules and powders. *Compt. Rend* **1936,** *202* (4), 309.
165. Upadhyay, S. K., *Chemical Kinetics and Reaction Dynamics by Santosh K. Upadhyay*. Dordrecht : Springer Netherlands: Dordrecht, 2006.
166. Bogerd, R.; Adelhelm, P.; Meeldijk, J. H.; de Jong, K. P.; de Jongh, P. E., The structural characterization and H_2 sorption properties of carbon-supported $Mg_{1-x}Ni_x$ nanocrystallites. *Nanotechnology* **2009,** *20* (20).
167. Huot, J.; Tremblay, M. L.; Schulz, R., Synthesis of nanocrystalline hydrogen storage materials. *Journal of Alloys and Compounds* **2003,** *356*, 603 – 607.
168. Seebauer, E. G.; Seebauer, A. C. F.; Kong, L. D.; Schmidt, The coverage dependence of the pre-exponential factor for desorption. *Surface science* **1988,** *193* (3), 417 – 436.
169. Kogut, I.; Record, M. C., Magnesium silicide thin film formation by reactive diffusion. *Thin Solid Films* **2012,** *522*, 149 – 158.
170. Vantomme, A.; Langouche, G.; Mahan, J. E.; Becker, J. P., Growth mechanism and optical properties of semiconducting Mg_2Si thin films. *Microelectronic Engineering* **2000,** *50* (1 – 4), 237 – 242.
171. Battiston, S.; Boldrini, S.; Fiameni, S.; Famengo, A.; Fabrizio, M.; Barison, S., Multilayered thin films for oxidation protection of Mg_2Si

thermoelectric material at middle–high temperatures. *Thin Solid Films* **2012,** *526*, 150 – 154.
172. Ivanenko, L.; Shaposhnikov, V.; Filonov, A.; Krivosheeva, A.; Borisenko, V.; Migas, D.; Miglio, L.; Behr, G.; Schumann, J., Electronic properties of semiconducting silicides: fundamentals and recent predictions. *Thin Solid Films* **2004,** *461* (1), 141 – 147.
173. Umeda, J.; Kondoh, K.; Kawakami, M.; Imai, H., Powder metallurgy magnesium composite with magnesium silicide in using rice husk silica particles. *Powder Technology* **2009,** *189* (3), 399 – 403.
174. Kogut, I.; Record, M.-C., Growth of magnesium silicide thin films on Si (100), Si (111) and SOI substrates during rapid thermal processing. *Intermetallics* **2013,** *32*, 184 – 193.
175. Sekino, K.; Midonoya, M.; Udono, H.; Yamada, Y., Preparation of Schottky contacts on n-type Mg_2Si single crystalline substrate. *Physics Procedia* **2011,** *11*, 171 – 173.
176. Galkin, N., Approaches to growth and study of properties of multilayer silicon–silicide heterostructures with buried semiconductor silicide nanocrystallites. *Thin Solid Films* **2007,** *515* (22), 8179 – 8188.
177. Kalarasse, F.; Bennecer, B., Electronic and optical properties of the antifluorite semiconductors Be_2C and Mg_2X (X= C, Si, Ge) under hydrostatic pressure. *Journal of Physics and Chemistry of Solids* **2008,** *69* (7), 1775 – 1781.
178. Akasaka, M.; Iida, T.; Nemoto, T.; Soga, J.; Sato, J.; Makino, K.; Fukano, M.; Takanashi, Y., Non-wetting crystal growth of Mg_2Si by vertical Bridgman method and thermoelectric characteristics. *Journal of crystal growth* **2007,** *304* (1), 196 – 201.
179. Imai, Y.; Watanabe, A., Energetics of compounds related to Mg_2Si as an anode material for lithium-ion batteries using first principle calculations. *Journal of Alloys and Compounds* **2011,** *509* (30), 7877 – 7880.
180. Baldi, A.; Gonzalez-Silveira, M.; Palmisano, V.; Dam, B.; Griessen, R., Destabilization of the Mg-H system through elastic constraints. *Physical Review Letters* **2009,** *102* (22), 226102.
181. Tsuzuki, T.; Ding, J.; McCormick, P. G., Mechanochemical synthesis of ultrafine zinc sulfide particles. *Physica B: Condensed Matter* **1997,** *239* (3 – 4), 378 – 387.
182. Bogdanović, B.; Bohmhammel, K.; Christ, B.; Reiser, A.; Schlichte, K.; Vehlen, R.; Wolf, U., Thermodynamic investigation of

the magnesium–hydrogen system. *Journal of Alloys and Compounds* **1999,** *282* (1 – 2), 84 – 92.
183. McDonald, G.; Lodge, N. M.; Walters, W., The Effect of Added Gases upon the Thermal Decomposition of Tetrahydrofuran-1. *Journal of the American Chemical Society* **1951,** *73* (4), 1757 – 1760.
184. Reule, H.; Hirscher, M.; Weisshardt, A.; Kronmuller, H., Hydrogen desorption properties of mechanically alloyed MgH_2 composite materials. *Journal of Alloys and Compounds* **2000,** *305* (1 – 2), 246 – 252.
185. Huot, J.; Liang, G.; Schulz, R., Mechanically alloyed metal hydride systems. *Applied physics. A, Materials science & processing* **2001,** *72* (2), 187 – 195.
186. Wu, H.; Zhou, W.; Udovic, T. J.; Rush, J. J.; Yildirim, T., Crystal chemistry of perovskite-type hydride $NaMgH_3$: Implications for hydrogen storage. *Chemistry of materials* **2008,** *20* (6), 2335 – 2342.
187. Sheppard, D.; Paskevicius, M.; Buckley, C., Thermodynamics of Hydrogen Desorption from $NaMgH_3$ and Its Application As a Solar Heat Storage Medium. *Chemistry of materials* **2011,** *23* (19), 4298 – 4300.
188. Polanski, M.; Bystrzycki, J., The influence of different additives on the solid-state reaction of magnesium hydride (MgH_2) with Si. *International Journal of Hydrogen Energy* **2009,** *34* (18), 7692 – 7699.
189. Chaudhary, A. L., Paskevicious, M., Sheppard, D., Buckley, C., Synthesis of Si Nanoparticles to Improve Reaction Kinetics in the Mg-Si-H system. In *Renewable Energy 2010 International Conference*, Yokohama, Japan, 2010.
190. Folland, N. O.; Bassani, F., Selection rules and Mg_2Si, Mg_2Ge and Mg_2Sn. *Journal of Physics and Chemistry of Solids* **1968,** *29* (2), 281 – 290.
191. Martin, J. J., Thermal conductivity of Mg_2Si, Mg_2Ge and Mg_2Sn. *Journal of Physics and Chemistry of Solids* **1972,** *33* (5), 1139 – 1148.
192. Zhou, D.; Liu, J.; Xu, S.; Peng, P., Thermal stability and elastic properties of Mg_2X (X = Si, Ge, Sn, Pb) phases from first-principle calculations. *Computational Materials Science* **2012,** *51* (1), 409 – 414.
193. Walker, G.; Abbas, M.; Grant, D.; Udeh, C., Destabilisation of magnesium hydride by germanium as a new potential multicomponent hydrogen storage system. *Chemical communications (London. 1996)* **2011,** *47* (28), 8001 – 3.

194. Imamura, H.; Yoshihara, K.; Yoo, M.; Kitazawa, I.; Sakata, Y.; Ooshima, S., Dehydriding of nanocomposite formed by ball milling of with Sn. *International Journal of Hydrogen Energy* **2007,** *32* (17), 4191 – 4194.
195. Zhong, H. C.; Wang, H.; Ouyang, L. Z.; Zhu, M., Microstructure and hydrogen storage properties of Mg–Sn nanocomposite by mechanical milling. *Journal of Alloys and Compounds* **2011,** *509* (11), 4268 – 4272.
196. Aizawa, T.; Song, R., Mechanically induced reaction for solid-state synthesis of Mg_2Si and Mg_2Sn. *Intermetallics* **2006,** *14* (4), 382 – 391.

Appendix A: DOE Targets

DOE Targets for Onboard Hydrogen Storage Systems for Light-Duty Vehicles

Table 2 Technical Targets: Onboard Hydrogen Storage Systems				
Storage Parameter	**Units**	**2010**	**2017**	**Ultimate**
System Gravimetric Capacity: Usable, specific-energy from H_2 (net useful energy/max system mass) [a]	kWh/kg (kg H_2/kg system)	1.5 (0.045)	1.8 (0.055)	2.5 (0.075)
System Volumetric Capacity: Usable energy density from H_2 (net useful energy/max system volume)	kWh/L (kg H_2/L system)	0.9 (0.028)	1.3 (0.040)	2.3 (0.070)
Storage System Cost [b]:	$/kWh net ($/kg H_2)	TBD (TBD)	TBD (TBD)	TBD (TBD)
• Fuel cost [c]	$/gge at pump	3-7	2-4	2-4
Durability/Operability:				
• Operating ambient temperature [d]	ºC	-30/50 (sun)	-40/60 (sun)	-40/60 (sun)
• Min/max delivery temperature	ºC	-40/85	-40/85	-40/85
• Operational cycle life (1/4 tank to full) [e]	Cycles	1000	1500	1500
• Min delivery pressure from storage system; FC= fuel cell, ICE= internal combustion engine	bar (abs)	5 FC/35 ICE	5 FC/35 ICE	3 FC/35 ICE
• Max delivery pressure from storage system [f]	bar (abs)	12 FC/100 ICE	12 FC/100 ICE	12 FC/100 ICE
• Onboard Efficiency	%	90	90	90
• "Well" to Powerplant Efficiency	%	60	60	60
Charging / Discharging Rates:				
• System fill time (5 kg)	min (kg H_2/min)	4.2 (1.2)	3.3 (1.5)	2.5 (2.0)
• Minimum full flow rate	(g/s)/kW	0.02	0.02	0.02
• Start time to full flow (20°C) [g]	s	5	5	5
• Start time to full flow (-20°C) [g]	s	15	15	15
• Transient response 10%-90% and 90% - 0% [h]	s	0.75	0.75	0.75
Fuel Purity (H_2 from storage) [i]:	% H_2	SAE J2719 and ISO/PDTS 14687-2 (99.97% dry basis)		
Environmental Health & Safety:				
• Permeation & leakage [j]	Scc/h	Meets or exceeds applicable standards		
• Toxicity	-			
• Safety	-			
• Loss of useable H_2 [k]	(g/h)kg H_2 stored	0.1	0.05	0.05

Useful constants: 0.2778 kWh/MJ; 33.3 kWh/kg H_2; 1 kg H_2 ≈ 1 gal gasoline equivalent.

Note: The above targets are based on the lower heating value of hydrogen. Targets are for a complete system, including tank, material, valves, regulators, piping, mounting brackets, insulation, added cooling capacity, and/or other balance-of-plant components. All capacities are defined as useable capacities that could be delivered to the powerplant (i.e. fuel cell or internal combustion engine). All targets must be met at the end of service life (approximately 1,500 cycles or 5,000 operation hours, equivalent of 150,000 miles). Unless otherwise indicated, all targets are for both hydrogen internal combustion engine and for hydrogen fuel cell use, based on the low likelihood of power plant specific fuel being commercially viable. Commercial systems must meet manufacturing specifications for cycle life variation; see note [e] to cycle life below.

Footnotes to Table 2

[a] Generally the 'full' mass (including hydrogen) is used; for systems that gain weight, the highest mass during discharge is used. All capacities are net useable capacity able to be delivered to the powerplant. Capacities must be met at end of service life.

[b] Note: Storage system costs targets are currently under review and may be changed at a future date.

[c] 2005 US$; includes off-board costs such as liquefaction, compression, fuel regeneration, etc; ultimate target based on H_2 production cost of $2 to $3/gasoline gallon equivalent untaxed, independent of production pathway.

[d] Stated ambient temperature plus full solar load. No allowable performance degradation from –20 °C to 40 °C. Allowable degradation outside these limits is to be determined.

[e] Equivalent to 200,000; 300,000; and 300,000 miles respectively (current gasoline tank spec). Manufactured items have item-to-item variation. The variation as it affects the customer is covered by the cycle life target of number of cycles. Testing variation is addressed by testing variation metrics. It is expected that only one or two systems will be fabricated to test life of early concepts. The data generated has great uncertainty associated with it due to the low number of samples. Thus a factor is required to account for this uncertainty. The effect is to increase the required cycle life based on normal statistics using the number of samples tested. The value is given in the form XX/YY where XX is the acceptable percentage of the target life (90 means 90%), and YY is the percent confidence that the true mean will be inside the xx% of the target life (99 indicates 99% confidence or an alpha value of 0.01). For demonstration fleets this is less critical and no target is specified to functionally enable single specimen testing. Variation testing needs to be included for general sales. By the time full fleet production is reached, testing levels will also need to tighten, but availability of multiple samples will no longer be a problem. This entire sequence is standard practice in the mass production of automobiles and their components. Units are in minimum percent of the mean and a percentage confidence level. The technology readiness goals are: minimum percentage of the mean of 90% at a 99% confidence level.

[f] For delivery the storage system, in the near-term, the forecourt should be capable of delivering 10,000 psi (700 bar) compressed hydrogen, liquid hydrogen, or chilled hydrogen (77K) at 5,000 psi (350 bar). In the long term, it is anticipated that delivery pressures will be reduced to between 50 and 150 bar for materials-based storage systems, based on today's knowledge of sodium alanate (Ti-catalyzed $NaAlH_4$).

[g] Flow must initiate within 25% of target time.

[h] At operating temperature.

[i] The storage system is not expected to provide any purification for the incoming hydrogen, and will receive hydrogen at the purity levels required for the fuel cell. The hydrogen purity specifications are currently in both SAE J2719: Technical Information Report on the Development of a Hydrogen Quality Guideline in Fuel Cell Vehicles (harmonized with ISO/PDTS 14687-2) and ISO/PDTS 14687-2: Hydrogen Fuel — Product Specification — Part 2: PEM fuel cell applications for road vehicles. Examples include: total non-particulates, 300 ppm; H_2O, 5 ppm; total hydrocarbons (C_1 basis), 2 ppm; O_2, 5 ppm; He, 300 ppm; N_2 + Ar combined, 100 ppm; CO_2, 2 ppm; CO, 0.2 ppm; total S, 0.004 ppm; formaldehyde (HCHO), 0.01 ppm; formic acid (HCOOH), 0.2 ppm; NH_3, 0.1 ppm; total halogenates, 0.05 ppm; maximum particle size, <10 μm; and particulate concentration, <1 μg/L H_2. These are subject to change. See Appendix on Hydrogen Quality in the DOE EERE Hydrogen Fuel Cells and Infrastructure Technologies Program Multiyear Research, Development and Demonstration Plan (www.eere.energy.gov/hydrogenandfuelcells/mypp/) to be updated as fuel purity analyses progress. Note that some storage technologies may produce contaminants for which effects are unknown; these will be addressed by system engineering design on a case by case basis as more information becomes available.

[j] Total hydrogen lost into the environment as H_2; relates to hydrogen accumulation in enclosed spaces. Storage system must comply with CSA/HGV2 standards for vehicular tanks. This includes any coating or enclosure that incorporates the envelope of the storage system.

[k] Total hydrogen lost from the storage system, including leaked or vented hydrogen; relates to loss of range.

Appendix B: Thesis Publications

REFEREED PUBLICATIONS

Paskevicius, M., Sheppard, D.A., **Chaudhary, A.L.**, Webb, C.J., Gray, E.M.A., Tian, H.Y., Peterson, V.K. and Buckley, C.E., (2011) *Kinetic limitations in the Mg-Si-H system*, International Journal of Hydrogen Energy 36 (17): 10779-10786.

PUBLICATIONS IN PREPARATION

Chaudhary, A.L., Sheppard, D.A., Paskevicius, M., Buckley C.E., (2014) *Synthesis of amorphous Si nanoparticles using mechanochemical ball milling* (Chapter 3)

Chaudhary, A.L., Sheppard, D.A., Paskevicius, M., Buckley C.E., (2014) *A kinetic study on the desorption of MgH_2 with Si* (Chapter 4)

Chaudhary, A.L., Sheppard, D.A., Paskevicius, M., Webb, C.J., Buckley C.E., (2013) *Synthesing Mg_2Si Nanoparticles for High Pressure Hydrogenation* (Chapter 5)

Chaudhary, A.L., Sheppard, D.A., Paskevicius, M., Buckley C.E., (2014) *Destabilistaion of MgH_2 and $NaMgH_3$ using Group IV elements Si, Ge and Sn* (Chapter 6)

CONFERENCES

Chaudhary, **A.L.,** Sheppard, D., Paskevicius, M., Webb, C., Buckley, C., (2012) *Synthesis and High Pressure Hydrogenation of Mg_2Si Nanoparticles*, Oral Presentation, International Symposium on Metal-Hydrogen Systems, Kyoto, Japan, Oct. 21 – 26.

Chaudhary A.L., Sheppard, D., Paskevicius, M., Buckley, C., (2011) *Influence of Si Particle Size in the Dehydrogenation of MgH_2*, Oral Presentation, AXAA National Conference, Sydney, Australia, Feb. 6 – 11, PP006.

Sheppard, D.A., Paskevicius, M., Tian, H., **Chaudhary A.L.**, Murshidi, J., Buckley, C.E., (2011) *Synthesis and characterisation of nanoparticles for hydrogen storage*,, Oral Presentation, AXAA National Conference, Sydney, Australia, Feb. 6 – 11, OC010.

Buckley**,** C.E., Sheppard, D.A., Paskevicius, M., Tian, H., **Chaudhary A.L.**, Murshidi, J., (2011) *Light Metals and Porous Materials for Hydrogen Storage*, IEA Hydrogen Implementing Agreement, Task 22 Fundamental and applied hydrogen storage materials development, IEA HIA Expert Workshop, Esplanade Hotel, Fremantle, WA, Australia, January 16 – 20.

Chaudhary A.L., Paskevicius, M., Sheppard, D., Buckley, C.E., (2010) *Synthesis of Mg_2Si nanoparticles to enable hydrogen reversibility via improved reaction Kinetics*, Alternate Energy Technology Symposium Pacificchem 2010, Honolulu, Hawaii, Dec. 15 – 20. ALTE 162, p. 237.

Chaudhary A.L., Paskevicius, M., Sheppard, D., Buckley, C.E., (2010) *Synthesis of Si nanoparticles to improve reaction kinetics and thermodynamic properties of magnesium hydride*, Proceedings of MH2010 International Symposium on Metal-Hydrogen Systems**,** Moscow, Russia, July 19 - 23, 2010.

Chaudhary A.L., Paskevicius, M., Sheppard, D., Buckley, C.E., (2010) *Synthesis of Si nanoparticles to improve reaction kinetics and thermodynamic properties of magnesium hydride*, Poster Presentation, Renewable Energy, Yokohama, Japan, June 27 – July 2, 2010.

Appendix C: Copyright Permission

Permission was granted to use the copyrighted images in the thesis and the letters of permission are given here.

RightsLink®

Home | Create Account | Help

Title: Altering Hydrogen Storage Properties by Hydride Destabilization through Alloy Formation: LiH and MgH_2 Destabilized with Si

Author: John J. Vajo et al.

Publication: The Journal of Physical Chemistry B

Publisher: American Chemical Society

Date: Sep 1, 2004

User ID

Password

Enable Auto Login

LOGIN

Forgot Password/User ID?

If you're a copyright.com user, you can login to RightsLink using your copyright.com credentials. Already a RightsLink user or want to learn more?

PERMISSION/LICENSE IS GRANTED FOR YOUR ORDER AT NO CHARGE

This type of permission/license, instead of the standard Terms & Conditions, is sent to you because no fee is being charged for your order. Please note the following:

- Permission is granted for your request in both print and electronic formats, and translations.
- If figures and/or tables were requested, they may be adapted or used in part.
- Please print this page for your records and send a copy of it to your publisher/graduate school.
- Appropriate credit for the requested material should be given as follows: "Reprinted (adapted) with permission from (COMPLETE REFERENCE CITATION). Copyright (YEAR) American Chemical Society." Insert appropriate information in place of the capitalized words.
- One-time permission is granted only for the use specified in your request. No additional uses are granted (such as derivative works or other editions). For any other uses, please submit a new request.

If credit is given to another source for the material you requested, permission must be obtained from that source.

BACK | CLOSE WINDOW

PERMISSION TO USE COPYRIGHT MATERIAL AS SPECIFIED BELOW:

FIGURE 1.4 page 12, CHAPTER 1

Figure Adapted from: Hydrogen Storage Capacities for a range of storage media, including system capacities for stores based on liquid hydrogen, compressed hydrogen and hydrides. For reference the density of liquid hydrogen and hydrogen gas at 700 bar are given on the right hand side of the graph. (N.B. gravimetric capacity for both is 100%).

Walker, G., *Solid State Hydrogen Storage Materials and Chemistry*.Woodhead Publishing Limited: Cambridge England, 2008.

I hereby give permission for Anna-Lisa Chaudhary to include the abovementioned material in her higher degree thesis for the Curtin University of Technology, and to communicate this material via the Australasian Digital Thesis Program. This permission is granted on a non-exclusive basis and for an indefinite period.

I confirm that I am the copyright owner of the specified material.

Permission to use this material is subject to the following conditions: [Delete if not applicable]

Signed:

Name: JULIE PLEASANCE

Position: TRANSLATIONS MANAGER

Date: 14/5/13

Please return signed form to Anna-Lisa Chaudhary

PERMISSION TO USE COPYRIGHT MATERIAL AS SPECIFIED BELOW:

Figure of (a) Schematic of a pressure-composition-temperature (PCT) isotherm. α is the solid solution of hydrogen and β is the hydride phase. (b) van't Hoff plot giving the enthalpy of hydride formation, ΔH

Hirscher, M., and K. Hirose. Handbook of Hydrogen Storage. Wiley, 2010. ISBN: 3-527-32273-6

I hereby give permission for Anna-Lisa Chaudhary to include the abovementioned material(s) in his/her higher degree thesis for the Curtin University of Technology, and to communicate this material via the Australasian Digital Thesis Program. This permission is granted on a non-exclusive basis and for an indefinite period.

I confirm that I am the copyright owner of the specified material.

Permission to use this material is subject to the following conditions: [Delete if not applicable]

Signed:

Name:

Position:

Date:

We hereby grant permission for the requested use expected that due credit is given to the original source.

WILEY-VCH, STM-Copyright & Licenses

Weinheim, May 22 2013

Please return signed form to Anna-Lisa Chaudhary

annalisa.chaudhary@curtin.edu.au